Alma Mater Studiorum - Università di Bologna

dottorato di ricerca in
Geofisica

Ciclo XXIX

Settore Concorsuale di afferenza: 04/A4
Settore Scientifico Disciplinare: GEO/10

MODELING UNCERTAINTY IN VOLCANIC HAZARDS WITH FOCUS ON PYROCLASTIC DENSITY CURRENTS FROM NEAPOLITAN VOLCANOES

Presentata da: Pablo Tierz López

Coordinatore Dottorato:
Prof. ssa Nadia Pinardi

Tutore:
Dott. ssa Laura Sandri

Supervisore:
Prof. Paolo Gasperini

Esame finale anno 2017

"Dicen que si continúas a algún lugar llegarás..."

Enrique Bunbury

UNIVERSITÀ DI BOLOGNA

Abstract

Faculty Name
Dipartimento di FIsica e Astronomia, DIFA

Doctor of Philosophy

Modeling uncertainty in volcanic hazards with focus on Pyroclastic Density Currents from Neapolitan volcanoes

by Pablo Tierz López

Pyroclastic Density Currents (PDCs) are fast-moving hot mixtures of volcanic gas and particles that can devastate significant areas surrounding explosive volcanoes. Moreover, volcanoes are typically multi-hazard environments where secondary processes, like volcaniclastic mudflows (lahars), can be equally or more dangerous than PDCs. In this view, quantitative volcanic (multi) hazard assessment is among the most pursued goals of modern volcanology. However, the assessment is affected by deep variability-related (aleatory) and knowledge-related (epistemic) uncertainties. De facto, hazard analyses of PDCs and lahars quantifying such uncertainties are uncommon because modeling their complex flow dynamics, in a stochastic scheme, has a high computational cost.

In this PhD, different probabilistic approaches to model and quantify uncertainty in volcanic hazard assessment are explored and implemented at two Italian volcanoes: Somma-Vesuvius and Campi Flegrei. First, it is demonstrated that simple PDC models (*Energy Cone*), coupled with Monte Carlo sampling, are able to: (1) reproduce the spatial extent of past PDC deposits, and (2) quantify epistemic uncertainty comprehensively. Secondly, by merging *Energy Cone* simulations with more complex statistical models (Bayesian Event Tree for Volcanic Hazard, *BET_VH*), a cutting-edge hazard product is computed: a multi-volcano, single-target probabilistic PDC hazard assessment over the central Campania region. Thirdly, through assembling more sophisticated PDC models (*Titan2D*) with Polynomial Chaos Quadrature and *BET_VH*, hazard curves for dense pumice flows from Somma-Vesuvius are obtained. These curves are extremely valuable for quantitative volcanic risk analyses. Finally, probabilistic volcanic multi-hazard assessment is performed at Somma-Vesuvius by combining a Bayesian Belief Network (*Multihaz*: which incorporates probabilistic hazard analyses of tephra fallout and dense PDCs and models aleatory uncertainty in lahar triggering) and a numerical model of lahars (*LaharFlow*: which allows to compute probabilistic hazard footprints). Future steps in probabilistic volcanic hazard assessment will likely require strategies that are multi-disciplinary and explicitly oriented to calculate volcanic hazard.

Acknowledgements

Vorrei cominciare i ringraziamenti di questa tesi con Laura Sandri, la mia supervisor principale durante 4 anni e mezzo di lavoro. È difficile riassumere tutto ciò che Laura ha fatto per me e quanto brava e gentile è stata come supervisor. Dalle prime mail che abbiamo scambiato prima che io arrivassi a Bologna per cominciare il mio lavoro all'interno di NEMOH (Numerical, Experimental, and stochastic Modelling of vOlcanic processes and Hazard), fino a questi giorni in cui stiamo finendo questo lungo ma eccezionale percorso che è stato il mio dottorato. Sento di essere molto fortunato di aver avuto una supervisor come Laura: sempre disponibile, sempre tranquilla, sempre infinitamente gentile. Direi che non abbiamo mai avuto uno scontro e non ho mai avuto la sensazione di essere poco seguito o trattato ingiustamente, anzi tutto il contrario. So che non molti dottorandi possono dire lo stesso e vorrei ringraziarla immensamente per il suo modo di essere. Nel collaborare con lei, ho anche sentito per prima volta che la mia ricerca era non solo apprezzata ma, soprattutto, utile per la ricerca degli altri. Dunque, è stato un infinito piacere lavorare assieme a lei durante tutto questo tempo e spero di poter continuare a collaborare con lei, e il suo gruppo, negli anni a venire.

Anche il mio co-supervisor, già dall'inizio del 2013, Warner Marzocchi, è stato un supporto eccelso per me e ho potuto imparare migliaia di cose da lui. Mi sono sempre sentito molto incoraggiato a fare la mia ricerca ed a credere nelle mie potenzialità grazie a lui. Sono molto contento che lui apprezzi il lavoro che ho fatto in questi anni e mi sento anche molto fortunato di aver potuto conoscerlo e lavorare con lui. Di nuovo, spero che il futuro ci permetta di collaborare insieme.

Ringrazio pure il Professore Paolo Gasperini, per essere stato il mio referente al Dipartimento di FIsica e Astronomia (DIFA) dell'Università di Bologna e per il suo input su alcuni aspetti della mia tesi di dottorato.

Vorrei ringraziare immensamente Antonio Costa per tutto il lavoro che mi ha aiutato a portare avanti e le sue idee, che hanno fatto migliorare molto la mia ricerca. Lui è diventato una sorta di co-supervisor, soprattutto nei primi anni di NEMOH e del dottorato. Sono molto felice di aver collaborato con lui e aver fatto i lavori che abbiamo fatto, sperando che ce ne siano di più nel futuro.

Ringrazio fortemente Roberto Sulpizio perché anche lui è stato un grande, continuo supporto durante tutto il mio dottorato e anche durante NEMOH. Le sue conoscenze sui flussi piroclastici mi hanno sempre motivato a voler sapere di più su questi complessi processi fisici. Scrivere dei lavori assieme a lui è stato un onore

e lo ringrazio profondamente per tutto il suo input.
Si ringrazia anche calorosamente Mauro Antonio Di Vito per essere stato una parte importante del "team" multidisciplinare che ha portato alla pubblicazione, ad oggi, dei due miei unici articoli come primo autore. Le sue conoscenze sui depositi del Vesuvio e Campi Flegrei, e la stratigrafia e sedimentologia dei depositi vulcanici, mi hanno aiutato tanto e mi hanno spronato a voler capire di più su tutti questi aspetti.
Lucia Zaccarelli è anche stata una parte integrante di questo "team" ed è fortemente ringraziata per tutte le sue idee, commenti e suggerimenti che hanno portato a grossi miglioramenti di questi lavori.
Vorrei anche ringraziare immensamente Jacopo Selva per tutte le discussioni su statistica e vulcanologia che abbiamo condiviso e per le collaborazioni che abbiamo sviluppato. Ho sempre trovato Jacopo molto bravo e gentile, appassionato per la ricerca e qualcuno che contagia questa passione tramite queste discussioni. Mi piacerebbe molto avere l'opportunità di collaborare di più con lui nel futuro.
Si ringrazia calorosamente il programma Marco Polo dell'Università di Bologna per avermi conferito la borsa di studio che mi ha permesso di fare il mio soggiorno di quattro mesi a Bristol (UK), nel 2015.
Ringrazio immensamente i seguenti progetti italiani: Futuro in Ricerca 2008 FIRB Project ByMur [RBFR0880SR], finanziato dal Ministero per l'Istruzione e la Ricerca (MIUR); DPC-INGV "V1 - Stima della pericolosità vulcanica in termini probabilistici", finanziato dal DPC; e ReLUIS, finanziato dal consorzio ReLUIS, di laboratori universitari di ingegneria sismica. Questi progetti mi hanno aiutato enormemente a sviluppare la mia ricerca e, per questo, sono sinceramente grato.
Si ringrazia infinitamente la Dott. ssa Chiara Cardaci e Luigi Coppola, del Dipartimento della Protezione Civile Italiana (DPC) a Roma, per avermi accolto calorosamente, e aver seguito, con impegno e gentilezza, le mie attività durante il mio soggiorno nell'Ufficio di Rischio sismico e vulcanico del DPC. Ringrazio fortemente il Prof. Mauro Rosi, referente del suddetto Ufficio, per avermi dato questa opportunità di imparare il funzionamento e le attività che ci si svolgono. Ringrazio anche immensamente Riccardo, Vittorio, Stefano e tutto il personale DPC che ci ha seguito, a me e al mio collega durante il soggiorno, il Dott. Facundo Casasola, che pure ringrazio fortemente per tutte le giornate che abbiamo condiviso dentro e fuori del DPC.
Ringrazio immensamente Andrea Panizza per essersi interessato al nostro lavoro e per lo sforzo che ha fatto per cercare di trovare lo spazio per una collaborazione.

Le sue spiegazioni sulle espansioni polinomiali, la *Polynomial Chaos Quadrature* in particolare, e gli strumenti e metodi per quantificare l'incertezza in generale, sono state estremamente preziose. Devo dire che sarei molto felice se questa collaborazione riuscisse a farsi nel futuro.
Ringrazio pure Anita Grezio per aver proposto una possibile collaborazione sulla pericolosità associata a tsunamis generati da flussi piroclastici al Vesuvio che spero si possa sviluppare nel futuro.
Nel contesto dei due lavori pubblicato fino adesso, si ringrazia Giuseppe Vilardo per aver gentilmente fornito dei prodotti DEM; Fawzi Doumaz per il suo lavoro nel compilare e rendere disponibili i dati contenuti sul sito *OpenMap*; Eliana Bellucci Sessa e Andrea Di Vico per supporto nel trattamento di dati GIS; Domenico Doronzo per aver condiviso la sua expertise in flussi piroclastici nella sua review al nostro articolo; e Lucia Capra per le energie profuse nel suo ruolo di editor.
Vorrei ringraziare la direttrice dell'INGV, sezione di Bologna, Dott. ssa Francesca Quareni, per il supporto logistico e burocratico che lei, gentilmente, mi ha dato durante tutti questi anni in cui ho avuto la fortuna di lavorare nel istituto.
Si ringrazia infinitamente Cristina Nannini per tutto il suo lavoro burocratico fatto nell'ambito del progetto NEMOH, senza il quale, il mio adattamento iniziale all'INGV e a vivere a Bologna e in Italia sarebbe stato profondamente più difficile.
Allo stesso modo, ringrazio infinitamente Anna Carta per tutto il supporto che mi ha dato e per l'immenso lavoro burocratico che ha fatto sempre per le mie missioni, contratti, ecc. In più, lei è stata sempre molto presente e disponibile nei miei confronti, sia dal punto di vista lavorativo sia umano.
Ringrazio fortemente Stefano Cacciaguerra per aver sistemato tutti i problemi tecnici che ho avuto con i miei accounts, passwords, con gli errori di programmazione che ho fatto negli anni, ecc ecc. Lui è stato molto gentile ed efficiente a risolvere tutto quanto e lo ringrazio molto per tutto.
Si ringrazia calorosamente anche Paolo Perfetti per il suo supporto tecnico, in particolare per quanto riguarda il suo aiuto che mi ha dato per cercare di sistemare il mio vecchio laptop e per l'acquisto del nuovo. Questo è sicuramente stato fondamentale per riuscire a finire il mio dottorato e quindi lo ringrazio tanto.
Ringrazio fortemente Roberto Tonini per tutti i suoi consigli, per aver cercato di trovarmi dei divertimenti al di fuori del lavoro (alla fine ho trovato le freccette) e per avermi fatto conoscere il sito di *tables generator*: mi è stato veramente utile nella scrittura della tesi.
Si ringrazia calorosamente Licia Faenza per tante belle chiacchierate e per avermi

aiutato a preparare al meglio la tesina per il corso di dottorato su pericolosità sismica. Se ho preso un bel voto è in gran parte grazie a lei.
Devo ringraziare tante altre persone che lavorano o hanno lavorato ogni giorno all'INGV, sezione di Bologna, e che ho avuto la immensa fortuna di conoscere. È stato un enorme piacere chiacchierare con tutti loro, sia di lavoro sia di altre cose, e una non piccola percentuale di loro sono diventati i miei amici qui a Bologna. Cercando di riassumere qualche *highlight* su di loro: Carlos e Alex sono stati i miei primi compagni d'ufficio e ho imparato molto da loro. Da Carlos, tutte le sue conoscenze storiche e politiche che tanto mi affascinano. Abbiamo condiviso tanti momenti negli anni e lo ritengo un caro amico. Da Alex, le sue conoscenze nel modellare i processi fisici in modo stocastico; abbiamo anche avuto il tempo di parlare di tante altre cose ed è stato assai bello averlo conosciuto. Dmitri è stato sempre una delle persone più vicine, ho apprezzato molto il suo modo di essere gioviale e tutte le volte che abbiamo discusso sui vulcani ed i loro processi. Ricorderò anche per sempre l'aver condiviso l'esperienza del *Cities on Volcanoes 8* a Yogyakarta (Indonesia). Anche Giovanni Chiodini mi ha reso partecipe di belle conversazioni sui vulcani, condividendo con me la sua sconfinata saggezza. Mi ha fatto anche piacere che lui apprezzi la mia condizione di *maño*. Irene mi ha aiutato molto, quando sono arrivato, con aspetti di programmazione a me sconosciuti e, nel tempo, abbiamo condiviso molti momenti, aperitivi, convegni, ecc; è stato un grosso piacere. Brunella è stata molto speciale come amica, probabilmente quella più vicina, e si può dire che è stata la mia insegnante non-ufficiale di italiano. La ringrazio molto per tutte le volte che mi ha insegnato/corretto delle parole. In generale, è stata molto brava, nonostante io pensassi che fucile e bruciare si scrivessero *fuscile* e *brusciare*. Letizia è stata un'altra persona che è diventata proprio una cara amica. Mi intristisce pensare che, probabilmente, dovrò andare via e non potrò chiacchierare con lei della vita, del lavoro, di tanti scherzi che ci siamo fatti, tante chiavette rubate, del suo bel matrimonio, dei modelli Bayesiani, ecc. Julie è stata compagna d'ufficio storica (oramai da 3 anni almeno) ed è una persona molto gentile e piacevole. Insieme a suo marito, Carmine, abbiamo condiviso tante serate di divertimento, specialmente, quella del loro matrimonio, che rimarrà per sempre come una delle serate più belle (se non la più bella) che ho avuto nel mio tempo a Bologna. Adriano Gualandi è stato anche un grande collega di lavoro e amico. Mi sarebbe piaciuto portarlo di più in giro ma mi sa che eravamo tutti e due troppo presi dal lavoro ed altri impegni. Comunque, è stato sempre un grosso piacere parlare con lui e condividere dei momenti insieme. In

particolare, devo ringraziarlo fortemente per avermi fatto scoprire che a Bologna si giocasse a freccette. Valentina è stata una gran collega di ufficio e anche una amica. Abbiamo avuto i nostri "scontri" come, ad esempio, la presunta cucina spagnola basata unicamente sul fritto, ma abbiamo condivisi tanti belli momenti, incluse le colazioni da Cuppi che saranno sempre originalmente dovute a lei. Simone è anche un collega storico, anche se non abbiamo mai condiviso l'ufficio. Ci siamo però divertiti abbondantemente e abbiamo riso con tante conversazioni all'ora di pranzo, nelle serate, nei matrimoni... Bella lì! Sarfraz has been another great colleague and friend. I thank him all his positive mind setting, his jokes and all his mathematical knowledge that he shared with me, freely and nicely. Adriano Cavaliere è stato anche assieme a tutti noi nei momenti migliori, come nei matrimoni, o le mitiche serate da Dynamo. Abbiamo avuto un gran divertimento insieme, insomma. Davide è diventato da subito un caro collega e un amico con cui parlare di mille cose anche se tante volte centrati su un tema particolare. Ringrazio lui per le birre Pietra, portate da La Spezia, per alleviare lo stress della scrittura di questa tesi. Paolo Oliveri è anche diventato un amico con coi parlare di temi vari, principalmente di tennis e la grandezza infinita del mitico Roger Federer. Ho conosciuto Giulia fuori dall'INGV, in quella meravigliosa scuola finale del progetto NEMOH a Linguaglossa, ma una volta che lei è arrivata in istituto, abbiamo costruito un bel rapporto di amicizia del cui sono molto contento. Con Damiano e Gelsomina ho condiviso delle belle pause caffè e abbiamo potuto parlare, molto gradevolmente, di come è fare un dottorato, cos'è la festa della saracca o dei giocatori più grandi della storia del calcio. Francesca è stata la nostra rappresentante dei 90s nella *80s' room*. È stato un grande piacere condivedere dei momenti al lavoro e fuori del lavoro con lei. Matthieu è anche stato collega di ufficio ed è stato bello parlare di vulcani con lui quando c'è stata la possibilità. È stato un grande piacere anche conoscere Manuel, ci siamo divertiti molto mentre lui è stato all'INGV e, alla fine, è stato l'unico spagnolo con cui ho avuto contatto all'istituto. *¡Salud Manuel!*. Ringrazio anche i colleghi di ufficio temporanei come Ka Lok e Kathrine e, soprattutto, il *trio* di NEMOH che è passato da noi: Alex, Karen e Edu (dopo parlo di tutti loro). Comunque, Alex è un caro amico e spero ci rivediamo presto. Durante il suo soggiorno a Bologna, abbiamo condiviso tanti bei momenti, inclusa una delle serata più grandi della mia storia bolognese in zona Zamboni... Con Karen abbiamo anche fatto dei bei giri, gelati in Piazza Maggiore, cene all'Osteria dell'Orsa,... mi son sempre trovato molto bene con lei.
Ringrazio pure Barbara Lolli per organizzare i seminari all'INGV, sezione di Bologna,

assieme a Lucia Zaccarelli. Ringrazio Silvia Pondrelli per utili conversazioni durante diverse pause in questi anni. Vorrei infine ringraziare immensamente Micol Todesco per l'accoglienza all'INGV dal mio primo giorno qui, per gli interessanti commenti che ha fatto durante i miei seminari e per tutta la sua energia dedicata ad organizzare, estremamente bene, la squadra INGV nella Notte dei Ricercatori 2016 a Bologna. Ringrazio molto anche tutta la squadra: è stata una esperienza fantastica averne fatto parte.
Vorrei ringraziare calorosamente Rosalino ed Ileana per la loro simpatia, amabilità e gentilezza con cui mi hanno sempre trattato.
Fuori dall'INGV, sezione di Bologna, ho avuto la fortuna di interagire con molti altri ricercatori e molte altre ricercatrici italiani/e, in situazioni e posti assai diversi (escludendo quelli più legati a NEMOH). Vorrei ringraziarli tutti per le chiacchiere di lavoro che abbiamo condiviso. Nonostante sia impossibile ricordarli tutti, lascio traccia di qualche nome (se dimentico qualche nome importante, scusatemi!): Matteo Taroni, Stefania Bartolini, Tommaso Esposti Ongaro, Andrea Bevilacqua, Matteo Cerminara, Matteo Bagagli, Chiara Montagna, Piero Dellino, Roberto Isaia, Salvatore Inguaggiato, Christian Bignami, Pamela Roselli, Irene Munafò, Antonio Rinaldi, Luigi Passarelli, Irene Manzella, ...
Ringrazio immensamente l'Università di Bologna, per avermi dato l'opportunità di fare un dottorato in geofisica. In particolare, ringrazio molto il DIFA per avermi invitato a dare un seminario sulle mie attività di ricerca e quelle dei miei colleghi di dottorato.
Questi colleghi di dottorato sono diventati in certo modo anche i miei amici, anche se non ci siamo visti tante volte. Però, le esperienze "estreme" dei corsi di dottorato ed il lungo percorso che ci ha portato alla consegna della tesi, con seminari di fine terzo anno in mezzo, ci hanno reso molto vicini. Siamo dovuti rimanere molto uniti e ci siamo dovuti aiutare molto per riuscire a finire questa tesi di dottorato. Mi sento molto fortunato di averli conosciuti e ho apprezzato immensamente la ricchezza che il nostro rapporto ha preso dalla varietà di origini, backgrounds e personalità che abbiamo tutti noi. È stato un enorme piacere essere parte del nostro gruppo. Grazie mille di tutto: Andrea, Davide, Ines, Luigi, Marco, Marcello e Grazia.
Si ringraziano i coordinatori del dottorato in geofisica che abbiamo avuto in questi tre anni e mezzo di percorso per il loro lavoro nel gestire, al meglio possibile, il dottorato: Prof. Michele Dragoni e Prof. ssa Nadia Pinardi.
Vorrei anche ringraziare calorosamente tutti i professori dei corsi di primo anno di

dottorato per la loro disponibilità, il loro entusiasmo e per averci dato un'ampia visione dei problemi geofisici, oltre le nostre specializzazioni della tesi di dottorato. Ringrazio infinitamente Giorgia, la mia insegnante di italiano quando sono arrivato a Bologna. Con la sua dedizione e attitudine possitiva, lei ha fatto possibile che io raggiungessi un livello della lingua adeguato in un breve periodo di tempo e questo mi è servito tanto nel svolgere le mie attività di ricerca, sia dentro all'interno dell'INGV di Bologna ma anche con tanti altri ricercatori italiani provenienti da altri enti di ricerca.

Per ultimo, fuori dell'ambito della ricerca, ho pure trovato molte persone a Bologna che sono state fortemente importanti per me, e hanno fatto che il mio periodo qui in Italia sia stato veramente piacevole e felice. I miei primi coinquilini: Nicolò e Miguel. Grazie mille di avermi ammesso in quella stupenda casa di fronte a Lucio Dalla. Abbiamo avuto tanti momenti di gioia ed è stato così bello avervi conosciuto. Anche con Lucía ci siamo divertiti tanto e, soprattutto con Trunkl, grandi serate all'Irish a parlare un po' di tutto. Dobbiamo venirti a trovare in Slovenia. Ringrazio immensamente il mitico Andrea, l'altro mio coinquilino durante i primi due anni a Bologna. È stato incredibilmente bello condividere casa e tante chiacchiere con lui, giornate di 25 Aprile al Pratello, cene al giapponese *all you can eat* e tutti i bei momenti che abbiamo condiviso. Ringrazio infinitamente tutti i miei coinquilini nella seconda casa a Bologna: Luigi, Gianfry, Julian, Emanuele, Marek, Trung, Tommaso e Riccardo. Luigi ci dà la felicità e la speranza nella vita e finirà che dopo aver consegnato la tesi andremo tutti insieme al Soda Pops. Gianfry sempre tanto carino, ci porta in Piazza dei Tribunali a bere dei cocktail ed essere fotografati dai paparazzi. Julian è stato il giovane della casa per tanti mesi e ci siamo divertiti molto, includendo le serate di Champions all'Irish. Con Emanuele abbiamo scherzato e riso fino all'infinito e abbiamo visto tante partite di tennis insieme, tra queste la mitica finale vinta da Wawrinka a Roland Garros. Marek è stato il mio sostituto mentre ero a Bristol ma dopo ho avuto la fortuna di conoscerlo e abbiamo parlato tante sere in inglese su mille argomenti diversi. Trung, il nostro cuoco internazionale, ci ha pure fatto passare dei bei momenti di convivenza. Tommaso, il nuovo giovane *toppe* della casa, ci racconta tutte le sue belle e variegate storie e mi fa parlare sui vulcani, e la scienza in generale, che fa molto piacere. Per ultimo, ma per niente meno importante, il grande Ric, che mi insegna a parlare come un autentico *regaz* bolognese (e.g. *oh vez, domani facciamo cabò e gran taffio in piazza*). In scambio, io gli insegno la vera parlata dei *cos* di Zaragoza, soprattutto i termini più importanti come *pillar, rayada, liada*,

ecc. Ci sono troppi momenti da ricordare e lo ringrazio molto di tutto. Comunque, secondo me Di Caprio in *Shutter Island* non è matto ma lo stanno imbrogliando perché lì fanno delle lobotomie ogni giorno.
Infine al paragrafo di ringraziamenti in italiano, non potevano mancare tutte le persone del mondo delle freccette che ho avuto l'immensa fortuna di conoscere qualche mese fa. Grazie mille a Luca per avermi introdotto nella squadra del Dragon Pub e, di conseguenza, nel meraviglioso mondo delle freccette nell'Emilia-Romagna. Con Riccardo e Sara abbiamo fatto un certo numero di serate al Dragon che sono state eccezionali: tante freccette lanciate, scherzi fatti, birre bevute, gramigna alla salsiccia e cotolette bolognesi mangiate... Assieme a Riccardo siamo pure andati a tre gare regionali di freccette che sono state sempre delle ottime esperienze sociali (inclusa l'ultima volta quando lui mi ha battuto 3-4 in una partita molto bella). Ringrazio fortemente tutti gli altri giocatori del Dragon e delle gare regionali, per l'accoglienza e tutto il divertimento che ho avuto con voi: Gallo, Vanes, Grillo, Simone, Michela, Anna, Cristina, Raffaele, Valentina, DePa, Catallo, ecc.

In the "English" part of the acknowledgements, I want to start with the EU FP7 project NEMOH (grant agreement no. 289976). Because everything started with NEMOH. Back to the beginning of 2013, NEMOH gave the opportunity to work as a researcher in an exceptional international environment. Many many thanks go to Paolo Papale, *papa* NEMOH, who led this astonishing and wonderful adventure. He gave all of us the means to grow, personally and scientifically, and I hope he feels we gave some good work back during our time as NEMOH fellows. Rafaela Pignolo, *mamma* NEMOH, was crucial for the success of NEMOH as well. She worked unbelievably hard to fix all the problems that we might have faced during NEMOH, many thanks for everything. Also Alessandro Fornaciai, *zio* NEMOH, put a lot of effort to kick off NEMOH and keep it going smoothly all the way. He is also a PhD colleague and it's been such a pleasure having got to meet him. All the lectures and researchers that took part in the NEMOH schools and events are extremely thanked for their time and their passion in teaching us so many different concepts of modern, quantitative volcanology. Special thanks go to Prof Willy Aspinall for all the discussions shared and all the advice he has given me during these years. His advice of attending the Cabot/CREDIBLE workshop on uncertainty in natural hazards in Bristol, back in July 2013, turned out crucial for the development of some aspects of my PhD. I strongly thank Dr Olivier Jacquet for showing his interest in my research during the mid-term NEMOH meeting. It would be great to collaborate in the future. And then, finally, all the NEMOH brothers

and sisters who complete the NEMOH family: Alex, Johannes, Claudio, Antonio, Cristian, Julie, Karen, Lena, Deepak, Edu, Damien, Samantha, Laura, Hannah, Francisco, Werner, Beatriz... 18 of us, sharing amazing experiences worldwide during three years of intense work but tons of great fun and joy with you. I must admit it was tough at the beginning. I'm a shy person, no matter how talkative or light-hearted or just stupid I may seem after I have become close to people. So it took me some time to really get the most out of our experiences. Nonetheless, during the first half of 2014, I started feeling better with myself and, since EGU 2014 and, especially, during the NEMOH school in Iceland, I truly considered myself a member of the awesome NEMOH family. I couldn't have been happier with all our meetings afterwards. I can recall Prague, Linguaglossa, Catania and the Christmas NEMOH reunion in Bristol (with Julie, Karen, Antonio and Johannes) as some moments in which we shared almost everything, had a tremendously wonderful time together and, I can tell, I really felt over the moon. Well, apart from the moment when Julie played that cylon trick on me.

The following EU FP7 research projects are also massively thanked for having supplied the financial resources to design and carry out part of the research activities during my PhD: MED-SUV (MEDiterranean SUpersite Volcanoes, grant agreement no. 308665), VUELCO (Volcanic unrest in Europe and Latin America: Phenomenology, eruption precursors, hazard forecast, and risk mitigation, grant agreement no. 282759) and REAKT (Strategies and tools for Real Time EArthquake RisK ReducTion, grant agreement no. 282862). Moreover, the NERC STREVA project (grant number NE/J019984/1) is kindly thanked for supporting the development of the lahar model (*LaharFlow*).

I would like to profoundly thank all the staff at the *My English School (Myes)* of Bologna for all the help they gave in improving my level of English and the positive vibrations I always encountered every time I went to lessons there. Special thanks go to Roxy for managing all my activities and bureaucratic stuff and for all the nice talks we shared during the years I went to Myes. Enormous thanks are given to all my teachers, I list some of them but they all were extremely gentle and great with me: Sarah, Liz, Ross, Mike, Aleks (with whom we also shared a lots of nice Spanish/English conversations outside of the school), TJ, Jessica, Clare, Melissa, ... (sorry for everyone I forget). Likewise, huge thanks go to all my partner students: Angela, Paolo, Rita, Michele, ... (I'm forgetting thousands here...). Many thanks to all of you!

A bunch of thanks are sent to Steven Gunn and Sunil Patel for producing and

distributing this nice LaTeX template which surely saved me quite an amount of time in writing this thesis down.
Since I arrived to Bologna, I have been able to visit, for several months, two different research institutions abroad. In 2013, I was a visiting J1 scholar at the Department of Mechanical and Aerospace Engineering, University at Buffalo (USA). I am extremely thankful to Prof Abani Patra who accepted me in his group and helped me learn a lot of aspects about numerical modeling of volcanic mass flows and uncertainty quantification techniques. Lots of thanks are also given to Prof Greg A. Valentine who introduced me to the Volcanology group at the Department of Geology, allowed me to participate in their blast experiments and shared with me his deep knowledge on volcanology and Pyroclastic Density Currents (PDCs), always treating me in a very nice and respectful manner. Ramona Stefanescu is extremely thanked for all the help and support she gave me during my four months of working in Buffalo. She was the closest person I had there and I am truly delighted to have met her. I thank Sarah Ogburn very much for providing me with her expertise in Titan2D modeling and for sharing the Montserrat data that, hopefully, we can put together into potential publication soon. My other office mates are also very thanked for all the good time we had together and all the great chats we had: Rohit, Topher, Hossein and Kyle. Likewise, I really thank Alison and Ingo for welcoming me at the Department of Geology and all the Volcanology group for letting me participate in their seminars from which I learned quite a lot. Very special thanks are given to the Center for Computational Research (CCR) at the University at Buffalo, for the resources they have supplied. In particular, I am deeply grateful to Ms Doris Sajdak who has taken a lot of her time to help me out with all the problems I have come across during these years. I thank Jorge Bajo so much for helping me find a place to live in Buffalo and I also thank my housemates for the good time we had together, especially the tennis matches with Eduardo (and Ramona) in the nearby courts. Finally, I thank Rajesh for all the times we went out for dinner or beers, especially the one in which we went to watch the Barcelona-Madrid match at noon on a Saturday. It was certainly peculiar to start drinking beers at that time of the day.
My second experience as a visitor in a research institution abroad was at the University of Brisolt (UK). From August to December 2015, I worked at the School of Earth Sciences, under the supervision of Dr Henry Odbert. I would like to thank him so very much for all the support he gave me since I first contacted him to ask whether I could go to Bristol until the very last days of my secondment, working

on the lahar data of Montserrat. I found a great pleasure to work with him and I wish him the best in his new position. Thanks to Dr Henry Odbert, I was introduced to Dr Jemery Phillips and Dr Mark Woodhouse and what we started during my time in Bristol is now turning into the forthcoming submission of, I reckon, a nice paper about probabilistic volcanic multi-hazard assessment. I am extremely thankful to Dr Jemery Phillips for showing interest in my research activities and for boosting great discussions about lahar triggering and propagation, numerical modeling and multi-hazard assessments. I have learned a lot from him and I hope I will learn even more during our collaboration. Similarly, gigantic thanks go to Dr Mark Woodhouse for sharing, in a very relaxed and super nice way, his broad knowledge in numerical modeling of geophysical flows. It's been fantastic to have had the chance to work with him and, hopefully, we will find more chances to collaborate in the future. A big deal of thanks also go to Dr Francesca Pianosi for her openness to exchange ideas about our working projects and for sharing with me her great knowledge in statistics and sensitivity analysis. It would be awesome to collaborate with her and her group if possible. Many thanks to Dr Matteo Taroni as well for involving me in interesting discussions about science, mathematics, statistical models of geophysical processes, etc. I always find talking to him very fruitful. Massive thanks are given to the hotstuff-seminars team, of the School of Earth Sciences, for inviting me to give a seminar about the research I had been developing during my PhD. It was great to see a nice interest in my research topics and many thanks for the questions! In particular, I thank Dr Susanna Jenkins very much, for she has always shown interest in my research since we first met in Indonesia, more than 2 years ago. Broadly, I would like to deeply thank all the department colleagues with who I had the joy to chat and exchange views about work and non-work aspects. I just write down some names, hoping no one feels excluded: Julie, Karen, Pablo, Mikel, Paul, Jonathan, Luke, Álvaro, Irving, Emma, Alia, Marit, Marzena, James, Ery, ... Marzena was also my table mate during my very first experience within NEMOH. I remember pleasingly our discussions about igneous petrology during the school. Huge thanks go also to the volcanology-coffee team on Thursdays. There were good times and I swear I tried my best to be there every Thursday and participate as much as possible in the friendly conversations that were created. My office mates were very special to me. I had great fun in sharing the office with them. María (*¿qué onda, morenita?*) adopted me like a brother since the very first day I went to the university. Despite being a *gachupín*, I think we got along with each other very well and we enjoyed a

lot joking around and talking about very diverse things. Tom was the other office mate when I arrived. I thank him a lot for trying to make me fit in and for all the discussions about statistical models of volcanic processes that we developed. Meeting Masako was an extremely nice experience. She was very sweet and polite. I thank her very much for being this way and for all the Japanese that she taught me. I keep all the pages with your writing. Chiara was also an important part of my stay in Bristol. We had lots of fun together, including the visit to Cardiff and its beautiful castle. I strongly appreciated the things that she told me about the *Friulano* as a language, it was fascinanting. A great pile of thanks go to Zhengquan for several different things: our discussions about PDCs; for allowing me to witness his experiments (which I hope went perfectly); for telling each other our respective ways of doing research about similar topics; for sharing his nice article with me... It was great when the new PhDs moved in as well. From Tim, I enjoyed his positive and fun attitude towards life and research. His passion for meteorites was just delightful and all his jokes were very amusing. Plus, I really loved his Manchester accent: if I ever develop a Bristish accent, I would like to have that one. Last but not least, the whole group of Mexican-Chilean-Italian-Japanese people: I already talked about María, Chiara, Matteo and Masako but there were Tatyana, Martín, Gaby, Irving, Alessandro, ... Tatyana was our lunch (and sometimes evening-coffee) mate for four months and meeting her was an elating experience. Alongside María, we joked around whatever aspect in life and I felt very glad and fortunate to have her and them everyday at the university. I met Martín shortly after I arrived to Bristol and it was just awesome to share my time there with him. All the information he gave you about Bristolian facts and all the great places (from museums to pubs) where he (and the rest) took me to. Thanks to this I could discover tens of different types of beer -a decent percentage from local breweries- that were served in Bristol: very tasty experience. Many many thanks to Gaby as well for telling me facts about the *Mapuches* and other native peoples of Chile. I profoundly hope that they all can be in peace with the rest of the community and they are treated with respect and honor. I also thank him for the cards game he gave me: you bet we had loads of fun playing with Isabel. Finally, all my house mates, including Kate with whom I didn't have the luck to live but I firmly believe that she is a wonderful person. I was quite touched by all the "presents" she left for me in her/my room when she left: it was a really nice gesture. Tara, who alongside Peter, cheered me up with "baby whiskies", her wide knowledge about movies and her sense of humour and her funny happy-go-lucky

stories. Many thanks for all that. Juliet was the first housemate I met when I arrived at Bristol. I am keenly grateful to her for all the conversations we had in the living room, for joining the NEMOH team during the reunion weekend and for being always so nice to me. And, Julie (*muahaha, kataboom!*), so special and unique. It was unbelievably terrific to share the house with you and the days we took to walk around Bristol were great fun. Many thanks for being Julie and for having offered me a place in your house.

There are some other people that deserve special thanks concerning my path towards the PhD completion. Dr Nick Varley is extremely thanked for having contacted me to collaborate on modeling uncertainty in PDC hazard at Volcán de Colima, in Mexico. I'm very glad with the results that have been already obtained and I look forward to keeping our collaboration going. I am deeply grateful to Dr Sylvain Charbonnier for, firstly, reviewing, in a very professional and dedicated way, the two papers that I have published as first author so far; and, secondly, for all the gratifying discussions about PDCs, and their modeling, that we have shared at several international meetings. It's been great to have started working together and, hopefully, our ongoing collaboration can be developed further in the near future. Dr Chris Newhall is sincerely thanked for all the work he did during the NEMOH school in Linguaglossa (Italy), for telling us some of his life experiences in a very respectful manner and for sharing part of his immense knowledge about volcanoes and volcanic hazard with me. I massively thank Prof Mark Bebbington for providing me with input about our probabilistic multi-hazard assessment of rain-triggered lahars during the very preliminary stages of the work and for reckoning that I could be a suitable candidate for his expert-elicitation exercise about volcanic hazard from New Zealand volcanoes. I felt incredibly honored and I learned a lot about these volcanoes along the process of compiling the questionnaire. Dr Peter Webley is enormously thanked for having thought of our AGU2013 conference proceeding as a potential contribution for their nice AGU monograph. It was very pleasing to take part in the project and Dr Peter Webley performed superbly as one of the editors (who are also kindly thanked) for this special volume. Prof James D.L. White is also greatly thanked for his work in handling the last editorial steps in the publication of our article in Bulletin of Volcanology. Many other researchers have provided me with very useful discussions, conversations and/or data about volcanic processes and hazard, uncertainty, physical and statistical modeling, etc. I am extremely thankful to all of them. Again, even though the list cannot be complete, I will cite some names: Mr Stuart Mead,

Prof Jan Lindsay, Dr Eliza Calder, Emeritus Prof Raymond Cas, Dr Ting Wang, Mr Leonel Lara Estrada, Prof Thomas Dunne, Dr Chris Johnson, Ms Aishling Barrett.

Finalmente, los agradecimientos para todas las personas que siguen en España o que hicieron (y hacen) mi vida durante todos los años que viví en Zaragoza. Sigo teniendo la esperanza de algún día volver por allí pero no estoy seguro de cuándo podrá ser. De momento, quiero agradecer al profesor Marceliano Lago San José por todo el apoyo y las fuerzas que me dió en el momento más difícil de mi vida. Si, a día de hoy, me puedo considerar un investigador es por el trabajo que empecé a desarrollar con él. Muchísimas gracias. A Carlos Galé por toda la ayuda y las ganas que me transmitió durante el tiempo que tuve la suerte de tenerlo como co-supervisor. Le agradezco mucho también que nos sigamos viendo y sigamos intentando hacer ciencia juntos, es todo un placer. Igualmente, Teresa Ubide fue una piedra clave para construir la base de mi corta carrera como investigador. Espero seguir en contacto con ella y el resto del grupo por muchos años. Patricia Larrea fue mi referente del grupo durante el máster y mientras estuve en Zaragoza. Le agradezco mucho que su experiencia me haya enseñado que se puede compaginar una vida sentimental plena con hacer investigación al más alto nivel internacional. ¡Mucha suerte con todo, chicos!

A Joan Martí, porque, en realidad, no todo empezó con NEMOH. Todo empezó a finales de 2012, con una maravillosa experiencia que fue el curso internacional de post-grado en vulcanología en Olot (Girona), organizado por el Institut de Ciències de la Terra Jaume Almera (ICTJA, CSIC, Barcelona), la Universitat de Girona y la Fundació d'Estudis Superiors (FES) de Olot. Durante el curso, pude aprender una amplia y variada colección de conceptos y aplicaciones para el estudio de la vulcanología: desde los depósitos y rocas volcánicas, hasta diversas técnicas cuantitativas para modelizar procesos volcánicos, monitorar volcanes o calcular peligrosidad volcánica. Indudablemente, este curso fue el primer paso que me llevó hacia NEMOH y hacia el doctorado en geofísica que estoy intentando obtener a día de hoy. Ha sido siempre un placer encontrar a Joan y sus colaboradores en las conferencias en las que he participado y le agradezco mucho todo lo que ha hecho por mí. También agradezco a los compañeros del curso el buen tiempo que pasamos juntos, en general, durante tres intensas semanas: Xevi, Dario, Stefania, Laura, Helena, Xavi, Carlos, Rubén, ... Os deseo lo mejor en el futuro y ojalá nos juntemos en algún otro momento (como aquel genial tapeo con Xevi y Dario cerca de Sant'Antoni (Barcelona) en 2013 o el curso de estadística Bayesiana de Warner

Marzocchi que seguimos con Stefania en 2014).
A mis amigos de toda la vida y el grupo de los Hoolies en su conjunto: Traso, Chorche, Feliz, Peines, Ave, Javi, Adrián, Nacho, Berroya, Héctor, Álvaro, Monty, Mostacero (trillones de gracias por la estupenda boda que nos brindasteis), Arturo, David, Miki (tu boda tampoco desmerecerá, eso está claro). El otro día echábamos cuentas con Traso que con él, Peines, Ave, ... nos conocemos desde hace ¡25 años! Me siento muy afortunado de haberos tenido siempre a mi lado, aunque sea en la distancia en los últimos años. Millones de gracias a Chorche (y Rocío), Traso (y Līva) y Anchel por el viaje que nos hicimos en Holanda a finales de 2015. Un enorme placer como siempre (*¡coño, Anchel! ¿Cuándo has llegao?*). Muchas gracias a Peines y Natalia y a Traso y Līva por las sendas maravillosas visitas que me han hecho durante el tiempo que he estado en Bologna. Espero que disfratarais de la comida, la ciudad, etc.
Agradezco mucho también a todos mis amigos y amigas del pueblo natal de mi padre (Huerto, Huesca) y a toda la gente que, cada vez que estoy allí, me hacen sentir como si no me hubiera ido nunca y disfrutamos de tantas fiestas, *charretas* y buen rollito todos juntos. Las fiestas de Huerto siguen siendo el acontecimiento del año para mí y espero veros a todos y todas allí este año.
Otro puñado gigante de gracias va dedicado para todos los geolocos y geolocas que hicieron la carrera y el máster uno de los mayores placeres que haya experimentado nunca en mi vida. Esto incluye, claramente, a todos y todas que no son geólogos pero es como si lo fueran, los queremos igual o más. Aquí hay demasiados como para nombrarlos a todos, basta con abrir el facebook y ver las fotos de nuestras cenas navideñas: una auténtica maravilla teneros cerca y espero que mantengamos la piña durante toda la vida. Cito los casos particulares del grupo de visitantes a Bologna: Isabel Chueca fue, si no me equivoco, la primera que me visito sin contar a Isabel (Marín). Hicimos buena fiesta con su hermano y fue genial. Calvín, Edu, Roi, Elisa, Ali e Isabel (Marín) fueron la primera visita en grupo que tuve. Me hizo muchísima ilusión teneros aquí y que pudierais ver los *Appennini*, visitar la ciudad y conocer míticos lugares como la plaza de los cristales. El Calvín estaba en su salsa, que no nos engañe. ¡Y Adelita! Que, pobrecica, tuvo que soportar temperaturas extremas y una fiesta, casi todavía más extrema, el día antes de una boda en Firenze. Le agradezco muchísimo la visita y esa noche fue mítica: vino blanco en la terraza, varios *negroni* por la ciudad y un super concierto de guitarra en Piazza Maggiore (que, a día de hoy, ha sido el único que he hecho en cuatro años).

Otra banda de sospechosos habituales... el Posturas Darts team: Etién (captain eterno), Darío, Ánchel, Chorche, Ave, Chabi, Anoro, Juanillo, Mostacero, Pelos y Rubén. Trillones de gracias por todos los momentos que disfrutamos, alrededor de birras, kalis y dianas, cada vez que puedo volver por Zaragoza. Y muchas gracias por haberme dejado jugar partidos oficiales desde que estoy aquí: me hicieron muy feliz todos. Espero veros muy pronto a todos: *you'll never dart alone*.

A todo el equipo de Red Alert, empezando con Mercè, a la cual agradezco enormemente la oportunidad que me dió de poder colaborar en un campo de refugiados. Fue una experiencia tan intensa como maravillosa. Puede que haya estado desconectado porque el terminar esta tesis ha consumido un enorme porcentaje de mis energías, pero me acuerdo de muchas caras, personas, historias que vi durante el tiempo que estuvimos allí con el grupo y no me olvido de todos ellos. Ojalá consiga volver a ponerme en marcha y ayudarles de nuevo. El grupo que conocí en el terreno: Mercè, Joan, Mireia, Luti, Ramón, Gemma, ... decir que sois maravillosos y que admiro profundamente vuestra fuerza, vuestras ganas, vuestra dedicación... Fue increíblemente genial estar allí con todos vosotros. Del mismo modo, el resto del grupo que aún no he conocido: mil millones de gracias por ser como sois y por todo el esfuerzo y trabajo que ponéis en la causa. Me quito el sombrero y espero dar un poco de más de mi parte en el futuro.

A Lauri, por ser esa estupenda amiga que no importa hace cuánto tiempo no hayas visto, siempre estará ahí disponible con una sonrisa y con ganas de escuchar y contar vivencias muy agradablemente. En este periodo, parece que tendrá más cosas que contar... ¡Muchísimas felicidades y muchas gracias por todo!

En 2011, al escribir los agradecimientos de mi tesis de máster, no mencioné a Vir. Quiero agradecerle aquí los buenos y los malos momentos que vivimos juntos. Los buenos (y muy buenos) porque hubo un tiempo que fuimos felices y fuiste mi primera pareja de largo recorrido que había tenido hasta entonces. Los malos porque creo que es cierto lo que dicen que se aprende más de una derrota que de una victoria. En mi caso, nuestra derrota me hizo crecer mucho como persona y si estoy aquí, en Bologna, escribiendo estas líneas y cerca de obtener un doctorado, es en parte gracias a que nos conocimos.

A la familia Marín Beltrán, por todo el apoyo que me han transmitido desde la distancia y desde la cercanía. Pablo Marín me visitó junto a su hermana e hicimos buenos paseos por *Parco Talon* y *San Luca*, una subida a la *Torre degli Asinelli* y disfrutamos de muy buena comida y bebida en una perfecta compañía. Fernando Marín (junto a Evgeny Polomoshnov) nos acogió, a mí y a Isabel, en un modo

excepcional en su casa de Zürich y los dos hicieron que nuestra visita a Suiza (para mí la primera y única hasta ahora) fuese maravillosa. Y José Mari Marín y Maribel Beltrán, que me han apoyado mucho y se han interesado por la temática de mi tesis y me han hecho sentir siempre muy agusto y apreciado. Muchísimas gracias a todos.

A la familia López (Trapisonda), por estar siempre pendientes de mí y de mi evolución en el extranjero y por brindarme tantas cenas maravillosas, vermuts, etc. con el cariño y la alegría que sólo la familia puede ofrecer. Os quiero mucho a todos y todas.

A Manoli y a Andrea, por acordarse de mí y desearme siempre lo mejor en la vida. Yo también se lo deseo y no importa los reveses que la vida pueda darnos, seguimos teniéndonos los unos a los otros y eso creo que debe darnos felicidad. Os quiero mucho.

A mi madre y mi hermano, simplemente por serlo, dije en 2011. Sigue siendo cierto: saber que sois mi madre y mi hermano me llena de orgullo, calma y una inmensa felicidad. Os echo muchísimo de menos y me encantaría estar con vosotros cada día pero supongo que los caminos de la vida no nos siempre fáciles. Espero volver tarde o temprano y, mientras tanto, pienso disfrutar de vosotros todo lo que pueda cada vez que nos veamos, aquí o allá, donde sea. Os quiero con toda mi alma. "*Venceremos*".

Y llegó el turno. A Isabel... ¿Qué te puedo decir después de 12 años de habernos conocido? ¿De 5 años de habernos decidido a construir un proyecto común juntos? ¿De más de cuatro años en diferentes ciudades? Te digo: *que el fin del mundo te pille bailando...* juntos los dos, por siempre. El doctorado está siendo un largo viaje pero es maravilloso estar recorriéndolo contigo. Hay demasiadas cosas por las cuáles agradecerte. Me quedo con la dulzura y el cariño que ofreces, ese corazón enorme y ese amor por la vida y las personas (en particular las más desfavorecidas) que no hay mecanismo de defensa que pueda ocultar. Eres una persona maravillosa y ser tu compañero de viaje es la experiencia más intensa y preciosa que he vivido hasta hoy. *A galopar, a galopar...* Te quiero mucho.

Contents

List of Figures

List of Tables

A mi padre,
que me enseñó que el éxito académico está distribuido como una campana de Gauss: existe una pequeña proporción de personas que, por aptitud innata, están situadas en los extremos del dominio de la variable. Sin embargo, la gran mayoría de las personas, debido a su aptitud innata media, están situadas en valores intermedios de la variable. Dada tu aptitud innata, cuánto eres capaz de desplazarte hacia valores elevados de la variable dependerá de tu trabajo y esfuerzo. "Actitud". Creo que la he tenido, la tengo y la tendré. Ojalá pudieras verlo por ti mismo... "Venceremos"

Chapter 1

Introduction and background

1.1 Explosive volcanism

Volcanic activity is one of the most powerful and spectacular phenomena that can be witnessed in nature. It is also the result of one of the most complex chains of physico-chemical processes within the natural world. Magma (a given volume of partially melted rock) is formed at depths which range between few kilometers at mid-oceanic ridges up to few hundreds of kilometers at subduction zones, depending on the P-T-X (pressure-temperature-composition) conditions that lead to the melting point on the specific environment. From their (usually) mantellic source, magmas rise towards the Earth's surface mainly driven by the density contrast between these partially-molten volumes and the rocks that surround them (known as country rocks). Once they approach the upper levels of the lithosphere, they can get stored to form large masses of plutonic rocks or they can break through the surface producing volcanic eruptions (Fig. 1.1). During such evolution, the magmas experience profound changes in their chemistry and physical properties as a consequence of processes like crystallization, assimilation of country rocks or volatiles exsolution (e.g. [1, 2]).

Depending on the specific magma origin and path towards the surface, volcanic eruptions can display very different pattern and behaviors. One basic classification of volcanic eruptions divides them into effusive and explosive eruptions [3, 4]. Effusive eruptions are commonly characterized by: (a) low-viscosity, low-volatile-content mafic magmas (i.e. rich in ferro-magnesian mineral phases such as olivine and pyroxene) being erupted; (b) low to moderate mass eruption rates (MER);

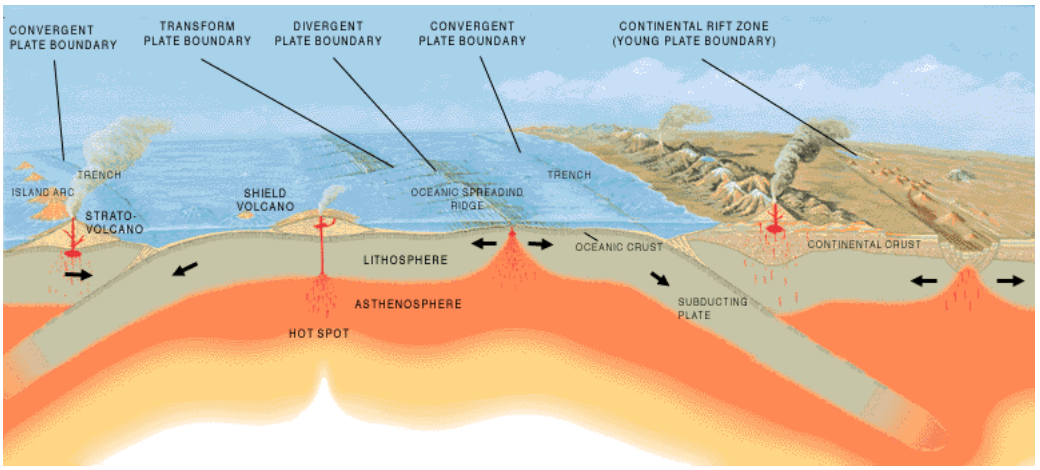

FIGURE 1.1: Artistic scheme displaying tectonic-plate dynamics, the main types of plate boundaries and the magmatic/volcanic activity associated with them. The differences between each tectonic setting (i.e. type of plate boundary) is reflected in both the geochemistry of the generated magmas and, accordingly, in the usual eruptive style exhibited by the volcanoes of that particular tectonic setting. Modified from https://pubs.usgs.gov/gip/dynamic/Vigil.html.

(c) modest degrees of magma fragmentation (i.e. the breakage of magma due to unrecoverable tensile strength [5]); and, thus, (d) eruptive styles which are dominated by lava fountaining and lava flows (e.g. [6]). On the other edge of the spectrum, explosive eruptions are commonly characterized by: (a) high-viscosity, high-volatile-content felsic magmas (i.e. rich in mineral phases such as feldespars and quartz -SiO_2-) being erupted; (b) potentially moderate to high MER values; (c) high degrees of magma fragmentation; and, therefore, (d) eruptive styles which are dominated by vertical jets of volcanic particles and gas (eruption columns, see subsection 2.1) which may sometimes collapse to form Pyroclastic Density Currents (PDCs, see subsection 2.2). Nevertheless, the previous does not always hold true since: (1) mafic magmas can be also responsible for highly-explosive eruptions (typically known as basaltic Plinian eruptions: e.g. [7, 8]); and (2) felsic magmas can also be erupted not explosively to form very-viscous masses of lava accumulated at the top of the volcano and known as lava domes (e.g. [6, 9]). Besides, the effect of external agents, such as water/ice, can modify the eruptive style to a great extent (e.g. [10, 11]).

Notwithstanding, explosive volcanism, and the hazardous processes associated with it, tend to occur at volcanoes with intermediate to felsic magma compositions and this type of volcano is not distributed randomly over the planet's surface (Fig. 1.2). Thus, they are typically located along the subduction zones where the

physico-chemical conditions favor the generation of viscous, volatile-rich eruptible magmas with a tendency towards explosive behaviors (e.g. [12, 13]). The most universal scale to classify explosive eruptions is the Volcanic Explosivity Index (VEI), developed by [14]. According to the VEI scale, the total erupted volume, which is linked to the MER and eruption column height (see next subsection 2.1), defines the level of explosivity according to a logarithmic scale. Thus, eruptions that produce, for instance, an amount of material in the order of $10^{-3} - 10^{-2}$km^3 are classified as VEI2 while eruptions that erupt around 1-10 km^3 are classified as VEI5 (so three VEI levels imply 3 orders of magnitude in the erupted volume). Descriptively, eruptions of VEI$\leq$3 are commonly called as Strombolian and/or Vulcanian (from the Italian volcanic islands *Stromboli* and *Vulcano*); eruptions of VEI4 are typically referred to as sub-Plinian and eruptions of VEI5 on tend to be known as Plinian eruptions (from *Plinius* the Younger, a witness and reporter of the largely explosive eruption of Somma-Vesuvius, Italy, in 79 AD).

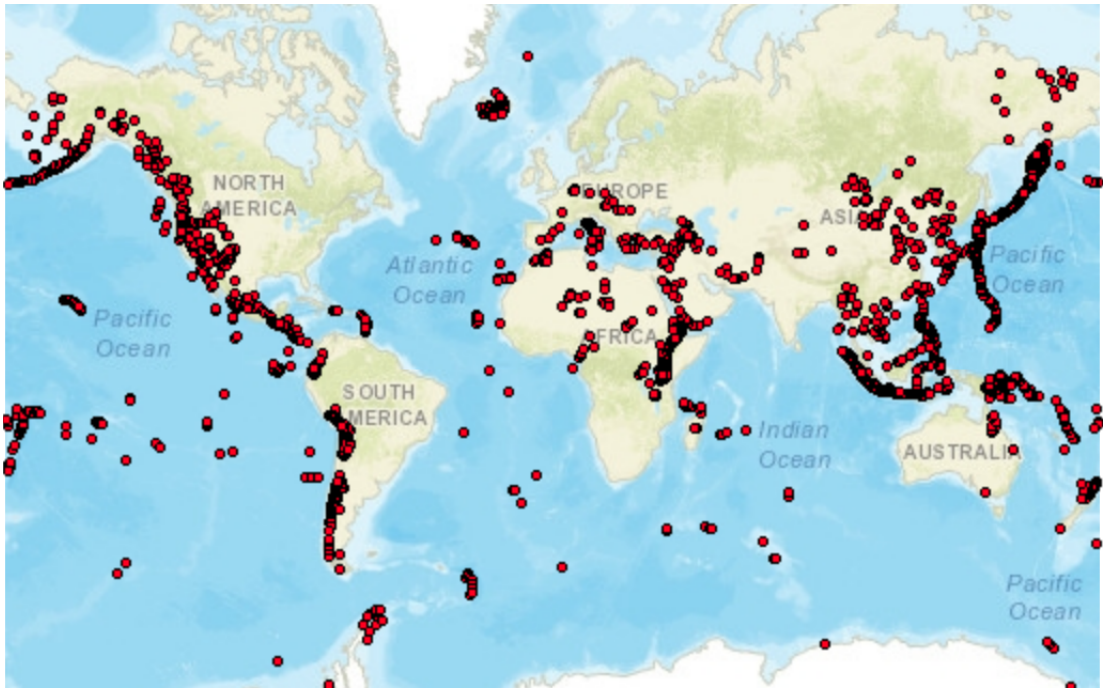

FIGURE 1.2: Worldwide spatial distribution of Quaternary ($\sim$ 2.6 Ma) large-magnitude (VEI$\geq$4) explosive eruptions (red points), according to the LaMEVE database [15]. Note how the density of points is greater along subduction zones like in Japan, Philippines, Indonesia or the occidental coast of the whole American continent (taken from http://www.bgs.ac.uk/vogripa).

1.2 Volcanic hazard assessments

Volcanic activity can cause serious impacts on both population and infrastructures located, not only in the vicinity of active volcanoes, but also at moderate-long distances from the volcanic vent (e.g. [16, 17]; see Chapter 2). Assessing the volcanic hazard existent at a given area or region is of paramount importance for: (i) land-use planning; (ii) management of volcanic crises; (iii) emergency planning before the onset of an eruption; (iv) assessing volcanic risk; (v) outreach and education; etc.

The most common way to show volcanic hazard assessments is through the compilation of maps (e.g. [18]). However, the content of these maps and the methodologies utilized to produce them, tends to be quite diverse: from geology-based and qualitative maps up to probabilistic maps, which incorporate a measure of, at least, the natural variability in the hazardous process (e.g. [18, 19]), also known as aleatory uncertainty or variability (see subsection 1.2.3). This lack of homogeneity may be due to a vague definition of what volcanic hazard means: sometimes it may simply refer to a hazardous process (e.g. [17]); or to the loss of life related to a hazardous process (e.g. [16]); or be a qualitative description of the likelihood that more than one hazardous process impacts a given area around the volcano (e.g. [20]); or be considered as the probability (per time window) of a hazardous process impacting a given area in space (e.g. [21]). All this mixture in interpretations and applications of hazard may come directly from the ethimology of the word, its general definition being: "a danger or risk" or "a potential source of danger" [22]. However, a second meaning is that of "chance; probability", which is closely related to the origin of the word hazard (from Old French *hasard*, from Spanish *azar*, from Arabic *az-zahr*: chance, luck; from Persian *zār* or Turkish *zar*: dice).

By the time this PhD began in 2014, hazard assessments of PDCs ranged from single-scenario (even single-simulation) up to probabilistic assessments, with quantification of uncertainty, even though they were only applicable to dense PDCs [23, 24]. Yet today, there is a certain number of different approaches proposed to quantify PDC hazard; these approaches tend to use one or a combination of the following methods: (a) collecting field data on past PDC deposits (e.g. [25, 26]); (b) running physical, theoretical and/or empirical models of PDCs (e.g. [27, 28, 29, 30]); and (c) using uncertainty quantification techniques, from Monte Carlo methods to expert-judgment analyses (e.g. [31, 32, 33]).

In the following subsections, we describe the bodywork done in volcanic hazard

assessments of PDCs and volcanic multi-hazard assessments, independently of the definition of hazard adopted by the authors or the final hazard product. In particular, three main approaches for PDC hazard assessment are detailed: (1) field-based hazard assessments; (2) scenario-based hazard assessments; and (3) probabilitistic hazard assessments.

1.2.1 Field-based PDC hazard assessments

Field-based (or geology-based) assessments are the most usual hazard products that are utilized world-wide, not only for PDCs but, in general, for volcanic hazards [18]. They are the result of individuating and mapping the extent of stratigraphic units from past eruptions (and, in this case, associated with PDCs) at a specific volcano of interest (Fig. 1.3a, e.g. [25, 26, 34]). The geological analysis takes into account the spatial distribution of the PDC deposits but also their thickness (values and spatial pattern) and, more importantly, their sedimentological structures and the way in which different units success each other vertically and laterally (e.g. [6, 35]). This is of crucial relevance for volcanic hazard studies of PDCs since it is the only way of extracting the eruptive behavior and the physical processes and patterns which may have occurred during past eruptions at a given volcanic system (e.g. [36, 37, 38]). Sometimes, the present eruptive behavior of the volcano may be completely different from what the volcano was capable of doing in the past and geology-based studies are the key to get to know such situations. For instance, volcanic systems which currently show mild-explosive behaviors (Strombolian/Vulcanian), like Mount Sakurajima (Japan), or even have not erupted for more than 1,500 yr, like the Taupo caldera (New Zealand), are known to have produced very-large, ignimbrite-forming eruptions in the past thanks to geological assessments (e.g. [39, 40]).

Nonetheless, field-based hazard assessments of PDCs do not fully account for the natural variability inherent to volcanic hazards (i.e. the aleatory uncertainty, see subsection 1.2.3) since what happened in the past does not represent *everything* that may happen in the future. Moreover, the eruptive record of a volcano is never one-hundred-percent complete (e.g. [15, 42, 43]) and the deposits left by large dilute PDCs may be quite thin and eroded shortly after the end of the eruption (e.g. [9]). These two factors (among others) add up epistemic uncertainty (see subsection 1.2.3) which cannot be resolved with the geology-based approach only.

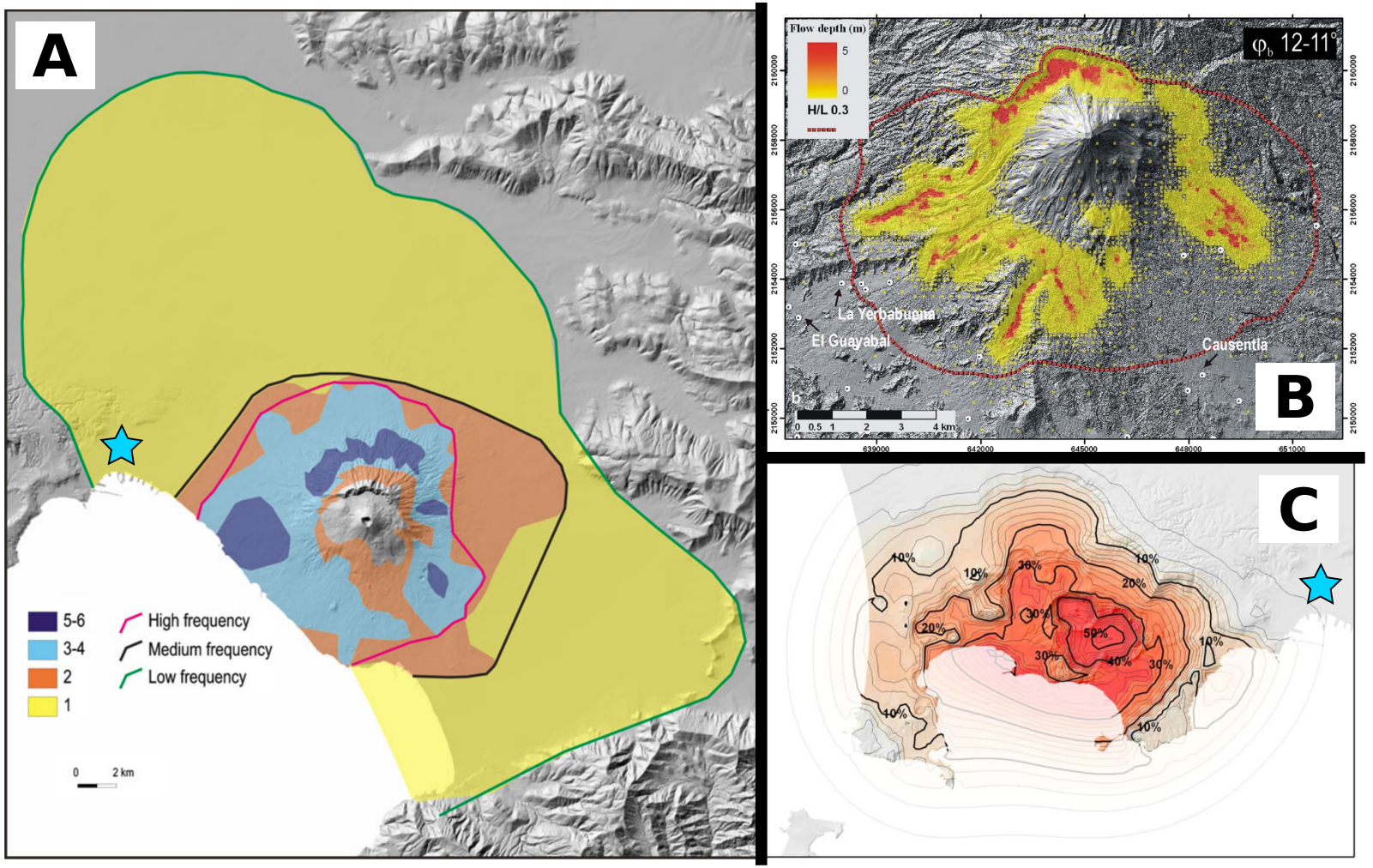

FIGURE 1.3: Example of PDC hazard assessments from recent literature: (A) field-based assessment carried out at Somma-Vesuvius (Italy) by [26]; the different colors indicate the number of past eruptions whose PDCs impacted each point of the hazard domain; (B) scenario-based assessment performed at Volcán de Colima (Mexico) by [41], according to the state of the volcano (e.g. lava-dome size and position) back in 2010; the flow-depth colorbar corresponds to a Titan2D simulation while the dashed red line delineates the extent of an Energy-Cone simulation; (C) probabilistic assessment computed at Campi Flegrei (Italy) by [33]; the contouring displays the best-estimate (mean) probability of PDC arrival at each point of the hazard domain, given the occurrence of an eruption of any size at the volcano. In (A) and (C), the light-blue star points to the downtown of Napoli. In (B), the city of Colima is located $\sim$ 20 km southwards of the lowermost limit of the map.

1.2.2 Scenario-based PDC hazard assessments

Scenario-based PDC hazard assessments are rooted in the detailed description of one or few eruptive scenarios (Fig. 1.3b) that, because of the present state of the volcano (e.g. [41]) or its past eruptive history (e.g. [44, 45]), are believed to be the most representative events to explore. Therefore, they may incorporate the information derived from field-based analyses but they focus on a specific subset of this past eruptive behavior. In some occasions, they can use physical models of PDCs to calculate the possible intensity of the PDC hazard for a given past eruption occurred at the volcano (e.g. [46]).
In principle, the degree of detail obtained with this approach is higher than in the case of probabilistic assessments (see subsection 1.2.4) mainly owing to the fact that the physical models[1] used in scenario-based hazard assessments can be more sophisticated (e.g. [44, 47, 48]). Consequently, variables such as dynamic pressure, particle concentration or even temperature can be analyzed in time and space, something that is not possible yet with the type of physical models used in probabilistic hazard assessments.

Nevertheless, the main drawback of scenario-based PDC hazard assessments is that they focalize on a (very) reduced subset of the possible eruptive events that might unfold at a given volcanic system. Thus, the aleatory uncertainty (see subsection 1.2.3) is far from being quantified with this kind of hazard assessment. Yet, scenario-based hazard assessments, because of their aforementioned superior level of detail, could be used to complement and improve field-based or probabilistic assessments by means of statistical models such as Bayesian emulators (e.g. [23, 31]) or logic- and event-trees (e.g. [49, 50, 51]).

1.2.3 Uncertainty in modeling volcanic hazards

The word uncertainty indicates a lack of certainty, of being certain, a term that comes from the Latin word *certus* (settled, sure [22]). Uncertainty is pervasive in volcanic hazards, as well as in natural hazards (e.g. [52, 53, 54]), not only because of the complexity, non-linearities and feedback effects in physical volcanic processes but also because of the impossibility, yet, to observe them directly (e.g. [1, 2, 5, 55, 56]).

[1] Or simulators. We use the two terms indistinctly along the thesis dissertation.

One main source of uncertainty in volcanic hazards is the natural variability, or stochastic behavior (from the Greek *stokhazesthai*: aim at, guess [22]), of volcanic systems, mainly in terms of the timing (e.g. [57]), location (e.g. [58]), duration (e.g. [59]), magnitude ([60]) and/or eruptive style (e.g. [11]) of their eruptions. This is commonly referred to as aleatory (from the Latin word: *aleator*: dice player [22]) uncertainty or variability (e.g. [52, 53, 54, 61]). Another main source of uncertainty arises from the very-limited direct access to volcanoes and, in general, relates to the incomplete knowledge about their components and behavior. This type of uncertainty is commonly known as epistemic (from the Greek: *epistēmē*, knowledge [22]) uncertainty (e.g. [52, 61]). A third principal source of uncertainty is defined by some authors as ontological (from the Greek words *onto*: a being, and *logos*: the study of) error [62]. This source is related to the fact that there might be unknown unknowns, that is, things that we do not know that we do not know. A volcano-related example of ontological error is the case of the 79AD eruption at Somma-Vesuvius (Italy): at that time, the Roman population living around the volcano did not know that that isolated mountain was actually a volcano [63].

Probability is a suitable way of quantifying uncertainty in general, and specifically in the case of natural and volcanic hazards (e.g. [53]), because: (i) its fundamental axioms are very simple [64]; (ii) it allows to reason about conditioning between outcomes/events; and (iii) there is a great variety of tools and methods to calculate probabilities (e.g. [65, 66]).
One probabilistic method that has been at the foundation of Probabilistic Volcanic Hazard Assessment (PVHA) is Bayesian inference, based upon the Bayes' rule (e.g. [21, 61, 67], see subsection 1.2.4 and Chapter 4). Bayesian inference can be defined as the process of fitting a probability model to a set of data (i.e. past hazard data at the volcano), and summarizing the result by a probability density function (PDF) of the parameters of the model [68] (see Fig. 1.4 for more details). One basic motivation for the use of Bayesian statistics in volcanic hazards is the fact that the frequentist approach to probability calculus (i.e. calculating the probability of an event as the limit of the frequency of occurrence of it when the number of reproducible experiments performed tend to infinite, e.g. [69]) cannot be utilized. In other words, volcanic eruptions (i.e. the experiment) do not occur every day at each single volcano around the world and, therefore, it is not possible to collect large numbers of outcomes/events from all of them (e.g. [21, 68]). Besides, it could be argued that they are not reproducible experiments, although this is usually overlooked, in a similar way as it is assumed when a die is rolled (obviously, a

person does not roll a die in the same exact manner twice and, therefore, the experiment would never be reproducible).

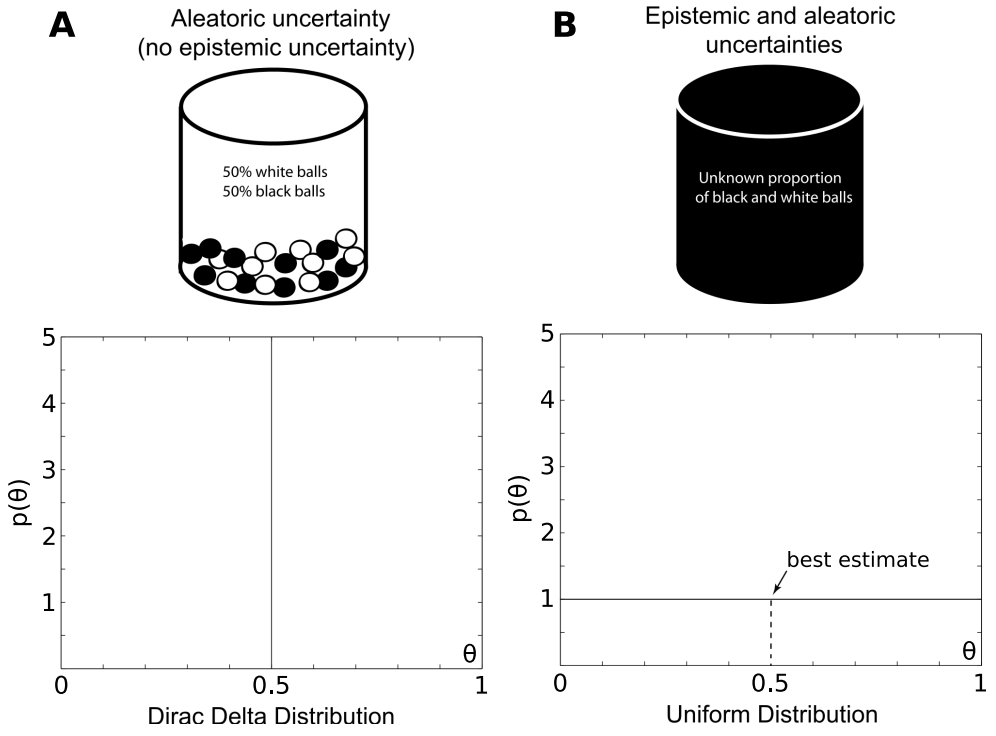

FIGURE 1.4: Exemplification of Probability Density Functions (PDFs), $p(\theta)$, and aleatory and epistemic uncertainties through the Ellsberg paradox (modified from [61]): (A) an urn containing the same proportion of black and white balls (50%); (B) an urn containing an unknown proportion of black and white balls. The variable θ denotes the proportion of black balls in the urn or, similarly, the probability of picking up a black ball in a single extraction from the urn. In (A), we *know* that this probability is 0.5 (or 50%) and this is indicated by a PDF with a domain $\theta \in [0.5]$ and an infinite density of probability at the only value of the domain (i.e. a Dirac Delta PDF). In (B), we *do not know* anything about the proportion of black balls so we may assume that any proportion (from 0% up to 100% is possible and equally likely). This is denoted by a domain for the variable $\theta \in [0, 1]$ and the same density of probability assigned to all the values within the domain (i.e. a Uniform PDF between 0 and 1). Therefore, in (A) there is aleatory uncertainty only (it is not certain that the next extracted ball will be black) while in (B) there are both aleatory and epistemic uncertainties (apart from what said about (A), the true probability of extracting a black ball is unkwnow). The paradox resides in the fact that the best estimate for the probability of extracting a black ball in (B) is just the same as in (A), that is: 0.5 (50%).

Aleatory uncertainty (or variability) in volcanic hazards is modeled through a PDF (Fig. 1.4) for variables like: erupted volume, the H_2O content of the magma, eruption duration, eruption column height, column collapse height and so forth (e.g. [23, 61, 70, 71, 72, 73]). The PDF shows two major aspects of the variable

being modeled (Fig. 1.4): (1) the domain of the variable, that is, the range of values that the variable can take; and (2) the density of probability associated to each value of the variable or, likewise, the likelihood of each value being true.
If epistemic uncertainty exists, then a single PDF may not be adequate to model the variable of interest. There are several types of epistemic uncertainty which can play a role in the (volcanic) hazard assessment (e.g. [54, 74, 75]). The result of incorporating epistemic uncertainty into the analysis is commonly, but not exclusively, that different types of PDFs or different parameterizations of the same type of PDF (e.g. Gaussian PDF) are explored. This is successfully handled with the Bayesian apparatus and usually translates into having alternative outputs for the hazard analysis (e.g. [49, 75, 76]).

1.2.4 Probabilistic hazard assessments

Probabilistic Volcanic Hazard Assessment (PVHA) aims at computing the probability of a hazardous process affecting a given point in space, over a given time window (e.g. [21, 49]). The volcanic hazard is interpreted as this very probability which corresponds to the aleatory uncertainty. Moreover, the epistemic uncertainty can be incorporated into the hazard analysis, for example, by assigning a PDF to that probability (Fig. 1.4, e.g. [49, 68]). Such probabilistic hazard assessment has been significantly developed and applied to tephra fallout (e.g. [19, 70, 71, 72, 77, 78]) but this has not been the case for PDCs, lahars or multi-hazard assessments.
One principal reason for the scarcity of PVHA for PDCs and lahars may reside in the fact these physical processes are extremely complex (e.g. [79, 80]). On the one hand, sophisticated physical models (e.g. [44, 81]) may be able to capture the properties and evolution of such complex flows but, unfortunately, they usually take too long to run which makes them inappropriate to explore aleatory and/or epistemic uncertainty in a robust manner (e.g. [82]). On the other hand, simple physical models, combined with the right statistical model(s), can serve to quantify aleatory and epistemic uncertainty (see Chapters 4,6,7,8).

Focusing on PDCs, the natural variability in their generation (i.e. column-collapse height, PDC mobility, collapsed mass, particle-volume concentration in the PDC, etc.) translates into aleatory uncertainty about whether a given point around the volcano will be inundated or not by PDCs, how thick these PDCs will be at that

point, how fast they will be when they pass through the point, and so on (e.g. [31]). As previously introduced, to calculate this probability, a full description of the aleatory uncertainty in terms of (at least some of) the aforementioned variables must be carried out and, thus, a probability for each hazard outcome (for instance: column-collapse height = 500 m and collapse mass = 5000 kg) must be assigned (e.g. [83]). Then, the aleatory uncertainty is usually propagated into the hazard domain by using the outputs from deterministic PDC simulators plus different uncertainty quantification techniques (see Chapter 4 for the methods utilized in this thesis dissertation). In this way, the probability of PDC arrival, PDC flow-depth and speed, etc. can be computed over the hazard domain (e.g. [23, 24]). These probabilities may be conditional to the occurrence of an eruption at the volcanic system of interest (e.g. [33]) or they can be absolute probabilities if the probability of eruption at the system is incorporated into the analysis (e.g. [32, 49]).

Again, the PDC simulators used to compute PVHA are forced to be computationally cheap. This is because propagating the aleatory uncertainty requires to compute a large number of hazard footprints (i.e. outputs from the simulator) in order for the hazard analysis to be statistically robust (e.g. [82]). Therefore, some of the PDC simulators utilized for scenario-based PDC hazard assessments (e.g. [44]), which need some days of computation on supercomputers, are not suitable for the statistical modeling needed in PVHA.
Besides aleatory uncertainty, a truly comprehensive probabilistic assessment of PDC hazard would need to include epistemic uncertainty into the analysis (e.g. [32, 33]). Sources of epistemic uncertainty can be varied (e.g. [75]), from uncertainty on the Digital Elevation Model (DEM) used to run the PDC simulator (e.g. [84, 85]) to uncertainty related to the model structure, sometimes explored via goodness-of-fit analysis of simulations and real PDC deposits (e.g. [86]).

On the whole, PVHA offers a very detailed analysis of the PDC hazard, including the aleatory and epistemic uncertainties associated with it (Fig. 1.3c). Nevertheless, it is a computationally-costly approach and, nowadays, there is still a strong dichotomy between the use of physically-complex (but more reliable) simulators mainly for scenario-based assessments (e.g. [47, 48, 80]) and the search for simpler models which are apt for PVHA of PDCs (e.g. [28, 31, 33]). In addition, probabilistic assessments of volcanic hazards are still in their infancy with respect to those in other fields of natural hazards such as climate, hydrology or seismology;

and there is still a long way to go in terms of understanding and communication of probabilities and uncertainties linked to volcanic hazards (e.g. [87, 88]).

1.2.5 Volcanic multi-hazard assessments

Volcanic systems, especially those explosive, tend to be multi-hazard, not single-hazard, environments and, thus, different hazardous processes may occur whether simultaneously or in succession (e.g. [17]). For instance, the occurrence of tephra fallout from Plinian eruption columns followed by (or in concomitance with) partial or total column collapses which generate PDCs is well documented to have happened at many volcanoes around the world (e.g. [57, 89, 90]). Else, dome explosions can also be followed by sustained eruption columns which produce tephra fallout (e.g. [91]).
Likewise, the input of pyroclastic material, as a result of tephra-fallout and PDC deposition, into the drainage basins and catchments surrounding the volcano alters the hydrogeological equilibrium at the local to regional scales (e.g. [92, 93]). This causes an increase in the frequency and magnitude of lahars from years to decades after the end of the eruption (e.g. [94, 95]).

Volcanic multi-hazard assessments target the evaluation of such type of hazardous situations. In some cases, the volcanic multi-hazard assessment may be an integration of field-based hazard assessments (sometimes combined with physical simulations) performed for several hazardous processes and integrated into a single map (e.g. [18, 20, 96], http://www.sernageomin.cl/volcanes-mapas.php). Other studies have produced semi-quantitative multi-hazard assessments by applying the information extracted from the eruptive history of the volcano(es) to rank and combine: (i) the likelihood (or return period) of different volcanic hazardous processes; (ii) the expected intensity and (iii) areal extent of each hazardous process (e.g. [97, 98, 99]).
Some research has also been done to compute probabilistic multi-hazard assessments but the hazardous processes are nonetheless analyzed independently of each other (e.g. [100]). Finally, in the case of lahars, some works have looked into the sequential nature of the hazardous processes: [101] simulate lahar propagation, at some areas likely to generate lahars, using the spatial distribution for the accumulation of tephra fallout as the input for the lahar volumes.

It is clear that multi-hazard assessments are more realistic than single-hazard assessments as they resemble more the actual behavior of explosive volcanoes. However, there is still the big challenge of properly accounting (in a probabilistic framework, ideally) for the cascade effects, common not only in volcanic hazards but, more generally, in natural hazards (e.g. [102]).

1.3 Contents and aims of this PhD

This thesis dissertation is conceived as an attempt to improve probabilistic hazard assessments of PDCs and lahars, the latter in a Probabilistic Volcanic Multi-Hazard Assesment (PVMHA) perspective. We adopt the definition of volcanic hazard proposed by [21, 49] and pursue two major specific goals:

1. Explore different combinations of physical and statistical models to quantify uncertainty in volcanic hazards, in particular of PDCs and lahars
2. Compute PVHA of these hazardous processes at the city of Napoli and its surroundings (Italy)

In Chapter 2, we describe the main physical features of the principal, and most common, hazardous processes associated with explosive eruptions: tephra fallout, PDCs and lahars.

In Chapter 3, we introduce the geographical and volcanological setting of the study area: the city of Napoli and surroundings, and summarize the main eruptive history and behavior of the two main volcanic systems in the area: Somma-Vesuvius and Campi Flegrei.

In Chapter 4, we detail the methods utilized in the PhD which basically consist of: (1) physical models of PDCs (Energy Cone and Titan2D) and lahars (*LaharFlow*); and (2) statistical models to quantify uncertainty, also known as uncertainty quantification techniques (Monte Carlo sampling -MC-, Polynomial Chaos Quadrature -PCQ-, Bayesian Event Tree for Volcanic Hazard -BET_VH-, and Bayesian Belief Networks -BBNs-).

In Chapter 5, we develop and carry out validation tests of the Energy Cone model at Somma-Vesuvius and Campi Flegrei in order to check for the suitability of

this simple PDC model to compute PVHA of PDCs. To do so, we quantify and propagate aleatory uncertainty through Monte Carlo sampling techniques and use past PDC deposits at the two volcanoes to assess the performance of the Energy Cone. The results from this study have been published in Bulletin of Volcanology [103].

In Chapter 6, we perform a detailed quantitative analysis of four different sources of epistemic uncertainty associated with PDC modeling at Somma-Vesuvius, using the Energy Cone model in conjunction with Monte Carlo sampling. The results from this study have been published in the AGU Geopysical Monograph Series volume 223 [104].

In Chapter 7, we use the data and insights obtained from Chapters 3 and 4 to compute an innovative type of PVHA: following the praxis utilized in probabilistic seismic hazard, we calculate a multi-source (Somma-Vesuvius and Campi Flegrei) site-specific (the city of Napoli and surroundings) PVHA of PDC arrival. We do so for both dense and dilute PDCs by combining Energy Cone simulations, Monte Carlo sampling and BET_VH. The results from this study will be submitted to an international journal soon [105].

In Chapter 8, we utilize a different PDC model, Titan2D, in conjunction with PCQ and BET_VH, to compute a single-source (Somma-Vesuvius) site-specific PVHA for dense PDCs. We are able to produce hazard curves for flow depth and speed of dense PDCs. These curves can be very informative to quantify volcanic risk associated with dense PDCs around the volcano. Part of the results from this study were presented at the EGU General Assembly 2014 [106]. The complete study is aimed at the submission of a paper during the following months [107]. Moreover, a certain percentage of these results was applied to other two papers to be submitted in the near future: [108] and [109] (see Chapter 9).

In Chapter 9, we propose and apply a methodology to calculate Probabilistic Volcanic Multi-Hazard Assessment (PVMHA) at Somma-Vesuvius, with focus on rain-triggered lahars. We use a BBN model to merge probabilistic hazard assessments of tephra fallout and PDCs with information coming from other datasets and literature data and, finally, we use a physical model of lahars to propagate the aleatory uncertainty in lahar generation towards the hazard footprints of these flows. The results from this study will be submitted to the special volume in

Frontiers in Earth Science: *Volcanic hazard assessment: rising to the challenges of data and model integration* [109].

In the end, Chapter 10 summarizes the main findings derived from this PhD and briefly suggests some future directions in the fields of PVHA of PDCs and PVHMA.

Chapter 2

Hazardous phenomena related to explosive volcanism

Three of the main (and most common) hazardous processes that unfold during explosive eruptions are the following: tephra fallout, Pyroclastic Density Currents (PDCs) and lahars, the latter being usually a secondary hazardous process, not produced by the eruption itself but by the interaction between the eruptive products and other external factors (see section 2.3). The following sections summarize some of the physical features and possible impacts of these hazardous processes.

2.1 Tephra fallout

Likely the most typical characteristic of explosive volcanism is the creation of volcanic jets of pyroclasts and gas which exit the volcanic vent at very high speed (in the order of hundreds of m/s) and reach altitudes up to 40 km, approximately, during ultra-Plinian eruptions (e.g. [55, 110]). These volcanic jets are known as eruption columns and are formed by very intense fragmentation of the magma when it is stretched beyond the limit of its tensile strength (e.g.[5, 111]). This is driven by feedback effects which involve large increases in viscosity and acceleration of the magma as it is strongly decompressed and volatiles rapidly exsolve during the very last stages of magma ascent towards the surface (e.g. [112, 113]). The mixture of pyroclasts and gas that forms the eruption column is clearly denser that the atmosphere when it exits the volcanic vent (a basaltic -mafic- rock has

densities around 2,800-3,000 g/cm^3 while an andesitic -intermediate- rock has densities about 2,500-2,800 g/cm^3). As the eruption column rises, it loses a great deal of momentum in its lowermost part but it also starts entraining some of the surrounding air which is then heated up and helps reduce the density of the pyroclast-gas mixture (Fig. 2.1). The lowermost region of the eruption column, which is dominated by the inertial forces induced by the exit velocity of the mixture, is known as gas-thrust region (e.g. [4, 114]). Its extent is minor compared to the total height of the eruption column: its height can be roughly estimated to be 10% of the total eruption column (e.g. [110]). Beyond the top of the gas-thrust region, the mixture has been able to entrain a quantity of surrounding air which is high enough for the eruption column to become less dense than the atmosphere and to rise under the main influence of thermal buoyancy (e.g. [110, 114]). This region is called convective region and, along it, the ascent velocity may increase significantly in comparison with the velocity at the zone of transition between the gas-thrust and the convective regions (e.g. [115]). Finally, the eruption column rises up to a point in which, due to the cooling of the mixture, it becomes as dense as the surrounding air and it spreads out laterally, being transported by the prevailing winds at the altitude at which this second transition occurs (Fig. 2.1). This uppermost region of the eruption column is called the umbrella region (e.g. [114]).

Tephra fallout is the physical process by which the remaining pyroclasts in the umbrella region of the eruption column are transported by the wind and fall out of the mixture onto the ground under gravity and according to, principally, the terminal fall (or settling) velocity of each pyroclast, which mainly depends upon size, shape and density of the particle (e.g. [117]). That is, if the vertical drag exerted, on a given particle, is not high enough to balance the force of gravity, the pyroclast will leave the current and fall onto the ground (e.g. [118, 119]).
The volcanic hazard associated with tephra fallout can be complex. During transport, airborne tephra can severely damage the engines of aircrafts which fly through the volcanic plume because of the vitrifying effect that volcanic ash can produce on the nozzle guide vanes and the turbine blades (e.g. [120]). The most direct consequence of this hazardous process is the accumulation of tephra (i.e. pyroclastic particulated material) over the proximal, medial and distal/very-distal areas from the volcanic source depending on the size of the specific eruption (and, therefore, depending on the height of the eruption column, the mass of the erupted material, and so on). Primarily, this accumulation can cause the collapse

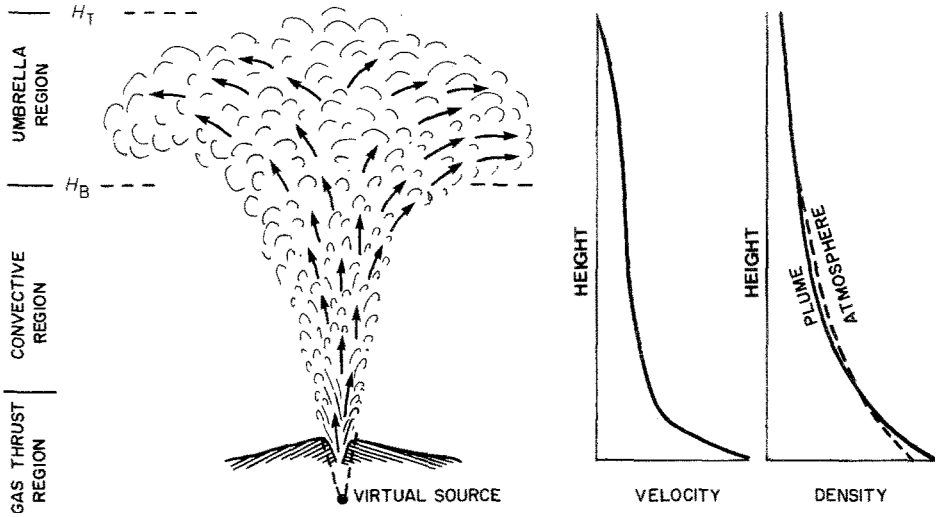

FIGURE 2.1: Simplified scheme of the vertical rise of an eruption column. The three main regions within the column (gas-thrust, convective and umbrella) are indicated. On the right, the profiles of the density and vertical velocity of the column as a function of height above the vent are shown. Note that the velocity profile may be different in the case of strong plumes (e.g. high MER) or if the exit velocity is not high enough to avoid a sharper drop in velocity along the gas-thrust zone before reaching buoyancy (e.g. [115, 116]). Modified from [114].

of the roofs of buildings surrounding the volcano, especially if the tephra is wet (e.g. [121]). In addition, the tephra cover (from milimetres up to several meters) strongly disturbs the vegetation of the area from grass and shrubs up to big trees which can see their foliage covered in ash (fine tephra), thus hindering or even precluding their photosynthesis activity (e.g. [122]). Similarly, toxic elements such as Cl, F or As, common in volcanic tephra, can represent a serious health threat to cattle but also to humans if aquifers used for drinking water are affected by leaching of these tephra layers (e.g. [123]).

2.2 Pyroclastic Density Currents (PDCs)

Pyroclastic Density Currents (PDCs) are ground-hugging mixtures of hot gas and pyroclasts that travel at moderate to very high speed along the surrounding areas of erupting volcanoes (e.g. [6, 9, 35, 124]). Even though the internal structure of a PDC cannot be directly seen, according to visual observations of PDC propagation and to the study of their deposits, PDCs are composed of two main layers (Fig. 2.2) which define a gradient in density and velocity from their lower/basal part (denser and tendentially slower) to their upper part (less dense -dilute- and faster,

e.g. [9, 125, 126]). These differences between the basal and upper part of PDCs are reflected into the dominating transport mechanisms over the whole current (e.g. [80]): in the basal part, particles are transported by traction and frictional behavior dominates; while, in the upper part, particles are transported by suspesion or saltation and turbulent behavior dominates (e.g. [124]). This marked difference in transport dynamics is of paramount importance to the modeling of PDCs as it is detailed in Chapter 2.

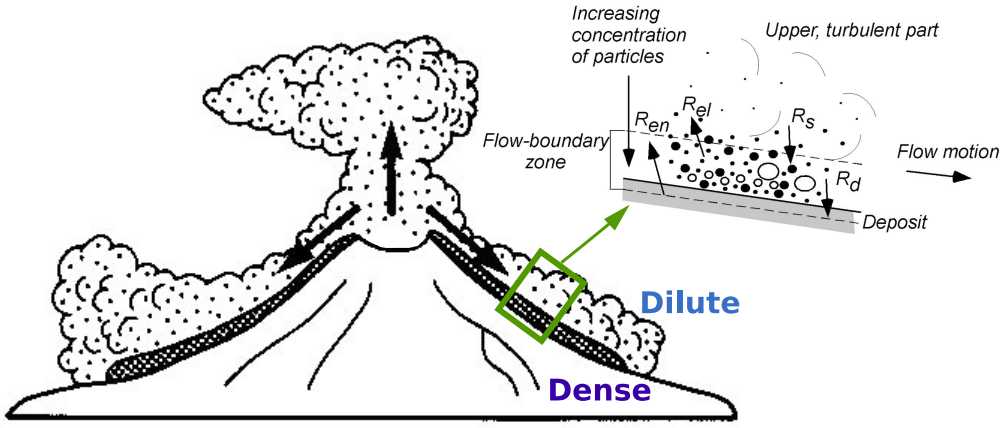

FIGURE 2.2: Simplified scheme of the structure of a PDC formed by intermittent column collapse (basal dense and upper dilute parts are highlighted in blue; modified from www.bgs.ac.uk). In the zoomed green inset, a more detailed scheme of the internal structure is given: an exchange of particles occurs between the deposit and the upper turbulent parts of the PDC, via the flow-boundary zone [35], which is the lower part of the PDC where deposition is promoted. R_en: rate of re-entrainment of particles in the flow; R_el: rate of elutration (i.e. escape) of particles from the flow-boundary zone; R_s: rate of supply of particles from the upper part of the flow into the flow-boundary zone; R_d: rate of deposition from the flow-boundary zone into the deposit (modified from [124]).

PDCs are generated typically at explosive volcanoes but they can occur without necessarily requiring an explosive eruption. In fact, the mechanisms that lead to the generation of PDCs are quite varied (Fig. 2.3, e.g. [6, 124]). A somehow general classification of PDCs, by mechanism, can be the following:

1. PDCs generated by the collapse of an eruption column, commonly known as pumice flows. The (total) collapse of the eruption column occurs when the volcanic mixture is not able to entrain enough air as to become lighter than the surrounding atmosphere; in this case, the drop in upwards velocity goes all the way down to zero and the mixture collapses to the ground (e.g. [116, 127]).

Pumice flows can result from continuous collapses (boiling-over), partial or total (intermittent) collapses or even radial collapses, when there is an important lateral component in their initiation (e.g. [6, 124, 128]). The latter are usually produced during phreatomagmatic explosions (i.e. there is efficient interaction between magma and water, e.g. [10]) and are known as base-surges (e.g. [129]).

2. PDCs generated from the disruption of a lava dome, commonly known as Block-And-Ash Flows (BAFs): they can be subdivided into Merapi-type BAFs, caused by gravitational collapse of the lava dome and Soufrière-type BAFs, triggered by a dome explosion (e.g. [41]).

3. PDCs generated as a consequence of the gravitational failure of part of the volcanic edifice, usually referred to as lateral blasts (e.g. [130]).

4. PDCs generated by caldera collapse, commonly known as ignimbrites (e.g. [35]).

Each mechanism of PDC generation leads to PDCs with certain characteristics which differentiate them from other types of PDCs. One of the characteristics that has received a great deal of attention is the PDC mobility (e.g. [9, 124, 129, 131], that is, the ability of PDCs to propagate for long distances and surmount topographic barriers. A simple definition of mobility is the ratio between the total difference in height between the initiation and the stopping point of the PDCs, ΔH, and the maximum distance reached by them, L (e.g. $\text{atan}\phi = \Delta H/L$ [129, 132], more details are given in Chapter 4), in a way that the more mobile the PDC, the smaller the value of $\Delta H/L$ (i.e. the longer it is able to propagate, for a given value of ΔH).
This PDC mobility has often been linked to the partition between dense and dilute members inside a given type of PDC [133, 134, 135, 136, 137, 138]. Thus, for a given flux of material occurring at a PDC, dilute PDCs are expected to travel further (and be more mobile) than dense PDCs because the particles transported by saltation and suspension will take longer to segregate towards the base of the current (and the deposition zone) and the whole current will take longer to come to rest (e.g. [124, 133, 139]). This is a simplified picture though, since entraining of air at the head of the PDC (e.g. [80, 140]) can induce a decrease in density large enough to make the whole dilute PDC to become lighter than the surrounding air

and lift, forming what it is known as coignimbrite plumes (e.g. [141, 142, 143]), and causing the PDC to stop.

Coming back to the mechanism-type of PDCs, pumice flows formed by vertical column collapses usually have both dense and dilute members well-developed. Mobility can be greatly influenced by the amount of material (or mass) that participates in the column collapse (e.g. [44]) and/or by the continuous/intermittent nature of the column collapse (e.g. [144]). In contrast, base-surges tend to be dominated by the dilute member altough they also have thin, subordinated dense-basal parts (e.g. [139]). Their mobilities tend to be relatively high (e.g. [137]), in part aided by the initial lateral momentum produced during phreatomagmatic explosions (e.g. [10, 128]). BAFs are characterized by an important dense component but significant secondary dilute PDCs (or ash surges) can be derived from the main PDC when BAFs interact with topography (e.g. [91, 145]). The mobilities of BAFs tend to be similar to, sometimes smaller than, pumice flows, e.g. [136, 138]) although the ash surge can significantly outrun its parent dense-dominanted PDC (e.g. [145]). Lateral blasts are very-energetic PDCs and, although a large proportion of the area covered by their deposits may be dilute-like (e.g. [130]), they also have an important part of their volumes transported as more dense-like PDCs (e.g. [130, 141]). Their mobilities tend to be quite elevated, especially because of the strong directionality and energy of the blast (e.g. [130, 132]). Finally, ignimbrites are characterized by depositing extremely huge amounts of pyroclastic material and traveling for tens of kilometers away from the vent (e.g. [9, 35]) so their mobilities are huge (e.g. [135]). There is still debate about the nature and behavior of ignimbrites (e.g. [124] and references therein), since the facies and spatial distribution of the deposits of some ignimbrites may resemble those of PDCs (with both dense and dilute members occurring), only that the volumes, areas, distances traveled, etc. are gigantic. However, there are other examples of ignimbrites which point to dense-like (maybe low-mobility) flows which, even though they may have propagated over almost flat topographies, they were able to maintain lateral motion for many kilometers away from the vent (e.g. [146, 147]). A slow-motion, long-lasting and very-large flux of material from the ring faults of the collapsed caldera (*lava-flow model*) is proposed by some authors to explain the emplacement mechanism of such very-thick, massive deposits of some ignimbrites [124].

Another classification of PDCs, based on the macroscale propagation mechanism

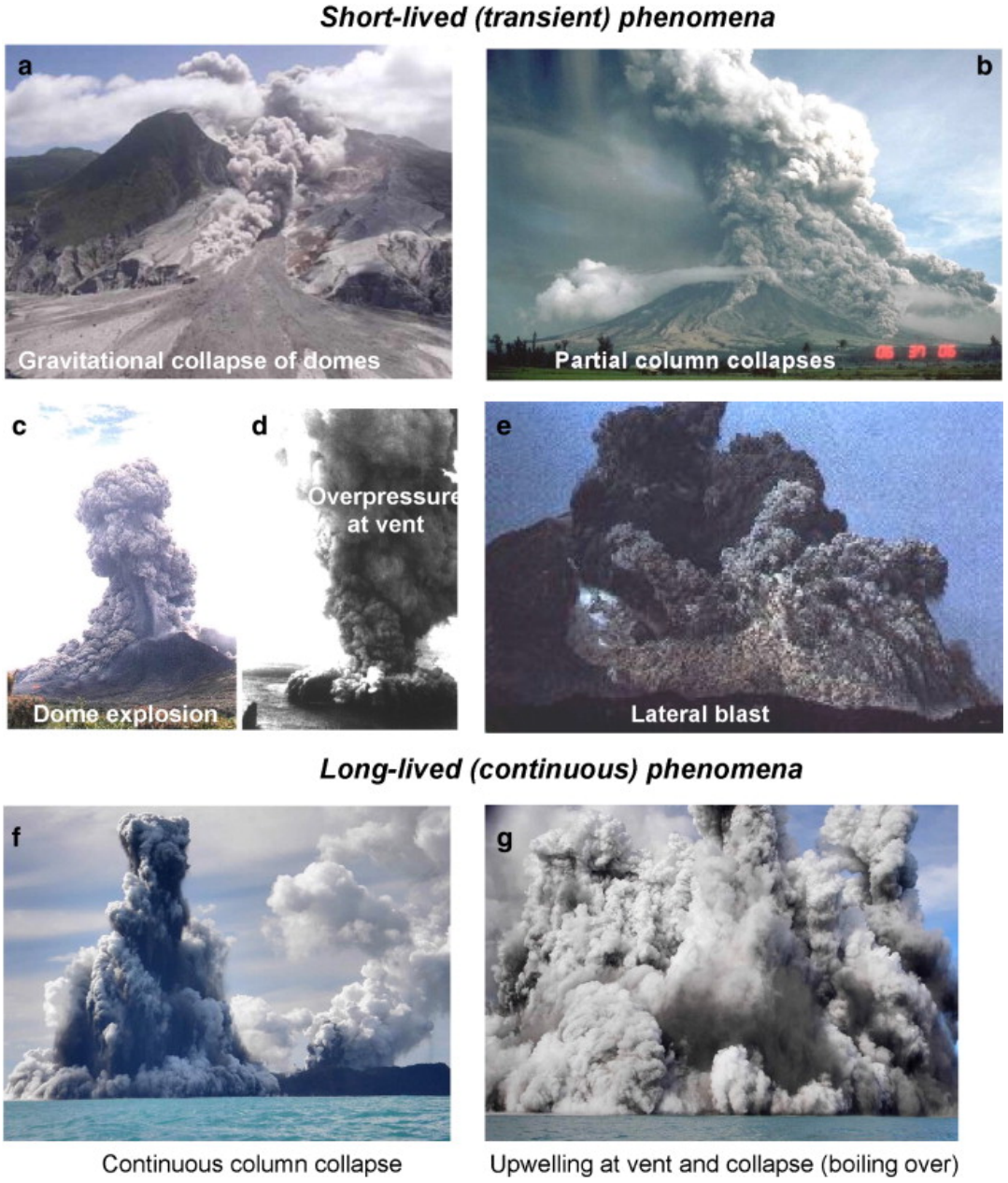

FIGURE 2.3: Worldwide examples of mechanisms of PDC generation (taken from [124]): (a) gravitational collapse of a lava dome at Soufrière Hills volcano, Montserrat; (b) column-collapse PDCs formed during the 1984 eruption at Mayon volcano, Philippines; (c) lava-dome explosion at Soufrière Hills volcano, Montserrat; (d) base-surge generated from a phreatomagmatic eruption at Capelinhos, Azores; (e) lateral blast triggered by the gravitational failure of part of the volcanic edifice of Mount Saint Helens volcano, USA, in 1980; (f) continuous column collapse from an eruption offshore of Tonga island; (g) boiling-over (upwelling and continuous collapse) PDCs formed during the same eruption offshore Tonga island.

that dominates the PDC (instead of using the particle concentration and transport), has been proposed by [148]. This classification focuses on the interaction with topography and divides PDCs into two main types (either they might be dense or dilute): forced convection-dominated flows and inertia-dominated flows. The former are characteristic of quasi-steadily fed PDCs (e.g. ignimbrites and boiling-over events), lateral blasts or PDCs strongly controlled by gravity (e.g. along steep flanks of stratovolcanoes, [148]). The latter are governed by their own inertia and may be more able to surmount topographic features. In reality, the two end-members can develop within the same flow (e.g. [149]) or can evolve from one to the other in a complex fashion during the transport and emplacement of PDCs (e.g. [150]).
Indeed, the interaction of PDCs with topography is a very complex aspect of PDC propagation, besides one of the most crucial for hazard assessment purposes (e.g. [91, 125]). As introduced above, not only does topography influence the propagation of PDCs and which types of PDCs will form after the interaction; but also the type of PDC that encounters a specific topographic structure (a narrow channel, a break in slope, a vertical barrier, etc.) will deeply change the typology of PDC that unfolds after the PDC and the structure have interacted (e.g. [28, 124, 125, 149, 150, 151, 152]).

Regarding volcanic hazard, PDC are among the most hazardous processes that are produced by volcanic systems worldwide. Their destructive potential, both in terms of structural damage (e.g. [153, 154]) and threat to human life (e.g. [155]), is huge. This is due to several factors such as their very high speed (up to hundreds of m/s), hot temperatures (sometimes well above 200°C, [156]), the presence of toxic gases (e.g. [155]) and the lethal concentration of particles of mixed grain size (from microns up to several meters). During the last 400 years, PDCs have been responsible for the largest number of fatalities related to volcanic eruptions ($\approx$ 100,000 lives, 33% of all fatalities, [157]). Among the most devastating events, we recall Mount Pelée 1902, Martinique [158]; Mount Lamington 1951, Papua New Guinea [159]; and El Chichón 1982, Mexico [160].

2.3 Lahars

Volcanic mudflows, commonly known by the Javanese word *lahar*, are volcaniclastic water-sediment flows with a particle-volume concentration greater than

10% (e.g. [161]). They tend to be divided into hyperconcentrated flows, if the particle-volume concentration is in between 10 and 50%, and debris flows, if the particle-volume concentration is above 50%.

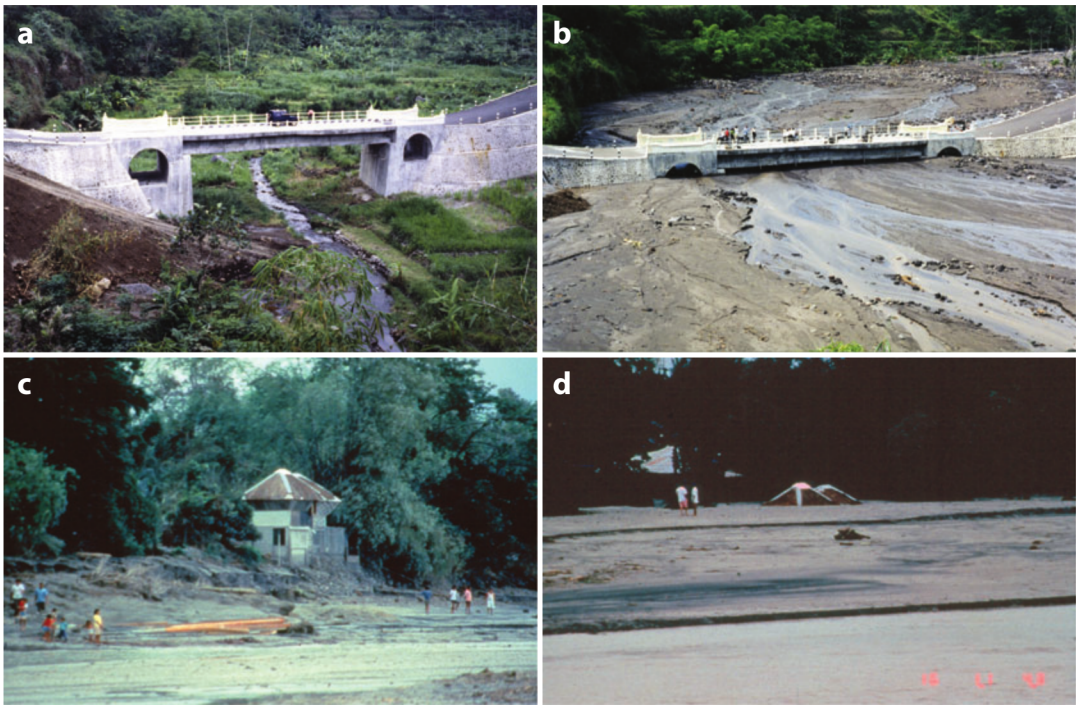

FIGURE 2.4: Two examples of the very high capacity of sediment transport and deposition that lahars can display: (a)-(b), 7 meters of aggradation (vertical accumulation of deposit), during a 3-month span, on the Boyong River, near Mount Merapi (Indonesia); (c)-(d), almost 9 meters of sediment deposited by a single lahar event on the Bamban River, Mount Pinatubo (Philippines); note the roof of the two houses. Modified from [92].

Lahars are formed in volcanic environments when four main controlling factors are present (e.g. [161, 162]): (1) a source of water; (2) easily erodible/entrained material; (3) steep slopes; and (4) a triggering mechanism. The source of water can be in the form of intense and/or sustained rainfall events (e.g. [163, 164, 165]), melted ice from glaciers capping the volcano (e.g. [166, 167]), or water released as the result of the breakout of, usually, a volcanic lake (e.g. [168]). The easily erodible/entrained material is typically pyroclastic material produced during recent explosive eruptions at the volcano and it is composed of tephra fallout and PDC deposits, principally (e.g. [90, 92, 169, 170]). However, debris flows can be triggered on pyroclastic soils even after more than 300 yr after the last significant input of pyroclastic material, as the infamous event of Sarno-Quindici (Italy) showed (e.g. [171, 172]). Steep slopes are almost guaranteed at many stratovolcanoes (due to the shape of these volcanic edifices), but they can also

characterize nearby topographic reliefs (e.g. [173, 174, 175]). Finally, the triggering mechanisms can be largely divided into: (a) efficient erosion due to significant surficial runoff (e.g. [92, 164, 176]); and (b) shallow-landsliding caused by water infiltration and a critical increase in pore pressure within the deposit (e.g. [162, 170, 177, 178]). The former may be typical of tropical volcanoes, where high rainfall intensities promote an efficient erosive runoff (e.g. [163, 179]), while the latter may be more characteristics of volcanoes located on temperate climates, where moderate-intensity rainfalls favor the built of pore-pressure that may generate the shallow landslides (e.g. [162, 170]).

During propagation, lahars only reach moderate speeds (up to few tens of m/s, [180, 181, 182]) but their high densities (above 1,400 g/cm^3, e.g. [183]) and viscosities, large sediment yields (Fig. 2.4, e.g. [90, 92]) and very long runouts (in the order of several km up to more than 100 km from the source, e.g. [166, 184]), make them an extremely serious hazard (e.g. [181, 185]). In fact, during the last four centuries, the number of fatalities caused by lahars is overcome only by that due to PDCs, indirect processes (e.g. starvation) and tsunamis [157]. When the largest volcanic disasters (including the tragedy at Nevado del Ruiz, Colombia, in 1985, when lahars hit the city of Armero, claiming more than 23,000 lives, e.g. [166]) are removed from the dataset, lahars become the second-most deadly volcanic phenomenon, only behind PDCs [157].

Chapter 3

Neapolitan volcanoes

The city of Napoli ($\sim$ 1M inhabitants), in Southern Italy, partially lies inside the active Campi Flegrei caldera and it is surrounded by two other active volcanic systems: Somma-Vesuvius and Ischia (Fig. 3.1). Ischia island, located towards the SW from Campi Flegrei, is a resurgent caldera [186] which has shown eruptive patterns characterized by long periods of quiescence alternated with periods of intense volcanic activity around 55-33 ka BP, 28-18 ka BP and 10 ka BP. The last eruption at the system occurred in 1302 AD [187]. Even though the eruptive behavior at Ischia tends to be explosive, with generation of base-surges (e.g. [187]), these PDCs would need to travel considerable distances over water before reaching the city of Napoli and its surroundings.
The focus of this thesis dissertation is on Campi Flegrei and Somma-Vesuvius because: (1) they are situated within the city of Napoli or quite close from it; (2) they are capable of producing (large) explosive eruptions whose PDCs may affect Napoli and its surroundings (e.g. [25, 26]); (3) they are able to produce secondary hazarddous processes such as lahars (e.g. [170]); and (4) the present state of volcanic unrest at Campi Flegrei (e.g. [188]) urges hazard scientists to produce quantitative hazard assessments (e.g. [33]) that can be useful for civil protection agencies.

Somma-Vesuvius and Campi Flegrei are two volcanic systems located on the Campanian plain, a Plio-Pleistocene graben structure formed by regional NW-SE and NE-SW trending normal faults and related to the extension produced during the opening of the Tyrrhenian sea [189]. Although they are located close to one another, each system is independent in terms of geochemistry of magmas involved,

vent-opening patterns, eruption dynamics and, as a result, in the types of PDCs generated (e.g. [25, 37, 89, 190, 191, 192]). A summary of some physical parameters inferred from the 24 explosive eruptions (6 at Somma-Vesuvius and 18 at Campi Flegrei) analyzed in Chapter 5 is given in Table 3.1.

3.1 Somma-Vesuvius

Somma-Vesuvius is a ∼1300 m-high stratovolcano located about 15 km away from the city of Napoli. Its main volcanic edifice has been built and destroyed several times during the last 20 kyr of volcanic activity [89, 196]. The complex eruptive history has produced a landscape where several topographic remnants of collapsed volcanic edifices are still recognizable, the most evident being Mt Somma [196], north of Vesuvius' cone. The latter has been shaped through the last 1.5 kyr, since the sub-Plinian Pollena eruption (472 AD, [144]). During the last 20 kyr, the volcanic activity at Somma-Vesuvius has been punctuated by large Plinian eruptions, with variable inter-Plinian intervals, alternated with sub-Plinian eruptions and also periods of open-conduit volcanism [89].

This pattern in eruption behavior began with the Pomici di Base eruption (20.5 cal. ka, [197]) and it is considered that the expected present evolution of the system, and therefore analysis of its hazards, should be assessed using the information gathered from the last 20 kyr [89]. Along this thesis dissertation, we follow a magnitude-based classification (e.g. [195]) for the possible eruption sizes expected in future eruptions at Somma-Vesuvius which, given the current repose of more than 70 years, are thought to be energetic enough to re-open the Somma-Vesuvius conduit (e.g. [61]). Therefore, we deal with three eruption sizes and explore the aleatory uncertainty within each of them: small size (comparable to the 1944 AD eruption), medium size (comparable to the Pollena eruption), and large size (comparable to the Pompeii eruption).

In terms of PDCs, the explosive eruptions at Somma-Vesuvius have generated dense and dilute PDCs as a result of transient eruption-column collapses, continuous collapses (pyroclastic fountaining) or very energetic phreato-magmatic explosions (e.g. [89]). The expected PDCs to occur during medium and large eruptions (Plinian and sub-Plinian I in the classification of [89]) consist of more or less radial PDCs produced by partial and total column collapses, pyroclastic fountaning

TABLE 3.1: Summary of some physical parameters estimated for the 24 volcanic eruptions of Somma-Vesuvius (6) and Campi Flegrei (18) studied in Chapter 5. MDR: magma discharge rate; A_{OBS}: area covered by PDC deposits (after [25, 26]); MR_{OBS}: maximum runout inferred from PDC deposits (after [25, 26]). (a) [89]; (b) [193], hot avalanches; (c) [26]; (d) [194]; (e) [195]; (f) assuming that, only at Campi Flegrei, PDC volume represents, on average, 75% of the total tephra volume (after [72, 195]); (g) mid-range value from [191] (and references therein); (h) this variable describes whether the PDCs for a particular eruption are inferred to have propagated following radial spreading (radial), channelized or strongly-blocked-by-topography spreading (blocked) or radial spreading with secondary topography blocking (radial-blocked). Modified after [103].

Eruption	**Volcanic System**	**Age**	**Eruption Size**	**Peak MDR [kg/s]**	**PDC volume [km^3]**	**PDC main spreading (h)**	**A_{OBS} [km^2]**	**MR_{OBS} [km]**	**MR : mR**
1944AD	Somma-Vesuvius	AD 1944	small	0.4-1.5 $\cdot 10^6$ (a)	0.006 (b)	radial	5.30	2.00	2.16
1631AD	Somma-Vesuvius	AD 1631	medium	1.5-8 $\cdot 10^7$ (c)	0.200 (c)	radial-blocked	162	10.4	2.08
Pollena	Somma-Vesuvius	AD 472	medium	0.7-3.4 $\cdot 10^7$ (c)	0.390 (c)	radial	182	11.3	1.79
Pompeii	Somma-Vesuvius	AD 79	large	0.8-1.5 $\cdot 10^8$ (c)	0.830 (c)	blocked	334	20.5	3.04
Avellino	Somma-Vesuvius	3.9 ka Cal (d)	large	0.6-1.7 $\cdot 10^8$ (c)	1.040 (c)	blocked	672	25.9	5.62
Mercato	Somma-Vesuvius	8.9 ka Cal (a)	large	2.8 $\cdot 10^7$ (c)	0.230 (c)	radial	173	9.64	1.77
Monte Nuovo	Campi Flegrei	AD 1538	small	2.0 $\cdot 10^6$ (e)	0.039 (f)	radial-blocked	6.07	2.35	4.55
Fossa Lupara	Campi Flegrei	4.1 ka Cal (g)	small	-	0.031 (f)	radial	8.88	1.80	1.17
Astroni 7	Campi Flegrei	-	small	-	0.087 (f)	radial	9.91	2.61	2.87
Astroni 6	Campi Flegrei	-	medium	7.4 $\cdot 10^6$ (e)	0.175 (f)	radial	28.7	4.18	2.11
Astroni 5	Campi Flegrei	-	medium	-	0.138 (f)	radial	28.0	3.95	1.95
Astroni 4	Campi Flegrei	-	medium	-	0.182 (f)	radial	50.1	5.67	2.19
Astroni 3	Campi Flegrei	4.2 ka Cal (g)	medium	-	0.211 (f)	radial	40.8	4.71	1.59
Astroni 2	Campi Flegrei	-	small	-	0.026 (f)	radial	18.6	3.22	1.70
Astroni 1	Campi Flegrei	4.2 ka Cal (g)	small	-	0.081 (f)	radial	38.3	4.48	1.52
Averno 2	Campi Flegrei	-	small	3.2 $\cdot 10^6$ (e)	0.104 (f)	radial-blocked	19.1	4.03	3.14
Solfatara	Campi Flegrei	4.2 ka Cal (g)	small	-	0.035 (f)	radial	4.29	1.89	2.24
Agnano-Monte Spina	Campi Flegrei	4.5 ka Cal (g)	large	1.2 $\cdot 10^8$ (e)	1.455 (f)	blocked	272	18.5	8.06
Paleoastroni 1	Campi Flegrei	4.8 ka Cal (g)	small	-	0.068 (f)	radial-blocked	18.1	5.19	8.02
Monte Sant'Angelo	Campi Flegrei	4.9 ka Cal (g)	small	-	0.094 (f)	radial-blocked	35.2	5.90	5.08
Agnano 3	Campi Flegrei	-	medium	-	0.250 (f)	radial	71.1	7.73	3.05
Cigliano	Campi Flegrei	-	small	-	0.070 (f)	radial-blocked	25.9	4.63	4.28
Averno 1	Campi Flegrei	5.2 ka Cal (g)	small	-	0.071 (f)	radial	19.2	3.66	3.39
Agnano 2	Campi Flegrei	-	small	-	0.019 (f)	radial	17.1	3.59	3.65

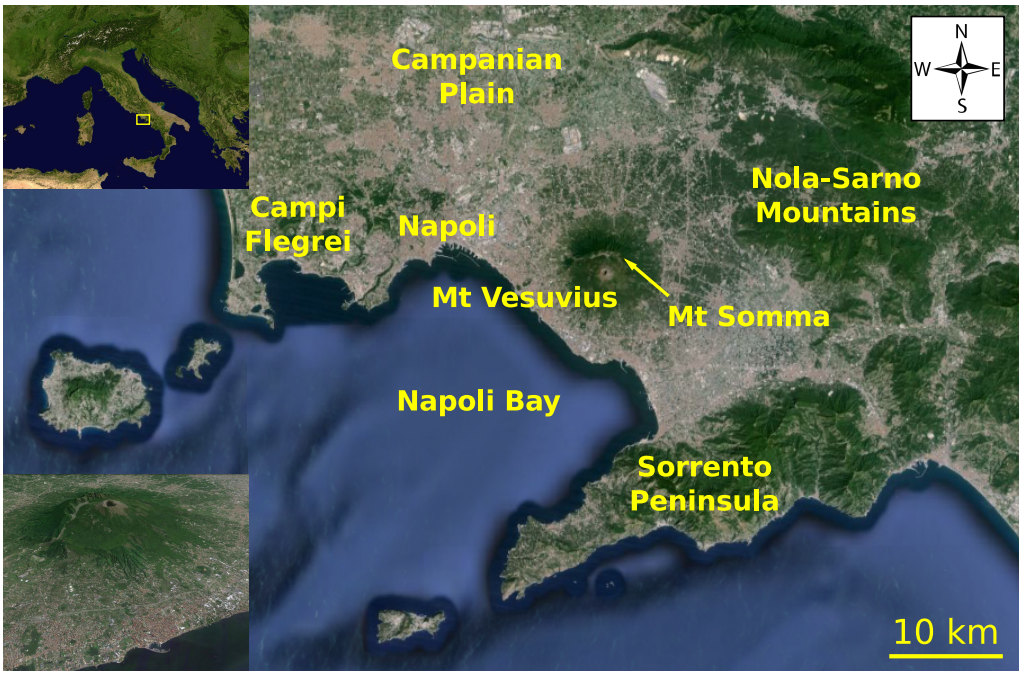

FIGURE 3.1: Geographical and volcanological setting of the Neapolitan area. On top left: map of South-Central Europe with Italy located in the middle of the map. The yellow square denotes the boundaries of the main image where different key locations are identified. The city of Napoli stands on or is surrounded by two principal volcanic systems: Campi Flegrei to the west, and Somma-Vesuvius to the east. The Campanian Plain is the tectonic basin where the two volcanic systems originated. Some geomorphological highs which limit the Campanian Plain are the Nola-Sarno Mountains (on the top-right of the map) and the Sorrento Peninsula (on bottom-right of the map). Northwards from Vesuvius, a remnant from previous edifice collapses is present: Mount Somma. A 3D view from the southwest (Torre del Greco is in the bottom-center of the caption) of the Somma-Vesuvius' cone and Mount Somma are shown in the inset on the bottom left of the figure. Source: Google, DigitalGlobe, December 11, 2014. From [104].

or phreatomagmatic explosions. In the case of small eruptions (sub-Plinian II and violent Strombolian in the classification of [89]), PDC events can vary from small-volume PDCs formed by column collapse to low-mobility hot avalanches (e.g. [193]).

Regarding the generation of lahars, the eruptions from Somma-Vesuvius have produced rain-triggered lahars whether as a result of post-eruption remobilization of the tephra deposits accumulated during medium and large eruptions (e.g. [170, 198]) or during the intervals between eruptions [199, 200]). The former type of flows generated deposits composed almost completely by tephra coming from the preceding eruption while the second type of flows produced deposits with a

mixture of tephra from different eruptions and also parts of the carbonate bedrock (e.g. [170, 201, 202]).
In the future, it may be expected that explosive eruptions at Somma-Vesuvius (from small up to large) will deposit a certain amount of pyroclastic material onto the slopes of the volcanic edifice as well as on the Apenninic reliefs towards the northeast, east and southeast of Somma-Vesuvius [26, 196]). Under this situation, tephra may be initially remobilized mainly by erosive runoff of the fine-grained upper-part of the deposit and then mainly by shallow gravitational failures as the coarser-grained underlying deposit is exposed (e.g. [170]).

3.2 Campi Flegrei

Campi Flegrei lies west of Somma-Vesuvius and is a nested caldera complex (Fig. 3.1) built mainly after two large eruptions at ∼39 ka (Campanian Ignimbrite, CI, eruption; [203] and references therein) and ∼15 ka (Neapolitan Yellow Tuff, NYT, eruption; [204] and references therein). After the latter, eruption occurrence has followed diverse spatial-temporal trends. Spatially, regional normal faults have tended to control the vent-opening pattern [25, 205, 206] while, temporally, volcanic events have clustered in three main epochs [25, 191]: epoch I (15-9.5 ka), epoch II (8.6-8.2 ka) and epoch III (4.8-3.8 ka).
During the first two epochs, the volcanic vents were located almost exclusively along the marginal faults associated with caldera collapse during the NYT eruption. Between epochs II and III, however, caldera resurgence led to strong uplift of the central sector of the caldera floor (*La Starza* block, [37]) and conditioned the vent-opening locations during epoch III, which mainly clustered over the NE sector of the NYT caldera floor [25]. Although some recent studies have also considered the both epochs I and II in their hazard analysis [33, 206], here we focus on information extracted from the last 5 kyr of volcanic activity, as did [25, 195] and [72]. This is based on the assumption that future behavior of the caldera system will be linked to the stress regime and deformation pattern established after uplift of the *La Starza* block and before the onset of epoch III of volcanic activity. The spatial distribution of volcanic vents during epoch III, as well as the present-day geothermal manifestations and the dynamics of recent episodes of unrest (e.g. [188, 207, 208]) are compatible with the tectonic model presented by [25].

Similarly to what proposed at Somma-Vesuvius, we use a magnitude-based classification of the explosive eruptions possible at Campi Flegrei (e.g. [195]) and explore three eruption sizes: small (comparable to Averno 2 eruption), medium (comparable to Astroni 6 eruption) and large (comparable to Agnano-Monte Spina eruption).

PDC generation at Campi Flegrei is strongly affected by the existence of well-established aquifers along a mature hydrothermal system (e.g. [209]), which has led to the generation of moderately to highly mobile pyroclastic surges (e.g. [25]). We focus on the eruptive behavior related to the III epoch of volcanic activity at Campi Flegrei (after [195]) and, thus, we do not consider the formation of very large ignimbrites, like the NYT or the CI, similarly to what has been recently done by [33] in their PDC hazard assessment.
The base surges expected to occur at Campi Flegrei may have moderate to high mobilities, similar to that associated with surges at other volcanic systems (e.g. [137]), and in approximate correspondence to their total volumes (e.g. [131]).

Chapter 4

Physical and statistical modeling of uncertainty in volcanic hazards

Uncertainty is pervasive in volcanic hazards so its quantification has become a major goal for volcanic hazard assessments of any kind of hazardous process (e.g. [21, 33, 49, 70, 101, 210, 211]). As previously discussed, not only does the natural variability of the process (i.e. aleatory uncertainty) affect the hazard assessment but also different sources of incomplete knowledge (i.e. epistemic uncertainty) have a major impact on the final assessment (e.g. [53, 54]). The quantification of these (large) uncertainties is extremely challenging and there might be several strategies to achieve this goal (e.g. [83]).

We choose probability as the way to quantify uncertainty because of the reasons related in Chapter 1. In the probabilistic view to uncertainty quantification, the hazard analyst commonly needs to (e.g. [83]): (1) define the spatial and/or temporal domain over which the hazard is quantified (the hazard domain); (2) define the set of events that are *possible* according to, for instance, the eruptive history of the volcano of interest (or that of analog volcanoes); (3) assign probabilities to all the hazard events defined in (2); and (4) propagate the hazard events into hazard outcomes. For us, the hazard domain is only spatial because we model hazard events that do not overlap in time. Therefore, the distinction between hazard event and outcome proposed by [83] is not relevant for our general modeling strategy. Altough such a strategy is a simplification of the complex temporal evolution of real eruptions (e.g. [3]), it still is the state of the art in volcanic hazard assessments (e.g. [31, 33, 54, 70]). Thus, we describe a hazard event as the features of the onset of the hazardous process, for example: PDCs triggered from

a collapse height of 1 km and that have a mobility of $\phi = 15°$ (see section 4.1.1). The hazard outcome is seen as the result of the hazard event, e.g. PDCs invade a specific point over the hazard domain. In summary, our hazard events can be interpreted as hazard outcomes of one single hazard event in [83] and our hazard outcomes can be viewed as realizations of the footprint function in [83], which we call hazard footprints. The footprint function is a tool that "imprints" the hazard event into the hazard domain and, thus, it produces a hazard outcome (or hazard footprint).

Commonly, the footprint function is a deterministic physical model of the hazardous process. The complicated part of the probabilistic volcanic hazard assessment is that the number of *possible* hazard events tends to be huge. Ensuring that the uncertainty quantified in step (3) above (usually by means of probability density function(s), PDF) is propagated into the hazard footprints of the physical process is the core of probabilistic hazard assessments. This procedure has a computational cost that depends on: (a) how fast the physical model (or footprint function) is; and (b) how many hazard footprints are needed to ensure that uncertainty has been propagated in a robust manner (e.g. [82]). Unfortunately, the fastest simulators are also the simplest (see Chapter 1). Similarly, uncertainty quantification techniques, UQT[1] that are easily implemented tend to be the ones that are less efficient, i.e. a higher number of physical-model runs are required to properly quantify uncertainty.

In this dissertation, we explore several combinations of physical models and UQTs that allow to compute probabilistic volcanic hazard of PDCs and lahars. In particular, the fastest physical model, Energy Cone (see subsection 4.1.1) is coupled with the least-efficient UQT, Monte Carlo sampling (see subsection 4.2.1); while a more sophisticated (but slower) physical model, Titan2D (see subsection 4.1.2), is coupled with a more-efficient UQT, Polynomial Chaos Quadrature (see subsection 4.2.2). The results derived from these hazard analyses are input into a versatile UQT, Bayesian Event Tree for Volcanic Hazard (see subsection 4.2.3), that permits the merging of probabilities of, say, PDC arrival with probabilities of eruption size or location at the volcanic system of interest. Likewise, another flexible UQT, Bayesian Belief Network (see subsection 4.2.4), allows us to combine probabilistic hazard assessments of tephra fallout and PDCs with other information to provide

[1] Along this dissertation, we also refer to them, more generally, as "statistical models".

probabilities for the occurrence and volume and rain-triggered lahars. The computation of the hazard footprints for these lahars is done through a dynamic physical model called *LaharFlow* (see subsection 4.1.3). Along this chapter, we summarize the main features of the 3 physical models and 4 UQTs aforementioned.

4.1 Physical models

4.1.1 Energy Cone model

The Energy Cone model (EC, [132]) is an analytical model based upon a simplified formulation of the energy conservation equation that can be derived from the Bernoulli's equation (e.g. [134]). The model assumes that PDCs have an initial potential energy expressed as the height above sea level (a.s.l.) from which they are generated. Thus, PDCs can be triggered at the top of the volcano (located at a height H_v a.s.l.): for instance, in the case of a lava-dome collapse or explosion (see Chapter 2); or they can form because of a collapse of the eruption column from a given height H_0 (above H_v). According to the model, the potential energy is converted into kinetic energy as the pyroclastic mixture (PDC) flows over the ground and travels away from the vent. During PDC motion, kinetic energy is dissipated by effective friction with the ground. PDCs are assumed to behave as a gravity-driven, cohesionless suspension of particles and gas with mass remaining constant [129]. Under these assumptions, the energy loss is simplified into a linear decay with distance, i.e. the Energy Line [212]:

$$[(H_v + H_0) - h(x)] \cdot g = 1/2 \cdot v^2(x) + gx \cdot \tan\phi \tag{4.1}$$

where $h(x)$ is the topographic height at distance x from the vent, g is the acceleration of gravity, $v(x)$ is the velocity of the PDC at distance x, and $\tan\phi$ denotes the equivalent coefficient of friction: a bulk measure of the PDCs resistance to flow or, in other words, the PDC mobility (the smaller ϕ, the more mobile the PDCs).

Along a given direction, PDCs terminate when all energy has been dissipated, i.e. when the Energy Line cuts the topographic surface (Fig. 4.1). At the point where the flow stops (x_{stop}), located at a horizontal distance from the vent equal to L and at a height, $h(x_{stop}) = H_{stop}$, we have:

$$v^2(x_{stop}) = 0 \implies (H_v + H_0) - H_{stop} = L \cdot \tan\phi$$
$$\implies \Delta H/L = \tan\phi \tag{4.2}$$

Note that L is the PDC runout in a given direction, and so the Maximum Runout (MR) is equal to $\max(L)$ among all the simulated azimuths. Equation 4.2 has been typically used to calculate the mobility of PDCs formed during a given eruption by measuring L on the deposits preserved from the eruption and giving an estimation of ΔH (e.g. [131, 213, 214]).

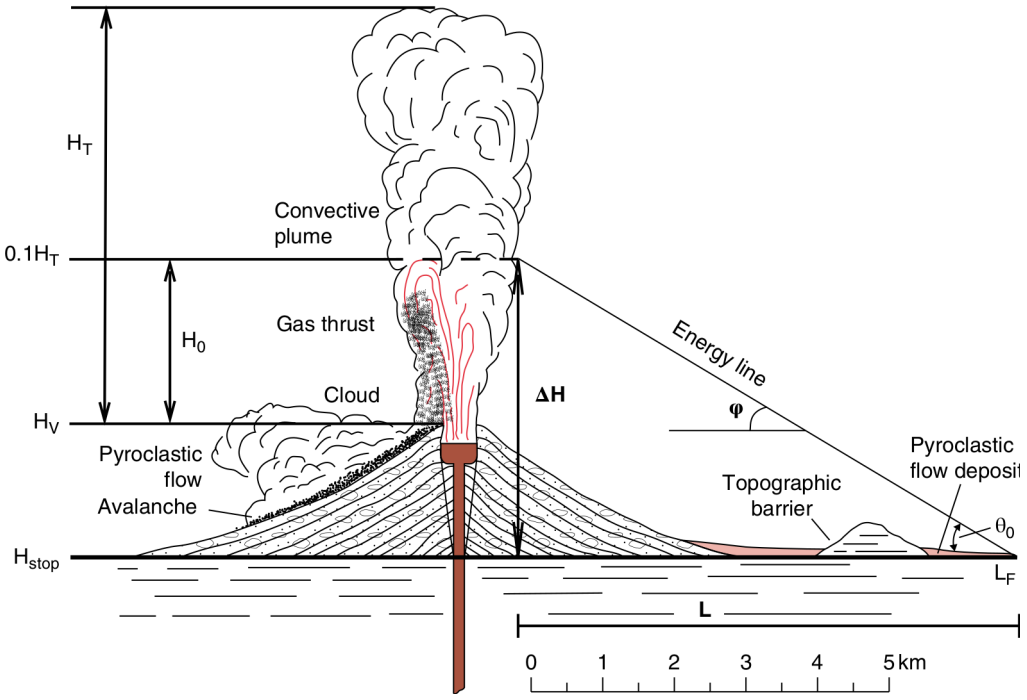

FIGURE 4.1: The Energy Line concept. PDC transport is dependent on the initial collapse height above the vent, H_0 (in the picture coincident with the top of the gas-thrust region: $\sim 0.1H_T$ -not to scale-; where H_T is the total eruption column height, above the vent) and the angle between the Energy Line and the horizontal (ϕ), a proxy for the PDC mobility. PDC runout is denoted by L. H_v: altitude of the volcanic vent (a.s.l.); H_S: altitude of the stopping point (a.s.l.); $DeltaH = (H_0 + H_v) - H_S$. From [103], after [215].

Regarding PDC modeling, EC was first presented by [132] who applied a 3D extrapolation of the Energy Line concept to the lateral blast produced during the 1980 eruption at Mt Saint Helens, USA. The Energy Line concept had been previously applied to model a phreatically originated block-and-ash flow at La Soufrière, Guadeloupe [216] and, since then, EC has been utilized to simulate

diverse types of PDCs, ranging from surges to phreatic explosions and including both column collapse and dome collapse processes (e.g. [41, 136, 137, 217]). Nevertheless, the application of the EC model (based on a balance of energies) is expected to be more appropriate for dense PDCs, for which this energy balance better predicts the distribution of the PDC deposit [124]. According to the PDC classification of [148] (see Chapter 2), EC applies better to forced convection-dominated PDCs although some effects derived from inertia-dominated PDCs (e.g. riding over topography) may be captured when the EC is used in a stochastic manner (e.g. [104], see Chapters 5, 6). Additionally, the application of the EC model to strongly channelized PDCs can be inadequate.

In this dissertation, we apply EC to Somma-Vesuvius and Campi Flegrei (Italy), two volcanoes for which the channelization problem should not be an issue, due to the high frequency of radially dispersed PDCs in their eruptive records (see Table 3.1, Chapter 3). Our way of applying the EC model is founded on the exploration of the model-parameter space (basically the parameters H_0 and ϕ), by means of Monte Carlo sampling (see subsection 4.2.1), in order to quantify aleatory and epistemic uncertainty linked to the modeling of PDCs via the EC model. We select this model because: (1) it is the simplest PDC model that can simulate, in principle, both dense and dilute PDCs; (2) its use has been widespread; (3) its computational time is very short (seconds to minutes per run); and (4) it can be run over a Digital Elevation Model (DEM). The first point is quite relevant since probabilistic hazard assessments of PDCs so far have utilized PDC models which can only deal with dense (e.g. Titan2D, [23, 31, 82]) or dilute PDCs (e.g. Box Model, [33]). Also point (4) is crucial because, among the aforementioned PDC models, the Box Model has not been yet implemented to run over real topography (e.g. a DEM, [33]), and the Titan2D has been demonstrated to be quite sensitive to the characteristics (e.g. horizontal resolution, vertical errors) of the DEM product used to run the model (e.g. [84, 85, 180]). On the contrary, the EC model does not seem to be much affected by the DEM utilized, at least in terms of horizontal resolution [104] (see Chapter 6). Nonetheless, before applying EC to compute probabilistic volcanic hazard of PDCs (see Chapter 7), we develop a robust procedure to test the suitability of this PDC model for this purpose [103], as related in Chapter 5.

4.1.2 Titan2D

The Titan2D model [218] is a numerical simulator initially conceived to simulate dry avalanches on volcanic environments. The model calculates the propagation of an incompressible continuum (e.g. a granular flow) that deforms brittly following a Mohr-Coulomb law [218]. Thus, normal and shear stresses control the loss of momentum of the flow by means of friction: (1) within the flow (internal friction); and (2) along the contact surface between the flow and the underlying terrain (bed or basal friction). The governing equations of Titan2D are derived from the debris flows equations [219]: a set of depth-averaged, frame-invariant hyperbolic equations for (fluidized) granular masses propagating over three-dimensional terrain (e.g. a DEM). Titan2D is based upon the dry limit (i.e. zero pore pressure) of the debris flow equations of [219]. Moreover, the model assumes that the simulated flow is very thin as compared to its lateral extension (shallow-layer approximation).

Under these assumptions, the momentum of the granular flow over directions parallel to the topographic surface (i.e. x, y; z is the direction normal to this surface) can be described in terms of the following equation (for the x axis in this case):

$$\partial_t(h\bar{v}_x) + \partial_x\left(h\bar{v}_x^2 + \frac{1}{2}k_{ap}g_z h^2\right) + \partial_y(h\bar{v}_x\bar{v}_y) =$$
$$g_x h - hk_{ap}\mathrm{sgn}(\partial\bar{v}_x/\partial_y)\partial_y(g_z h)\sin\phi_{\mathrm{int}} - \frac{\bar{v}_x}{\sqrt{\bar{v}_x^2+\bar{v}_y^2}}\left[g_z h(1+\frac{\bar{v}_x}{r_x g_z})\right]\tan\phi_{\mathrm{bed}} \quad (4.3)$$

where h is the flow depth; $\bar{v}_x$ and $\bar{v}_y$ are the depth-averaged velocities on the x and y axes, respectively, that is (for the x axis):

$$h\bar{v}_x = \int_b^s v_x d_z$$
$$h(x,t) = s(x,t) - b(x,t) \quad (4.4)$$

where $s(x,t)$ denotes the free surface (top) of the granular flow, and $b(x,t)$ denotes the basal surface, interface between the granular flow and the topography. These free and basal surfaces are actually functions that evolve in space and time as the flow propagates [218].

In equation 4.3: g_x and g_z are the components of the acceleration of gravity on the x and z axes, respectively; k_{ap} is a variable that serves to define the state of stress over an element of the flow as active (if the element is elongated) or passive (if the element is compressed) [218]; sgn is the sign function; r_x is the local radius of curvature (of the topographic surface) along the x axis; and ϕ_{int}, ϕ_{bed} are the angles of internal and basal (or bed) friction, respectively (see below).
The principal governing equation of the Titan2D model states that: (1) the granular flow basically acquires momentum due to the force of gravity; (2) the granular flow loses momentum due to internal friction at a rate that increases with the flow speed along the x axis (in equation 4.3), the flow depth, the internal friction angle and with flows that converge or are "compressed" (according to the definition of k_{ap}, [218, 219]); (3) the granular flow loses momentum due to basal (bed) friction at a rate that increases with the flow speed along the x axis, the difference in flow speed between the x and y axis, the flow depth, the local curvature of the topography along the x axis, and the bed friction angle.

We describe the main parameters of Titan2D below. For a more detailed description of the numerical model see the Titan2D user guide [220]. Instead, for the parameterization that we implement to model column-collapse dense PDCs at Somma-Vesuvius see Chapter 8:

- Internal friction angle (ϕ_{int}): it represents the angle of repose (e.g. [221]) of a pile of (simulated) material that stands on a horizontal surface, that is, the maximum angle that the conical surface of the pile can form with the aforementioned surface. It is a property of the material only and it has been demonstrated to have a limited impact on the Titan2D outputs (e.g. [222]).

- Bed friction angle (ϕ_{int}): it represents the angle that an inclined plane must reach for a static pile of (simulated) material resting over it to start moving down the plane. It is a property of both the flow and the underlying surface (e.g. [41, 82] and its importance has been shown paramount in controlling the output of the model (e.g. [23, 27, 180, 222]).

- Number of piles (N): the model allows to use one or more piles of material, each of them with different characteristics, set by the variables described below. Moreover, the user may select pile sources but also flux sources (e.g. [27]).

- Major and minor radii of the pile (R, r): they define the shape of the base of each pile of material, which can range from a circle (i.e. $R = r$) to different types of ellipses, when $R \neq r$.

- Strike of the major radius (θ): it defines the orientation of each pile as the angle between the East and the major axis of the pile (measured counter-clockwise from the East).

- Location of the center of the pile (x, y): it indicates the Universal Transverse Mercator (UTM) coordinates of the center of the pile.

- Pile height (h_0): it denotes the vertical dimension of each pile. Together with R, r and the shape of the pile, it determines the initial volume of dense PDCs that is simulated (see below).

- Pile shape: Titan2D can work with elliptic paraboloids or elliptic cylinders as the pile shapes. The choice of the pile shape affects the calculation of the total volume (V_0) of material present in each pile: $V_0 = \frac{1}{2}\pi R r h_0$ for an elliptic paraboloid and $V_0 = \pi R r h_0$ for an elliptic cylinder.

- Initial speed (v_0): it defines whether the simulated dense PDCs have an initial lateral speed when the simulation starts. Such a feature can be used, for instance, to model dome-collapse $(v_0 = 0)$ and dome-explosion PDCs $(v_0 \neq 0)$ differently.

- Initial direction (θ_{v_0}): it indicates the azimuth for the initial propagation of dense PDCs as an angle measured counterclockwise from the East.

Titan2D has become very popular among the volcanological community that has used it, principally, to simulate dense PDCs, in particular Block-And-Ash Flows, BAFs (e.g. [27, 41, 145, 222, 223, 224, 225]). The reasons for its success are varied. From the computational point of view, Titan2D gives accurate and precise solutions of the (adapted) debris flow equations at a reasonable computational cost. Firstly, the model is written using free software tools and libraries and it runs in parallel (i.e. the code is executed by multiple processors simultaneously). This can be exploited at several scales, from that of a multi-core laptop up to that of large-scale cluster computers. Secondly, the model uses a computational mesh that is adapted (i.e. refined and unrefined), at each time step of the simulation, according to two aspects: (1) where the greatest fluxes of material are located; and (2) where

the local changes in flow depth occur (e.g. at the flow front, [218]). Thirdly, the model is coupled with a scheme for dynamic load balancing (e.g. [226]) through which the work given to each processor is evenly distributed as the simulation proceeds. All these aspects together reduce significantly the computational time of each run of Titan2D and make it one of the fastest simulators available to model PDCs (e.g. [227]).

From the volcanological point of view, the greatest advantages of Titan2D are the following: (1) it provides a detailed physical description of the dense basal part of PDCs; (2) each model run is typically started from a pile of material, a setting that resembles the triggering of BAFs; (3) the simulator is user-friendly enough to be run by a wide variety of hazard analysts, not only by those with a strong background in computer science. Finally, the Titan2D is a versatile simulator because of the wide applicability of its governing equations. Thus, some other studies have applied it to simulate: (i) column-collapse PDCs (e.g. [106], see Chapter 8); (ii) lahars of different origin (e.g. [228, 229, 230]); (iii) debris avalanches (e.g. [222, 231]).

Nonetheless, there are also limitations and disadvantages of the Titan2D model for simulating PDCs and for estimating the probabilistic volcanic hazard associated with them. First of all, the Titan2D model is only valid for dense PDCs (see Chapter 2). This excludes its application to volcanoes (like Campi Flegrei, Italy, e.g. [25, 37]) or to eruptions (like the Avellino eruption at Somma-Vesuvius, Italy, e.g. [232]) characterized by generating predominantly-dilute PDCs. Another issue that arises in the application of Titan2D to reconstruct past PDC deposits and/or for volcanic hazard assessments is the fact that each Titan2D simulation needs to be "stopped" after a given total time of simulation (or after a given number of time steps). Otherwise, the simulated flow does not stop and, moreover, as its depth (h) approximates zero, its speed can tend towards infinity because the flow speed is calculated as flow momentum (hv) divided by the flow depth (the thin-layer problem, e.g. [82]). Some solutions based on scaling and thresholding the flow depth, speed or flow fluxes have been presented by [82]. Other works have proposed global and local stopping times that are functions of some Titan2D parameters [108, 233] but a general solution still has to be found.
Other sources of epistemic uncertainty known to exist in Titan2D modeling are the DEM resolution (e.g. [84, 85, 86, 180]) and the link between the PDC volume and the bed friction angle, ϕ_{bed} (e.g. [131, 138, 234]). A major problem for

probabilistic hazard assessment of dense PDCs performed via the Titan2D is that all these sources of epistemic uncertainty still need to be fully understood (see Chapter 8): they have just been quantified to some extent (e.g. [84, 85, 222]) but it is still strongly unclear which of these sources is most crucial in modifying the outputs of the Titan2D model and whether they are all similar in importance or one of them dominates over the rest (e.g. [75, 104]).

4.1.3 *LaharFlow*

In Chapter 9 of this dissertation, we couple a physical model of lahars with a Bayesian Belief Network to provide a probabilistic multi-hazard assessment of rain-triggered lahars at Somma-Vesuvius (Italy). Our multi-hazard approach allows the coupling of any lahar-transport model with the BBN model. In this dissertation, we utilize a dynamic lahar model called *LaharFlow* [235]. We briefly summarize the key features of the model and the boundary conditions adopted in Chapter 9 in the following subsections.

Model description

LaharFlow adopts a shallow-layer formulation, in which the flowing layer is depth-averaged, similarly to many models of earth surface flows. The equations governing the evolution of the lahars are derived from conservation of mass and momentum, and are applied on a DEM. The model also includes a description of solids transport, which plays a crucial role in the dynamics. The solid phase is assumed to be transported at the bulk horizontal velocity of the flow, but can settle from the fluid phase and be deposited. Additionally, solids can be entrained into the flow by erosion of the underlying topography. The erosion and deposition alters the topography, and this morphodynamics is coupled to the flow dynamics in *LaharFlow*.

We describe erosion by adopting a Shields criterion (e.g. [236]), whereby material is entrained into the flow when the Shields stress (the non-dimensional shear stress acting on the base boundary of the flow) exceeds a threshold value that is dependent on the properties of the bed (specifically the grain size and density). When the critical Shields stress is exceeded, material is entrained from the bed into the

flow at a rate that is a function of the excess of the Shields stress. This entrainment model is commonly applied in hydraulic models, and we have calibrated this description for use in a model of lahars.

In contrast to many hydraulic flows, the solids phase can constitute a very substantial proportion of lahars and significantly influence the flow dynamics. In *LaharFlow*, we model the influence of the solid phase primarily through the basal frictional resistance to motion, referred to as the basal drag. Our model adopts a basal drag that varies as the concentration of solids in the flow evolves. At low concentrations we expect the solids to have relatively little dynamical influence, and so model the flow as a turbulent fluid with a basal drag that is velocity dependent; we take a Chézy drag formulation where the resistance takes the form:

$$F_f = C_D|\boldsymbol{u}|^2 \tag{4.5}$$

where C_D is referred to as the Chézy drag coefficient and $\boldsymbol{u}$ is the depth-averaged flow velocity. If the solids concentration increases sufficiently the flow can transition to a (lubricated) dense granular flow. For granular flows, experiments suggest that a Coulomb basal drag is appropriate, where $F_g = \mu g h$ with μ referred to as the friction coefficient, g is the gravitational acceleration and h is the thickness of the flowing layer. Here we adopt a granular drag model proposed by [237], noting that while this model was proposed on the basis of experiments with dry grains, the relationship is calibrated using observations of lahars [235]. The model of [237] specifies a non-constant granular friction coefficient μ, allowing uniform flows to exist over a range of inclinations of the bed (as observed in experiments). At intermediate concentrations, we expect both fluid-like velocity-dependent and granular-like depth dependent basal drag forms to contribute to the bulk flow resistance. We model this transition between regimes by introducing a switching function, so that the basal drag is:

$$F = (1 - f(c))F_f + f(c)F_g \tag{4.6}$$

with $f(0) = 0$, $f(c_m) = 1$ and $f(c)$ monotone increasing for $0 < c < c_m$ where c_m is the maximum packing fraction of the grains. In this study, we take $f(c) = 1/2(1 + \tanh(\gamma(c - c_0)))$ with the parameters γ and c_0 calibrated against observations of lahars [235].

4.2 Statistical models

4.2.1 Monte Carlo sampling

Monte Carlo sampling methods are based upon the generation of random (or pseudorandom) numbers in order to solve different kinds of problems such as numerical integration, inverse modeling or statistical inference (e.g. [238, 239]). The name Monte Carlo makes reference to the administrative area of the Principality of Monaco and was coined by researchers of the Manhattan Project at Los Alamos National Laboratory (NM, USA) in the late 40s.
In the field of probabilistic volcanic hazard assessment, where aleatory (and sometimes epistemic) uncertainty tends to be defined through PDFs for the parameters of a given physical model, the main objective of Monte Carlo sampling methods is to approximate a specific PDF as a (large) compilation of random samples from the distribution. In other words, by randomly drawing thousands to millions of realizations from a given PDF, it is possible to obtain samples whose mean, variance and percentiles approximate those of the actual distribution (e.g. [239]). By the central limit theorem, the standard error of the mean calculated via Monte Carlo sampling tends to zero as the number of realizations tends to infinity. Therefore, the number of realizations required to obtain two and three significant figures of accuracy in the final results is 10^4 and 10^6, respectively. Each of these realizations implies one run of the physical model used as the footprint function (i.e. to propagate hazard events into hazard outcomes). Thus, it is clear that Monte Carlo sampling methods may be of application only with very simple physical models, for which the runtime ranges from seconds to minutes (e.g. Energy Cone). More sophisticated simulators, such as Titan2D, would require more than 215 days of non-stop computation to be able to run 10^6 simulations [82].

The number of different methods to perform Monte Carlo sampling is huge (e.g. [239]) and distinct geophysical problems may need specific methods to be considered. In our case, we sample the PDFs of interest following the inversion method, which is simple and efficient (e.g. [239]). The procedure for one uncertain variable (x), with PDF $f(x)$, reads as follows:

1. Calculate the Cumulative Distribution Function, CDF ($y = F(x)$), for the variable:

$$y = F(x) = \int_X f(x)dx \tag{4.7}$$

where X denotes the domain of the variable ($x_i \in X \forall x_i$). The domain of the variable y is [0, 1].

2. Generate (equiprobable) random numbers in the interval [0, 1].

3. For each random number, calculate the value of the inverse CDF: $x' = F^{-1}(y)$. The values of x' are actually random samples of the PDF $f(x)$.

In most of our applications of Monte Carlo sampling to probabilistic volcanic hazard assessment, we use sample sizes of 10^4 (see Chapters 5, 6, 9). In some cases, where the target PDF is the Uniform distribution, we may use sample sizes of 10^3 (see Chapter 7). This is because the Uniform PDF can be well approximated with random samples of such size, something that might not be true for other distributions with more complex shapes or with long right-hand tails (e.g. [83, 239]).

4.2.2 Polynomial Chaos Quadrature

Polynomial Chaos Quadrature (PCQ) is an uncertainty-quantification technique aimed at obtaining a functional approximation of a given simulator (e.g. Titan2D) by combining polynomial expansion procedures and numerical quadrature (e.g. [24, 82]). The basic target is the computation of a continuous response function, Y, from a collection of discrete realizations, y_i. These realizations are extracted from the outputs of the simulator that, in turn, depend on the specific values of the model paramaters used to run the simulator. The model parameters explored (i.e. assumed to be uncertain: $X = (X_1, \ldots, X_d)$ are usually selected because of their high impact on the model outputs (e.g. [222, 225]). Thus, the response function, Y, represents a link between the parameters of the model and its outputs. Here, we illustrate the very basics of the PCQ derivation in the case in which $d = 2$ (i.e. $X = (X_1, X_2)$). Let us consider the response function:

$$Y = f(X_1, X_2) \tag{4.8}$$

where aleatory uncertainty in X_1, X_2 is modeled through marginal distributions with finite moments: $w_1(X_1), w_2(X_2)$. The variables need to be independent of each other (or very-weakly related) for the PCQ procedure to be implemented successfully. The joint distribution of X_1, X_2, given independence between the variables, can be written as follows:

$$w(X) = w_1(X_1) \cdot w_2(X_2) \tag{4.9}$$

Following the Karhunen–Loève theorem, we can describe $f(X_1, X_2)$ in equation 4.8 as an infinite linear combination of orthogonal polynomials, Φ_i, and unknown coefficients, c_i (e.g. [82]):

$$Y = \sum_{i=0}^{\infty} c_i \ \Phi_i(X_1, X_2) \tag{4.10}$$

The set of polynomials in equation 4.10 is chosen to be orthogonal (see equation 4.11 below) to the marginal distributions $w_1(X_1)$, $w_2(X_2)$ and are known for a variety of probability distributions such as the Gaussian or Beta PDFs (e.g. [24, 82]). Orthogonality allows exponential convergence (i.e. error reduction) in deriving the statistical moments of the reponse function, Y. Note that the use of an infinite number of polynomials and coefficients is not feasible for real-world problems and, therefore, the polynomial expansion is truncated at a given finite number of these polynomials (n). Given the truncation, the actual response function Y cannot be retrieved but what is obtained is an estimator of the response function: $\tilde{Y}$. The higher the number of polynomials used, the closer the estimator will be to the true response function (e.g. [82]).

Orthogonal polynomials can be defined as those that satisfy the following equation:

$$\int_{-\infty}^{\infty} \Phi_j(X_1, X_2) \prod_{i=0}^{\infty} \Phi_i(X_1, X_2) \ w_1(X_1) w_2(X_2) \ dX_1 dX_2 = \delta_{ij} \tag{4.11}$$

where δ_{ij} is the Kronecker delta. As previously mentioned, there are families of polynomials that are orthogonal to different common PDFs such as the Hermite polynomials for Gaussian dsitributions, the Jacobi polynomials for Beta distributions or the Laguerre polynomials for Exponential distributions (e.g. [24]). Thus,

the only unknowns present in equation 4.10 are the coefficients c_i. Let us analyze the following integral:

$$\iint_{\mathbb{R}^2} \sum_{i=0}^{\infty} c_i \; \Phi_i(X_1, X_2) \; \Phi_1(X_1, X_2) \; w_1(X_1) \; w_2(X_2) \; dX_1 \; dX_2 \tag{4.12}$$

which can be re-written as follows:

$$\iint_{\mathbb{R}^2} c_1 \; \Phi_1^2(X_1, X_2) \; w_1(X_1) \; w_2(X_2) \; dX_1 \; dX_2 \tag{4.13}$$

because of orthogonality (equation 4.12). Consequently, we can derive that:

$$c_1 \iint_{\mathbb{R}^2} \Phi_1^2(X_1, X_2) \; w_1(X_1) \; w_2(X_2) \; dX_1 \; dX_2 \; = \; c_1 \tag{4.14}$$

Thus, the integral 4.12 equals c_1 and the same applies to the n terms of the polynomial expansion. In addition, we note that the member $\sum_{i=0}^{\infty} c_i \; \Phi_i(X_1, X_2)$ in integral 4.12 is equivalent to the definition of the response function, given in equation 4.10. Therefore:

$$c_1 = \iint_{\mathbb{R}^2} Y(X_1, X_2) \; \Phi_1(X_1, X_2) \; w_1(X_1) \; w_2(X_2) \; dX_1 \; dX_2 \tag{4.15}$$

Given the assumption that the response function, Y, can be described as a polynomial of a specific degree, numerical integration can be approximated through Gaussian quadrature (e.g. [82]), that is: as a weighted sum of the integrand evaluated at a collection of quadrature points. The total number of quadrature points (Q_{tot}) needed to carry out the PCQ procedure is given by the maximum order of polynomials used in the expansion ($N_{polymax}$) and the number of uncertain model parameters considered (d) as follows: $Q_{tot} = (N+1)^d$, where $N_{polymax} = 2N + 1$ (e.g. [82, 240]). Therefore, PCQ is subject to the "curse of dimensionality" (e.g. [241]) and it is expected to outperfom Monte Carlo sampling only if the number of uncertain model parameters is around three (e.g. [24]).

The collection of quadrature points (Q) belongs to the model parameter space ($Q = \{(X_{1_i}, X_{2_i}), \ldots, (X_{1_{Q_{tot}}}, X_{2_{Q_{tot}}})\} \in X$) and the location of each quadrature point along this parameter space is given by the Gaussian quadrature rule and

the PDFs selected to model uncertainty in the model parameters (e.g. [24, 240]). At the coordinates of the model parameter space indicated by each quadrature point (e.g. X_{1_1}, X_{2_1}), one simulation of the physical model is run. Using the full collection of Q_{tot} simulations, all the PCQ coefficients are calculated and one estimator of the response function, $\tilde{Y}$, can be computed at each grid point over the hazard domain. By Monte Carlo sampling of these estimators (i.e. surrogates of the simulator), the probability of exceedance for different values of any output variable of interest to assess volcanic hazard (PDC speed, PDC flow depth, PDC volume at given catchment) can be extracted (see Chapters 8, 9).

4.2.3 Bayesian Event Tree for Volcanic Hazard

The Bayesian Event Tree for Volcanic Hazard, BET_VH [49, 242], is a statistical model conceived to estimate the probability of different volcanic hazardous events, at a specific volcano(es) of interest, by applying Bayesian statistics. The core of the latter is the Bayes' theorem (e.g. [65]), which can be stated as:

$$P(A|B) = \frac{P(A \bigcap B)}{P(B)} = \frac{P(B|A) \cdot P(A)}{P(B)} \tag{4.16}$$

where, in the simplest case, A and B are two related events, P(A) denotes the probability of A happening and is commonly known as prior probability, P(B|A) denotes the probability of B happening given that A has already happened and is commonly known as likelihood function, P(A|B) denotes the probability of A happening given that B has already happened and is commonly known as posterior distribution, and P(B) denotes the probability of B happening and acts as a normalising factor (note that P(B) must be greater than 0).

The general structure of the BET_VH model is displayed in Figure 4.2. The model is made up of nodes, such as *eruption*, which contain events, such as *eruption* and *no eruption*. Nodes can be thought of as processes or phenomena while the events are particular realizations of the process or of a specific type of phenomenon (e.g. *PDC*). These entities (nodes and events) are arranged in a somehow logical way in BET_VH: the events located towards the left preceed, logically and sometimes temporally, the events located towards the right. For instance, the occurrence (or not) of an eruption (nodes 1-2-3) preceeds where the eruption occurs (i.e. its vent location, node 4). Of course, in the absence of an eruption, a volcanic vent

fed by magma will not form. The nodes 1-2-3 in BET_VH are derived from a previous BET model: Bayesian Event Tree for Eruption Forecasting, BET_EF [68], where node 1 describes the occurrence (or not) of volcanic unrest, node 2 describes the origin of the unrest (magmatic or not) and node 3 describes the occurrence (or not) of an eruption, at the volcanic system of interest. Again, the occurrence of magmatic unrest is a necessary condition for the occurrence of a volcanic eruption. However, other type of eruptions (e.g. phreatic eruptions) can occur even when magma in the movement is not the cause of the unrest. Such situations have been recently incorporated into the BET modeling framework and applied to some volcanic systems that may feature this kind of eruptive behavior [243, 244, 245].

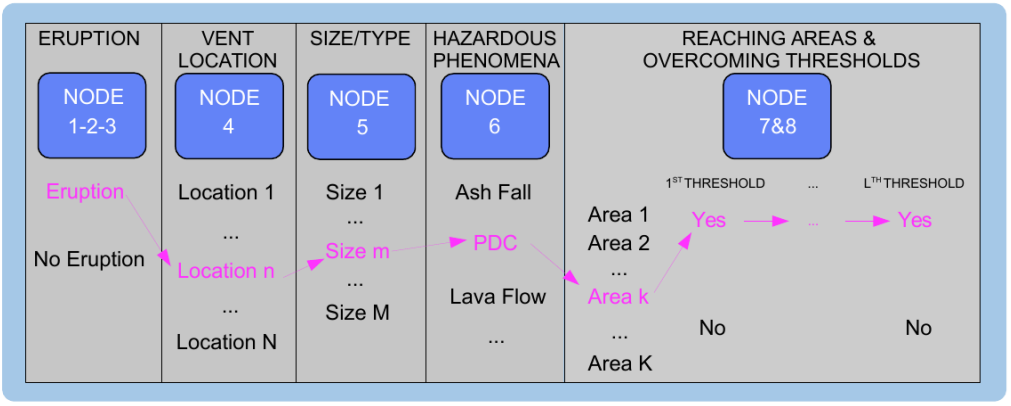

FIGURE 4.2: The structure of the BET_VH model, arranged in nodes (processes or phenomena) and events (realizations of the former). There is a logical path through BET_VH in the sense that nodes located on the left side of the model tend to be a necessary condition for the nodes placed rightwards. The presence of many overcoming thresholds, for a given hazardous process and reaching area, is a representation of hazard curves (e.g. [76, 83]. See text for more details. Modified after [49].

The BET_VH model provides a methodology to calculate absolute and conditional probabilities of volcanic hazard by exploring different paths along its structure. Absolute probabilities are understood as the marginal probabilities, of a specific event, computed from the joint PDF of a chain of events [49]. For example, we can compute the absolute (or total) probability of PDCs impacting area k by applying the chain rule of probability calculus (e.g. [69]):

$$P(area_k) = \sum_{e=1}^{E}\sum_{n=1}^{N}\sum_{m=1}^{M} P(eruption_e)\cdot P(location_n|eruption_e)\cdot P(size_m|location_n, eruption_e)\cdot P(PDC|size_m, location_n, eruption_e)\cdot P(area_k|PDC, size_m, location_n, eruption_e) \quad (4.17)$$

which can be simplified into:

$$P(area_k) = \sum_{n=1}^{N}\sum_{m=1}^{M} P(eruption_1)\cdot P(location_n|eruption_1)\cdot P(size_m|location_n)\cdot P(PDC|size_m, location_n)\cdot P(area_k|PDC, size_m, location_n) \quad (4.18)$$

where $eruption_1$ means there is an eruption. We can simplify equation 4.17 because the probabilities of *size*, *PDC* and *area* are independent of eruption, given location (as aforementioned, if there is no eruption, there is no volcanic vent and, likewise: if there is a volcanic vent, then there is an eruption). Elsewhere, the values of n, m and k corrospend to the events inside each specific node of BET_VH.
On the contrary, the conditional probability of PDCs impacting area k given that, for instance, there is an eruption with a volcanic vent situated at location 10 and eruption size equal to 4; would be given by the expression:

$$P(area_k|eruption_1, location_{10}, size_4) = P(location_{10}|eruption_1)\cdot P(size_4|location_{10})\cdot P(PDC|size_4, location_{10})\cdot P(area_k|PDC, size_4, location_{10}) \quad (4.19)$$

Moreover, the BET_VH model does not treat the probability of occurrence of each event as a single value (e.g. [21]) but it interprets the probability of occurrence

of the event as its real frequency [62] and models this frequency as an uncertain variable for which a PDF can be defined (e.g. [49, 68]). This approach allows to account for both aleatory and epistemic uncertainty (see Fig. 1.4 in Chapter 1): the former is estimated as a central value of the PDF (e.g. the mean or the median) while the latter epistemic uncertainty is estimated as the dispersion around this central value (e.g. the variance).
This hybrid statistical approach, where the probability is conceived as a frequency (e.g. [246]) but this frequency is treated as a random variable (or parameter of the model) in a Bayesian framework (e.g. [65, 247]) offers two major advantages, especially in the field of volcanic hazards, for which the number of data is commonly very scarce and reproducibility could be strongly contested (e.g. [67, 248, 249, 250]): (1) the interpretation of the probability of an event as a frequency (and not as a degree of belief, e.g. [65]) offers the opportunity for statistical testing of the probabilistic assessments given by BET_VH (e.g. [62]); and (2) the Bayesian framework allows to combine different strands of information (volcanological data, physical models, other statistical models, etc) into a homogeneous probabilistic assessment of volcanic hazard (e.g. [19, 21, 32, 49, 68, 100]).

The generalization of the Bayes' theorem to work with PDFs instead of single values of probability can be written as follows [68]:

$$[\theta_i^{(j)}|y] = \frac{[\theta_i^{(j)}]_{prior}[y|\theta_i^{(j)}]}{[y]} \tag{4.20}$$

where $[\cdot]$ denotes a PDF over the variable enclosed by the square brackets, in the case of BET_VH the frequency of a given event (j) inside a given node (i): $\theta_i^{(j)}$. Therefore, $[\theta_i^{(j)}|y]$ denotes the posterior distribution (i.e. PDF), $[\theta_i^{(j)}]_{prior}$ denotes the prior distribution, $[y|\theta_i^{(j)}]$ denotes the likelihood function, and $[y]$ is the normalizing factor (see equation 4.16).

In BET_VH, the procedure developed to parameterize the prior distribution and likelihood function of each node is slightly dissimilar. For nodes 1-5, the distributions are parameterized through a common multivariate distribution of J_i variables (where J_i is the number of events inside the node i): the Dirichlet distribution for the prior distribution and the Multinomial distribution for the likelihood function [68]. This choice implies that the events of the nodes 1-5 are mutually exclusive and exhaustive between each other. For instance, the probability of a volcanic vent opening at any point (given an eruption) is 1. Besides, the model assumes

that only one vent will open.
For nodes 6-8, the prior distribution and likelihood function are constructed individually at each event of each specific node, e.g. area k. The distributions used are the Beta and the Binomial PDFs, the univariate equivalents of the Dirichlet and the Multinomial distributions (note that the Uniform distribution is a special case of the Beta PDF, e.g. [68]). The total number of variables being modeled at each node $i = 6, 7, 8$ is still J_i but these events are modeled through J_i PDFs and not through a multivariate PDF of J_i variables like in nodes 1-5. This implies that the events in nodes 6-8 are not mutually exclusive and exhaustive. That is, lava flows and PDCs can both occur during a given eruption. Likewise, area k and area $k + 1$ can be both invaded by PDCs during this (or another) eruption [49].

Independently of these differences among nodes 1-5 and 6-8, the reasoning behind the parameterization of the prior distribution and likelihood function, as well as the construction of the posterior distribution from them, is homogeneous along the whole structure of BET_VH. The prior distribution is usually parameterized using several sources of information: volcanological data, physical and/or theoretical models, etc (e.g. [19, 32, 100], see Chapters 7, 8, 9). The likelihood function, in turn, is commonly parameterized by using past data from the volcano of interest [49] (and assuming there is reproducibility, since the past events are taken as random samples from the Multinomial or Binomial distribution). For instance, if area k has been invaded by PDCs during three out of four eruptions of size 4 from location 10, we can parameterized the Binomial PDF for area k through the number of "trials" (i.e. eruptions: 4) and "successes" (i.e. times that PDCs have impacted area k: 3) recorded at area k (e.g. [19, 49, 68]).
The posterior distribution in BET_VH is modeled through a Dirichlet PDF (nodes 1-5) or many Beta PDFs (nodes 6-8). The use of this type of distributions is a mathematical consequence of the choice for the prior distribution and the likelihood function. Thus, it occurs that the Dirichlet and the Multinomial (or the Beta and the Binomial) PDFs are conjugate distributions, that is, the product of a Dirichlet (or Beta) PDF and a Multinomial (or Binomial) PDF is another Dirichlet (or Beta) PDF (e.g. [65]). The parameters of the computed posterior distributions, which ultimate define the mean (i.e. aleatory uncertainty) and variance (i.e. epistemic uncertainty) of the PDF, are derived from the parameters of the correspondent prior distributions and likelihood functions at the node or event of interest [68]. The specific choices that we adopt to parameterize and apply the BET_VH model to asses the probabilistic volcanic hazard associated with PDCs

at Somma-Vesuvius, Campi Flegrei and the city of Napoli and surroundings (in Italy) are described in Chapters 7 and 8.

4.2.4 Bayesian Belief Networks

A Bayesian Belief Network (BBN) is a graphical representation of the joint probability distribution of a given set of (random) variables (e.g. [247, 251]) and can be thought of as a combination of a graphical and a probabilistic model [252]. The basis of a BBN, as in the case of BET_VH, is Bayes' theorem (e.g. [65]).
A BBN is a directed acyclic graph composed of nodes, each representing a random variable (usually discretised) of the system being modeled, and arcs, which denote conditional dependences between the variables (see Figure 9.2 in Chapter 9). A given node is a parent node if it has one or more arcs pointing towards other nodes (which are its children). Note that a node can be both a parent and a children. The BBN is directed because the arcs point from parent to children nodes (unlike Markov networks, for instance, that have undirected arcs) and it is acyclic because Bayesian updating cannot be solved for a cycle of variables which are conditionally dependent on each other. By definition, a given BBN structure defines a particular set of unconditional and conditional independences between the variables (nodes) in the network [253]. This actually represents one of the main foundations of BBNs: by applying the chain rule of probability calculus, and exploiting the unconditional/conditional independences within the network, the joint probability distribution of the whole model can be calculated at a reduced parametric and computational cost [253]. That is, let us consider a joint distribution of three variables A, B and C each having three states (e.g. B_1, B_2, B_3). The joint distribution, P(A,B,C), can be calculated as: P(A,B,C) = P(C|B,A) x P(B|A) x P(A), and it contains $3^3 = 27$ probability values. However, if we build a BBN like: A $\rightarrow$ B $\rightarrow$ C (the arrows indicate the arcs), then C is independent of A given B, i.e. (C $\perp$ A | B), and the joint distribution becomes: P(A,B,C) = P(C|B) x P(B|A) x P(A), which contains 9 + 9 + 3 = 21 probability values (or parameters in the BBN; see next paragraph). This reduction in the number of parameters gets more important as the number of nodes (and states within them) augment. Moreover, the reduction speeds up the Bayesian updating that the BBN performs when new evidence is introduced into the BBN (e.g. [252]).

A BBN (made of discretized nodes) is parameterized through Prior Tables (PTs) and Conditional Probability Tables (CPTs). If a node has no parents, then it is parameterized through a PT which has as many parameters as the number of states within the node. This PT expresses the discrete PDF of the node. When a node has one or more parents, it is parameterized through a CPT which has as many parameters as the product of the number of states of the child and all the parent nodes (e.g. P(C|B) above would have a CPT with $3 \cdot 3 = 9$ parameters). The CPT is a discrete representation of the conditional PDF between the child node and its parents, and indicates the probability of each state of the child node to be true given that one state (or a combination of states) from its parent node(s) is true (see Chapter 9).
Second-order independencies can be introduced in the BBN by means of the parameterization of its CPTs. Let us consider another simple BBN with the following structure: $D \rightarrow E \leftarrow F$, and two states per node. According to the BBN structure, the variable E is dependent on both D and F (its parents). However, if the CPT of E is set in a way that: $P(E_1|D_1,F_1) = P(E_1|D_1,F_2) = 0$, then it is seen that E is independent of F given D_1, i.e. $(E \perp F \mid D_1)$. This independence is only a consequence of the way we parameterize the CPT and it is unrelated to the BBN structure (e.g. [253]).

Finally, a BBN is highly modular which is clearly advantageous as the complexity of the probabilistic model increases. For instance, let us assume that the variable D above can be modeled in a more precise way by introducing two new variables (X, Y) that act as parents of node D. The BBN previously described would be expanded to include these two new nodes but the only part of the model that we would need to re-parameterize is the CPT of node D, that is: P(D|X,Y). In contrast, the CPT of node E would remain unchanged because the distribution P(E|D,F) only depends on the specific states of D and F being true and not on their relative probabilities (which in the case of node D, they now depend on nodes X and Y).

Chapter 5

Suitability of Energy Cone for Probabilistic Volcanic Hazard Assessment: validation tests at Somma-Vesuvius and Campi Flegrei (Italy)

Abstract

Pyroclastic Density Currents (PDCs) are gravity-driven hot mixtures of gas and volcanic particles which can propagate at high speed and cover distances up to several tens of kilometers around a given volcano. Therefore, they pose a severe hazard to the surroundings of explosive volcanoes able to produce such phenomena. Despite this threat, Probabilistic Volcanic Hazard Assessment (PVHA) of PDCs is still in an early stage of development. PVHA is rooted in the quantification of the large uncertainties (aleatory and epistemic) which characterize volcanic hazard analyses. This quantification typically requires a big dataset of hazard footprints obtained from numerical simulations of the physical process. For PDCs, numerical models range from very sophisticated (not useful for PVHA because of their very long runtimes) to very simple models (criticized because of their highly simplified physics). We present here a systematic and robust validation testing of a simple PDC model, the Energy Cone (EC), to unravel whether it can be applied to PVHA

of PDCs. Using past PDC deposits at Somma-Vesuvius and Campi Flegrei (Italy), we assess the ability of EC to capture the values and variability in some relevant variables for hazard assessment, i.e. area of PDC invasion and maximum runout. In terms of area of invasion, the highest Jaccard coefficients range from 0.33 to 0.86 which indicates an equal or better performance compared to other volcanic mass-flow models. The p-values for the observed maximum runouts vary from 0.003 to 0.44. Finally, the frequencies of PDC arrival computed from the EC are similar to those determined from the spatial distribution of past PDC deposits, with high PDC-arrival frequencies over a 8 km radius from the crater area at Somma-Vesuvius and around the Astroni crater at Campi Flegrei. The insights derived from our validation tests seem to indicate that the EC is a suitable candidate to compute PVHA of PDCs.

5.1 Introduction

Pyroclastic Density Currents (PDCs) are among the most hazardous processes that are produced by volcanic systems worldwide (e.g. [35, 124]). PDCs are ground-hugging mixtures of hot gas and pyroclasts that travel at moderate to very high speed along the surrounding areas of erupting volcanoes. Due to the physical complexity of processes governing PDCs, considerable uncertainties inherent to their natural variability, e.g. initiation height, volume, mobility, etc. (hereinafter referred to as aleatory uncertainty) as well as related to incomplete knowledge, e.g. links between volume and mobility, simplified modeling, etc. (hereinafter referred to as epistemic uncertainties) occur in the hazard analysis (e.g. [33, 104]).

The most common practices in assessing PDC volcanic hazard have either used the areal distribution of past deposits of PDCs (e.g. [25, 26]), or have evaluated selected scenarios (e.g. [41, 44, 225]). Few studies have produced structured quantifications of the uncertainties involved in the PDC hazard assessment (e.g. [23, 24, 33, 84, 104]). In contrast, Probabilistic Volcanic Hazard Assessment (PVHA) has been carried out for other volcanic hazards (e.g. tephra fallout: [70, 71]; lahars: [100]; lava flows: [254]), and has proved to be a valuable method that can account for and quantify the aforementioned uncertainties. One of the main features of PVHA is that it takes into consideration the natural variability observed in the eruptive process. In other words, rather than selecting one or a

few specific scenarios, PVHA has to deal with a complete set of possible eruptive settings. This mostly translates into accounting for different vent positions, eruptive styles, eruption sizes and related source parameters (e.g. Mass Eruption Rate -MER-, erupted mass, column collapse height, PDC mobility, etc.). Each of these elements is then combined into a unique PVHA through the total probability theorem [69]. In order to fully explore this variability, one needs to be able to simulate the hazardous phenomenon under many different eruptive conditions and compute PVHA in a reasonable computational time, which during volcanic crises can be on the order of hours to days [76].

In this view, the main challenges in using PVHA for PDCs lie in the demanding computational needs and in dealing with physical processes that are not well understood (e.g. kinematic response of PDCs interacting with topographic barriers) that can affect PDC dynamics. On the one hand, very sophisticated simulators, able to describe the evolution of several important variables such as temperature, dynamic pressure or particle concentration, exist but have extremely long runtimes (e.g. PDAC, [44]). This makes them impractical for use in quantifying uncertainties for probabilistic hazard assessments, which would require very large numbers of runs. On the other hand, simple models (e.g. Energy Cone, EC, [132]) that describe a few crucial hazard-related variables such as maximum runout or area of PDC invasion have been criticized because they are rooted on a very small number of physical components, which has been argued to make them incapable of capturing the intrinsic complexities of PDC transport. A sound approach designed to avoid both "trifle worship" attitudes [255] and reliance on models that are problematically oversimplified is to compare model forecasts with the kinds of observations that are relevant for PVHA purposes. In particular, the quantification of the possible impact of PDCs in terms of maximum runout and area of invasion still represents a vital aspect for the hazard assessment of this phenomenon. It becomes even more crucial in highly exposed areas as the city of Napoli, in southern Italy.

In this work, we develop a systematic and robust validation procedure of EC applied to Somma-Vesuvius and Campi Flegrei (Italy), selected because of their significant potential of producing (large) explosive eruptions whose PDCs may reach the city of Napoli and surroundings. This validation is set up in a completely blind manner, meaning two different things: (1) the data used to configure the EC simulations are fully independent of the data utilized to validate them (i.e. we try

to avoid over-fitting at all costs); and (2) the EC simulations are set up to capture the natural variability (aleatory uncertainty) attainable during an eruption of a given size. This means that the simulations are by no means restricted to the types of past events known from the volcanic systems under study.

Our validation procedure aims to unravel whether EC is able to produce hazard footprints that are statistically reliable when compared to real data from PDC deposits, in terms of maximum runout and area of PDC invasion. It is also important to stress here that the focus of the study is not on deriving possible values of physical parameters for PDC generation during the past eruptions. For this purpose there are much more comprehensive simulators which can serve to invert observed field data and describe the evolution of some PDC-governing parameters (e.g. [44]). In contrast, the global methodology is designed to determine whether the preserved PDC deposits and statistical samples of simulated PDCs have some features in common, by answering the question: given the present-day topography and expected eruptive behavior of the studied volcanoes, can a statistical sample (and/or all samples as a whole) of EC simulations capture the values and variability of some parameters measured from deposits of past PDCs? Should the validation demonstrate that EC is able to capture such hazard-related variables, it would justify its application for computing PVHA of PDCs over the surroundings of Somma-Vesuvius and Campi Flegrei.

5.2 Simulation and validation strategies

5.2.1 Uncertainty description and propagation

We describe aleatory uncertainty through the definition of Probability Density Functions (PDFs) for the EC model parameters (see Figure 5.1 and Table 5.1): Truncated Exponential PDF for H_0, and Truncated Gaussian (Somma-Vesuvius) and Uniform (Campi Flegrei) PDFs for ϕ. The reasoning behind selecting each specific type of PDF, as well as the way in which they are parameterized, is detailed in A. We propagate aleatory uncertainty by performing Monte Carlo sampling on the EC parameters' PDFs and running 210,000 simulations of the EC model over a 40m-resolution Digital Elevation Model. Firstly, we sample 10,000 pairs of H_0-ϕ values from the PDFs built for each eruption size and volcanic system. Then,

we run 10,000 simulations per each studied case, according to its eruption size and its vent position. At Somma-Vesuvius, we run 30,000 simulations and we use the current central crater area as the common vent position [104]. Moreover, we set $H_0 = 0$ at the height of the crater rim in order to simulate only eruptions which generate appreciable PDCs. At Campi Flegrei, we run 180,000 simulations because the vent position changes from one case to the other. We select each vent position as the grid point in [205] which is closest to the inferred vent location for the eruption [25]. We use 18 eruptions (see Table 3.1, Chapter 3) instead of the 21 used by [33] for epoch III (plus Monte Nuovo eruption) because we discard: (i) Nisida and Capo Miseno eruptions due to substantial loss of PDC deposits under the sea; and (ii) Paleoastroni 2 eruption owing to inconsistencies between the PDC deposit distribution and the eruptive vent location inferred from tephra fallout deposits [25].

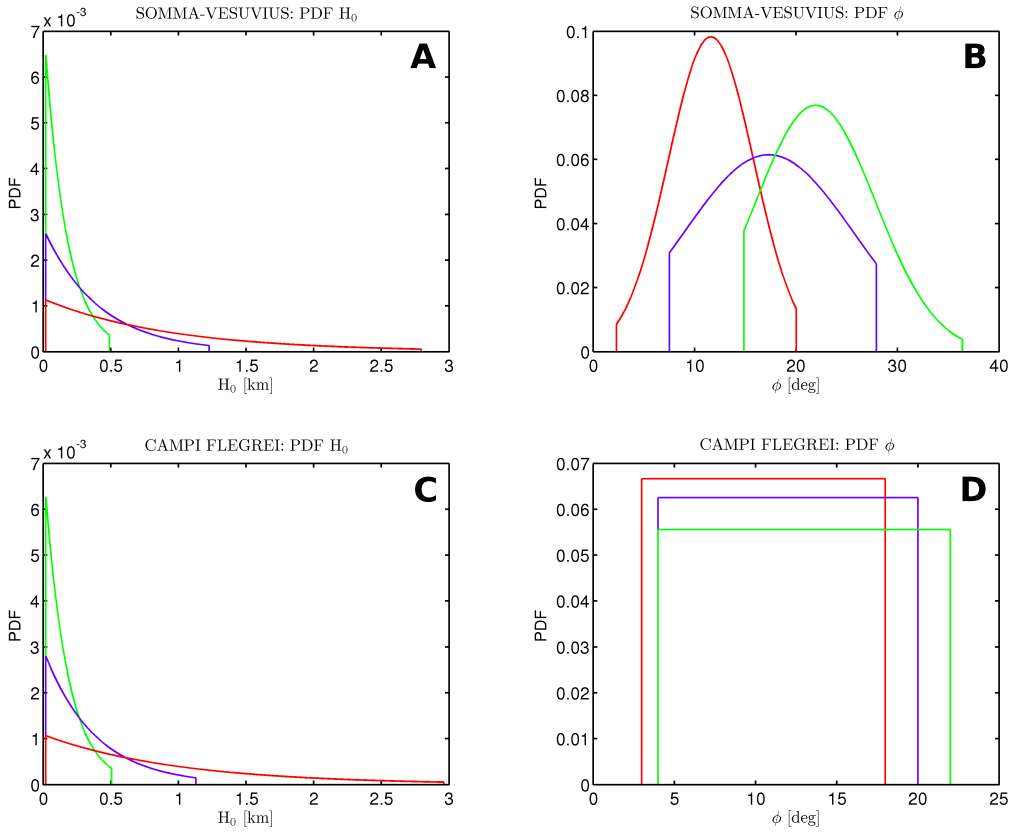

FIGURE 5.1: Probability Density Functions (PDFs) chosen for the two EC model parameters: H_0 and ϕ, at the two volcanic systems of interest: Somma-Vesuvius (A, B) and Campi Flegrei (C, D), in Italy. Different colors refer to different eruption sizes (total deposit volumes): small (green), medium (blue) and large (red). From [103].

We justify the independent sampling of H_0 and ϕ because no clear relationships can be straightforwardly inferred from the available data on ΔH and ϕ [104] (Fig. 10B, A). Nonetheless, possible influences of H_0 on PDC mobility (thus on ϕ) are in effect addressed by: (a) trying out, within each eruptive size class, different ϕ values for similar collapse heights, acknowledging the fact that the mass participating in PDC generation might be different [44]; and (b) assigning, among eruption sizes, smaller values of ϕ to higher values of H_0 as more dilute and mobile PDCs may be formed when collapses are triggered from higher levels in the eruption column [133].

5.2.2 Energy Cone validation

From each EC simulation performed, a value of maximum runout and area of PDC invasion (MR_{SIM}, A_{SIM}) is retrieved. Past PDC-deposit variables (MR_{OBS}, A_{OBS}) are extracted from the literature [25, 26, 193]. In all the cases where the extent of the deposits under the sea is not known, the polygons are closed along the coastline. On the contrary, and even though EC cannot deal with either over- or under-water PDC transport [134], the outputs are not modified to close along the coastline, in order to avoid overestimating the goodness-of-fit between A_{SIM} and A_{SIM}. Here, we stress that MR_{OBS} and A_{OBS} may depend upon post- and syn-eruption processes such as erosion/remobilization or lack of sedimentation. This can be crucial for large dilute PDCs, which are able to travel for long distances only depositing a very thin layer of pyroclastic material that might be eroded rapidly after emplacement [9, 91], and may introduce a bias in validation procedures based upon the extent of preserved PDC deposits. We then check the ability of EC to reproduce these key hazard-related PDC variables in three different ways. Firstly, we create a set of quantitative validation metrics for area of PDC invasion (Fig. 5.2; see subsection 5.3.1):

- Areal Fit (AF): is the ratio between the intersection area, $A_{INT} = A_{OBS} \cap A_{SIM}$, and the union of areas, $A_U = A_{OBS} + A_{SIM} - A_{INT}$, a measure commonly known as the Jaccard similarity coefficient [256]. Hence: $AF = A_{INT}/A_U$. This metric is dimensionless and can range from 0 to 1. $AF = 1$ only in the case that the simulated area is exactly equal to the preserved PDC area. Whenever A_{SIM} is bigger, smaller or does not coincide in space

TABLE 5.1: Summary of the shape parameters of PDFs for H_0 and ϕ (before truncation), considering three eruption sizes (total deposit volumes; small, medium and large) and two different volcanic systems: Somma-Vesuvius (SV) and Campi Flegrei (CF), in Italy. All ϕ values are rounded. λ is indicated as the mean value from all λ calculated from the H_T values in [70] (see Appendix A for more details). From [103].

Eruption Size	**Volcanic System**	**H_0: Truncated Exponential PDFs**			**ϕ: Truncated Gaussian (SV), Uniform (CF) PDFs**			
		λ [m^{-1}]	min H_0 [m]	max H_0 [m]	μ [deg]	σ [deg]	min ϕ [deg]	max ϕ [deg]
Small	Somma-Vesuvius	$5.6 \cdot 10^{-3}$	20	870	22	6	15	36
Medium	Somma-Vesuvius	$2.2 \cdot 10^{-3}$	20	1900	17	8	8	28
Large	Somma-Vesuvius	$1.2 \cdot 10^{-3}$	20	3400	12	4	2	20
Small	Campi Flegrei	$5.6 \cdot 10^{-3}$	20	800	-	-	4	22
Medium	Campi Flegrei	$2.2 \cdot 10^{-3}$	20	1900	-	-	4	20
Large	Campi Flegrei	$1.2 \cdot 10^{-3}$	20	3500	-	-	3	18

with A_{OBS}, the fit is penalized and $AF < 1$, reaching zero in the case that no overlapping occurs between both areas.

- Areal Overestimation (AO): is a measure of the over- or under-estimation of A_{SIM} with respect to A_{OBS} : $AO = A_{OVER} - A_{UND}$; where A_{OVER} is the simulated area that exceeds the area covered by deposits and A_{UND} is the invasion area of the deposits that is not covered by the simulation. If $AO > 0$, that means that the simulation overestimates the PDC deposit area; if $AO < 0$, then the simulation underestimates the PDC deposit area. The units of AO are km^2.

- Areal Misfit (AM): is a measure of the total discrepancy between the simulated and observed area of PDC invasion, expressed as the total area that lies outside A_{INT}, i.e. $AM = A_{OVER} + A_{UND}$. The units of the metric are km^2.

Secondly, we look at the probability of simulating a value equal or greater that MROBS per each studied eruption (see subsection 5.3.2). In the end, we qualitatively evaluate the resemblance between the spatial distribution of the frequencies of PDC arrival computed from ASIM and AOBS (see subsection 5.3.3).

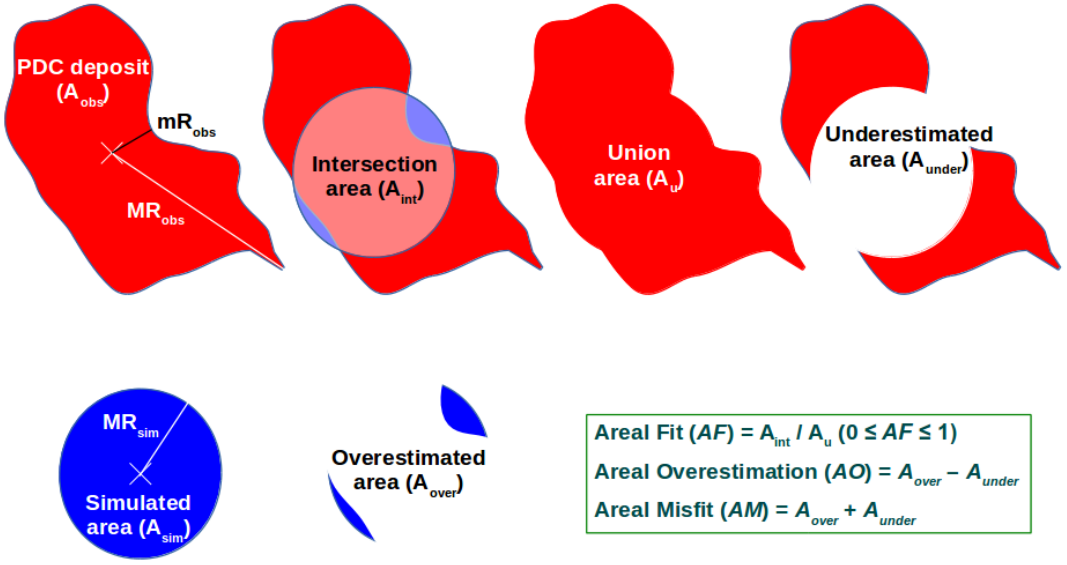

FIGURE 5.2: Validation metrics utilized to test the performance of the Energy Cone, mainly for reproducing areas of PDC invasion. See text for more details. From [103].

5.3 Results

5.3.1 Areal distribution

For all the studied eruptions, the values of areal fit (Jaccard coefficients) across the model parameter space show the same pattern (Fig. 5.3): there is one region characterized by high areal fit values which is surrounded by regions with smaller to very low values of areal fit. The former shows an elongated positive-sloped linear shape which indicates that similar values for area of invasion (and, therefore, areal fit) can result from combining either small initial energy (small H_0) with high mobility (small ϕ) or high initial energy (high H_0) with more-reduced mobility (higher ϕ). By looking at the distribution of minimum areal misfits (white stars, Fig. 5.3) we can identify sectors in the parameter space over which both the areal fit is the highest and the areal misfit is minimum. We identify such sectors for most of the eruptions, although there are some cases in which the minimum misfits are located towards the underestimation region: $AO < 0$ or $A_{OVER} < A_{UND}$ (Fig. 5.3). The location of the minimum areal misfits in terms of collapse height (H_0) shows a division between eruption sizes independently of the volcanic system studied. Thus, minimum misfits tend to fall around $H_0 = 0.5$ km, $1 \leq H_0 \leq 1.5$ km and $H_0 \geq 1.5$ km for small, medium and large eruptions, respectively (Fig. 5.3). We also observe that, typically, the sector with the highest areal fits tends to be symmetrically divided by the $AO = 0$ line (that is, $A_{OVER} = A_{UND}$; Fig. 5.3).

Other eruptions may show the $AO = 0$ line towards the upper limit (e.g. Pompeii eruption, Somma-Vesuvius) or the lower limit (e.g. Agnano-Monte Spina eruption, Campi Flegrei) of the high-AF sector (Fig. 5.3). The absolute values of areal misfit can vary from a few km^2 (e.g. 1944 eruption at Somma-Vesuvius; or Astroni 1 at Campi Flegrei) to maximum values exceeding 3,000 km^2 in the cases of large eruptions (e.g. Mercato or Avellino at Somma-Vesuvius; or Agnano-Monte Spina at Campi Flegrei). The very large mismatches occur for a small percentage of the simulations (commonly $< 1\%$) and are related to particularly high values of A_{OVER} produced when there are very high H_0 values combined with very low ϕ values. Furthermore, in our case, a tangible percentage of the "misfitted" area of PDC invasion corresponds to marine sectors of A_{SIM}, which we decide not to exclude in order to avoid increasing the areal fit (and decreasing the areal misfit) in a somehow artificial way.

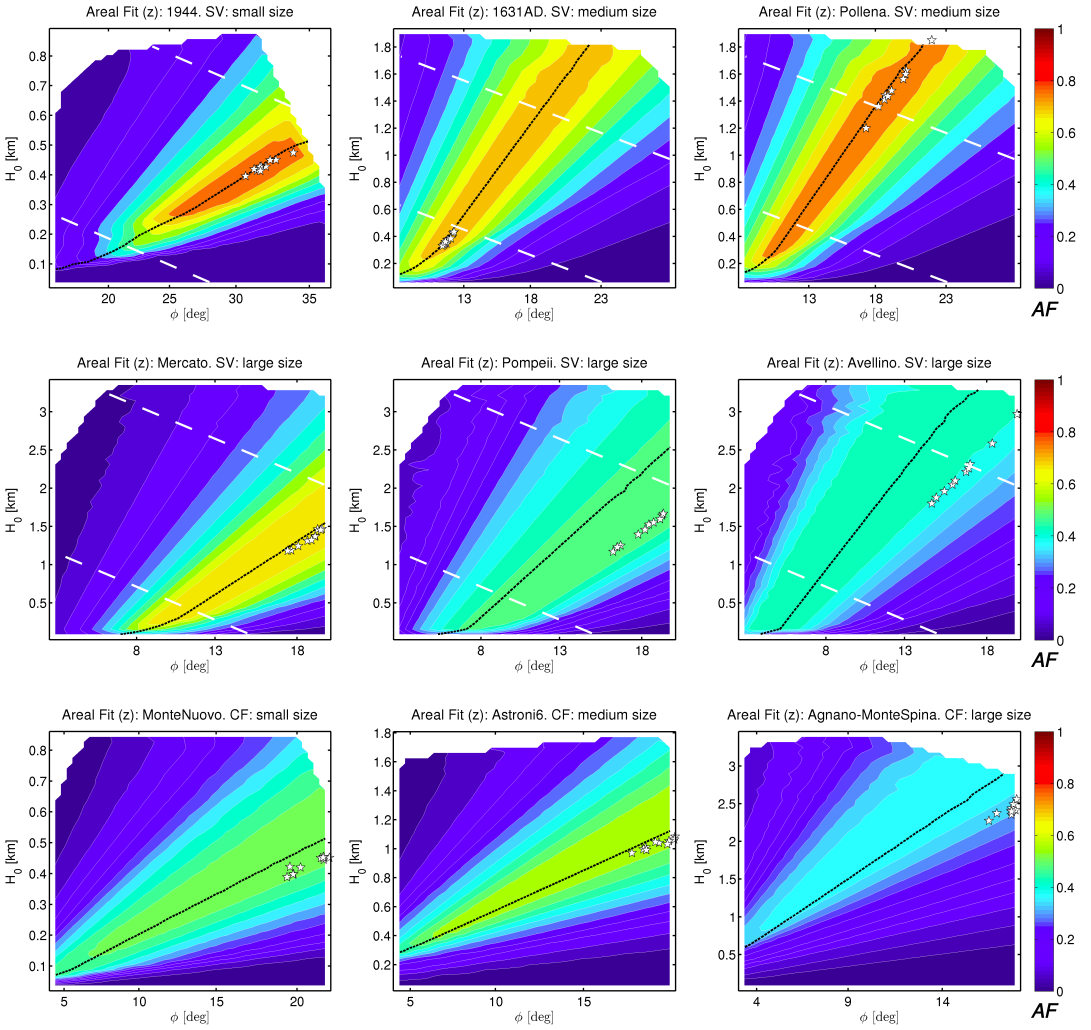

FIGURE 5.3: Areal Fit (AF) values calculated by comparing the areas of PDCs simulated with EC modeling to the actual areas of PDC deposits preserved at Somma-Vesuvius (SV) and some selected eruptions at Campi Flegrei (CF). Black dashed lines indicate simulations for which $AO = 0$, i.e. $A_{UND} = A_{OVER}$. White stars locate the 10 minimum values of areal misfit. The area between the white dashed lines indicates the approximate location for the direct-pattern simulations of [104]. From [103].

5.3.2 Maximum Runout

The histograms of simulated maximum runouts (MR_{SIM}) generally reveal large numbers of events with small-moderate maximum runouts, with fewer towards high or very high values (Fig. 5.4). In statistical terms, the probability of simulating a value equal to or more extreme than a given value (e.g. PDC deposit maximum runout, MR_{OBS}) is equivalent to the p-value:

$$p\text{-value} = 1 - F(MR_{SIM} = MR_{OBS}) \tag{5.1}$$

where $F(x)$ is the Empirical Cumulative Distribution Function (ECDF) of the 10,000 MR_{SIM} values for a given size of eruption, for each volcanic system. The p-value is a statistical indicator of model reliability: on average, the smaller the p-value, the more likely that the model is incorrect. A p-value close to zero indicates that the model is not compatible with available data. For the EC model, all MR_{OBS} values fall inside the range covered by the MR_{SIM} histograms: more than 95% of the cases have p-values greater than 10^{-2} while only one case (Monte Sant'Angelo eruption from Campi Flegrei) has a very small p-value, about 10^{-3} (Fig. 5.5). We also calculate histograms of maximum runout (and p-values) for the Box Model presented by [33] at Campi Flegrei (l_{max} formula, Appendix B). To do this, we use the parameter ranges and probability distributions reported by [33] for all variables except the PDC volume, for which we use the total PDC volume as shown in Table 3.1, Chapter 3 (note that, in this way, l_{max} represents the longest possible runout, since the volume of all PDC deposits is released in a single pulse). In this case, 40% of the obtained p-values are greater than 10^{-2}, around 10% are very small, between 10^{-2} and 10^{-4}, and the other 50% are extremely small, below 10^{-4} (Fig. 5.5).

5.3.3 Frequencies of PDC invasion

The spatial distribution of sites where PDCs arrive in EC simulations (f_{SIM}) is similar to that of sites with deposits of past PDCs (f_{OBS}) at the two volcanic systems studied (Fig. 5.6). Zones frequently affected by PDCs at Somma-Vesuvius are proximal and medial areas (up to 8 km, approximately) around the main crater area (Fig. 5.6). Beyond, the frequency of PDC arrival decays with distance and reaches negligible values (i.e. $f_{SIM} \approx 10^{-4}$; last gray corona, Fig. 5.6A) at limits similar to those beyond which no PDC deposits are known (e.g. the main topographic barriers like the Sorrento peninsula or the Nola-Sarno Mountains: Fig. 5.6). At Campi Flegrei, PDCs most frequently affect the area near Astroni crater (Fig. 5.6C, D). The sites affected only very rarely in simulations show extents comparable to those of the least abundant PDC deposits in the southwestern part of the non-submerged caldera but are situated around 2 and 4 km beyond the most distal known deposits in the northwest and south-southeast, respectively (note that

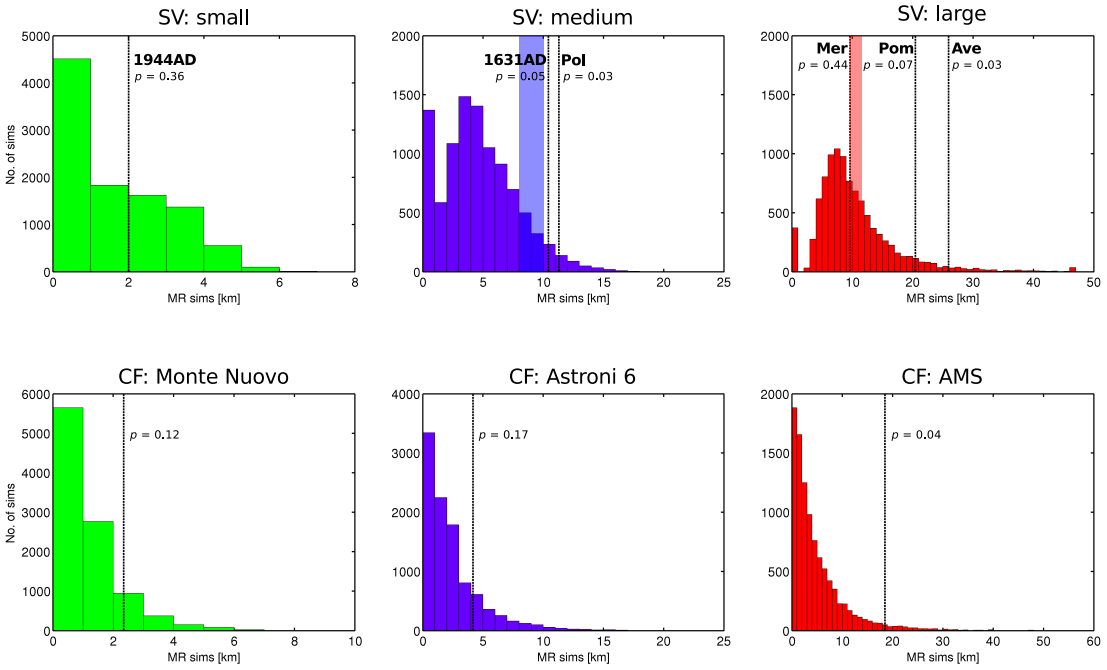

FIGURE 5.4: Histograms of MR_{SIM} computed with EC simulations for Somma-Vesuvius (SV; top) and some selected cases for Campi Flegrei (CF; bottom). Dashed lines denote MR_{OBS} (p-values, p, are given) while colored boxes indicate maximum runout ranges reported by [26] for 1631AD-Pollena (Pol) and Mercato (Mer) eruptions. Elsewhere: Pom, Pompeii eruption; Ave, Avellino eruption; AMS, Agnano-Monte Spina eruption. Different colors indicate different eruption sizes: small (green), medium (blue) and large (red). From [103].

PDC deposits are mapped only on land, while the EC simulations extend offshore). Towards the northeast, the last gray corona covers an area approximately 80 km^2 smaller and 9 km less distant from the source than known PDC deposits from the Agnano-Monte Spina eruption (4.5-4.6 Mod. Cal. ka; [37, 191]).

5.4 Discussion

The presented methodology allows testing of whether the EC model captures key PDC hazard variables (maximum runout and area of PDC invasion) at two volcanic systems, Somma-Vesuvius and Campi Flegrei in Italy. These systems have diverse topography and different types of PDCs, although in both systems most PDCs are radially dispersed and lack strong channelization. Despite the fact that the EC model may not be based on a detailed understanding of the physical processes behind PDC generation and transport, our results indicate that it can be useful

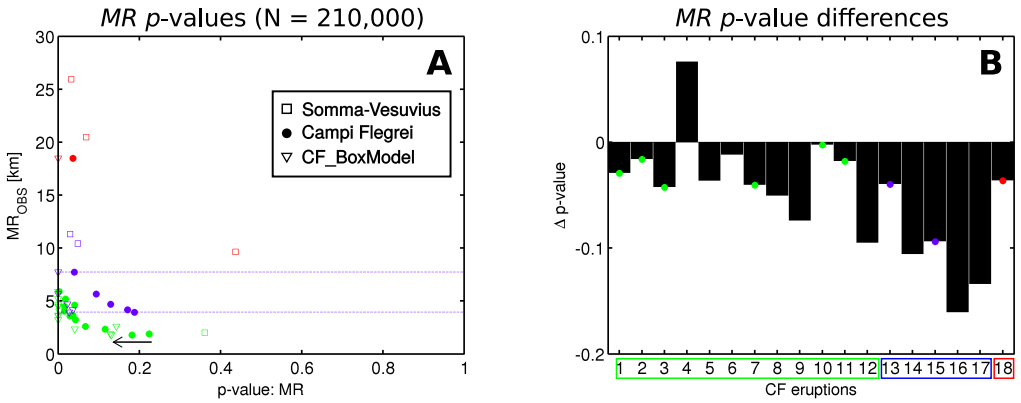

FIGURE 5.5: Calculated p-values of MR_{OBS} (A) according to the Empirical Cumulative Distribution Functions (ECDFs) built from the EC simulations and, at Campi Flegrei, also from the Box Model formula provided by [33]. A tendency towards smaller p-values in the Box Model is indicated by the black arrow in A and quantified in B, where negative differences in the p-value imply that the likelihood of simulating a value of maximum runout equal to or larger than MR_{OBS} is higher when using the Energy Cone model than with the Box Model (1: Agnano2, 2: Astroni1, 3: Astroni2, 4: Astroni7, 5: Averno1, 6: Averno2, 7: Cigliano, 8: Fossa Lupara, 9: Monte Nuovo, 10: Monte Sant'Angelo, 11: Paleoastroni1, 12: Solfatara, 13: Agnano3, 14: Astroni3, 15: Astroni4, 16: Astroni5, 17: Astroni6, 18: Agnano-Monte Spina). Fine-dashed blue lines in A show the lowest and highest MR_{OBS} from medium eruptions at Campi Flegrei. Filled circles in B denote cases for which $p - \text{value}_{BoxModel} < 10^{-}4$. Colors indicate eruption sizes: small (green), medium (blue) and large (red). From [103].

in quantifying the areal extent of sites that will be affected by PDCs, and at what frequency.

5.4.1 Areal validation metrics

Within the 210,000 simulations performed, there are 24 (one per each eruption analyzed) that best reproduce the observed areas: $0.33 \leq AF \leq 0.86$. Around 70% of them have best areal fits of 0.5 or greater (Fig. 5.7A). This represents quite a good performance when compared to areal fit values published for other volcanic mass flow simulators (e.g. $0.35 \leq AF \leq 0.69$ for lava flows at Mt Etna, Italy: [257]; $\max(AF) \approx 0.6$ for BAFs simulated via Titan2D at Mt Taranaki, New Zealand: [225]; or $0.07 \leq AF \leq 0.72$ for a 2006 BAF at Mt Merapi, Indonesia, simulated with Titan2D and using DEMs with different resolutions: [86]). In addition to our simulations that fit well the past deposits, there are other simulations that

show small values for areal fit. This is not necessarily a model failure –the full simulation set is intended to represent not only the recorded (past) events, but also smaller and larger events: that is, those with $AO < 0$ and $AO > 0$ (Fig. 5.3). This is the key reason for exploring aleatory uncertainty of geophysical processes for the purpose of probabilistic hazard assessment (e.g. [49, 76, 100]).

Generally, the best AF values coincide with simulations displaying $AO = 0$ (Fig. 5.3) which means that the model is not especially biased through a tendency to underestimate (in such a case, we would observe $AO < 0$ for high areal fit values) or overestimate (conversely, $AO > 0$ would be linked to high areal fit values). Nonetheless, we see some cases of both. There is underestimation for the Pompeii eruption, in which the PDC deposits indicate limited PDC propagation beyond Mt Somma in contrast to the known long runout towards the SE-ESE [26]. The underestimate occurs because, when Mt Somma is substantially surmounted, the areal fit is significantly penalized due to the large simulated area that is found beyond the Pompeii PDC-deposit limits. There is overestimation for the Agnano-Monte Spina eruption, where simulated PDCs extensively overrun the CI caldera scarp of Marano di Napoli hills (Fig. 5.6C). The areal misfit values generally tend to a minimum when the areal fit is maximum (Fig. 5.3). For values of column collapse height, H_0, that yield the minimum areal misfits, there are some exceptions to the aforementioned pattern (i.e. the larger the eruption size, the higher the H_0 associated with the minimum areal misfit). These cases are the 1631 AD, Pollena, and Mercato eruptions for Somma-Vesuvius. For 1631 AD, the minimum misfits result when $H_0 \approx 0.35$ km and this may be related to the extensive propagation of PDCs towards the topographically lower southern sector of the volcano [198]. PDC deposits from 1631 have been found at only one site beyond the topographic barrier of Mt Somma [26]. In contrast, for the other medium-sized eruption at Somma-Vesuvius, the Pollena eruption, PDC deposits cover a considerable area north of Mt Somma [26]. Hence, Pollena eruption minimum misfits occur for $H_0 \approx$ 1.6 km (Fig. 5.3). The minimum misfits obtained for the Mercato eruption are for $H_0 \approx 1.4$ km. This value is smaller than those of the other large eruptions (Pompeii, $H_0 \approx 1.5$ km; and Avellino, $H_0 \approx 2$ km) but it is also lower than the value inferred for the Pollena eruption. Although classified as VEI5 based on its total deposit volume (e.g. [89]), the Mercato eruption displays peak MER, PDC volume, A_{OBS} and MR_{OBS} values more similar to those of medium eruptions than of large eruptions (see Table 3.1, Chapter 3). Lastly, highly asymmetric PDC deposits may be linked to lower AF values and $AO < 0$. In this respect, it might appear as

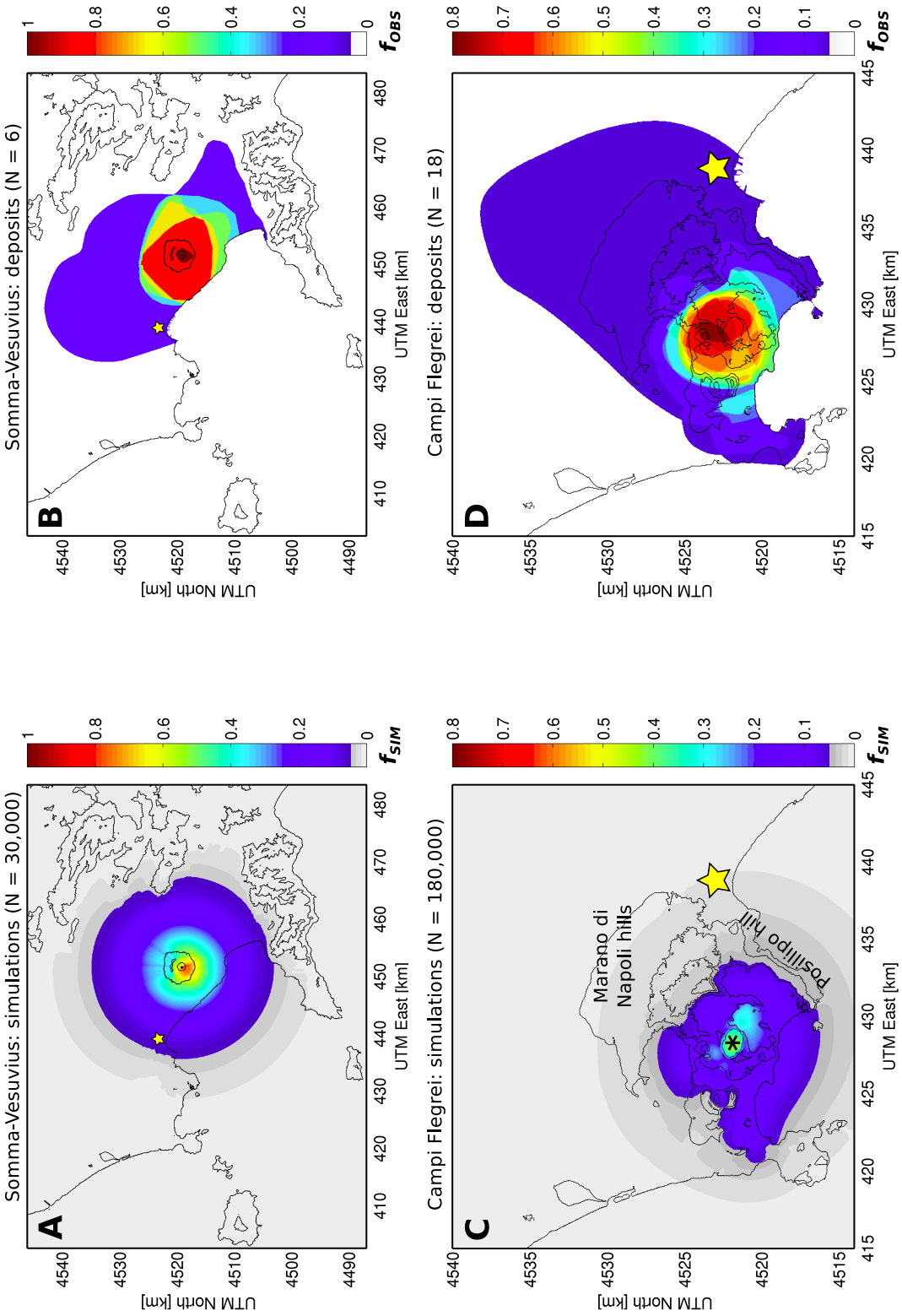

FIGURE 5.6: Frequencies of PDC arrival computed using EC simulations (f_{SIM}) and PDC deposits (f_{OBS}) at Somma-Vesuvius (A, B, respectively) and Campi Flegrei (C, D, respectively). Downtown Napoli (yellow star) and Astroni crater (black asterisk) are shown. Intensely colored contours enclose points with $f \geq 0.05$. Pale gray areas that cover the whole DEM are related to $f_{SIM} \leq 10^{-4}$. N.B. Colorbar scales are different for the two volcanic systems. From [103].

though areal fit decreases as eruption size (total deposit volume) increases (Fig. 5.3). It is, however, the ratio of the maximum to the minimum runout (MR:mR ratio) that is more important, and this ratio seems to be independent of eruption size (Fig. 5.7B), instead directly measuring the asymmetry of the deposit (the larger the ratio, the more asymmetric the deposit) with respect to the (inferred) vent location. We observe that the more asymmetric the deposit, the smaller the best AF (Fig. 5.7B). This is in part because the EC concept does not capture PDCs that exhibit preferential spreading in one direction (as mentioned above), unless there is (or there was at the time of the eruption) a clear topographic control on this spreading. As an example, the inferred vent location for the Avellino eruption is located along the western slopes of the Somma-Vesuvius edifice [232]; this may have reduced Mt Somma's capability to efficiently block PDC propagation towards the northwest and it is, in fact, to the northwest that deposits from the longest-runout PDCs of the eruption have been measured [26].

5.4.2 Maximum runout validation metrics

Although the EC model seems able to capture the MR_{OBS} value for every individual eruption (Figs. 5.4, 5.5), there are some cases in which the probability of simulating MR_{OBS}, given the EC and the PDF parameterization used here (i.e. p-value), is low to very low. In the case of the Box Model [33], half of the p-values computed are smaller than 10^{-4} (Fig. 5.5). These situations have one (or a combination) of three causes: (1) the simulator fails to reproduce the observed values of past PDC deposits; (2) the model parameter space does not capture the PDC phenomena for an eruption of a particular size; and (3) the studied event is genuinely very extreme (i.e. its theoretical probability is relatively small) considering the typical PDCs generated during an eruption of the analyzed size.
We argue that, given the results obtained in this chapter and in [33], the first cause is not the general case for either the EC or the Box Model. Nonetheless, there might be circumstances in which EC models struggle to accurately reproduce past PDC deposits. This is usually related to PDCs that become strongly channelized despite modest topography, yielding deposits with a high MR:mR ratio (Fig. 5.7B). The second and third causes may explain other cases for which small or very small p-values are computed. The Box-Model p-values tend to be smaller than those computed from the EC (Fig. 5.5A, B) and this may be due to the selected ranges of model parameters. For instance, maximum runouts equal to MR_{OBS} are

obtained for approximately half and one quarter of the eruptions when assigning particle settling velocities of $w_s < 0.05$ m/s and $w_s < 0.02$ m/s, respectively (here we use again the total PDC volume and, for the rest of the parameters, the highest value reported by [33]). The lower bound proposed by [33] is $w_s = 0.05$ m/s which might be too high for some cases, given the complex transport histories of particles within turbulent PDCs in which particle comminution and resuspension of fine particles, for instance, can play an important role in the motion and final maximum runout of the current [35, 124, 139].

We consider that for medium-size eruptions at Somma-Vesuvius there may also be issues with model parameterization, specifically a lack of completeness in the dataset employed for this size (only 4 data are available to parameterize the PDF for ϕ). Incomplete datasets can give rise to irregularities in the consequent cumulative distribution (ECDF) of MR_{SIM}. The minimum value of the probability density function (PDF) is $\phi = 7.5°$ while the mean is placed at $\phi \approx 17°$. Given the PDC phenomenology reported for the 1631AD [198] and Pollena eruptions [144] and their medium-long-runout MR_{OBS} (these being equal or greater than the one recorded during the large-size Mercato eruption, [26], see Table 3.1, Chapter 3), the cited ϕ values (e.g. mean = 17°) may be too big to capture the moderate to high-mobility PDCs generated during medium-size eruptions at Somma-Vesuvius. Using a different PDF parameterization (e.g. lower mean ϕ) would shift the histogram towards longer maximum runouts. Another way to obtain a similar result would be to perform a sampling of H_0 values conditional to the sampled ϕ values; for instance, we could sample only high H_0 (collapse heights) when low ϕ (equivalent friction) values are sampled (direct pattern in theoretical uncertainty; [104]).

Concerning the cluster of low p-values for some small eruptions at Campi Flegrei, we see that their values of maximum runout are equal to or greater than those for the majority of medium eruptions (Fig. 5.5A). Particularly, the small Monte Sant'Angelo eruption [37](p-value = 0.003) has a maximum runout greater than all but one medium-size eruption: Agnano 3 (MR = 7.73 km) which, in turn, displays values of PDC volume, maximum runout and area of PDC invasion that, compared to the average values for the rest of medium-size eruptions at Campi Flegrei, are around: 40%, 70% and 95% greater, respectively. Therefore, we might classify the PDCs from some of these eruptions as actually being low-probability events, in the light of the typical PDCs expected to form at Campi Flegrei during small or medium eruptions.

The Agnano-Monte Spina eruption from Campi Flegrei (p-value ≈ 0.04) was quite

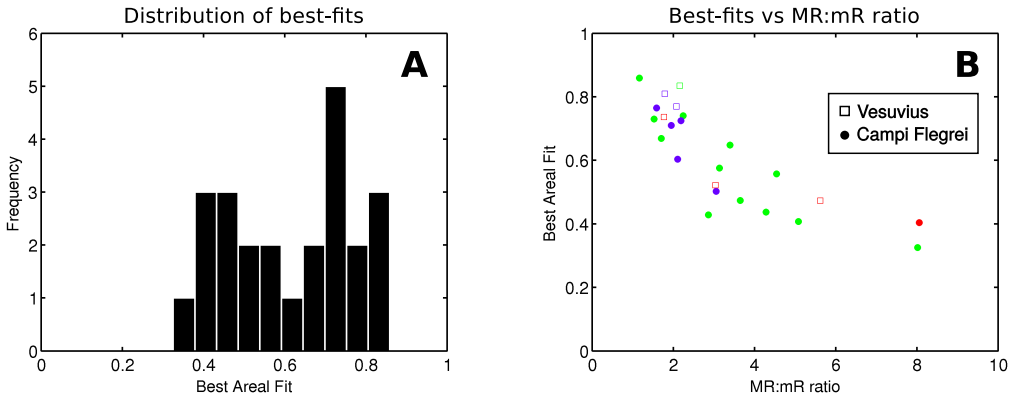

FIGURE 5.7: Best Areal Fit patterns extracted from EC simulations carried out at Somma-Vesuvius and Campi Flegrei (Italy). A: histogram of best areal fit values; B: best areal fit versus $MR : mR$ ratio. Different colors indicate different eruption sizes (total deposit volumes): small (green), medium (blue) and large (red). From [103].

complex [258] with several different phases that led to the generation of diverse PDCs. The dynamics of water-magma interaction changed significantly during the eruption, causing transiently unstable eruption columns, modifications in the depth of the fragmentation level and other related processes [258]. Above all, the last phases of the eruption were linked to a volcano-tectonic collapse which eventually produced: (1) a northeast-wards migration of the eruptive vents; and (2) very dilute and high-mobility PDCs that surpassed the topographic barrier north of the Agnano plain [258]. In the absence of other large-size events registered during epoch III of eruptive history at Campi Flegrei, the Agnano-Monte Spina eruption could be considered as an extreme event that would justify the low probability of observing the actual MR_{OBS} value of this eruption.

5.4.3 Frequencies of PDC arrival

As previously described, the simulated frequencies of PDC arrival resemble those inferred from deposits of past PDCs at both volcanic systems studied. At Somma-Vesuvius, the difference in frequencies between the southern and northern flanks of the volcano is evident, reflecting the role of Mt Somma in hindering PDC propagation towards the north [44, 104]. Over distal sectors, the main topographic highs seem to control the furthermost extent of PDCs [26]. At Campi Flegrei, the general pattern of frequencies of PDC arrival mostly reflects topographic control by

the caldera rims of the NYT and CI eruptions [25]. Even though we do not explore the whole range of possible vent locations [205, 206], we observe, for instance, that the frequency along the Posillipo hill (eastern scarp of the NYT caldera) is greater than zero, as also presented recently in the probability map by [33]. The clearest discrepancy between the EC frequencies and those inferred from deposits of past PDCs is found towards the north, where there are PDC deposits of the Agnano-Monte Spina eruption. Nonetheless, the computed frequencies are not zero indicating that such an event is still possible within our modeling framework. The next step must be to consider all vent locations and their specific probabilities of opening.

5.5 Conclusions

In this chapter, we quantify the ability of the EC model to capture the natural variability of PDC generation and emplacement in a way that is useful for hazard assessment. We test whether the preserved PDC deposits share with our statistical sample of PDCs modeled with EC the predominant features of: (1) invaded area, (2) maximum runout, and (3) frequency of PDC arrival. With this target, we have developed a systematic and robust validation procedure of the EC model. Our results show that a statistical sample of EC simulations seems able to capture the aleatory variability of these three variables at Somma-Vesuvius and Campi Flegrei (Italy).

This is a very important result as it might open the door to probabalistic volcanic hazard analysis for dilute and dense PDCs. Such an assessment of this hazard has hardly been attempted, because simple simulators (e.g. EC) have been considered inadequate, and because of the intractability of probabilistic analyses if they are performed only with very sophisticated simulators (e.g. PDAC: [44]). Some approaches have been carried out using robust simulators for dense PDCs (e.g. Titan2D: [23, 24]), using a mixture of physical and statistical forward models for PDCs (e.g. [100]), or combining information from deposits of past PDCs with inverse physical modeling of PDCs and expert elicitation techniques ([33]). Nevertheless, there remains no general implementation of probabalistic hazard analysis for PDCs.

Despite the strong physical simplifications applied in EC modeling (e.g. some physical processes such as PDC channelization and dense-dilute PDC decoupling

are difficult to describe, [104]), such modeling remains an option for reliable probabilistic hazard analysis of PDCs based on the results presented here, and given the current absence of computationally cheap but physically robust simulators of dilute PDCs.

Finally, even though EC modeling captures the aleatory variability in a satisfactory way, we argue that probabilistic hazard analysis also requires a full description of the epistemic uncertainty. This may be achieved by merging the output of different reliable PDC models (e.g. [51]). For instance, the output of EC simulations covering extensively the model parameters' space (and/or the spatial hazard domain) may be combined with the output of other more elaborate and/or computationally time-consuming PDC models (e.g. Titan2D, VolcFlow, Box Model) that explore the aleatory variability in well-defined sub-regions of specific interest.

Chapter 6

Uncertainty assessment of Pyroclastic Density Currents at Somma-Vesuvius (Italy) simulated through the Energy Cone Model

Abstract

Pyroclastic Density Currents (PDCs) are extremely dangerous phenomena so their modeling is essential for hazard and risk purposes. However, PDCs are governed by very complex processes, making their deterministic prediction impossible. Probabilistic approaches are in a pioneering phase and feature large (and still unknown) uncertainties, from the natural variability of PDCs (aleatory uncertainty) to the main sources of epistemic uncertainty (input, parametric, theoretical and structural). In this chapter, we quantify these uncertainties by using the Energy Cone Model (ECM) in a Monte Carlo scheme applied to Mount Vesuvius. According to our results, theoretical uncertainty has the largest impact, 5-100 times bigger than input uncertainty which seems to play a minor role. We find that conditional probabilities of PDC arrival (given an eruption of a specific size) show spatial distributions related to the surrounding topography. In particular, for medium and large eruptions, the conditional probability of PDCs traveling beyond Mount Somma is [1-15]% and [50-60]%, while they reach the Napoli airport in about [0-1]% and [0-15]% of the simulations, respectively. Small-eruption PDCs remain

restricted to the south flank and summit area. These results may guide future research devoted to reduce epistemic uncertainties and improve volcanic hazard analyses associated with PDCs.

6.1 Introduction

Phenomena related to explosive volcanic systems threaten life and property of many millions of people around the world. In particular, Pyroclastic Density Currents (PDCs) are one the most destructive physical phenomena, both in terms of structural damage [153] and threat to life [155]. PDCs are composed of a hot gravity-driven mixture of gas and solid particles which travels at high speed along the area surrounding the volcanic vent [6, 9, 35, 124]. Their high potential damage is due to several causes, such as lateral impact, elevated temperature, fine- and coarse-particle concentration, toxic gases, etc. [155].

During the last 400 years, PDCs have been responsible for the largest number of fatalities related to volcanic eruptions ($\approx$ 100,000 lives, 33% of all fatalities, [157]). Among the most devastating events, we recall Mount Pelée 1902, Martinique [158]; Mount Lamington 1951, Papua New Guinea [159]; and El Chichón 1982, Mexico [160].

The extreme complexity of PDC generation, transport, and deposition processes makes PDC modeling extremely challenging. For this reason, the first attempts to evaluate the hazard posed by PDCs were mostly based on maps describing PDC deposits from past eruptions (e.g. [20, 25, 26]). On the other hand, Probabilistic Volcanic Hazard Assessment (PVHA) [21, 61, 67] requires proper quantitative PDC modeling strategies that are able to describe the inherent complexity of the process (the aleatory uncertainty), and the incomplete knowledge of the system (the epistemic uncertainty). Although the distinction between aleatory and epistemic uncertainties has been often considered inherently ambiguous, we adopt the taxonomy of uncertainties proposed by [62] in which aleatory variability and epistemic uncertainty can be unambiguously distinguished. The inclusion of aleatory and epistemic uncertainties is essential for any reliable PVHA and it allows scientists to provide quantitative assessments that can be used in rational decision making (e.g. [259]).

Presently, PVHA has been already carried out for tephra fallout (e.g. [71]), lava flows (e.g. [210]) or lahars (e.g. [100]). Conversely, only a few studies have

looked into a systematic characterization of the uncertainties associated to numerical modeling of PDCs (e.g. [84, 85, 260, 261]) or have produced PVHA of this phenomenon (e.g. [23, 24, 33, 231]). This is mainly owing to the difficulty to simulate PDCs, in terms of numerical algorithms and computational resources. PDC simulators that aim to reproduce the most detailed physics of the process are computationally expensive (e.g. [44]) and, therefore, not suitable for the exploration of the large uncertainties involved in the hazard assessment.

In this chapter, we opt for a widely-used PDC model, the Energy Cone Model (ECM), applied to Somma-Vesuvius, in Italy. Explosive eruptions at the volcano have generated dense and dilute PDCs as a result of transient eruption-column collapses, continuous collapses (pyroclastic fountaining) or very energetic phreato-magmatic explosions (e.g. cioni2008). By means of extensive Monte Carlo sampling of the model parameters, we investigate the role of different types of uncertainty in describing the PDC invasion around the volcano. The aleatory uncertainty is addressed by building and sampling Probability Density Functions (PDFs) of the model eruptive parameters (collapse height, H_0, and PDC mobility, ϕ). Epistemic uncertainty is examined by the specific contribution of four distinct sources (after [75]): input, parametric, theoretical, and structural uncertainties.

Input uncertainty refers to the lack of knowledge about boundary conditions, for instance the real terrain over which PDCs propagate; here we quantify input uncertainty by running equivalent sets of simulations over Digital Elevation Models (DEMs) with different horizontal spatial resolutions. Parametric uncertainty stems from the fact that we do not know exactly the PDFs for sampling the eruptive parameters describing the aleatory uncertainty; here we describe the effects of using different kinds of PDFs on model output. Theoretical uncertainty is linked to the assumptions adopted in the simulation strategy, for example, whether considering the model parameters as independent or not; this source of epistemic uncertainty is addressed by testing several possible relationships between the ECM parameters. Finally, structural uncertainty derives from all the simplifications of the model itself; in other words, it is the uncertainty that remains after having run the model using perfect-known boundary conditions and the 'best' parameter values [75]. We evaluate structural uncertainty by using computed values of misfit between the 'best' set of ECM simulations and past PDC deposits at Somma-Vesuvius.

Exploring all these sources of uncertainty allows us to quantify their specific contribution as recorded in the model outputs. We express such a quantification

through: (1) Empirical Cumulative Distribution Functions (ECDFs) of two important variables in terms of volcanic hazard posed by PDCs: area of invasion and maximum runout; and (2) conditional-probability maps of PDC invasion in the area around Somma-Vesuvius (given the occurrence of an eruption of a specific size).

The implications of this study are twofold: on the one hand, it allows for ranking the different types of uncertainty and checking, quantitatively, their effect on the model outputs. On the other hand, it provides a detailed and structured quantification of epistemic uncertainty associated to the simulation of PDCs through the ECM. This can be applied to assess epistemic uncertainty within PVHA tools and, in the end, may help to improve quantitative volcanic risk assessments.

6.2 Methods

6.2.1 Quantification of Aleatory Uncertainty: Intrinsic Randomness

Given a specific eruptive size, the randomness in PDC generation (see PDC phenomenology above) can be simulated through a set of possible values for the ECM parameters, ϕ and H_0 (Fig. 3). Again, we do not take into account vent locations outside the current crater owing to the very high vent-opening probability over the crater. Nonetheless, a complete PVHA procedure should include the possibility of vents opening on the flanks of the volcano.

In our approach, we account for aleatory uncertainty by describing the ECM parameters through bounded PDFs[1] (Table 6.1, [104]) for each eruptive size: Truncated Gaussian (ϕ) and Truncated Exponential (H_0) PDFs (see the motivation for these choices in section 6.3.3).

We propagate aleatory uncertainty by sampling from such PDFs, through a Monte Carlo inversion method [239], 10000 pairs of values for ϕ and H_0 per each eruptive size. These 30000 pairs are finally used to run the ECM over a 40 m-resolution DEM. This choice is motivated by a potentially wider applicability of the obtained results (high-resolution DEMs are not always available). Nonetheless, as we shall

[1]Negative or infinity values of the parameters are not physically possible.

TABLE 6.1: Shape parameters of the selected Probability Density Functions, PDFs. λ^{-1} are mean values for each eruptive size. NB. All values are ceil-rounded. ECM: Energy Cone model; *a*: lower-end of the Tukey plateau; *b*: upper-end of the Tukey plateau. From [104].

ECM parameter →	**ϕ [degrees]**								**H_0 [meters]**				
PDF type →	Truncated Gaussian				Asymmetric Tukey Window				Truncated Exponential			Linear Decay	
Eruption size	μ	σ	min	max	a	b	min	max	λ^{-1}	min	max	min	max
Small	23	6	15	36	18	28	15	36	173	20	1000	20	1000
Medium	17	8	8	28	10	25	8	28	441	20	2000	20	2000
Large	12	4	2	20	10	15	2	20	807	20	3500	20	3500

see in section 6.4, our results indicate that input uncertainty is, by far, the smallest source of epistemic uncertainty.

6.2.2 Quantification of Input Uncertainty: Incomplete Knowledge on Boundary Conditions

Input uncertainty is here explored by running the same set of ECM simulations (as described above in section 6.2.1) over DEMs with varied horizontal resolutions, namely: 10, 20, 40 and 80 meters (Fig. 6.1). This totals 120000 ECM simulations. The DEM mean vertical errors, although not treated in the analysis, are, respectively: 3.5 [262], 10, 10 and 10 meters. Thus, we assess input uncertainty linked only to sparse topographic data. A more complete quantification of input uncertainty may include the DEM vertical errors, spatial correlation between errors and could even model the entire DEM as an uncertain variable ([84]).
The 10 m DEM is constructed with data downloaded from OpenMap and it is based on data derived from the Italian Regional topographic maps, GPS points, ground based and radar altimetry data [262]. The 20 m DEM is derived from interpolation of contour lines and spot heights present in the 1:25000 Italian topographic maps. Finally, the 40 m and 80 m DEMs are derived from resampling of the 20 m DEM. The 10 m DEM is taken as the reference model (i.e. the closest representation of the real terrain) and its associated input uncertainty is assumed to be negligible [85].

6.2.3 Quantification of Parametric Uncertainty: Incomplete Knowledge on Model Parameterization

Parametric uncertainty is examined by imposing different PDFs for ϕ and H_0. In principle, and given the scarce amount of real data available for both parameters, several PDFs could be used. Here, we quantitatively assess how much the ECM outputs change when different PDFs are explored.

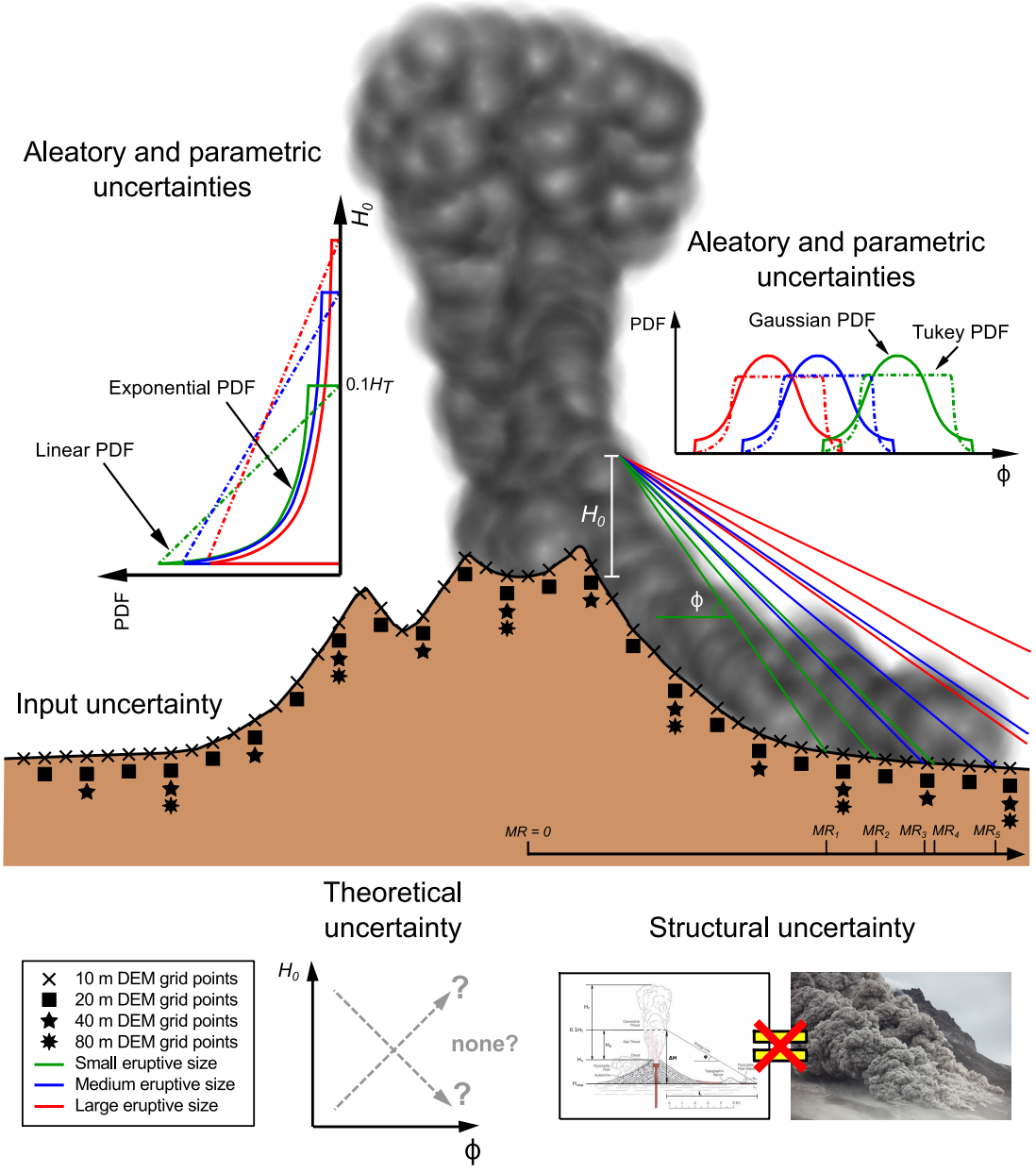

FIGURE 6.1: Schematic representation of the origin and way of addressing the different types of uncertainty (aleatory and epistemic) quantified in this chapter. Aleatory uncertainty (solid lines) is described through Probability Density Functions (PDFs) of the Energy Cone Model (ECM) parameters: collapse height, H_0, and PDC mobility, ϕ (note that H_0 values are not to scale and ϕ values might seem greater than the actual values used in the chapter). Every simulation provides a value of area of PDC invasion (not shown here) and maximum runout (MR; bottom right of the cartoon). Input uncertainty is explored by running the ECM over Digital Elevation Models (DEMs) with diverse spatial resolutions (also notice that only the horizontal position of the 20, 40 and 80 m DEM grid points has to be considered). Parametric uncertainty is characterized by means of alternative choices for the PDFs (e.g. Tukey or Linear PDFs; dotted-dashed lines). Theoretical uncertainty arises from the fact that possible relationships between H_0 and ϕ are not known. Finally, structural uncertainty derives from all the simplifications adopted by simulating the real phenomenon, PDCs, via the ECM (see text for more details). From [104].

PDFs for ϕ

Concerning the ϕ parameter, we rely on a worldwide database of PDC mobility that contains volcanic systems morphologically similar to Somma-Vesuvius [138]. We initially explore three different PDFs (in brackets we list their parameters):

- Uniform (min and max limits). This PDF represents the "maximum ignorance" as no value, within the selected domain, is preferred.
- Truncated Gaussian (mean, μ; standard deviation, σ; min and max limits). This PDF is chosen as previous works have indicated that Gaussian PDF may be consistent with ϕ data from Volcán de Colima, Mexico [136].
- Asymmetric Tukey window (high-probability plateau, a, b; min and max limits; Fig. 6.1, [104]). This PDF is chosen following the idea that ϕ could follow a distribution characterized by a higher likelihood in its central values.

Then, we perform one-sample Kolmogorov-Smirnov tests [263], using ϕ data in [138], to test the null hypothesis of such data having been sampled from each PDF. We find that the null hypothesis can only be rejected, at the 1% level of significance, for the Uniform PDF. Therefore, we discard this PDF and use Truncated Gaussian and Asymmetric Tukey window PDFs to assess how much they influence the ECM outputs. Their parameters are derived from [138] after applying some constraints. Firstly, ϕ values are partitioned into VEI $\leq$ 3, VEI4, VEI $\geq$ 5 eruptions. As we mentioned above, expected PDCs during VEI $\approx$ 3 at Somma-Vesuvius can show large variability. For this reason, we decide not to exclude the ϕ values related to VEI $\leq$ 3 eruptions since we consider they are compatible with the PDC phenomenology (e.g. low-mobility hot avalanches) attainable during small eruptions.
Secondly, data from Block and Ash Flows (BAFs) and ignimbrites are discarded since the occurrence of such types of PDCs is unlikely (i.e. their deposits have not been observed in the last 20 ka of stratigraphic record at Somma-Vesuvius, [26, 89]). Thus, we only use data from pumice flows (formed by column collapse) in [138].
For each eruptive size, Truncated Gaussian μ and σ are constrained using data from [138] and, similarly, Tukey high-probability plateaus are placed, subjectively, between the 20th and 80th percentiles of these samples. The latter implies that

60% of the ϕ values are placed inside the plateau (approximately the same density of probability ($\approx 68\%$) is located within $\mu \pm \sigma$ in a Gaussian PDF). Minimum and maximum ϕ values, for Gaussian and Tukey PDFs, are those found in [138].

PDFs for H_0

In the absence of real data for H_0, our choice for the PDFs is based on the assumption that high column collapses are less likely than low ones and that column collapse will occur within the gas-thrust region whose top is roughly estimated as 10% of the total height of the eruption column, H_T [110].
The PDFs used are the following (in brackets we list their parameters):

- Truncated Exponential (mean, λ^{-1}; min and max limits).
- Linear-decaying (min and max limits).

For each eruptive size, we set the minimum and maximum limits of the Linear PDF at 20 m and $0.1H_T$, respectively [104]. Nonetheless, alternative choices of the minimum limit, at $H_0 = 10$ m and $H_0 = 50$ m, are tested for consistency and no significant differences can be recognized in the ECM outputs. The distribution for H_T is derived from eruption column simulations at Somma-Vesuvius [264]. In that work, H_T values were calculated from MER [265], after having sampled, from proper PDFs, values of total erupted mass and eruption duration.
The parameter λ defining the Truncated Exponential PDF is inferred by assuming that the 95th percentile[2] of the corresponding non-truncated Exponential PDF (i.e. $f(x) = \lambda e^{-\lambda x}$) is equal to $0.1H_T$ (i.e. the top of the gas-thrust region). The obtained Exponential PDFs are then truncated and renormalized between $H_0 = 20$ m and $H_0 = 0.1H_T$.

Combinations of ϕ and H_0 sampled pairs

For each eruptive size, we test three different combinations of PDFs. The combination Gaussian-Exponential is taken as reference since: (a) Gaussian PDFs have

[2]The selected percentile is a subjective choice guided by a precautionary principle since assigning a higher percentile (e.g. 99th) would produce PDFs with higher density at the smaller H_0 values and lower density at larger values.

been previously proposed as the PDF for ϕ [136]; and (b) the consideration that many natural phenomena follow exponential-like distributions.
In order to highlight the deviations from this reference combination we test only its alternatives: (1) Tukey-Exponential; and (2) Gaussian-Linear combinations. Again, 10000 pairs of ϕ-H_0 (per eruptive size) are sampled from each combination via the Monte Carlo inversion method. In total, 90000 simulations of the ECM are run.

6.2.4 Quantification of Theoretical Uncertainty: Incomplete Knowledge on Theoretical Assumptions

PDC mobility stands as an important variable to assess the potential extent of PDCs at a given volcanic system. However, there is not a complete agreement upon either which is the principal factor controlling ϕ or what might be the relationship (if any) with other variables: e.g. PDC volume [214, 266, 267], ground surface characteristics [222], ground slope [27], or column collapse height [44, 133].
Here, we estimate theoretical uncertainty by exploring three different hypotheses on the relationship between ϕ and H_0 within each eruptive size[3]:

- Direct pattern: column collapse height and PDC mobility are directly related, that is, the higher the collapse, the smaller the value of ϕ. For example, the dilute part of PDCs in the model developed by [133] would follow this direct pattern.
- Inverse pattern: column collapse height and PDC mobility are inversely related, that is, the higher the collapse, the larger the value of ϕ. [44] simulations for a VEI4 scenario at Somma-Vesuvius would agree with this inverse pattern.
- Independent pattern: no relationship exists between collapse height and PDC mobility (at least within a given eruptive size). Data in [138] as well as in [266] would support the independent pattern (i.e. the ECM parameters are not related).

[3]The eruption column heights [264] and ϕ values [138] determine a direct pattern among eruption sizes.

Our description of aleatory uncertainty comes from the independent pattern. Direct- and inverse-pattern are obtained as subsets of such description. In order to obtain reasonable subsets sizes, the parameter space (ϕ-H_0) is divided into the 9 sectors shown in Fig. 6.2. Boundaries are, subjectively, placed at the 20th and 80th percentiles of the ϕ-H_0 sample distributions in order to ensure that the parameter space is properly separated into regions of low ϕ-high H_0, high ϕ-high H_0 and so forth. However, both the direct- and inverse-pattern ϕ-H_0 samples are continuous throughout the parameter space since the magenta areas in Fig. 6.2 indicate ϕ-H_0 values which belong to both patterns. Finally, theoretical uncertainty is quantified using the ECM outputs from each pattern and building output ECDFs accordingly (Fig. 6.3).

6.2.5 Quantification of Structural Uncertainty: Incomplete Knowledge Reflected in the Model

Structural uncertainty is quantified by comparing the 'best' ECM outputs against real data that, in our case, are the PDC deposits preserved from past eruptions. Here, six eruptions of Somma-Vesuvius are used: the 1944 AD eruption [268] for the small eruptive size; Pollena eruption, 472 AD [269], and the 1631 AD eruption [270] for the medium eruptive size; and Mercato eruption, 8540 ± 50 cal. yr. BP [271], Avellino eruption, 3945 ± 10 BP [194, 232] and Pompeii eruption, 79 AD [272], as representative of large eruptions.

Following the validation carried out by [103], we firstly compute the areal misfit, $\mathcal{M}_{A_{ij}}$, associated to the 'best' 250 simulations (5% of the total, see note [5]), i.e. those with highest Areal Fit, $AF = A_{inter}/A_{tot}$ (where A_{inter} is the intersection area between the simulated area, A_{sim}, and the area of the PDC deposit, A_{obs}; and A_{tot} is the union area between A_{sim} and A_{obs}), per each selected eruption[5].

$$\mathcal{M}_{A_{ij}} = A_{sim_{ij}} - A_{obs_j} \qquad i = 1, ..., 250 \quad j = 1, ..., N_{erup} \tag{6.1}$$

[5]The total number of simulations utilized to quantify structural uncertainty (whether for area of invasion or maximum runout) is: 250 sims × 6 eruptions = 1,500 simulations. This corresponds to the 5% of the total number of simulations: 10,000 sims × 3 = 30,000 simulations. Therefore, our quantification of structural uncertainty gives equal weight to the misfit distributions estimated from each eruption, as far as there is not evidence to proceed differently.

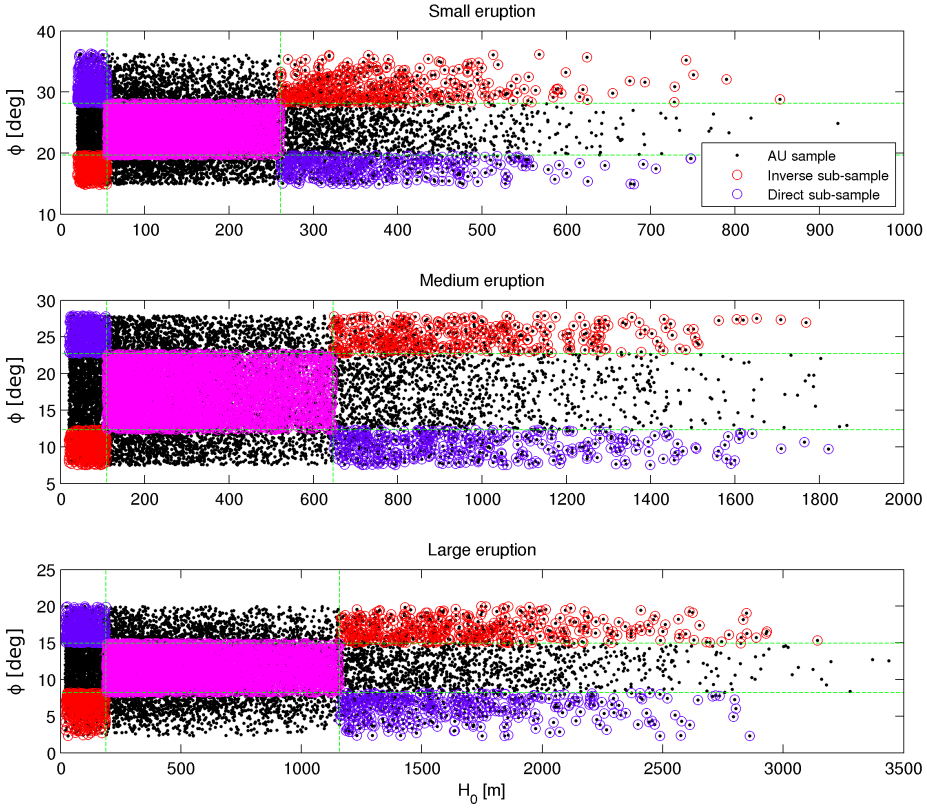

FIGURE 6.2: Sub-sampling of the Gaussian-Exponential, 40 m DEM configuration (aleatory uncertainty, AU) to explore theoretical uncertainty. Each graph delineates the ECM parameter space according to three eruption sizes: small (top), medium (middle) and large (bottom). Black dots indicate pairs of ϕ and H_0 as sampled from the aleatory-uncertainty configuration. Red open circles denote the inverse-pattern sub-sample and purple open circles denote the direct-pattern sub-sample. Magenta circles represent points shared by both inverse and direct sub-samples. From [104].

where $A_{sim_{ij}}$ is the area recorded in the i-th 'best' simulation of a specific eruptive size and eruption j, A_{obs_j} is the area of the PDC deposits preserved from the j-th eruption of this size and N_{erup} is the number of eruptions for this size.

The simulations are extracted from the configuration: Gaussian-Exponential PDFs run over 10 m DEM (i.e. the other sources of epistemic uncertainty are minimized, [75]).

We repeat the same process for the misfit on maximum runout ($\mathcal{M}_{MR_{ij}}$), selecting the 250 simulations, per eruption, with the closest maximum runout to the real observations.

We then build ECDFs based upon the obtained misfits of area and maximum

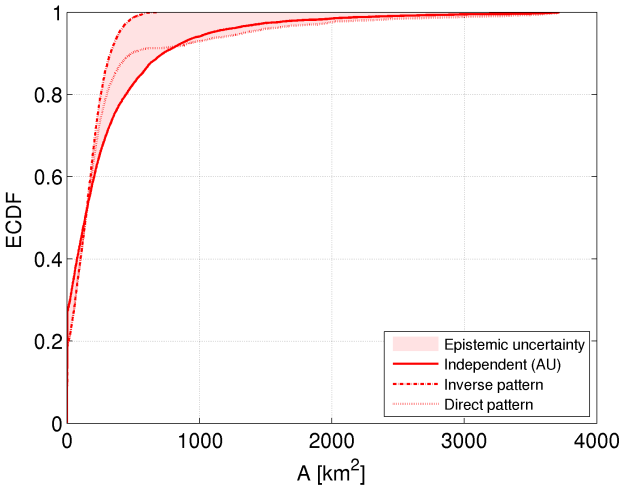

FIGURE 6.3: Epistemic uncertainty description taking as example the case of theoretical uncertainty and area of PDC invasion. Aleatory uncertainty (AU) corresponds to the solid red line (independent pattern). Epistemic uncertainty is defined as the pale red area between the three Empirical Cumulative Distribution Functions (ECDFs). Horizontal distances between the curves demark possible ranges of the output variable considering both aleatory and epistemic uncertainties (see text for more details). From [104].

runout according to the number of eruptions in each eruptive size (e.g. the misfit distribution for the large eruptive size contains 750 values of misfit). We add the misfit values (which can be negative[6]) along the whole aleatory uncertainty output ECDF and compute the final quantification of structural uncertainty from the minimum and maximum alternate ECDFs (Fig. 6.4).

This way of quantifying structural uncertainty is neither unique nor exhaustive. We note that the use of alternative PDC simulators for characterization of processes not accounted for here would improve the structural uncertainty quantification. In addition, our misfit distributions are based upon a reduced number of realizations of the 'true model' (the PDC deposits) and therefore we are adding a source of aleatory uncertainty within our quantification. Nevertheless, we consider that even a preliminary quantification of structural uncertainty is still better than assuming a 'perfect' model [75].

[6]NB. Nonetheless, negative values of area and maximum runout are not allowed.

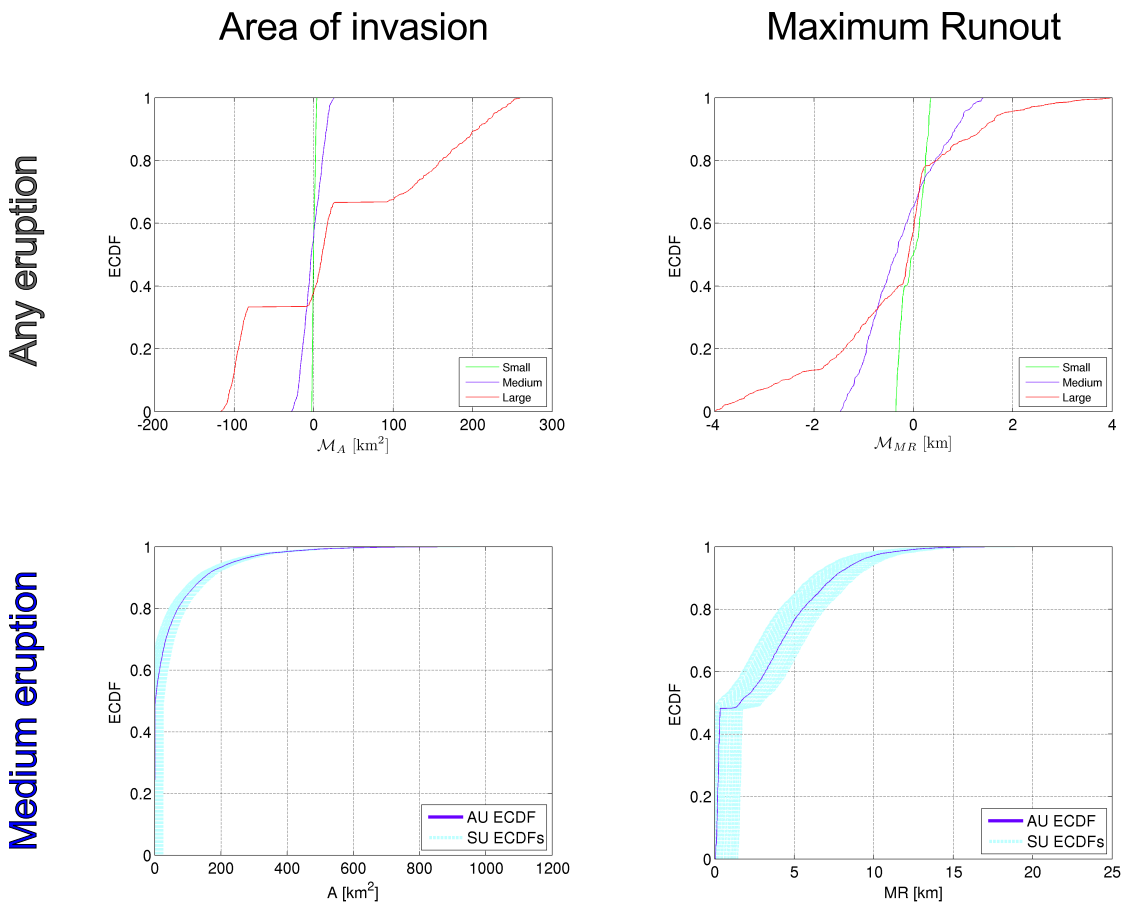

FIGURE 6.4: Structural uncertainty (SU) description. Top: misfit distributions of area of invasion (top-left) and maximum runout (top-right) according to three different eruption sizes at Somma-Vesuvius (Italy): small (green), medium (purple) and large (red). Bottom: medium-size structural-uncertainty representation in the form of SU ECDFs (dashed cyan lines) computed from aleatory uncertainty (AU ECDF, solid purple line) by adding distinct values of areal misfit, $\mathcal{M}_A$ (bottom-left), and maximum-runout misfit, $\mathcal{M}_{MR}$ (bottom-right), picked up from the graphs on top (see text for details). Note that the horizontal distance between the minimum-maximum SU ECDFs in the bottom graphs corresponds to the domain of $\mathcal{M}_A$ and $\mathcal{M}_{MR}$ (top graphs), i.e. around 50 km^2 and 3 km, respectively, in the medium eruption size. From [104].

6.3 Results

Our results are visualized in two different ways: (1) plots of ECDFs for invaded area and maximum runout; and (2) conditional-probability maps of PDC arrival (given an eruption of a specific size) over the surroundings of Somma-Vesuvius. As introduced before, aleatory uncertainty is described by the range in model outputs, in terms of invaded area and maximum runout, derived from the configuration: "Gaussian-Exponential, 40 m DEM, independent pattern" (Fig. 6.5). Epistemic

uncertainty (Fig. 6.6) is quantified by the range in model outputs obtained by: (i) running the ECM with "Gaussian-Exponential, independent" samples over different DEMs (input uncertainty); (ii) sampling the ECM parameters from alternate configurations (parametric uncertainty); and (iii) analyzing specific subsets of the aleatory uncertainty simulations (theoretical and structural uncertainties).

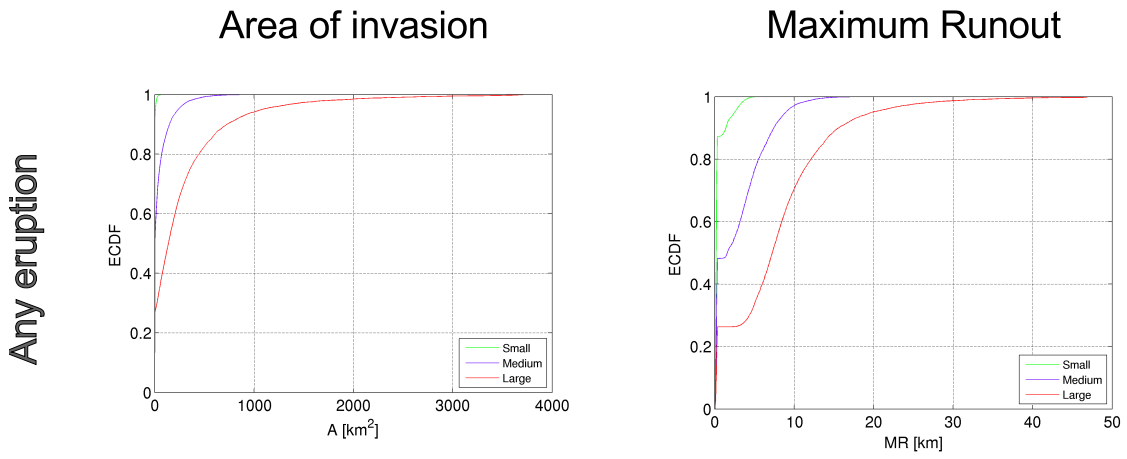

FIGURE 6.5: Aleatory uncertainty description, in terms of output Empirical Cumulative Distribution Functions (ECDF) for area of invasion and maximum runout (A and MR) of Pyroclastic Density Currents simulated with ECM at Somma-Vesuvius (Italy), according to three different eruption sizes: small (green), medium (purple) and large (red). From [104].

Figure 6.3 exemplifies our uncertainty quantification in terms of ECDFs. Aleatory uncertainty (due to randomness in the process) is given as the probability: Prob($X \leq x$); where X represents the ECM output variable, e.g. invaded area. Hence: Prob($X_{large} \leq 450\ \text{km}^2$) $= 0.8$, is a measure of aleatory uncertainty. In other words, the quantification of aleatory uncertainty is provided by different percentiles in the model output variable (in the above example, 450 km^2 is the 80-*th* percentile). Epistemic uncertainty (due to incomplete knowledge) is measured by the range in model outputs for any given percentile. In the example above, the 80-*th* percentile is in the range $[250, 450]$ km^2, when accounting for epistemic uncertainty.

Figure 6.7 shows the spatial distribution of aleatory and epistemic uncertainties over the surroundings of Somma-Vesuvius. In the leftmost column, we plot the conditional probability of PDC arrival, at each grid point, given the occurrence of an eruption of a specific size ($CP = Prob(PDCs|Eruption, Size)$); as computed from the aleatory uncertainty simulations. Examples of epistemic uncertainty (Fig. 6.7; right-hand side columns) are given as differences in conditional probability, ΔCP, among aleatory and epistemic uncertainty simulations. For the sake of

brevity, we focus on the configurations which lead to the highest absolute ΔCP values (Fig. 6.7).

6.3.1 Aleatory Uncertainty

The aleatory uncertainty ECDFs (Fig. 6.5) show that, respectively for small, medium and large eruptions, 85%, 50% and 25% of the ECM simulations correspond to PDCs with negligible area of invasion and maximum runout (i.e. they remain almost inside the crater). The simulations that escape the crater provide areal values rapidly increasing to reach maxima around 100, 1000 and 3700 km^2, respectively. In the case of maximum runout, the increase is not continuous. A lack of values (nearly horizontal ECDFs) occurs between 300 m and 1, 1.5 and 3 km of maximum runout in small, medium and large eruptive sizes, respectively. This is due to heterogeneities in crater-rim altitude and the fact that, for a given simulated Energy Cone, a small number of Energy Lines might escape the crater while others remain inside it. This produces an abrupt increase in the maximum runout (but not in the invaded area) of the simulation. Maximum runout values reach maxima around 6, 19 and 47 km, for small, medium and large eruptions, respectively.

Extreme values of both output variables are restricted to very high percentiles. For instance, considering large eruptions, $MR \approx 30$ km occurs around the 99th percentile while $A \approx 1,000$ km^2 occurs around the 95th percentile. In other words, 1% of the simulations record $MR \geq 30$ km while 5% of the simulations cover $A \geq 1,000$ km^2.

Regarding the conditional-probability, the contrast among eruptive sizes is obvious (Fig. 6.7). Small-size simulations are restricted to the southern flank of the volcano, cover small areas and have modest runouts. Medium-size simulations cover larger areas with moderate conditional probabilities ($CP > 0.4$) remaining over the South, East and West flanks of Somma-Vesuvius. The area with $CP \geq 0.05$ (colored area) has a radius of about 9 km around the volcano. An area similar to this is covered by $CP \geq 0.4$ in large-size simulations where, in turn, the $CP \geq 0.05$ area shows a radius of ≈ 22 km. Nonetheless, distal topographic highs such as the Sorrento Peninsula and the Nola-Sarno Mountains influence the runout blocking the simulated PDCs. Almost the entire city of Napoli lies inside the $CP \geq 0.05$ area. The topographic effect of the natural barrier of Mt Somma is recognizable for all eruptive sizes (Fig. 6.7).

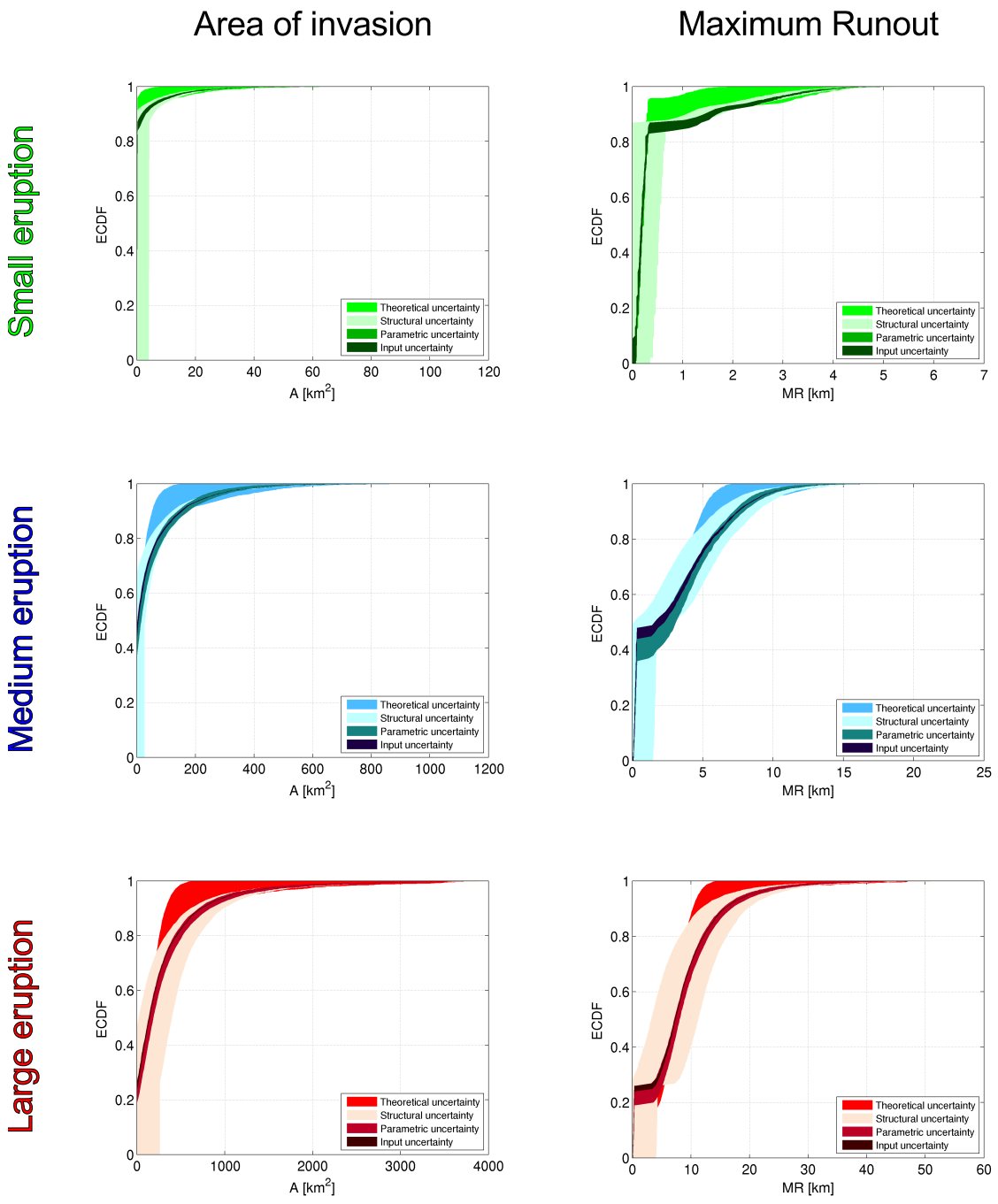

FIGURE 6.6: Comprehensive epistemic uncertainty description for the area of invasion (A) and maximum runout (MR) of Pyroclastic Density Currents at Somma-Vesuvius (Italy) according to three different eruption sizes: small (green), medium (blue) and large (red). Aleatory uncertainty (Fig. 6.5) lies inside the band of input uncertainty. Note how the contribution of each type of epistemic uncertainty to the total uncertainty changes along the graphs. From [104].

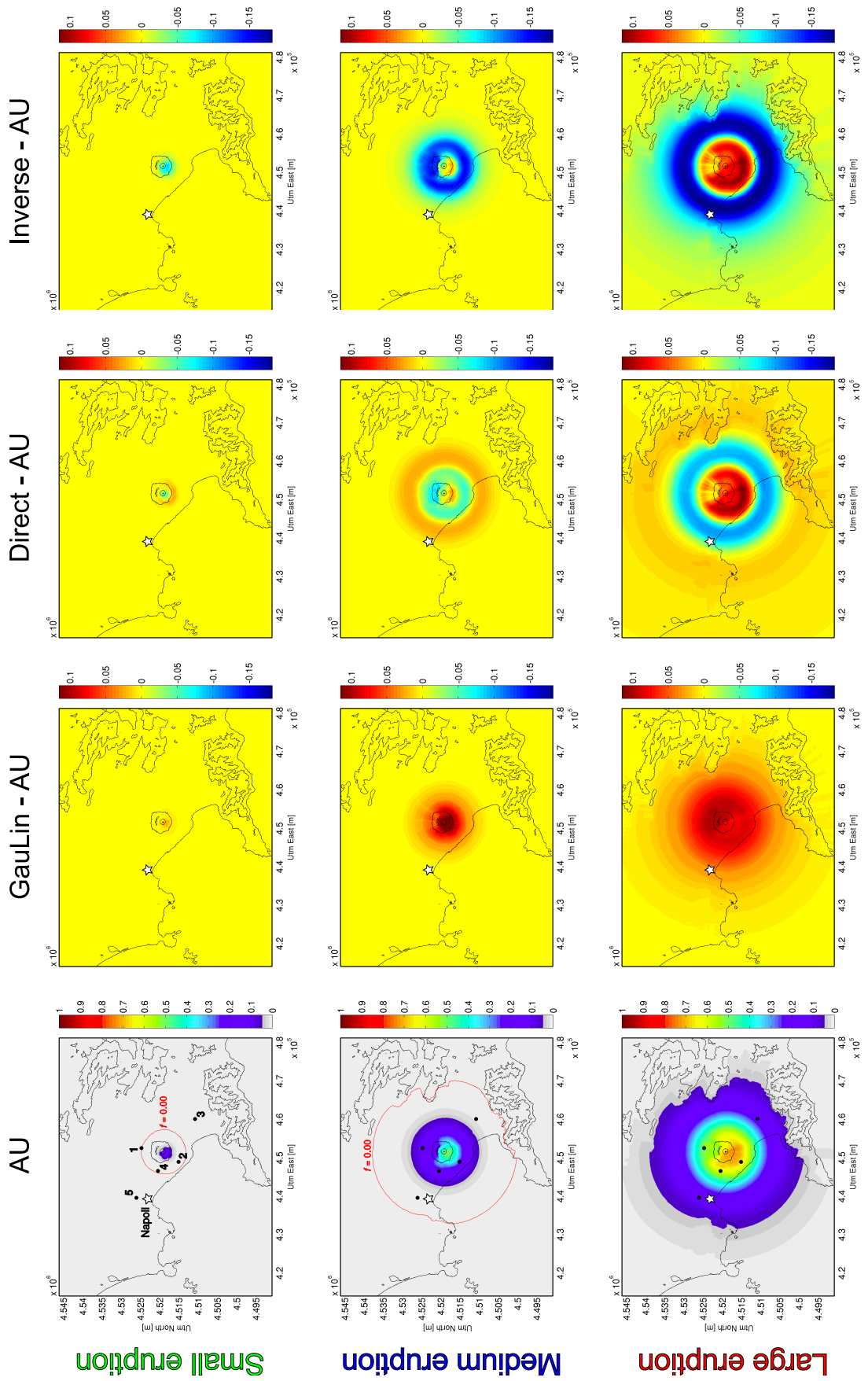

FIGURE 6.7: Conditional-probability (CP) maps of PDC arrival (given the occurrence of an eruption of a specific size) for three different eruption sizes: small (green text), medium (blue text) and large (red text). Lefmost-side maps are actual CP of PDC arrival (between 0 and 1) while the other three maps show the differences in CP, at each grid point, between alternate configurations (parametric Gaussian-Linear -2nd column-; theoretical direct pattern -3rd column-; and theoretical inverse pattern -4th column-) and the aleatory-uncertainty (AU) configuration (see text for more details). Colored zones in AU maps indicate $CP > 0.05$ and the solid red line displays the limit of $CP > 0$. The white star indicates the location of the city of Napoli. 1: Somma Vesuviana; 2: Torre del Greco; 3: Scafati; 4: hospital in Massa di Somma; 5: Napoli-Capodichino airport. From [104].

6.3.2 Input Uncertainty

Input uncertainty, investigated using differing DEM resolutions, is the source of epistemic uncertainty with the smallest contribution, taking into account all sizes and both output variables. Quantitatively, its maximum absolute values are, respectively, $\approx$ 3, 7, 25 km^2 for area of invasion and $\approx$ 1, 1.5, 3.5 km for maximum runout in small, medium and large eruptions. These values are hardly distinguishable, particularly in the medium- and large-size ECDFs of area of invasion. In terms of maximum runout, input uncertainty has a larger effect on total epistemic uncertainty. Its maximum extent coincides with the first simulations exiting the crater and this is recognized in all eruptive sizes (Fig. 6.6).
Due to its very small contribution, we do not show any conditional-probability map for input uncertainty, since these maps are very similar to those calculated from aleatory uncertainty (i.e. $\Delta CP \sim 0$).

6.3.3 Parametric Uncertainty

Parametric uncertainty, investigated using different PDFs for the model parameters, has a larger impact than input uncertainty on both output variables and, mostly, in medium and large eruptions. In small eruptions, parametric and input uncertainties are superposed (Fig. 6.6). Maximum parametric-uncertainty absolute values are about 20, 300, 700 km^2 for area of invasion and 1, 4, 8 km, for maximum runout in small, medium and large sizes, respectively.
Regarding the conditional-probability maps, we only display the Gaussian-Linear (40 m, independent pattern) simulations which show clear positive ΔCP values over the whole map (Fig. 9). These ΔCP values are bigger in the vicinity of the volcanic vent and get smaller at increasing distances. For large-eruption simulations, ΔCP is approximately +0.1 over the whole North sector (Fig. 6.7) which implies that most of the Gaussian-Linear large size simulations produce PDCs overcoming Mt Somma (i.e. the conditional probability over the North flank is similar to that on the other flanks of the volcano).

6.3.4 Theoretical Uncertainty

Theoretical uncertainty, investigated analyzing different relationships between the model parameters, gives the largest contribution to total epistemic uncertainty. Maximum theoretical uncertainty, in absolute terms, reaches around 90, 850, 3000 km^2 for area of invasion and 3, 11, 33 km, for maximum runout in small, medium and large eruptions, respectively. This is due to two reasons: (a) the inverse-pattern ECDF has a much narrower range of possible (smaller) values of area of invasion and maximum runout than the aleatory-uncertainty output ECDF; and (b) the direct-pattern ECDF shows a significant break-in-slope (Fig. 6.3) and its tail is slightly heavier than what seen in the aleatory-uncertainty output ECDF. Considering the conditional-probability maps, the direct and inverse pattern display remarkably different features as well. Direct-pattern difference maps are characterized by a common spatial distribution of ΔCP, independently of eruptive size (Fig. 6.7): proximal areas display positive ΔCP values; in medial areas (e.g. about 4 and 7 km from the crater in medium and large sizes, respectively), we observe negative ΔCP values; and, then, at more distal locations (e.g. beyond the $CP \geq 0.05$ limit in aleatory uncertainty), ΔCP changes sign again, although the positive differences here are smaller than in proximal areas. By and large, Mt Somma barrier seems to prevent PDC propagation northwards. The inverse-pattern maps also display positive ΔCP values over proximal sectors. However, beyond the positive-negative ΔCP boundary (Fig. 6.7), ΔCP gets strongly negative, decaying to smaller negative ΔCP values only at distal locations. This reflects the fact that no inverse-pattern simulation reaches medial and distal areas.

6.3.5 Structural Uncertainty

In regard to structural uncertainty, we only present ECDFs since this type of epistemic uncertainty cannot be directly mapped in this study. Here, we use the 'best' ECM simulations to characterize the misfit distributions and we apply the latter to build the final quantification of structural uncertainty (see subsection 6.2.5). However, estimating the effect of structural uncertainty on conditional-probability maps would require a procedure able to incorporate this source of epistemic uncertainty in the model itself, maybe as some sort of asymmetric buffer depending on the surrounding topography (e.g. [30]). This propagation of structural uncertainty to the conditional-probability maps should rely upon misfit distributions,

as previously estimated.
In terms of ECDFs, structural uncertainty is the most uniform source of epistemic uncertainty (Fig. 6.6). The maximum absolute values can get as high as ≈ 6, 50, 380 km^2 for area of invasion and ≈ 0.7, 3, 8 km for maximum runout in small, medium and large eruptions, respectively.

6.4 Discussion and future directions

Computing PVHA is time- and resources-consuming and not all numerical simulators or uncertainty quantification techniques are suitable for this purpose. The combined use of the ECM and Monte Carlo sampling supplies a comprehensive description of aleatory and epistemic uncertainties for PDCs at Somma-Vesuvius, Italy (Figs. 6.6, 6.7 and 6.8), that may be incorporated into PVHA.

6.4.1 A comprehensive uncertainty description

In order to compare the different sources of epistemic uncertainty among them and across eruptive sizes, we calculate the relative maximum expected deviation as: $\delta_{ij} = \Delta_{ij}/x_{50_i}$, where, for a given size i, Δ_{ij} is the maximum horizontal distance between the aleatory-uncertainty ECDF and the alternate ECDFs of the j-th source of epistemic uncertainty; and x_{50_i} is a common reference value: the 50th percentile of the aleatory-uncertainty ECDF, again for size i. Note that $\delta_{ij} > 1$ implies that maximum expected deviation is greater than the median, x_{50_i}. Concerning area of invasion, $\delta_{A_{ij}}$ spans from 10^{-1} to 10^3 considering all sources. The largest deviations occur on parametric and theoretical uncertainties in all eruptive sizes but especially in the small and medium sizes where $\delta_{A_{ij}}$ reaches values on the order of 10^2-10^3 (Table 6.2. Among all types of epistemic uncertainty, input uncertainty has the smallest effect on the areal outputs.

In the case of maximum runout, the obtained values are much more homogeneous, spanning only three orders of magnitude ($\delta_{MR_{ij}} \sim 10^{-1}$ to 10^1), considering all sources. Again, small and medium sizes show greater deviations in the outputs with respect to the large size. Theoretical uncertainty is confirmed to give the largest contribution. Input and structural uncertainties exhibit the smallest deviations even though the former plays a role in the small-size epistemic uncertainty,

TABLE 6.2: Relative maximum expected deviations from aleatory uncertainty considering area of PDC invasion and maximum runout (δ_A, δ_{MR}) and four different sources of epistemic uncertainty. IU = input, PU = parametric, TU = theoretical, SU = structural. From [104].

Variable →	$\boldsymbol{\delta_A}$				$\boldsymbol{\delta_{MR}}$			
Eruption size	IU	PU	TU	SU	IU	PU	TU	SU
Small	32.34	432.6	1168	53.81	5.595	5.404	18.37	1.921
Medium	3.569	130.7	402.2	12.87	0.927	2.073	7.312	0.926
Large	0.201	4.312	22.48	1.889	0.491	0.993	4.529	0.550

probably due to a stronger interaction of its simulated PDCs with the proximal topography (e.g. the crater and Mt Somma caldera rim). Figure 6.8 shows a South-North profile covering our study area, where topographic altitude is plotted against conditional probabilities of PDC arrival taking into account both aleatory and epistemic uncertainties. The smaller the eruptive size, the greater the influence of Mt Somma. The different shape of the conditional-probability profiles over the North flank (Mt Somma) compared to the South flank of the volcano is recognizable for all sizes. Nonetheless, the profile is more homogeneous in the case of a large eruption. This is in agreement with the general idea that large PDCs are less controlled by topography than smaller ones (e.g. [9]).

The very small contribution of input uncertainty to simulation results of medium and large sizes could be related to two main factors. Firstly, our case study is based on a topographic setting controlled by a high-standing stratocone (Somma-Vesuvius) surrounded by a quite flat area (Campanian plain). Assessing the importance of input uncertainty linked to ECM simulations on other volcanic systems featured by more complex topographies (e.g. Campi Flegrei, Italy) could be of particular interest for PVHA. The example of Campi Flegrei is relevant here as PDC propagation could be controlled by: (1) the complex morphology of the volcanic system (where caldera- and edifice-collapse structures are spatially combined with preserved eruptive cones, e.g. [25, 37]); and (2) the vent-opening spatial variability that can be expected from future eruptions (e.g. [205]).
Secondly, it should be stressed that the topographic control on PDC propagation that can be captured using the ECM is limited. Some effects such as channelization of PDCs [44, 91] or dense-dilute PDC decoupling [125] are not captured by such a simple model. Still, these effects can be crucial for PVHA and adequate scientific support for risk management. On the one hand, single-simulation or single-scenario (composed of few ECM simulations) approaches will likely fail in

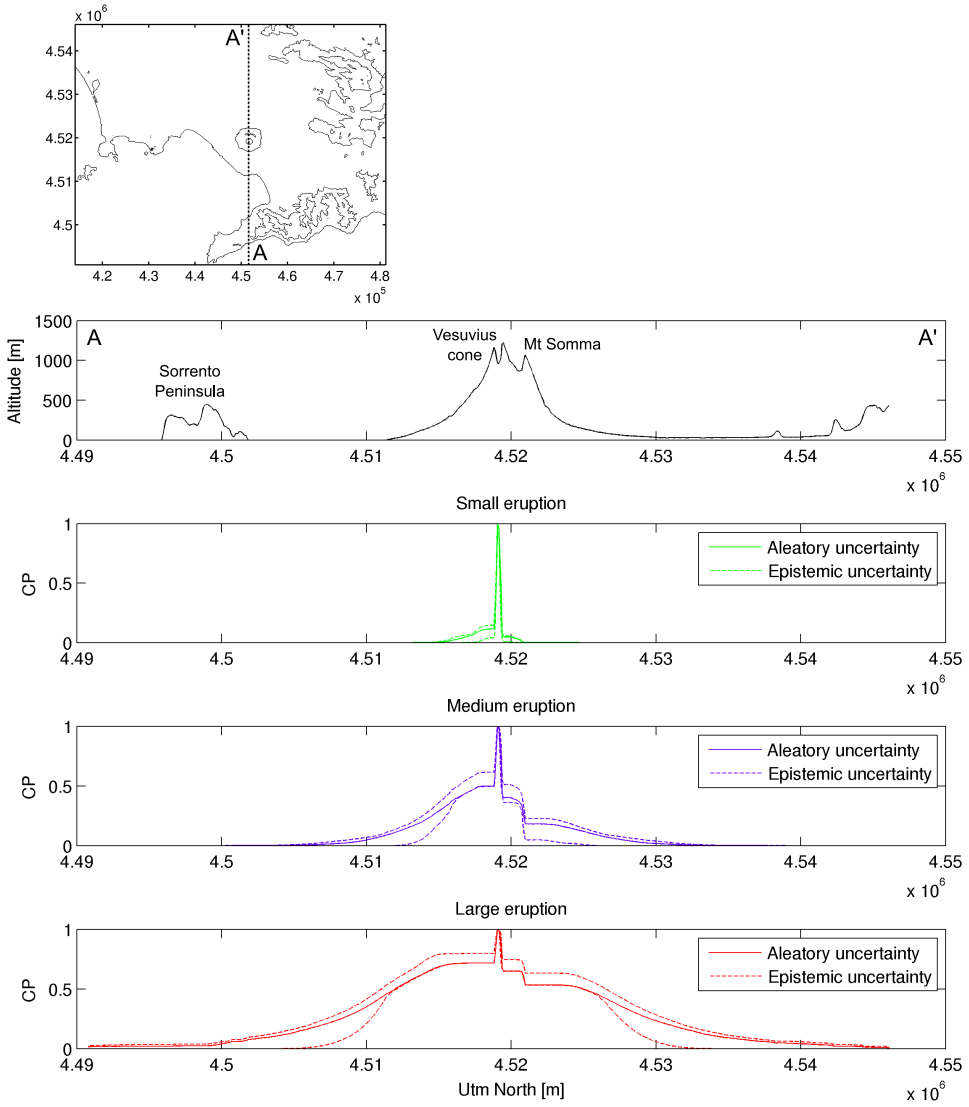

FIGURE 6.8: South-North profile (A-A') of the study area (map on the left). Top: altitude profile where some regional topographic highs are identified. The three other profiles, from top to bottom, show the conditional probabilities of PDC invasion computed from ECM simulations at Somma-Vesuvius and taking into consideration three eruption sizes: small (green), medium (purple) and large (red). Solid lines indicate the value of conditional probability as calculated from aleatory-uncertainty simulations. Dashed lines denote the minimum and maximum values of conditional probability taking into account all sources of epistemic uncertainty but the structural uncertainty (see text for more details). The link between topography and PDC invasion can be visualized in all three eruption sizes. From [104].

describing the possible extent of surge-decoupling processes as one might expect to occur, for instance, when PDCs encounter Mt Somma (there are other situations in which surge-decoupling is favored, such as sharp variations in channel capacity and/or sinuosity (e.g. [145]). On the other hand, structured analyses quantifying both aleatory and epistemic uncertainties (where many thousands of simulations, covering coherent ranges of ϕ and H_0, are run), may be able to somehow assess this extent, since they generate a statistical sample of ECM outputs which in part end before/at Mt Somma but in part go beyond it (Figs. 6.7, 6.8). As refers to PDC channelization, little can be done with the ECM and more sophisticated simulators are needed to evaluate the importance of such a phenomenon in the final PDC extent (see, for instance, Fig. 7 in [44]).
In order to statistically test which alternate configurations significantly change the output ECDFs of area of invasion and maximum runout from the aleatory-uncertainty output ECDF, we perform two-sample Kolmogorov-Smirnov tests, one per each epistemic-uncertainty ECDF tested against the aleatory-uncertainty ECDF (Table 6.3). This test evaluates the null hypothesis that both ECDFs (each epistemic one and the common aleatory) have been sampled from the same underlying distribution, i.e. a theoretical CDF (e.g. [273]). By means of the K-S tests, we want to find out whether the epistemic ECDFs are significantly different from the aleatory ECDF and, hence, quantifying epistemic uncertainty provides useful information about the ECM outputs. The only alternate configuration for which we cannot reject the null hypothesis, at the 5% significance level, is the Tukey-Exponential combination (parametric uncertainty). This fact reaffirms the choice of not exploring the Tukey-Linear configuration as we may assume their outputs would not be significantly different from Gaussian-Linear ones.

By taking into account all other epistemic uncertainties, instead, we observe a statistically significant variation of the final distribution for both area and maximum-runout values (Table 6.3). This means that, although input uncertainty changes these values by a small δ_{ij} amount, it is sufficient to modify the output ECDFs. More generally, it suggests that all types of epistemic uncertainty analyzed in this study are able to significantly change the resulting output values compared to those obtained when considering only aleatory uncertainty.
Finally, we can provide the probability ranges (considering both aleatory and epistemic uncertainties), conditional to the generation of PDCs and given the occurrence of an eruption of a specific size; for different locations being invaded by PDCs in case of small, medium, and large eruptions at Somma-Vesuvius. For

TABLE 6.3: Two-sample Kolmogorov-Smirnov tests performed by comparing the aleatory-uncertainty output Empirical Cumulative Distribution Function (ECDF) against diverse alternate output ECDFs (epistemic-uncertainty configurations) for two different output variables (area of invasion and maximum runout) and three eruptive sizes at Somma-Vesuvius (Italy). Null: null hypothesis decision (0: not to reject; 1: reject); p: p-value; gauexp: Gaussian-Exponential; tukexp: Tukey-Exponential; gaulin: Gaussian-Linear; 10, 20, 40, 80: DEM horizontal resolution (in meters); ind: independent pattern; inv: inverse pattern; SUmin: minimum structural-uncertainty; SUmax: maximum structural-uncertainty. From [104].

ECM output →	**Area of PDC invasion**						**Maximum Runout**					
Eruption size →	Small		Medium		Large		Small		Medium		Large	
ECDF	Null	p	Null	p	Null	p	Null	p	Null	p	Null	p
gauexp10ind	1	$< 10^{-5}$	1	$< 10^{-5}$	1	0.026	1	$< 10^{-5}$	1	$< 10^{-5}$	1	$< 10^{-5}$
gauexp20ind	1	$< 10^{-5}$	1	0.003	0	0.144	1	$< 10^{-5}$	1	$< 10^{-5}$	1	$< 10^{-5}$
gauexp80ind	1	$< 10^{-5}$	1	$< 10^{-5}$	1	$< 10^{-5}$	1	$< 10^{-5}$	1	$< 10^{-5}$	1	$< 10^{-5}$
tukexp40ind	0	0.927	0	0.287	0	0.374	0	0.871	0	0.058	0	0.374
gaulin40ind	1	$< 10^{-5}$	1	$< 10^{-5}$	1	$< 10^{-5}$	1	$< 10^{-5}$	1	$< 10^{-5}$	1	$< 10^{-5}$
gauexp40inv	1	$< 10^{-5}$	1	$< 10^{-5}$	1	$< 10^{-5}$	1	$< 10^{-5}$	1	$< 10^{-5}$	1	$< 10^{-5}$
gauexp40dir	1	$< 10^{-5}$	1	$< 10^{-5}$	1	$< 10^{-5}$	1	$< 10^{-5}$	1	$< 10^{-5}$	1	$< 10^{-5}$
SUmin	1	0.000	1	0.000	1	0.000	1	0.000	1	0.000	1	0.000
SUmax	1	0.000	1	0.000	1	0.000	1	0.000	1	0.000	1	0.000

illustrating this, we report some examples of conditional probabilities (Fig. 9) for PDCs arriving: (1) beyond Mt Somma (e.g. Somma Vesuviana); (2) at Torre del Greco (Napoli-Reggio Calabria highway and train station); (3) at Scafati (E-SE from Somma-Vesuvius); (4) at the hospital in Massa di Somma; and (5) at the Napoli-Capodichino airport (Table 6.4).

6.4.2 Applicability to Other Volcanoes

As indicated before, quantifying uncertainties is often a computationally expensive procedure. In spite of this, uncertainty is unavoidably linked to volcanic hazards (e.g. [274]). A better understanding of its sources, and how it can be whether reduced or, when not possible, quantified properly, will be beneficial for decision-making and risk mitigation [259]. Moreover, exploring the best ways of visualizing and communicating uncertainty requires close collaboration between scientists and decision-makers (e.g. [275]).

Accordingly, uncertainty characterization should be gradually included in volcanic hazard products as it has become a routine procedure in other natural hazards, such as earthquakes (e.g. [276, 277]).

The ECM has been one of the most-used models in volcanic hazard mapping studies [41, 132, 136, 217, 278, 279] because of its capability to capture some first-order characteristics of PDCs and its computational efficiency. The results presented in this chapter may be used to include preliminary uncertainty quantifications into single-scenario or even single-simulation hazard studies. Despite being an order-of-magnitude estimation of aleatory and/or epistemic uncertainty, this can enrich the information provided in the hazard analysis. Besides, getting an understanding of where or why different sources of uncertainty may arise, can guide future research efforts to better describe and/or reduce them.

For these reasons, the application of the presented approach to other volcanic systems (as well as to other PDC simulators) might serve to bridge the gap between some current practices, which lack of any uncertainty description, and an eventual common framework for uncertainty quantification in PVHA of PDCs.

TABLE 6.4: Conditional probabilities of PDC invasion (CP, in percentage) on five selected points over the surroundings of Somma-Vesuvius (Italy), as calculated from ECM simulations and taking into account both aleatory and epistemic uncertainties for three different eruption sizes: small, medium and large. For the sake of consistency, structural uncertainty is not included in the calculations although this type of uncertainty is one of the less efficient in modifying the aleatory-uncertainty values (see text for more details). Minimum critical values of ϕ-H_0 which allow the ECM simulations to surpass Mount Somma (arriving to Somma Vesuviana) are $\phi \leq 13°$ for $H_0 \approx$ 300-500 m up to $\phi \approx 23°$ for $H_0 \approx 1700$ m. d: distance from the vent; minEU, maxEU: minimum and maximum CP values taking into account epistemic uncertainty; AU: CP value considering only aleatory uncertainty; SoVe: Somma Vesuviana; TdG: Torre del Greco; Scf: Scafati; MdSH: Massa di Somma Hospital; NCA: Napoli-Capodichino Airport.

Eruption →		Small			Medium			Large		
Location	d[km]	minEU	AU	maxEU	minEU	AU	maxEU	minEU	AU	maxEU
SoVe	5.8	0	0	0	1.4	13	15	51	51	60
TdG	4.8	0	0.1	0.3	12	25	31	66	67	77
Scf	12	0	0	0	0.0	1.2	2.8	2.9	20	25
MdSH	5.2	0	0	0	4.1	19	23	60	61	70
NCA	14	0	0	0	0	0.3	0.7	0	12	15

6.4.3 Applicability to PVHA

Epistemic uncertainty represents an essential part of uncertainty assessment procedures. Quantifying the extent to which our knowledge is limited requires, first of all, to have an idea on what are the missing processes, the ill-constrained data, etc. In other words, we need to be aware of what we *don't know* [74].

This implies that epistemic uncertainty may increase or decrease as knowledge about volcanic systems changes over time. For instance, before the tragic eruption of Mt Saint Helens (USA) in 1980, little was known about the possibility of a gravitational failure of part of the volcanic edifice which triggered the devastating lateral blast (e.g. [280]). Consequently, at that time, the epistemic uncertainty associated to a nearly unknown outcome would have been very low. After the eruption, we discover an ontological error [62]. Many horseshoe-shaped morphologies on different volcanoes around the world were recognized afterwards and volcanic hazard scientists would start including the possibility of flank failure in their assessments (e.g. [281]). However, the causal links between magma ascent, emplacement or eruption, and the triggering of a flank collapse are not perfectly known. This means that epistemic uncertainty about the probability of flank failure has increased over time even though the knowledge about volcanic systems has clearly increased during the last 35 years.

This changing nature of epistemic uncertainty copes well with Bayesian methodologies, where new information can be incorporated to previous states of information in a structured manner (e.g. [239]), and with the taxonomy of uncertainties proposed by [62].

PVHA has been connected to Bayesian theory since its beginnings [21, 61, 67]. Some development in formal frameworks to evaluate epistemic uncertainty was published afterwards (e.g. [68]). In these works, a necessarily subjective (although expert) choice must be made in order to assign a degree of confidence on the proposed model, with respect to other possible models and observed data. This is ultimately linked to the selected modeling procedure, including: the simulator itself, the underlying assumptions, the DEM, the number of simulations, etc. (e.g. [19]). In this respect, we think that our study (and similar studies) can provide useful insights for assigning the subjective degree of confidence based upon a more robust, transparent and justifiable procedure, taking into account all the information about the morphology and magnitude of epistemic uncertainty

gathered from the presented results.

Chapter 7

Probabilistic Volcanic Hazard Assessment of PDCs in Central Campania (Italy)

Abstract

In this chapter, we incorporate the results of Energy Cone simulations of PDCs, from Somma-Veusvius and Campi Flegrei volcanoes separately, into the Bayesian Event Tree for Volcanic Hazard (BET_VH), to compute the probability of invasion by PDCs, from each of these volcanoes, over the central Campania region (the city of Napoli and surroundings) in the next 50 years. The probability of PDC invasion due to the two volcanoes is then combined, by assuming independency in the activity at the two volcanic systems, to obtain a Probabilistic Volcanic Hazard Assessment (PVHA) for PDCs in the target region in the next 50 years. The method used is doubly stochastic, allowing us to provide percentile maps to display the epistemic uncertainty associated with our best estimation. Since the probability density function of the model parameters of the Energy Cone is not known, we propose an ensemble of different hazard assessments based on different assumptions on such unknown probability density functions. The ensemble describes the merging of two plausible distributions for the collapse height and this reflects a source of epistemic (specifically, parametric) uncertainty. Notably, we include both dense and dilute PDCs in our hazard analysis that, in addition, is entirely based on forward modeling. We also apply a novel quantification of epistemic

uncertainty associated to PDC simulations: in this study, we compute spatially-varying evaluations of epistemic uncertainty, by using the characterization of the largest source of epistemic uncertainty, that is the theoretical uncertainty, revealed by [104].

7.1 Introduction

Pyroclastic Density Currents (PDCs) are ground-hugging hot mixtures of gases and pyroclasts, traveling at high speed over the flanks of, commonly, explosive volcanoes. Together with lahars, they have been the volcanic phenomenon responsible for the highest death toll in the last four centuries [157], and are among the causes of major concern in volcanic emergency management, as the most safe action to protect population against PDCs is the call for evacuations, sometimes on a large scale (e.g. [282]).
The generation, transport and deposition of PDCs are governed by a chain of very complex processes, that have long attracted the attention of scientists as a challenging problem to be modeled: in particular, a whole range of different simulators have been proposed, from very simple ones like the Energy Line (or Energy Cone in 3D, [132]), to more detailed numerical models considering friction within the flow and between the flow and the underlying ground (e.g. Titan2D and VolcFlow, see respectively [218, 283]), up to very complex models that are able to consider the multi-phase and multi-component nature of PDCs (e.g. [44]).

So far, the use of PDCs simulators has been mostly twofold: on the one hand, they have been used to reconstruct the dynamics (and related variables) of some past eruptions, by best-fitting the direct observations (e.g. [145, 284]) or some features of their PDCs deposits (e.g. [27, 285]; on the other hand, they have been used to model the hazard posed by PDCs at a given volcano (e.g. [45, 286]). For the former use it is likely that the more sophisticated the simulator, the more detailed the information retrieved; however, for the latter use, the output of few simulations from a very detailed model cannot guarantee the full characterization of all the uncertainties involved in forecasting future activity, and its resulting impact. Indeed, in modeling the hazard posed by such complex processes, a necessary balance must be reached between model complexity (the more complex the simulator, the higher its computational cost) and the possibility to fully explore the model parameters' space. In any case, the physical complexity of PDC-related processes

implies that there are subtantial uncertainties that cannot be neglected, stemming from intrinsical natural variability of such processes (aleatory uncertainty) and from our lack of knowledge or available data (epistemic uncertainties).

In this view, a few works in recent years have tried to fully account for uncertainties in modeling the hazard posed by PDCs. In particular, [24] have applied Titan2D model to Colima volcano (Mexico), to produce probability maps conditional to the occurrence of PDCs within a given volume range. [23] and [31] have developed a Bayesian emulator (built on Titan2D simulations) to produce hazard curves (e.g. [242]) at some points around Soufrière Hills volcano at Montserrat. These hazard curves were conditional to the occurrence of PDCs or applicable to a given time window. Nonetheless, the physical assumptions at the basis of Titan2D equations make it suitable only to simulate dense (and not dilute) PDCs.

More recently, [33] have produced probability maps of the invaded area in case of an inland explosive eruption from Campi Flegrei (Italy): here, the authors applied an integral model based on the box model [287], assuming the topography of the Campi Flegrei caldera as a sub-horizontal one, and using the areas of past deposits to build up a set of statistical distributions that quantify the aleatory and epistemic uncertainty in the PDC-invaded area for the next eruption. By sampling such distributions of areas and applying the box model in an inverse fashion, the authors retrieved the mass of pyroclastic material required to invade such an area, given a specific vent position and surrounding topography. The effect of topography on the propagation of the PDCs has been accounted for as in previous applications of the Energy Line model [288], i.e. by comparing the flow-front kinetic energy to the potential energy required to overcome topographical barriers along the flow path.
Unfortunately, the integral model based on the box model used by [33] can only be applied when the flow propagates over a subhorizontal surface. This hampers its use on volcanic systems with predominant topograhical structures, such as stratovolcanoes (e.g. Somma-Vesuvius). Further, this inverse scheme requires the availability of a significant number of data on the areas invaded by past PDCs at the volcano of interest, and this favourable situation is not very common.

In order to explore the possibility of using the Energy Cone model to produce probability maps of areas invaded by PDCs, [104] have studied how aleatory and epistemic uncertainties influence the outputs of the Energy Cone (in terms of invaded area A, and maximum run-out distance MR) at Somma-Vesuvius, when:

- running the Energy Cone on Digital Elevation Models (DEMs) of increasing resolution
- using different statistical distributions (reflecting different hypothesis on the flow generation and propagation) for the model parameters (i.e., the height of collapse H_0, and the flow mobility, usually parameterized by the ϕ angle: the larger the ϕ angle, the less mobile the flow)
- exploring diverse theoretical assumptions on the correlation patterns between the model parameters (independent, inverse or direct)
- quantifying, in a preliminary way, the intrinsical limitations of the Energy Cone model.

According to such study, all the types of epistemic uncertainty explored affect significantly the final output of the Energy Cone model, in terms of A and MR. Furthermore, a major contribution to epistemic uncertainty results from the so-called theoretical uncertainty (third item in the list above). Such correlation is controversial, as some authors (e.g. [133]) tend to assume a direct correlation between collapse height and mobility, while some others (e.g. [44]) are inclined towards an inverse one.

Further, [103] have proposed a quantitative procedure to validate the output of the Energy Cone model at Somma-Vesuvius and Campi Flegrei. In particular, they blindly tested the corresponcence between simulated and observed (from past deposits) A and MR values. By using independent data from worldwide PDCs deposits [138], they set up probability density functions for the model parameters of the Energy Cone model (H_0 and ϕ). Then, by sampling the parameters' values in a Monte Carlo scheme, they ran the Energy Cone model many thousands of times, obtaining the distributions of the simulated A and MR. These were statistically compared to the values observed in 24 mapped PDC deposits: 18 from Campi Flegrei [25] and 6 from Somma-Vesuvius [26, 193]. The comparison has shown that the real values are generally in statistical agreement with the simulations from the Energy Cone. In other words, despite being an extremely simple model (e.g. [289]), such studies on the Energy Cone model have highlighted its skill in quantitatively capturing the natural variability that an adequate hazard assessment should display.

Under these premises, in this chapter, we apply the Energy Cone model to simulate the invasion of PDCs from Somma-Vesuvius and Campi Flegrei on the Napoli metropolitan area in Southern Italy where about 3 million people live. The results of the simulations are included in a Bayesian Event Tree for Volcanic Hazard (BET_VH, [49] scheme, to produce long-term probability maps of invaded areas by PDCs on the target area, which is among the ones exposed at highest volcanic risk in the world, being densely inhabited and hosting strategical economic infrastructures at national scale. As in [33], the method is doubly stochastic, allowing us to provide percentile maps to display the epistemic uncertainty.

Three main novelties characterize this study. First, in analogy with probabilistic seismic hazard studies [290], the focus of our study is not a single source of hazard, but the target area. In this respect, we account for all the potential sources of the considered hazardous event (PDCs), i.e. Somma-Vesuvius and Campi Flegrei, threatening the metropolitan area of Napoli. The total hazard due to both these sources, considered independent, is thus evaluated and properly combined. This represents a first step towards the inclusion of probabilistic hazard studies on PDCs into quantitative risk and multi-risk studies, in order to rank risks and prioritize mitigation actions (e.g. [291]. We remark that, in the past, very few studies in volcanology (e.g. [292, 293]) have evaluated multi-source PDC hazard, as the generally accepted approach is to focus on a single volcano. Nevertheless, the studies by [292, 293] focused on peculiar events (i.e. single and subjectively adopted scenarios) from each volcano, rather than exploring the natural variability displayed by volcanic activity.
In this view, here we fully explore the model parameters' space (for both volcanic systems separately) in order to account for all the uncertainties involved. In other words, we do not subjectively choose *representative* scenarios, but we account for all the possible eruption sizes and eruptive vents for both volcanic sources, by adopting a novel approach as regards the eruption sizes recently proposed by [70].

Secondly, we include both dense and dilute PDCs in our hazard analysis, which is entirely based on forward modeling. This includes the quantification of epistemic uncertainty, which, up to now, has been mainly derived from expert judgement (e.g. [33]). In the case of previous BET_VH studies (e.g. [32, 100], epistemic uncertainty was measured in terms of the equivalent sample size Λ (e.g. [19]), guided by experts' choice. In this study, we compute spatially-varying Λ values, using the information contained in the simulations carried out by [104] and focusing

on the largest source of epistemic uncertainty identified by the authors: that is, the theoretical uncertainty.

Finally, since the probability density function of the model parameters of the energy cone model is not known, we propose a final hazard assessment based on the ensemble of different hazard assessments [76, 242]; each of them is based on different assumptions on the probability density function for the collapse-height parameter (H_0). The ensemble aims at evaluating this source of parametric uncertainty (e.g. [75, 104]).

7.2 Methods

In order to assess the probabilistic hazard from PDCs invasion, we follow the general scheme of BET_VH probabilistic model [49]. In particular, we divide the whole process, from the occurrence of an eruption to the impact on a given grid point in the target area, into three main logical steps:

- *Eruption forecasting* - in this step we assess a Probability Density Function (PDF) for the occurrence of an eruption (corresponding to Nodes 1-2-3 in BET_VH) in a given time window, that here we set to 50 years for long-term hazard purposes. For both volcanic systems, we use the assessment made in previous studies, i.e., [61] for Somma-Vesuvius, and [294] for Campi Flegrei. For Campi Flegrei, we see that our estimates are within the bounds proposed by [295].
- *Scenario forecasting* - in this step we assess a PDF for the location of the vent, given the occurrence of an eruption, and a PDF for the size of the eruption, given a position of the vent. These two PDFs respectively correspond to Nodes 4 and 5 in BET_VH.
- *Impact forecasting* - in this step we assess a PDF for the probability of generating PDCs and of reaching a given point in the target area (Naples metropolitan area), given the occurrence of an eruption of a given size class and vent. These two PDFs respectively correspond to Nodes 6 and 7 in BET_VH. Since we use a very simple simulator, we are not able in this study to compute the hazard curves (that would correspond to Node 8 in BET_VH, as in [242]).

7.2.1 Scenario forecasting

7.2.1.1 Spatial probability of vent opening

In the case of Campi Flegrei we use the long-term spatial probability of vent opening proposed by [205], which was the first one produced, and covers the whole caldera. We also test significant differences when using a more recent map proposed by [206].

In the case of Somma-Vesuvius, previous studies (e.g. [68]) concentrated most of the vent opening probability on the present Gran Cono crater, due to the persistent activity from this vent in the last 2ky. Here, we take a step forward and, by following an approach similar to [19], we try to use both prior knowledge due to the morphological features of the volcanic edific and the location of eruptions in the last 20ky.
To do so, we cover the volcano edifice (that we approximate as a circular area with center at (40.821N,14.426E), and radius of 6 km, see Figure 7.1a) with a regular grid of 500m spacing, totalling N_v=441 grid points. As in [205], we describe the spatial probability of vent opening by a Dirichlet distribution characterized by a set of parameters $(\alpha_1, ...\alpha_{N_v})$, and describing an exhaustive set of N_v mutually exclusive random variates [65]; in other words, our distribution for the spatial probability of vent opening is computed under the assumption that, in case of an eruption at Somma-Vesuvius, only one vent will open, and it will be within the area covered by the grid. The set of parameters $(\alpha_1, ...\alpha_{N_v})$ fully describe the aleatory and epistemic uncertainty, and are univocally linked to the mean probability of each grid points and to a number of equivalent data (or equivalent sample size) Λ, characterizing the dispersion around such mean values (see also [296].

In order to assign a prior probability distribution over the grid points, we divide them into three categories: 1 grid point in the center (the Gran cono's crater), 48 grid points belonging to the area enclosed by caldera collapses (identified by [25, 196]) and the remaining 392 "lateral" grid points. We assign a subjective prior mean probability of 0.90 to the crater point and 0.09 to the caldera points (uniformly spread, i.e., a mean probability of $\sim$ 0.002 for each of them). This is justified by the inferred location of Somma-Vesuvius's conduit below the Gran Cono position, and implies a larger probability of vents over the summit area. This is in agreement with [68], who assigned a general 0.99 probability to the opening

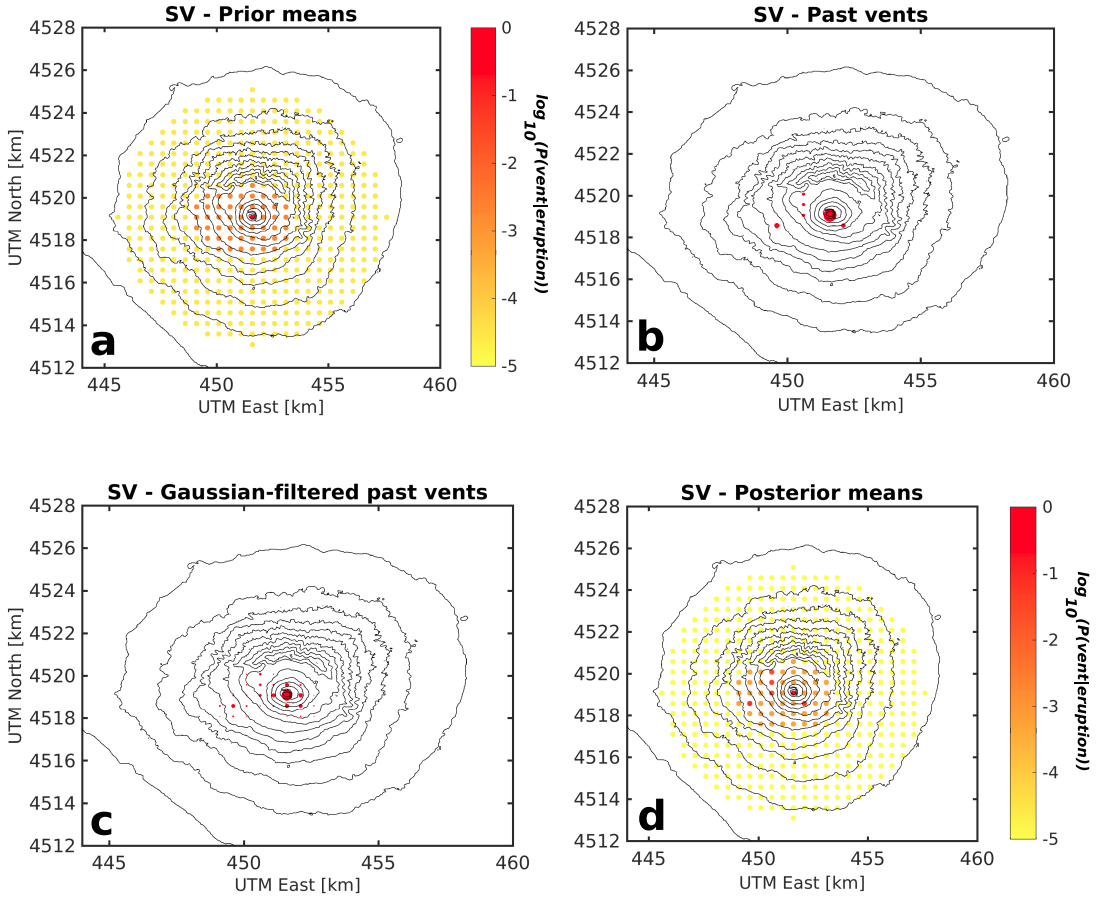

FIGURE 7.1: Spatial probability of vent opening, given an eruption, proposed for Somma-Vesuvius (Italy). (a) prior Dirichlet distribution showing high probabilities of vent opening over the present cone and the area covered by past volcanic-edifice collapses (calderas' floor); (b) number and location of past eruptive vents at Somma-Vesuvius (see Table 7.1); (c) number and location of past eruptive vents after applying a Gaussian filter to account for uncertainty in the inferred location for these vents; (d) posterior Dirichlet distribution computed after updating the prior distribution using the (filtered) past-vent locations. Probabilities in (a), (d) are expressed in $\log_{10}$ scale. In (b), (c) the size of the red circles indicates the number of past events (the bigger the circle, the higher the number). See text for more details. From [105].

of a vent in the summit area of Somma-Vesuvius. However this model does not exclude the (unlikely) event of a lateral opening outside the summit area (Gran Cono crater and caldera collapses): the lateral points are characterized by a prior mean probability, spread uniformly around all the points, of the remaining 1% (i.e., a mean probability of 2.6 10^{-5} per lateral grid point).

A moderate degree of confidence, expressed in terms of equivalent sample size Λ (see [296] for more details) is given to these prior mean probabilities (Λ=10). We

then use the location of past VEI≥3 explosive events in the last 22 kyr [89] (see Table 7.1) shown in Figure 7.1b, to condition such prior probability distribution. By using past locations as counts of "successes" in a Bernoulli multinomial scheme ($n_1, ...n_{N_v}$, where n_i is the number of recorded past eruptions in vent position i), we can exploit the conjugacy property of the Dirichlet distribution with the Multinomial function to compute the posterior probability distribution, conditional to the occurrence of an eruption at Somma-Vesuvius, which would be again a Dirichlet distributions with parameters $(\alpha_1 + n_1, ...\alpha_{N_v} + n_{N_v})$. In practice, since the exact position of some past vents is not known, first we apply a a Gaussian filter with null mean and σ=250m [205] to the counts of past vents in every possible location. The standard deviation value reflects the expected error in past vents' location, and it is of the order of the main crater's radius.

Given a number of recorded past eruptions n_j in vent position j, the Gaussian-filtered count n'_j will be:

$$n'_j = \frac{\sum_{i=1}^{N_v} w_{ij} n_i}{\sum_{i=1}^{N_v} w_{ij}} \tag{7.1}$$

where

$$w_{ij} = \exp(-d_{ij}^2/(2\sigma^2)) \tag{7.2}$$

and d_{ij}^2 is the metric distance between grid points i and j (in case $i = j$, such distance is obviously 0 and the weight $w_{ii} = 1$). The map of the filtered counts is shown in Figure 7.1c. The resulting posterior distribution is then computed as a Dirichlet distributions with parameters $(\alpha_1 + n'_1, ...\alpha_{N_v} + n'_{N_v})$; the map of the posterior mean values is shown in Figure 7.1d.

7.2.1.2 Probability distribution for the eruption size

We use the probability distribution for the eruption size proposed by [70], independently on where the vent is. In particular, to avoid assuming a set of subjectively chosen representative scenarios, we first define some broad size classes based on different ranges in the total erupted mass. For Somma-Vesuvius, we define three

TABLE 7.1: Age, some physical parameters and vent position estimated for VEI≥3 explosive eruptions at Somma-Vesuvius (Italy) during the last 22 kyr of volcanic activity (after [89]). Only eruptions for which the position of the eruptive vent is relatively well constrained are included. *Cioni2008 size* refers to the classification given by [89]: 1 = Ash Emission (AE), 2 = Violent Strombolian (VS), 3 = Sub-Plinian II (SPl2), 4 = Sub-Plinian I (SPl1), 5 = Plinian (Pl). UTM coordinates correspond to zone 33N. (a) Abbreviations of the eruption names are taken from [89]; (b) VEI size is calculated from the total erupted volume, in terms of tephra fallout (TF) and PDC volume; (c) a value of 1.5 indicates that [89] classified the eruption as AE-VS; (d) this age denotes the beginning of the eruptive cycle. From [105].

Eruption (a)	**Age**	**TF volume [km^3]**	**PDC volume [km^3]**	**VEI (b)**	**Cioni2008 size**	**ventUTMx [m]**	**ventUTMy [m]**	**References**
Pomici di Base	22 ka Cal	4.4	0.18	5	5	450371	4518947	[26, 89, 190]
Greenish pumice	19 ka Cal	0.5	0.02	4	4	450382	4519688	[26, 89, 190]
Mercato	8.9 ka Cal	1.4	0.23	5	5	451600	4519080	[26, 190, 297]
Avellino	3.9 ka Cal	1.57	1.04	5	5	449420	4518674	[26, 194, 298]
AP1	3.5 ka Cal	0.147	-	4	3	449420	4518674	[89, 190, 299]
AP2	3.5 ka Cal	0.143	-	4	3	449420	4518674	[89, 190, 299]
AP3	2.8 ka Cal	0.15	-	4	1	451600	4519080	[89, 190, 299]
AP4	-	0.122	-	4	1.5 (c)	451600	4519080	[89, 299]
AP5	-	0.084	-	3	1.5 (c)	451600	4519080	[89, 299]
AP6	216-217 BC	-	-	1	2	451600	4519080	[190, 299]
Pompeii	79 AD	2.9	0.83	5	5	452132	4518798	[26, 297]
Santa Maria cycle	172 AD (d)	0.15	-	4	1.5 (c)	452132	4518798	[89, 300]
Pollena	472 AD	1.38	0.39	5	4	450769	4520035	[26, 89, 144]
AS1	512 AD	0.025	-	3	3	451600	4519080	[301, 302]
AS2	540 AD	0.04	-	3	2	451600	4519080	[89, 190]
AS3	640 AD	0.12	-	4	2	451600	4519080	[89, 190]
AS4	790 AD	0.01	-	3	2	451600	4519080	[89, 190]
AS5	1410 AD	-	-	1	2	451600	4519080	[190]
AD1631	1631 AD	1.09	0.2	5	4	451600	4519080	[26, 89, 270]
SO1	1660 AD	-	-	1	1	451600	4519080	[89, 303]
SO2	1682 AD	0.0056	-	2	2	451600	4519080	[89, 303]
SAD1	1707 AD	0.0013	-	2	2	451600	4519080	[89, 303]
FdL	1723 AD	0.008	-	2	2	451600	4519080	[89, 303]
T1	1730 AD	0.0012	-	2	2	451600	4519080	[89, 303]
OTV	1779 AD	0.0061	-	2	2	451600	4519080	[89, 303]
CFM	1794 AD	-	-	1	1	451600	4519080	[89]
AD1822	1822 AD	0.038	-	3	2	451600	4519080	[89, 303]
AD1906	1906 AD	0.071	-	3	2	451600	4519080	[89, 303]
AD1944	1944 AD	0.066	$5.7 \cdot 10^{-3}$	3	2	451600	4519080	[89, 193, 304]

eruption size classes (small, medium and large, all characterized by explosive activity), assuming that next eruption will have a minimum eruptive energy to re-open the conduit [61]. For Campi Flegrei, we define four (effusive, small explosive, medium explosive and large explosive). Then we build a volcano-specific power law on the total erupted mass in explosive events, constrained by previous occurrences of each size class [70] (see Table 7.2). In this way, every simulation run of the Energy Cone is associated with a specific weight corresponding to its probability, given the occurrence of an eruption at the considered volcano.

7.2.2 Impact forecasting

7.2.2.1 Probability of PDC generation

Here, we use the statistics provided by [21] to define the prior means, grouped by eruption size. In particular, we give a null mean probability to Campi Flegrei effusive eruptions to generate PDCs. For eruptions falling in the small size class, at both volcanic systems, we give a mean probability of 0.35, while for larger eruptions we give a mean probability of 0.7. We give very low confidence on such prior mean values, assigning a $\Lambda = 1$ (Table 7.2), thus building up little-informative prior Dirichlet distributions. We then use past frequencies to condition the prior Dirichlet, again in a Bernoulli trial scheme as for the spatial probability of vent opening. In particular, all of the explosive eruptions at the two volcanoes have generated PDCs.

At Campi Flegrei, we also take into account the possibility of a vent opening in deep waters: in such a case, explosivity is likely to be suppressed by the pressure exerted by the water column above the vent (e.g. [32, 305, 306]). Thus, whatever the explosive size class, we assume that PDCs are not generated if the vent opens at a depth larger than 10 m, in accordance with [32, 305].

7.2.2.2 Probability of PDCs reaching target grid points

As regards the probability of reaching a given target point, we make use of simulations performed specifically with the Energy Cone model that are illustrated in this section. The general approach is similar to the one adopted by [103, 104]: for every volcanic system, vent position and size class, we first define a suitable model

parameter space and distribution for the Energy Cone parameters, collapse height (H_0) and PDC mobility[1] (ϕ). We then sample tens of thousands of pairs of values from this parameter space and, for each pair, we run an Energy Cone simulation. Then, at a given target grid point, we compute the frequency of simulations that reach that point, which is adopted as our best-estimate value (the mean) of the probability of reaching that point.

In this study, we sample the mobility ϕ from truncated Gaussian and Uniform distributions for Somma-Vesuvius and Campi Flegrei, respectively, as in [103, 104]. These two distributions reflect the evidence emerging from the catalog by [138] and from the data of the two specific volcanoes.
As a novelty, here we explore how results change when considering two "end-member" assumptions on the probability distribution of the collapse height H_0. In particular, we run two separate sets of simulations considering:

- a truncated Exponential probability distribution on H_0 (as in [103, 104]), accounting for the general idea that large column collapse heights are by far less likely than smaller ones, reflecting a common feature of frequency-size relationships in nature (e.g., the Gutenberg-Richter law for earthquakes)
- a Uniform probability distribution on H_0, reflecting maximum ignorance on the real relative frequency of large to small collapse heights.

In both cases, we assume that column collapse will occur within the gas-thrust region whose top is roughly estimated as 10% of the total height of the eruption column [110].

The results of the two simulation sets are then merged together through an ensemble model, that is a statistical mixing in which we give equal weight to the two end-member assumptions. In Appendix B, we provide a detailed description of the evidence upon which we build up the two different probability distributions.

Further, we use sub-groups of simulations to infer the confidence on such best estimates. As mentioned in the Introduction, [104] found that the largest contribution to epistemic uncertainty on MR and A, when using the Energy Cone model, comes from alternative hypothesis on possible correlations between values of H_0 and ϕ, namely a "direct" correlation (the largest the H_0, the more mobile the

[1]Note that, in reality, the smaller the ϕ value, the larger the mobility (see Chapter 4).

flow and thus the smaller the ϕ angle, and vice versa, e.g. [133]), and an "inverse" one (the largest the H_0, the less mobile the flow and thus the larger the ϕ angle, and vice versa, e.g. [44]). In order to assess how constrained is our best-estimate frequency value, we extract, from our simulations, two sub-groups of simulations, whose model parameters' pairs are in agreement with either one of the two correlation patterns: the sub-set of pairs in agreement with the direct pattern (in which the H_0 values are either below the 20^{th} percentile or above the 80^{th} percentile, and the corresponding ϕ values are respectively either above the 80^{th} percentile or below the 20^{th} percentile) and the sub-set of pairs in agreement with the inverse pattern (in which the H_0 values are either below the 20^{th} percentile or above the 80^{th} percentile, and the corresponding ϕ values are respectively either below the 20^{th} percentile or above the 80^{th} percentile). In this way, for a given target grid point, we obtain a set of 3 estimated values for the frequency of PDC arrival: one considering all the simulations, and two considering the theoretical uncertainty on the link between the Energy Cone parameters. We best-fit these 3 values with a Beta distribution, thus retrieving the best-estimate value for the frequency, and an associated Λ value (equivalent sample size). At a given target grid point, these two values fully define the Beta distribution for the Node 7 in BET_VH (for every given volcano, vent position and size class).

7.2.3 Ensemble probability of invasion from each volcano, and PVHA in 50 years

For both volcanic sources (Somma-Vesuvius and Campi Flegrei), after having set the probability distributions at all the nodes of BET_VH, and for any given grid point in our hazard domain, we sample 1,000 variates from these distributions at each node and combine them to obtain 1000 values of the probability of PDCs invading that grid point. We repeat this for both the end-member assumptions on the PDF governing the collapse height parameter of Energy Cone model (Exponential and Uniform), obtaining two different maps of the probability of invasion by PDCs in 50 years, for every volcano. The two maps quantify the parametric uncertainty deriving from the unknown shape of the PDF for H_0. In order to obtain a single probability map for every volcanic source, these two maps are statistically mixed, with equal weight, to obtain the ensemble probability of invasion in 50 years (7.2 for Somma-Vesuvius, and 7.3 for Campi Flegrei).

TABLE 7.2: Parameterization of the posterior distributions in the BET_VH model for Somma-Vesuvius and Campi Flegrei volcanoes, in Italy, that allows to compute the aleatory and epistemic uncertainty in probabilistic volcanic hazard of PDCs over the surroundings of the two volcanoes (e.g. the city of Napoli). Beta^1 indicates that a single Beta PDF is used to model the node (e.g. P(eruption)) while Beta^n indicates that many Beta PDFs are used to model the node, in particular, one Beta PDF for each event within the node (e.g. P(area$_i$), being impacted by PDCs). (a): values in square brackets correspond to Nodes 1-2-3 in BET_VH, respectively; (b): values in square brackets indicate the parameters for small, medium and large eruption sizes, respectively; (c) μ_7 and λ_7 values are common to both the Exponential and Uniform parameterizations of the aleatory uncertainty in the collapse height, H_0. See text for more details. From [105]

PDF type	**Parameters**		**Somma-Vesuvius (SV)**	**Campi Flegrei (CF)**	**Reference(s)**
Beta^1 (a)	μ_{123}		[0.0026; 0.5; 0.5]	[0.027; 0.5; 0.12]	[68, 294]
	λ_{123}		[385; 1; 1]	[307; 1; 4.7]	
Dirichlet	μ_4	min	$7 \cdot 10^{-6}$	0	This study (SV) [205] (CF)
		max	0.77	0.048	
	λ_4		39	29	
Dirichlet (b)	μ_5		[0.65; 0.24; 0.03]	[0.62; 0.22; 0.07]	[70]
	λ_5		8	27	
Beta^n (b)	μ_6		[0.57; 0.88; 0.88]	[0.92; 0.93; 0.93]	[21, 61] (SV) [21, 25, 191, 195] (CF)
	λ_6		[2; 4; 4]	[16; 8; 8]	
Beta^n (b)(c)	μ_7	min	[0; 0; 0]	[0; 0; 0]	This study and [103, 104]
		max	[1; 1; 1]	[1; 1; 1]	
	λ_7	min	[1; 1; 1]	[1; 1; 1]	This study and [104]
		max	[>1000; >1000; >1000]	[>1000; >1000; >1000]	

Finally, we combine the two volcanic sources by assuming independency in the volcanic activity at Somma-Vesuvius and Campi Flegrei, that is, at any given grid point i we compute the probability of experiencing *at least* one PDC arrival in 50 years ($PVHA_i$) by:

$$PVHA_i = 1 - (1 - PVHA_{SV_i}) \cdot (1 - PVHA_{CF_i}) \tag{7.3}$$

where $PVHA_{SV_i}$ and $PVHA_{CF_i}$ are the probabilities at grid point i to be invaded by PDCs arrival, respectively from Somma-Vesuvius and Campi Flegrei, in the next 50 years, as computed above. The resulting PVHA maps are given in Figure 7.4.

7.3 Results

In Figures 7.2 and 7.3 we show the probability of invasion of PDCs in all the grid points in the next 50 years, at different percentiles (the best-estimate value given by the mean, and epistemic uncertainty expressed by 10^{th} and 90^{th} percentiles, i.e. an 80% confidence interval), for Somma-Vesuvius and Campi Flegrei, respectively and separately. These results account for both the end-member assumptions on the distribution governing H_0 (Exponential and Uniform), as they show the statistical mixture of the two end-member models (with equal weight, see previous subsection 7.2.3).

At Somma-Vesuvius, the highest probabilities of PDC arrival are observed over the southern flank of the volcano, with mean values around or above 10% (in 50 years) extending for about 4 km towards the southeast (Fig. 7.2). The shape of Mount Somma is mapped, very neatly, by the northern limit of the isoline of mean probability corresponding to 8% (Fig. 7.2d). Moreover, the central, most elevated part of Mount Somma is evidenced by the shape of the 6-8% color contouring towards the north. According to the 10^{th} percentile of the distribution over the frequency of PDC arrival, it is observed that this frequency is below 0.5% (i.e. white countouring) for any grid point apart from those located on the proximal sector (∼2 km from the crater) of the southern flank (Fig. 7.2a). In contrast, according to the 90^{th} of such distribution for the frequency of PDC arrival, areas up to 10^3 km^2 are covered by probabilities of PDC arrival, in the next 50 years, greater

than 0.5%. Nevertheless, the probabilities over medial-distal sectors (beyond ∼8 km) are below 5% and confined by the Appenninic topographic over the S-SE and N-NE (Fig. 7.2b). The values of probability of PDC arrival towards the west must be taken with extreme care because, even though PDCs in our simulations are allowed to propagate over the sea water, the Energy Cone model is not suitable to model this type of PDC propagation (e.g. [134]). The analysis of differences in the percentile maps indicates that the summit part of Somma-Vesuvius has an 80% confidence interval approximately [0.5% - 40%] in 50 years; the same quantities, for PDCs generated from Somma-Vesuvius invading the city center of Napoli (gray star in Figure 7.2) are between [0.02% - 3%], with a mean value of 1% (Fig. 7.2).

At Campi Flegrei, the maximum probability of PDC invasion, in the next 50 years, is about 7% (mean value) and ranges between [0.3% - 16%] (80% confidence interval) when epistemic uncertainty is taken into consideration. These maxima in probability of PDC arrival are located in the Eastern caldera sector, in particular over the Astroni crater and the Agnano plain (Fig. 7.3d). The general spatial pattern of the mean probability of PDC arrival shows that values equal to or greater than 3% (in 50 years) are restricted to the structural boundaries of the calderas formed during the Campanian Ignimbrite and the Neapolitan Yellow Tuff (e.g. [203, 204] and references therein). Nonetheless, in our maps the gradient in the mean probability values is not extremely sharp across the caldera's boundary: for example, the Posillipo hill (located beyond the Eastern border of the Neapolitan Yellow Tuff caldera, and part of the municipality of Napoli) has a mean probability of 2-3% to be hit by PDCs from Campi Flegrei. At the city center of Napoli (gray star in Figure 7.3), mean probabilities of PDC arrival are around 0.5% and [0.01% - 1%] considering the aforementioned 80% confidence interval. At farther distances, mean values of probability of PDC arrival $\geq$0.5%, in 50 years (colored contouring), are obtained for grid points up to 10-12 km from the center of the Campi Flegrei caldera (Fig. 7.3c). When accounting for epistemic uncertainty, the probability of PDC arrival can range from less than 0.5% over the whole caldera (10^{th} percentile of the distribution for this probability, Fig. 7.3a) to values generally greater than 7% over the whole caldera and values above 0.5% at distances almost of 20 km (northwards, for instance) from the center of the caldera (90^{th} percentile of the probability of PDC arrival, Fig. 7.3b).

In Figure 7.4, we show the map of the combined PDC hazard calculated for the

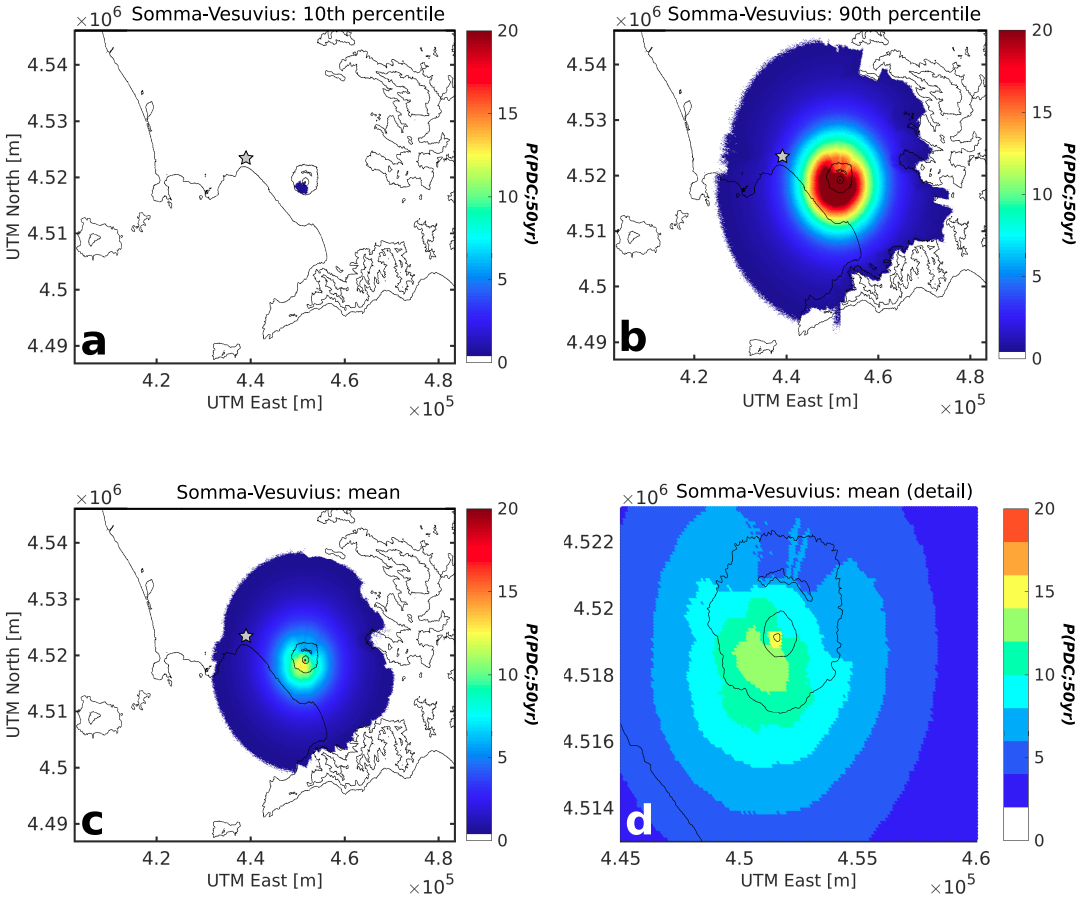

FIGURE 7.2: Probability maps displaying the probability (or future frequency) of PDCs, from Somma-Vesuvius, arriving at each grid point over the hazard domain (light-gray star points downtown Napoli) in the next 50 years, $P(PDC; 50yr$, according to the ensemble model for the collapse height (H_0). Our integrated probabilistic approach allows to compute a PDF for each frequency of PDC arrival. The different plots show diverse "slices" of such distributions: (a) 10th percentile, (b) 90th percentile (NB. The colorbar of this map does not show its maximum values, which are around 40%), (c), (d) mean value. Note how: (1) the distributions tend to have positive skewness, i.e. mean values are closer to the 90th than to the 10th percentile; and (2) due to large epistemic uncertainty in the hazard assessment, the probability maps for the 10th and 90th percentiles are very different. See text for more details. From [105].

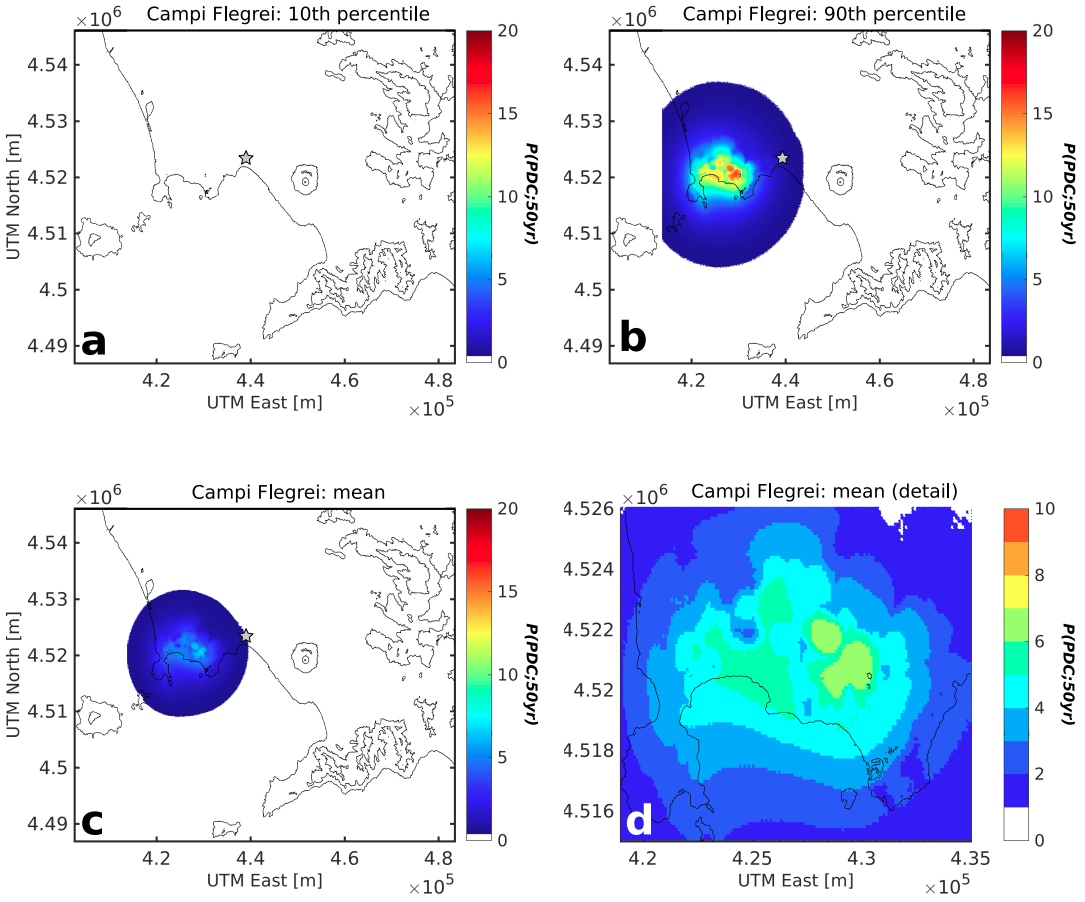

FIGURE 7.3: Probability maps displaying the probability (or future frequency) of PDCs, from Campi Flegrei, arriving at each grid point over the hazard domain (light-gray star points downtown Napoli) in the next 50 years, $P(PDC; 50yr$, according to the ensemble model for the collapse height (H_0). Our integrated probabilistic approach allows to compute a PDF for each frequency of PDC arrival. The different plots show diverse "slices" of such distributions: (a) 10th percentile, (b) 90th percentile, (c), (d) mean value. Note how: (1) the distributions tend to have positive skewness, i.e. mean values are closer to the 90th than to the 10th percentile; and (2) due to large epistemic uncertainty in the hazard assessment, the probability maps for the 10th and 90th percentiles are very different (in fact, the 10th of $P(PDC; 50yr$ from Campi Flegrei is below 0.5% -white color in inset (a)-). See text for more details. From [105].

activity at the two volcanoes, assumed to erupt independently. Thus, the probability of PDC arrival displayed in this figure corresponds to the probability of PDCs, from at least one of the two volcanoes, invading each grid point over our hazard domain: the central Campania region (see subsection 7.2.3). These multi-source probability maps are very similar to the single-source maps (Figs. 7.2, 7.3) in the vicinity of each volcano, as far as the PDCs from one of them are not able to propagate far enough to invade grid points over the proximal sector of the other volcano, apart from some unlikely cases (Figs. 7.2, 7.3). The city of Napoli has its western part located on the Campi Flegrei caldera and its center and eastern part in between the two volcanoes. The probabilities of PDC arrival (in 50 years) shown in Figure 7.4 are greater than the probabilities computed from either single volcanic source (see equation 7.3). In particular, the whole city center is placed over grid points with mean probability of PDC arrival, in 50 years, of 1-2%. These mean values reach 2-3% over the eastern end of the city and 4-5% over the western areas of the municipality (Fig. 7.4d). According to the 10^{th} percentile of the distribution for the probability of PDC arrival (in 50 years), the city of Napoli is less than 0.5% probable to be impacted by PDCs in the next 50 years (Fig. 7.4a). However, if the 90^{th} percentile of the distribution is considered, the city center of Napoli is associated with values over 5% (in 50 years), while the western sector of the city is about 10% probable to be impacted by PDCs (Fig. 7.4b).

7.4 Discussion and Conclusions

7.4.1 Simple insights into PDC propagation

Even though the PDCs from Campi Flegrei tend to be more mobile than the ones from Somma-Vesuvius (see Chapter 3 and Appendix A), the summit part of Somma-Vesuvius is much more likely to experience PDC invasion than any other point along the hazard domain. This is mostly due to two reasons. First, there is a "dissipating" effect caused by the much larger uncertainty on the vent position at Campi Flegrei: while the distance between any given grid point within the Campi Flegrei caldera and the next opening vent is very uncertain (it can range from meters to kilometers with similar probability, e.g. [205, 206]), the points nearby the Somma-Vesuvius summit are highly likely to be close to the next opening vent, as Somma-Vesuvius summit caldera area concentrates almost all the probability

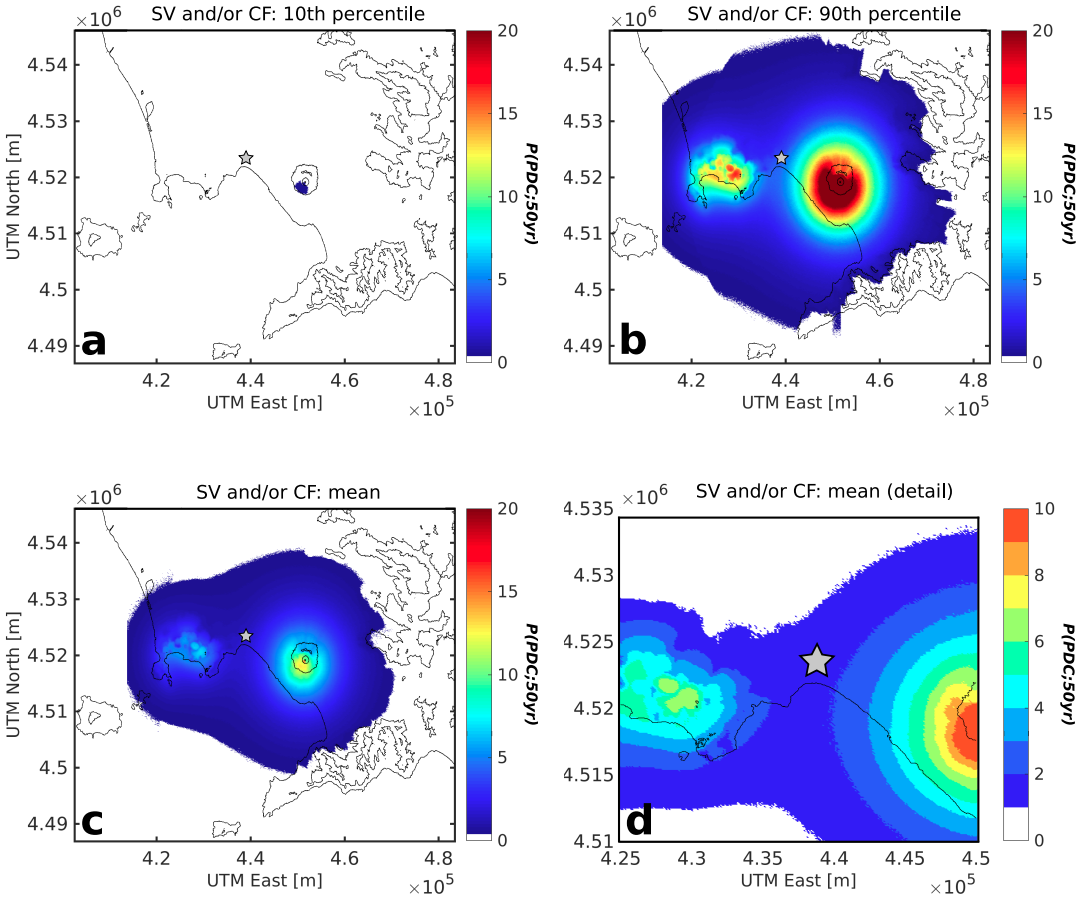

FIGURE 7.4: Probability maps displaying the probability (or future frequency) of PDCs, from Somma-Vesuvius (SV) and/or Campi Flegrei (CF), arriving at each grid point over the hazard domain (light-gray star points downtown Napoli) in the next 50 years, $P(PDC; 50yr$, according to the ensemble model for the collapse height (H_0). Our integrated probabilistic approach allows to compute a PDF for each frequency of PDC arrival. The different plots show diverse "slices" of such distributions: (a) 10th percentile, (b) 90th percentile, (c), (d) mean value (NB. The colorbar in (b) and (d) does not show the maximum values in probability, which are around 40% and 16%, respectively). Note how: (1) the distributions tend to have positive skewness, i.e. mean values are closer to the 90th than to the 10th percentile; and (2) due to large epistemic uncertainty in the hazard assessment, the probability maps for the 10th and 90th percentiles are very different. See text for more details. From [105].

of vent opening (Fig. 7.1). Secondly, the predominant topographical structure of Somma-Vesuvius stratovolcano allows PDCs to propagate, at least, towards the south and west where there is no barrier (e.g. Fig. 5.6, see Chapter 5). On the opposite, in our simulations, the rough topography of the Campi Flegrei caldera often stops small PDCs (by far the most likely ones, at least in the case of H_0 being sampled from an Exponential distribution) close to their originating vent. In other words, PDCs from Campi Flegrei are entrapped by neighbouring topographical heights at short distances from the point they originate.

Our novel approach of quantifying the equivalent number of data (Λ in [49, 68]) for Node 7 (Λ_7), at each grid point and based on the simulations of the physical model (instead of deriving it from expert judgement, e.g. [19, 32, 100]), permits the analysis of the spatial patterns in this BET_VH parameter. Therefore, areas where epistemic uncertainty[2] is high (i.e. low Λ values; minimum Λ is 1) or low (i.e. high Λ values; maximum Λ shown is 1000) can be identified and related to the main morphological features of the study volcanoes. In Figure 7.5, we show the spatial distribution of $\log_{10}(\Lambda_7)$ for different eruption sizes from the most probable vent location at Somma-Vesuvius (central-summit crater) and Campi Flegrei (Astroni crater).

At Somma-Vesuvius, the maps are characterized by a region of low uncertainty (yellow ring for medium and large size, proximal area to the SE for the small size) which is where the three patterns in the Energy Cone paramaters that define theoretical uncertainty (independent, direct and inverse; see 6) lead to similar output frequencies of PDC arrival (Fig. 7.5). We interpret this zone as the one having an approximately equal number of simulations with smaller and larger model-parameter values (H_0, ϕ). In this view, half of the simulations produce shorter runouts (or smaller areas of PDC invasion) and the other half produce larger runouts (or larger areas of PDC invasion). The in-between zone, characterized by frequencies around 50%, is reached with a similar frequency no matter the relationship between H_0 and ϕ. The location of this zone of minimum epistemic uncertainty for the medium size, before the Mount Somma, suggests the importance of this topographic barrier for medium-size PDCs (e.g. [44, 307]): grid points beyond Mount Somma are more uncertain to be invaded by PDCs than points just before the barrier (Fig. 7.5). Large-size PDCs in turn, are less influenced by Mount Somma and the yellow zone is located some kilometers away

[2]In our case, theoretical uncertainty (see subsection 7.2.2.2).

from the barrier. Additionally, the maps for the small and medium eruption sizes also show a low-uncertainty zone (i.e. high Λ) at large distances from the central crater due to the fact that no simulated PDCs (of these sizes) are able to invade those distal grid points (Fig. 7.5).

At Campi Flegrei, maps are characterized by a low-uncertainty zone surrounding the Astroni crater, the larger the eruption size, the wider this zone. We interpret this zone as the one invaded by all the PDCs that make it out of the Astroni crater. Inside the crater itself, the variability is a bit larger as very small PDCs probably do not invade all of the crater area. Again, at large distances from the crater, there is a low-uncertainty zone that is where no simulated PDCs arrive (Fig. 7.5). According to our results, the simulated PDCs are not strongly confined by the presence of the scarps that delineate the boundaries of the Campi Flegrei caldera (e.g. [25, 33]). In other words, a certain (albeit small, Fig. 7.3) number of PDCs are able to overcome the caldera boundaries and invade grid points towards the north. Therefore, the epistemic uncertainty at the caldera boundaries and beyond is relatively high (Fig. 7.5).

Finally, a limit in our simulation strategy, in terms of PDC propagation, is that we neglect the presence of the sea in the propagation of PDCs; in other words, when a flow reaches the sea, the EC model propagates it as if there was land, which is obviously a crude approximation (e.g. [134]). In practice, our probability maps might include some simulations from Campi Flegrei in which PDCs unrealistically flow across the Pozzuoli Bay or the Gulf of Napoli. Analogously, a few PDCs simulated from Somma-Vesuvius might reach the Posillipo coast after having traveled, unrealistically, over the sea water of the Gulf of Napoli. However, these "fake" simulations represent a very small percentage of the total number of simulations run and, hence, the final probability maps are not significantly affected by them.

7.4.2 PDC hazard assessments at Somma-Vesuvius and Campi Flegrei

Our final probability maps cannot be really compared with previous works, even in the case of a single volcanic source, as there is no previous map having all the features that ours possess. That is, for each volcano analyzed (Figs. 7.2, 7.3) and for the two volcanoes jointly (Fig. 7.4), our maps display: the probability of PDC

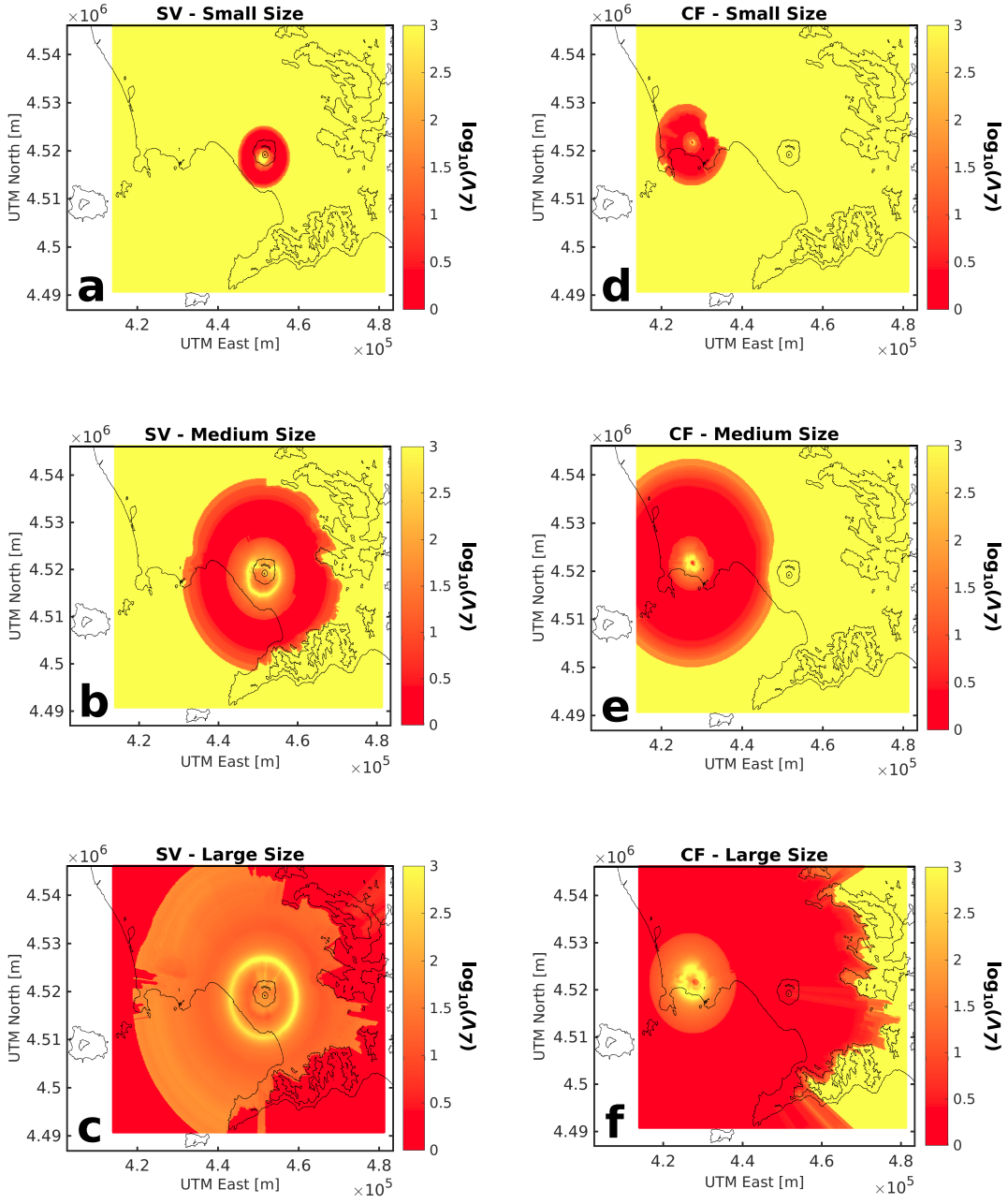

FIGURE 7.5: Examples of the spatial distribution of the equivalent number of data used to parameterize the Beta PDFs (there is one PDF per each grid point) for the Node 7 of the BET_VH model (Λ_7, see Table 7.2). The Λ_7 values displayed are computed by exploring theoretical uncertainty via the Energy Cone model (after [104]) for three eruption sizes and two volcanic systems (Somma-Vesuvius -SV- and Campi Flegrei -CF-, in Italy). The maps for Somma-Vesuvius (a,b,c) are based upon Energy Cone simulations starting from the current central crater of the volcano while those for Campi Flegrei (d,e,f) correspond to Energy Cone simulations starting from the closest vent position to the Astroni crater. See text for more details. From [105].

invasion, in a specific time window, from an eruption of any size and from any possible vent.

Nevertheless, in the case of Somma-Vesuvius, a qualitative comparison of our maps for the probability of PDC invasion in the next 50 years can be made with the PDC hazard assessments of [26] (based on past PDC deposits) and [307] (based on expert elicitation and numerical modeling of PDCs).
A comparison of Figure 7.2 with the most recent frequency map of PDC deposits around Somma-Vesuvius (Figure 6 in [26]) informs that the isoline enclosing the area having experienced at least 2 PDC arrivals in the last 22 kyr coincides approximately with the one with a mean probability of at least 1% in 50 years (Fig. 7.2c). By using our mean probability value, and assuming a Binomial PDF to model the arrival of PDCs (in n time windows) at a given grid point, the probability of observing at least 2 PDC arrivals in that area in 440 time windows of 50 years each (i.e. 22 kyr in total) is about 99%. Accounting for uncertainties both in our model and in the field data (e.g. possible incompleteness in the field observations), this crude comparison highlights that our mean probability values seem statistically consistent with the observed frequency of PDCs reported by [26].

On the other hand, if we compare our ensemble probabilities of PDC arrival (for any size and any vent, Fig. 7.2) with the 90% confidence interval provided by [307] for different sectors around Somma-Vesuvius (given an eruption of medium size or "Sub-Plinian 1" [89], Fig. 7.6a), we observe that the spatial pattern is similar: both the study of [307] and ours confirm the importance of Mount Somma in hindering PDC propagation towards the north. In terms of probability values, the comparison with Figure 7.2 is difficult because the study by [307] shows elicited probabilities conditional to the occurrence of a medium size eruption from the main crater, while we show absolute probabilities for the next 50 years from any kind of eruption (any size and vent). Nevertheless, our mean probability of PDC invasion beyond Mount Somma is between 4 and 6 %, which is about half the probability on the opposite southern flank, at a similar distance (between 10 and 12%, Fig. 7.2c,d). This spatial pattern is in agreement with the one for the elicited values by [307] (e.g. median probabilities of PDC invasion are around 90-95% over the southern, western and eastern flanks of the volcano but only 45% on the northern flank, beyond Mount Somma).
If we compare the results presented by [307] with the probabilities of PDC arrival,

given a medium-size eruption from the central crater, computed from our two end-member models for the collapse height, H_0 (Fig. 7.6), we note that the hazard assessment of [307] is somehow intermediate between the two end-member models. Thus, the 50%-probability points of the Exponential model (Fig. 7.6c) show a strong influence of the Mount Somma in hindering PDC propagation towards the north, similar to what proposed by [307], but maximum runouts a bit shorter than those presented by [307] for the same probability of PDC arrival (green lines, Fig. 7.6b). In contrast, the 50%-probability points of the Uniform model display maximum runouts that are closer to the ones given by [307] over the southern, western and eastern flanks of the volcano. On the northern flank, the probabilities of PDC arrival obtained with the Uniform model are not much influenced by the presence of Mount Somma (Fig. 7.6d), which is in disagreement with the hazard assessment of [307]. Nevertheless, it could be argued that, independently of the proportion of PDCs that are able to overcome the topographic barrier of Mount Somma (i.e. frequency of PDC arrival beyond it), the ones that actually propagate further northwards might reach maximum runouts that are not very different from the ones recorded over the southern flank (e.g. [155, 308]), hence the probabilities of PDC arrival for large (infrequent) PDCs are less constrained by the presence Mount Somma (Fig. 7.6c, d).

In the case of Campi Flegrei, we compare some of our partial results with the ones obtained by [33]. In particular, in Figure 7.7, we show the difference between the probability of invasion of PDCs, conditional to the occurrence of an eruption of any size from an inland vent of Campi Flegrei caldera, obtained by [33] and by our hazard assessment [105]. We show such difference for both end-member assumptions on the PDF for the collapse height: Exponential and Uniform (Fig. 7.7). It is seen that the differences with [33]:

- are always positive, implying that our method produces, sistematically, either comparable or smaller probabilities of PDC invasion;
- are particularly large over the Astroni crater and the Agnano plain (absolute values are up to ∼40% and ∼30% for the Exponential and Uniform H_0 models, respectively);
- are less significant along elevated areas (e.g. Posillipo hill) and the western sector of the caldera, especially in the case of the Uniform model for H_0.

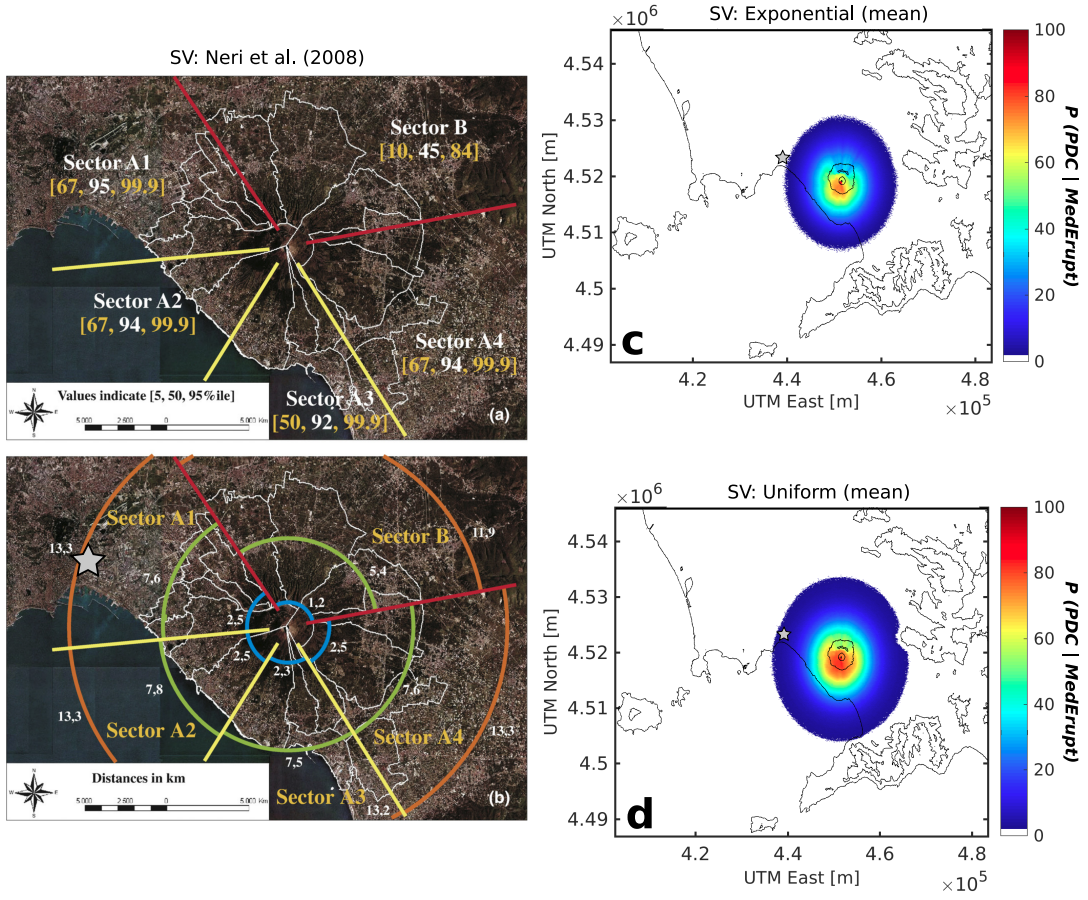

FIGURE 7.6: Qualitative comparison between the PDC hazard analysis carried out by Neri et al. (2008) at Somma-Vesuvius (SV) and part of the results derived from our study. (a): probability (in %) of PDCs invading each of the sectors displayed, given the occurrence of a sub-Plinian 1 eruption (e.g. [89]) from the central crater, according to the expert elicitation performed by [307]: the values in brackets indicate the 5^{th}, 50^{th} (median) and 95^{th} percentiles of the distribution built for such probability; (b) maximum-runout estimates (white numbers, in km) for PDCs generated during a sub-Plinian 1 eruption, according to [307]: blue, green and orange lines correspond, respectively, to probabilities of exceedance of 95%, 50% and 5% for the values of maximum runout on each sector; (c) probability of PDC arrival, given an eruption of medium size from the central crater ($P(PDC|MedErupt)$, in %), according to the Exponential model for H_0 presented in this chapter; (d) probability of PDC arrival, given an eruption of medium size from the central crater, according to the Uniform model for H_0 presented in this chapter. Gray star points to the downtown of Napoli. From [105].

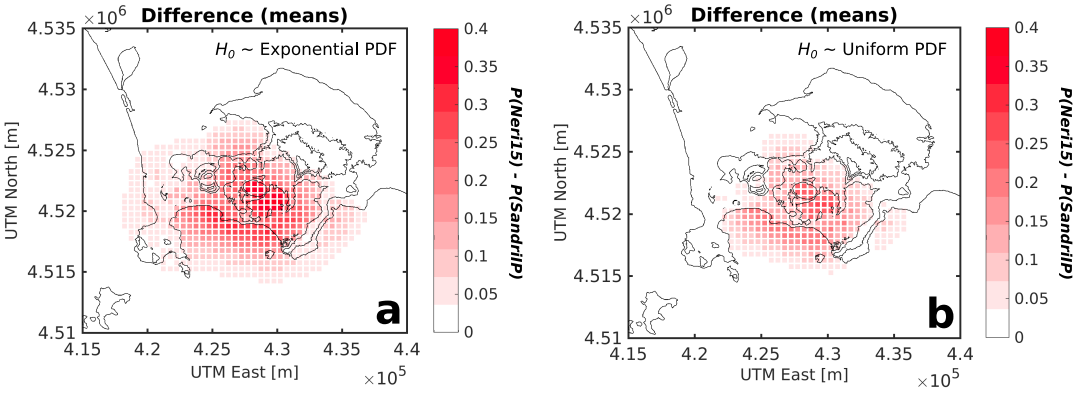

FIGURE 7.7: Differences in the mean probability of PDC arrival, conditional to the occurrence of an eruption from an inland vent at the Campi Flegrei caldera, computed by [33] minus that computed in this chapter [105]: Neri2015 - SandriIP (where IP means *in preparation*). Positive values (red) indicate that the probability of PDC arrival is greater in [33]. The differences are expressed in the unit interval: $[0, 1]$. (a) Exponential model for the collapse height (H_0); (b) Uniform model for the collapse height (H_0). See text for more details. From [105].

We interpret such differences as linked to one (or a combination) of the following causes, which may have led to an overestimation of the probabilities of PDC arrival presented by [33]:

1. The PDFs for the areas invaded by PDCs used by [33] to construct their probability maps (at least for the last 5 ka, i.e. our temporal range of study, e.g. [103]) are based upon eruptions that predominantly occurred in the central part of the inland sector of the caldera [25, 206]; however, the authors utilized the same PDF to simulate PDC invasion associated with any vent position along the whole (inland) caldera [33]; we argue that eruptions of the same scale as those that happened during the last 5 ka (III epoch) would have produced a different PDF of areas of PDC invasion depending on the location of each eruptive vent: in particular, for vents opening closer to the main caldera scarps, we might expect smaller areas to be invaded by PDCs.

2. The aforementioned PDFs for the areas of PDC invasion might suffer from under-recording, especially of small-size eruptions (e.g. [43]) that can leave minor, erodible PDC deposits (e.g. [9]); in this respect, we find interesting to observe that PDCs formed during many small eruptions at Campi Flegrei

have preserved maximum runouts comparable to the maximum runouts of PDCs formed during medium eruptions [103] (see Figure 5.5 in Chapter 5).

7.4.3 Multi-source volcanic hazard assessments

The PVHA for PDCs from both volcanoes (Fig. 7.4) may look similar to the one proposed by [292] (their Figure 1) or [293] (their Figure 5, a zoom on the city of Napoli). However, there are substantial differences with our work:

- here, we consider all possible eruption sizes and eruptive vents, combined through the total probability theorem, without selecting a reference size or scenario as in [292, 293], who, for example, selected a specific reference size (a VEI=4 for Campi Flegrei) or specific past eruptions (only the PDC deposits from the Avellino, 79 AD and 472 AD (Pollena) eruptions for Somma-Vesuvius)
- in our work, we produce a best-estimate map (based on the mean expected frequencies, or probabilities, that we compute) accompanied by percentile maps that express our degree of confidence on our best-estimate map (the so-called "doubly stochastic approach" by [33])
- our maps provide numerical values of probability of arrival in 50 years, that can be interpreted as expected frequencies, and can be used by decision-makers as input for rational decisional protocols (e.g. Cost-Benefit Analysis, [282, 309]) without any subjective discretization made by scientists; on the opposite, in [292, 293] the authors, which are scientists, dicretize the hazard maps in "Low", "Medium" and "High" hazard areas, which in turn is equivalent to decide thresholds (in probability) above which a given action should be taken to mitigate a risk (see e.g. the hazard-risk separation principle in [310]). This is clearly a decision that goes beyond the typical background and skills of volcanologists.

Chapter 8

Probabilistic Volcanic Hazard Assessment of dense PDCs from Somma-Vesuvius (Italy)

Abstract

Pyroclastic Density Currents (PDCs) are hot, very fast volcanic flows composed of gas and pyroclasts and densities which vary (even along a single flow) from tens to thousands of kg/m^3. Their capacity for destruction is by no means only relevant in terms of loss of life but PDCs are able to damage buildings and critical infrastructure in a severe way. Quantitative risk assessments of PDCs are commonly derived from scenario-based hazard analyses which clearly overlook the large aleatory and epistemic uncertainty associated with this volcanic hazard. In this work, we develop a three-steps procedure to address and quantify such uncertainties for dense pumice flows in a robust manner. The Titan2D model is first coupled with a method of polynomial expansion (Polynomial Chaos Quadrature) to assess aleatory uncertainty and, then, the obtained results are further merged with the Bayesian Event Tree for Volcanic Hazard (BET_VH) tool. The resulting hazard products are probabilistic hazard curves that indicate the probability of exceeding different values of dense-PDC variables such as flow depth and speed. The application of our procedure to Somma-Vesuvius (Italy) shows that high values of exceedance probability (40-70%) can occur on the first 2-3 km around the

current crater, for flow depths of 1 m and flow speeds of 2 m/s, when considering aleatory uncertainty only. Besides, relatively rare events (10% of exceedance probability) can create dense-PDCs overcoming speeds of 30 m/s over areas about 100 km^2 around the crater. Such events could entirely devastate the buildings in the proximal-medial sectors of Somma-Vesuvius, according to previous studies on the resistance of circum-Vesuvian buildings to PDC passage. Probabilistic hazard assessments of dense PDCs similar to the novel presented here can prove invaluable inputs to quantitative multi-hazard assessments and quantitative analyses of volcanic risk.

8.1 Introduction

Pyroclastic Density Currents (PDCs) are devastating phenomena that commonly occur at explosive volcanic systems. They are gravity-driven mixtures of gas and fragments of volcanic material (pyroclasts) that can travel at speeds up to few hundreds of m/s, reach temperatures of several hundreds of °C and exert dynamic pressures above 100 kPa (e.g. [6, 35, 124, 153]). Therefore, their potential for destruction is huge as it has been demonstrated in terms of major loss of life and property due to PDCs in recent historical times (e.g. [155, 157, 311, 312]). Loss of life is commonly related to impact of missiles carried by the current, extremely severe burns due to elevated temperature and varied respiratory damage owing to a combination of high temperatures, toxic gases and fine-particle concentration (e.g. [16, 155]). Destruction of infrastructure (collapse of buildings, for instance) is usually associated with high dynamic pressures, missiles impact and internal combustion of the building triggered by hot ash that penetrates when openings, such as doors and windows, are broken by PDCs (e.g. [311, 313]).

At Somma-Vesuvius (Italy), several studies have investigated the impact of PDCs on the buildings surrounding the volcano following diverse methodological approaches. [314] and [315] utilized the outputs from a multi-phase, 2D-axisymmetric PDC model (PDAC2D, [308, 316]), run to simulate an eruptive scenario similar to the 1631 AD eruption (e.g. [198]), to evaluate the possible impact of such PDCs on the buildings of different localities along the south flank of the volcano. The authors described the structure of diverse types of buildings and assessed their resistance to PDC passage by means of analytical methods and load-failure experiments. Some of the findings indicated that, given the specific scenario explored,

a low percentage of dwellings (∼7%) would be invaded by PDCs and, generally, expected damage to buildings should be irrelevant or light (e.g. [315]). [154] used new 3D simulations of surge-like (dilute) PDCs expected to occur during an eruption similar to the 1631 AD eruption [44] combined with deterministic and probabilistic analyses of the buildings' resistance to dilute PDCs to estimate the damage expected on different buildings according to specific values of dynamic pressure. According to the methodology, the percentage of collapsed buildings (for the weakest type of structure) can be above 50% from dynamic pressures of 6 kPa or greater. The percentage of collapsed buildings in the case of stronger structures could range from 5 to 80% [154]. Nevertheless, studies at other volcanoes seem to indicate that collapse is rather likely to occur above 3 kPa, even for dilute PDCs, because the building openings would tend to fail at these dynamic pressures (e.g. [313]) and internal combustion would promote the failure of the whole building (e.g. [311]).

An aspect that has been overlooked in volcanic risk assessments of PDCs at Somma-Vesuvius is the fact that PDC phenomenology can be quite variable both at the inter- and intra-eruption-size scales (e.g. [26, 144, 198, 232, 271]). This natural variability needs to incorporated into the hazard analysis of PDCs (e.g. [23, 31, 32, 33, 100]) for it is crucial to assess: (i) how likely the given scenario is (e.g. [61, 307]); and (ii) how likely the different points around the volcano are to be invaded by PDCs (e.g. [103, 104, 105], see Chapter 7).

In this work, we develop a three-stages methodology to improve the assessment of this natural variability (or aleatory uncertainty, e.g. [52]) in flow depth and speed of (dense) column-collapse PDCs at Somma-Vesuvius, Italy. We explore three different eruption sizes: small, medium and large (see Chapters 5, 6, 7). Besides, we also provide a quantification of epistemic uncertainty in the hazard analysis.
Our procedure is based on the combination of one physical simulator for dense PDCs (Titan2D, [218], see Chapter 4) and two uncertainty-quantification techniques: Polynomial Chaos Quadrature (PCQ) and Bayesian Event Tree for Volcanic Hazard (BET_VH, [49, 242], see Chapter 4). The merging of Titan2D and PCQ (first two stages) guarantees a robust quantification of aleatory uncertainty in dense-PDC propagation (e.g. [24]). Additionaly, coupling this assessment with the BET_VH model allows to: (1) quantify volcano-specific uncertainty (e.g. probability of eruption, vent-opening probabilities; see Chapter 7); and (2) provide a measure of epistemic uncertainty to the Titan2D-PCQ hazard analysis.

The strategy is equivalent to the one implemented by [105] for PDC arrival using the Energy Cone model coupled with Monte Carlo sampling and BET_VH (see Chapter 7). The main differences in this chapter are the following:

- The PDC model used here is more sophisticated and, thus, its runtimes are quite longer ($\sim$ 30-60 minutes per simulation, e.g. [82]). This makes Monte Carlo sampling unsuitable to quantify aleatory uncertainty via Titan2D so PCQ is utilized as the alternative (e.g. [24]).
- The epistemic uncertainty in BET_VH is not quantified through the Titan2D simulations (like it is done by [105]) but it is set according to general considerations about the modeling strategy (e.g. [19, 32, 100]).
- The governing equations of the Titan2D model are only applicable to a granular continuum that resembles the dense basal part of PDCs but not the upper dilute part (see Chapters 2, 4). Thus, the probabilistic hazard analysis presented in this chapter is only valid for dense PDCs while the one by [105] is justifiable, in principle, for both dense and dilute PDCs (see Chapters 4, 7).

Several novelties highlight our approach: (1) it is one of the first times that the Titan2D model is used to model pumice flows (e.g. [317]); (2) it is the first time that Titan2D and PCQ are combined with BET_VH to obtain both a robust quantification of aleatory uncertainty plus a measure of epistemic uncertainty (previous studies have whether computed just aleatory uncertainty through Titan2D and PCQ, e.g. [24], or calculated both aleatory and epistemic uncertainty but the former was quantified through a few Titan2D simulations, e.g [100]); and (3) it is the first time in a hazard analysis of dense PDCs that hazard curves and probability and hazard maps are explicitly computed for all the grid points over the hazard domain and different thresholds of the hazard variable of interest: dense-PDC depth and speed[1] (previous studies have focused on computing hazard curves at specific grid points and/or for a single threshold that leads to a *catastrophe*, e.g. [23, 31, 318]). We strongly believe that quantitative risk assessments of dense PDCs can largely benefit from our probabilistic hazard analysis and similar ones.

[1]We actually compute the maximum values of flow depth and speed recorded during each Titan2D simulation. Along the chapter, each time we mention these variables, we refer to their maximum values.

8.2 Methods

Our procedure developed to compute probabilistic volcanic hazard of dense PDCs at Somma-Vesuvius (Italy) can be divided into several steps: (i) parameterization of the initial conditions for the Titan2D simulations (the DEM used to run the model and the number and location of the initiation piles, see subsection 8.2.1); (ii) parameterization of Titan2D in terms of the type of dense PDCs simulated (dense-PDC volumes and friction angles, see subsection 8.2.2); (iii) propagation of the aleatory uncertainty in dense-PDC volume and bed friction angle into the Titan2D outputs (see subsection 8.2.3); and (iv) coupling of the quantification of aleatory uncertainty via Titan2D with the description of epistemic uncertainty provided by BET_VH (see subsection 8.2.4).

8.2.1 Titan2D initial conditions

The most important initial conditions to set up before running the Titan2D model are: the DEM utilized to run the simulator and the location (and number) of piles of material that act as the source of the dense PDCs. We briefly describe these two components in the following subsections.

Digital Elevation Model

The choice of the DEM can have a strong influence on the computed outputs as it has been demonstrated by several recent works (e.g. [84, 85, 319]). We select a 10m-resolution DEM with an associated altimetric error of about ±5 m. The DEM was produced by the Italian *Ministero dell'Ambiente* as an update of a previous DEM (constructed by the Italian *Istituto Geografico Militare*) of 20 m of horizontal resolution (±10 m of altimetric error) derived from the isolines of altitude and topographic landmarks of the 1:25,000 maps of the Italian territory. This update to the 10m DEM consisted of adding breaklines (detailed point-sequences in a topographic survey) and new topographic landmarks to the ones utilized to build the precedent DEM product.
The horizontal resolution we use is in the range proposed by [319] (5-10 m) to obtain accurate results when running Titan2D. Moreover, we deem the 10m DEM as a suitable elevation model in our particular application to Somma-Vesuvius

because: (1) the flow volumes that we simulate tend to be relatively big (especially for medium and large eruptions, see subsection 8.2.2) and the outputs of this kind of flows have been found to be less sensitive to the DEM resolution [85]; and (2) the topography of Somma-Vesuvius is not very rough[2] so, again, the impact of the DEM resolution (and the altimetric errors associated) should have a smaller effect on the Titan2D outputs [84].

Starting piles

The location (and number) of the piles of material has also a major effect on the outputs of the Titan2D model. Single-pile simulations are usually preferred when the scope is to model Block-and-Ash Flows formed by the collapse or explosion of a lava dome (e.g. [27, 41, 82]). Given that these collapses or explosions may trigger dense PDCs with different azimuths of initial spreading, the aleatory uncertainty in the initiation azimuth needs to be accounted for (e.g. [31, 82]). In our case, we simulate dense PDCs that are formed by the collapse of an eruption column. Therefore, we assume that radial spreading of dense PDCs away from the volcanic source is likely to occur at Somma-Vesuvius (see Chapter 5). In particular, we take the present central crater of the volcano as the volcanic vent because its probability of opening is much greater than that of other vents along the volcanic edifice (e.g. [68, 103, 104, 105, 321]). In addition, we simulate the radial collapse of the eruption column by means of 8 piles (elliptic cylinders) of material distributed over the external rim of the central crater (Fig. 8.1). Our assumption is that the dense basal part of the generated PDCs forms immediately after the collapsing mass of gas and pyroclasts hits the ground. This may be representative of approximately short collapses, such as in boiling-over events, but it might not be the case when PDCs are formed from tall collapses dominated by fine particles (e.g. [133]).

The piles are arranged around the Somma-Vesuvius crater as to cover its whole external rim, the centers of the ellipses oriented towards the 8 principal cardinal directions from the approximated geometrical center of the crater (Fig. 8.1). The dimensions of these ellipses (185 m, 135 m of major and minor axes, respectively) are chosen with the same purpose and avoiding significant superpositions among the piles. The orientation of the major axis of each ellipse is set tangent to the crater rim. Finally, the piles are left to collapse under their own weight once the

[2]Terrain roughness can be computed from the standard deviation of the slope or the altitude, the planimetric-to-surface area, etc., e.g. [320]

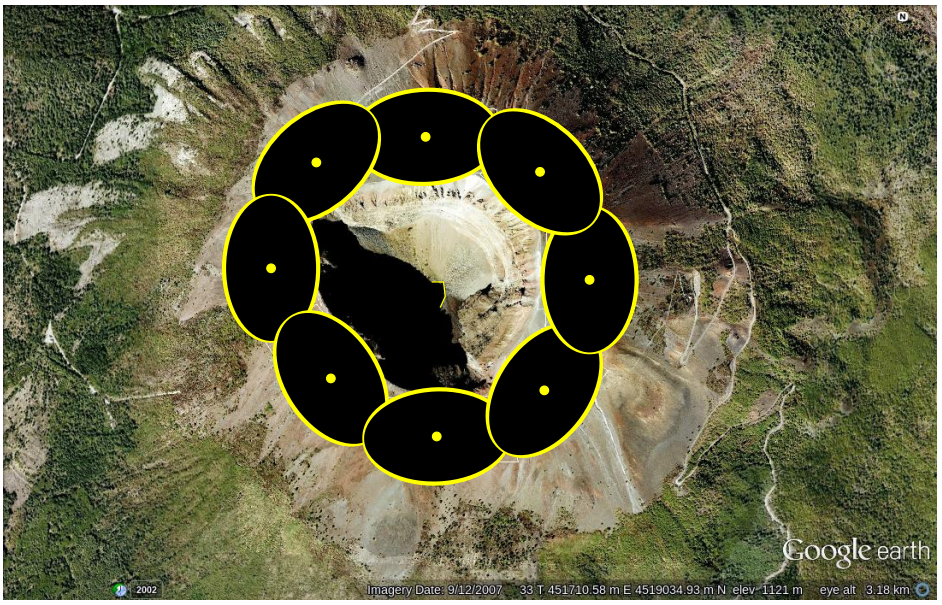

FIGURE 8.1: Set up of the elliptic cylinders (piles) of material used to run the Titan2D simulations aimed at describing the generation of dense PDCs from column collapse at Somma-Vesuvius (Italy). The surface ellipses of all piles have the same dimensions: $[R, r] = [185, 135]$ m, where R and r are the major and minor axes of each ellipse, respectively. The centers of the ellipses are displayed as yellow dots. See text for more details. Source: Google, DigitalGlobe, October 8, 2013. From [107].

Titan2D simulation starts. That is, we do not introduce any lateral initial speed or azimuth of propagation for the simulated dense PDCs. The initial velocity is only vertical and it is determined by the collapse height (i.e. the height of each elliptic cylinder). All piles share the same height and, hence, the same dense-PDC volume (see next subsection 8.2.2). After the initial collapse, the modeled dense PDCs flow away from the source according only to the topography they encounter as they propagate.

8.2.2 Dense-PDC volumes and friction angles

The Titan2D parameters that serve to define the typology of the simulated dense PDCs are primarily the following (see Chapter 4): (1) the volume of released material (V_0); (2) the bed friction angle (ϕ_{bed}); and (3) the internal friction angle (ϕ_{int}). The outputs of Titan2D are not very sensitive to the value of the internal friction angle (e.g. [222]) unless the dense PDCs propagate through narrow and deep gullies. Therefore, it is common practice to set ϕ_{int} to a fixed value and

explore different values of the bed friction angle. Generally, it is assumed that 30° is a representative value for dry granular materials (e.g. [27, 41, 224, 233]) and we use this value for ϕ_{int}. For the other two model parameters (V_0, ϕ_{bed}), we use values compiled from past dense PDCs and hot avalanches at Somma-Vesuvius. Similarly to the hazard analyses described in Chapters 5, 6 and 7, we focus on three eruption sizes: small (comparable to VEI≈3), medium (comparable to VEI4) and large (comparable to VEI≥5). The eruptions that we select to inform the Titan2D parameterization for each size are the following: the 1822 AD (e.g. [303]) and 1944 AD eruptions (e.g. [193, 268]) for the small size; the Pollena (e.g. [144, 269]) and 1631 AD eruptions (e.g. [198, 270]) for the medium size; and the Mercato (e.g. [271]) and Pompeii eruptions (e.g. [272]) for the large size.

PDFs for PDC volume and bed friction

Given our setup for the starting piles detailed in subsection 8.2.1, the volume of material released during each simulation of Titan2D (V_0) is defined only by the height of each elliptic cylinder. In reality, we define the parameter space for V_0 and then we calculate the pile height that corresponds with each volume of dense-PDC. The volume V_0 is partitioned equally among the 8 piles that surround the crater of Somma-Vesuvius. For example, if $V_0 = 8 \cdot 10^6$ m^3, then each pile has a volume of $V_0^p = 10^6$ m^3, where the superscript p denotes the common volume for each single pile. Given the common major and minor radii of each pile ($[R, r] = [185, 135]$ m), the common pile height (h_0^p) is calculated as: $h_0^p = V_0^p / \pi R r$ ($\sim$ 13 m in the example).

To model the aleatory uncertainty in V_0 we define Uniform PDFs for the variable, one per each eruption size previously described. Even though previous studies have used PDFs with monotonically-decreasing probability as V_0 increases (e.g. [23, 24]), these studies dealt with single-event BAFs, not with column-collapse dense PDCs. Besides, we simulate whole-eruption volumes (e.g. [33]), for the medium and large eruption size, because it is very difficult to extract single-event volumes for dense PDCs at the Somma-Vesuvius stratigraphic record (e.g. [144, 269, 271]). Given the scarcity of data at our target volcano (5 eruptions; there is no volume data for the 1822 AD eruption) and, to our knowledge, the complete absence of data about the possible distribution of volumes for dense PDCs generated by column collapse[3], we consider that a first step in modeling the aleatory uncertainty

[3]For instance, data in [138] refer to total PDC volumes, not to dense-PDC volumes.

in the volumes of such dense PDCs may be to use an uninformative distribution like the Uniform PDF (e.g. [49, 68]).

The lower and upper limits of the Uniform distributions are reported in Table 8.1 and are selected as follows: (1) for the small size, we take the volumes of single hot avalanches reported by [193] during the 1944 AD eruption; (2) for the medium and large sizes, we take the volumes of whole-eruption PDCs reported by [26] for the eruptions of each size; and, finally, (3) for the medium and large sizes, we apply a correction to account for the fact that, with Titan2D, we are modeling dense-PDC volumes and not total PDC volumes: we assume that the ratio $\delta_V = V_{\text{PDCdense}} : V_{\text{PDCdilute}}$ might range from 0.01 to 1, the lower bound being calculated from the actual value of δ_V measured from the preserved PDC deposits of the Pollena eruption [144, 269].

TABLE 8.1: Shape parameters of the selected Uniform Probability Density Functions (PDFs) for dense-PDC volume (V_0; V_0^p indicates the volume of each pile) and bed friction angle (ϕ_{bed}). min, max: lower and upper limits of the Uniform PDFs. From [107].

	V_0 [10^6 m^3]: Uniform PDF				**ϕ_{bed} [deg]: Uniform PDF**	
Eruption Size	min V_0	max V_0	min V_0^p	max V_0^p	min ϕ_{bed}	max ϕ_{bed}
Small	0.18	1.15	0.02	0.14	13	30
Medium	2.01	390	0.25	48.8	5	30
Large	2.31	831	0.29	104	5	25

Regarding the bed friction angle (ϕ_{bed}), we also choose Uniform PDFs for the three eruption sizes explored. This is justified by the scarcity of data available at Somma-Vesuvius but also by the fact that world-wide data on PDC mobility (e.g. [138], $\phi_{\text{bed}} \sim \text{atan}(\Delta H/L)$) are not fully incompatible with the Uniform distribution [103]. Thus, while ϕ_{bed} values for dense and dilute PDCs formed by column collapse (i.e. pumice flows) may not have been sampled from a Uniform PDF, these ϕ_{bed} values for the group of pumice flows together with hot avalanches as well as for groups of pumice flows separated according to eruption size may have actually been sampled from such a distribution [103]. Nonetheless, it is also important to stress that such measures of PDC mobility [138] are usually calculated from deposits of dense plus dilute PDCs.

Previous probabilistic hazard assessments of dense PDCs (BAFs, specifically) based on Titan2D simulations have used: (a) fixed values of ϕ_{bed} (e.g. [23]); (b) ϕ_{bed} that is distributed following a Uniform PDF (e.g. [24]); or (c) ϕ_{bed} that is stochastically correlated to the value of PDC volume (e.g. [31]), that is: the bed friction angle and the PDC volume are modeled as inversely correlated (e.g.

[131, 138, 234, 267]) but the specific correlation function is taken as uncertain and explored within the probabilistic hazard analysis.

In our parameterization of the Uniform PDFs for ϕ_{bed} at Somma-Vesuvius, we derive the lower and upper limits of the distributions for each eruption size from data compiled for the aforementioned eruptions at our target volcano (e.g. [26, 193, 198, 270, 303]). The specific values of bed friction angle are reported in Table 8.1. For large eruptions, despite some PDC deposits having $\phi_{\text{bed}} < 5°$, we set the limit of the Uniform PDF at $\phi_{\text{bed}} = 5°$. This is due to the fact that, around and below this value, the thin-layer problem becomes especially acute and the Titan2D outputs may show unrealistic jumps during dense-PDC propagation (e.g. Fig. 4A in [225]).

8.2.3 Aleatory-uncertainty propagation

The aleatory uncertainty in dense-PDC generation by column collapse at Somma-Vesuvius is described by the Uniform PDFs of V_0 and ϕ_{bed} previously reported. In order to propagate this aleatory uncertainty into hazard footprints of dense PDCs, we utilize the Titan2D model combined with Polynomial Chaos Quadrature (PCQ, see Chapter 4). The greatest assumption of our methodology, necessary to ensure the convergence of the PCQ procedure, is that the two uncertain model parameters are independent of each other. This assumption has been made in previous studies (e.g. [24]) but it is thought to be generally incorrect (e.g. [31, 131]). However, we argue that, as recent works have demonstrated, the tendency of large-volume PDCs to have smaller ϕ_{bed} values is clear from PDC deposits of many volcanoes taken as a whole (e.g. [131]) but it may be not so evident when considering ϕ_{bed} values for individual volcanoes (e.g. [234]). In the case of Somma-Vesuvius, we have four eruptions with pumice flows[4] and this makes very hard to extract any relationship between the two variables that is applicable, specifically, to our target volcano. Moreover, the log-log correlation between PDC volume and ϕ_{bed} described by several authors (e.g. [131, 234, 267]; and displayed in Figure 8.2 for pumice flows in [138] (plus the data for Somma-Vesuvius) implies that the influence of the PDC volume on the bed friction angle is very important for small values of PDC volume (Fig. 8.2B and [234]) but it is less crucial as PDC volume increases. In particular, we observe that similar ϕ_{bed} values (about 10-20°) occur for PDCs that

[4]The data that we have for the 1944 AD eruption [193] are related to hot avalanches, not pumice flows.

have volumes ranging 1-2 orders of magnitude (Fig. 8.2B). We do acknowledge the general correlation of PDC volume and ϕ_{bed} (i.e. more voluminous PDCs tend to be more mobile) in the definition of the model parameter space for each eruption size (colored boxes, Fig. 8.2) but we explore all combinations of the two model parameters within each eruptive size. In the light of the data available [138], and considering the large uncertainties that may affect these estimations (e.g. ϕ_{bed} estimates for pumice flows require to know the collapse height but, typically, this can be, at best, approximately inferred: [132, 213]); we consider that our model parameter spaces, based upon the eruptive history of Somma-Vesuvius, are still compatible with published data on PDC mobility.

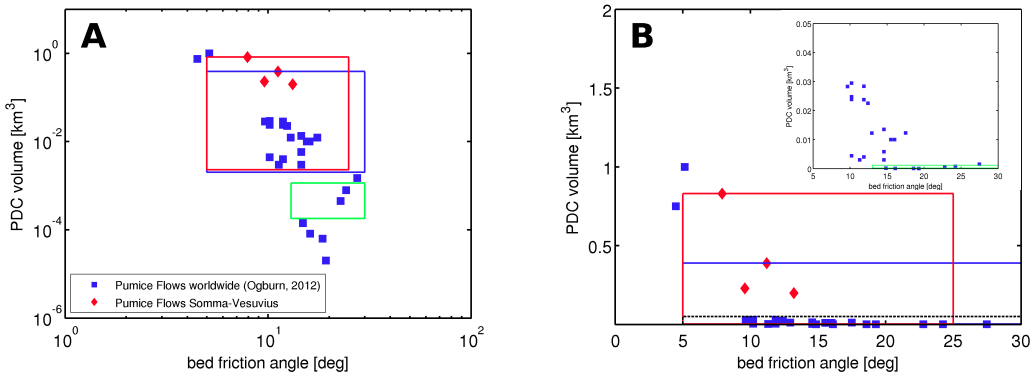

FIGURE 8.2: Pumice-flow data for bed friction angle ($\phi_{\text{bed}} \sim \text{atan}(\Delta H/L)$) and PDC volume in [138] and some eruptions at Somma-Vesuvius (Mercato [322], 1631AD [198, 270], Pollena [144, 269], and Pompeii [272]). A: plot in log-log scale that shows a roughly linear relationship between the variables (e.g. [234]). B: plot in linear-linear scale that evidences how the influence of PDC volume on ϕ_{bed} is stronger for low PDC volumes rather than for high PDC volumes. Colored boxes indicate the model parameter space that we explore in this chapter, for each eruption size: small (green), medium (blue) and large (red). The dashed-black box in B indicates the location of the inset displayed on the upper-right part of the plot. See text for more details. From [107].

The PCQ procedure we implement to propagate aleatory uncertainty from the Titan2D parameters into hazard footprints of dense PDCs is based on the following steps (see Chapter 4):

1. Select the quadrature points according to the joint PDF of V_0 and ϕ_{bed} (we select 64 quadrature points along the model parameter space).

2. Run the Titan2D model with parameter values corresponding to each quadrature point.

3. Calculate the coefficients of the PCQ polynomials, at each grid point over the hazard domain, according to the Titan2D outputs from each simulation.

4. Sample the obtained polynomial expression that links model-parameter values and model outputs through Monte Carlo sampling (sample size = 10^4).

5. Calculate exceedance probabilities from these samples for different output variables, specifically: flow depth and speed.

6. Repeat step 5 with different thresholds of the output variables to obtain hazard curves at each grid point over the hazard domain.

During the simulation stage (step 2), we apply a stopping-time criterion modified after [233]. We find that the stopping time proposed by [233] is quite dependent on the value of ϕ_{bed} utilized in the simulation (Fig. 8.3).

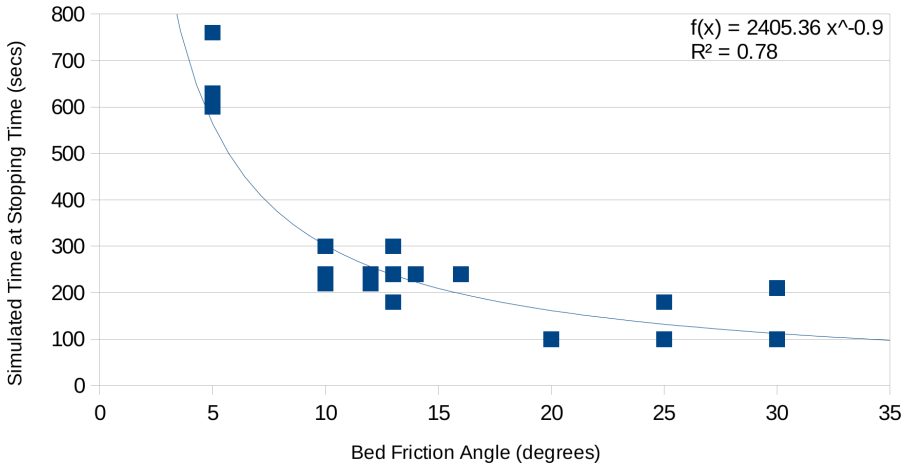

FIGURE 8.3: Power-law relationship between the stopping time defined by [233] and the bed friction angle (ϕ_{bed}) extracted from some Titan2D simulations, performed with calibration purposes, at Somma-Vesuvius (Italy). See text for more details. From [107].

We preliminarly fit a power-law function to quantify this dependence:

$$t_{\text{stop}} = 2405.36 \cdot \phi_{\text{bed}}^{-0.9} \tag{8.1}$$

where t_{stop} is the stopping time computed with equation 19 in [233]. Thus, we set the simulation time of each run to match the t_{stop} value derived from equation 8.1. A more sophisticated statistical model, which incorporates data from several

volcanoes and links t_{stop} with bed friction angle, PDC volume and time of collapse, is now under development [108].

8.2.4 BET_VH parameterization

The methodology described in the previous section allows us to quantify the aleatory uncertainty in column-collapse dense-PDC propagation at Somma-Vesuvius, given the occurrence of an eruption of a specific size from the current central crater of the volcano. However, this hazard analysis does not provide the probability of occurrence for each eruption size or the probability of PDCs occurring as a result of an eruption of each size (e.g. [21]). In addition, the epistemic uncertainty is not assessed by any means. To overcome these two limitations, we couple the Titan2D-PCQ hazard assessment with the BET_VH. The result is a probabilistic hazard assessment of dense PDCs at Somma-Vesuvius, given the occurrence of an eruption from the central crater of the volcano.
The nodes 5 (eruption size) and 6 (hazardous phenomena) of BET_VH are parameterized in the same way as in Chapter 7. In nodes 7-8, we use the hazard curves obtained with Titan2D and PCQ to set the best-estimate parameters in the BET_VH model. We set the number of equivalent data (λ, e.g. [49, 68]) to: $\lambda = 20$. This choice is intermediate between assuming that the Titan2D-PCQ assessments are very uninformative (in which case $\lambda = 1$) and assigning a high degree of confidence to the assessments (in which case $\lambda \geq 50$ may be used; e.g. [76]).

8.2.5 Final probabilistic hazard products

The use of the Titan2D model allows to compute probabilistic measures of the two hazard (or output) variables previously mentioned. Consequently, three valuable hazard products can be derived: (1) probability maps; (2) hazard maps; and (3) hazard curves. The first type of map displays the probability of exceedance of a given threshold of the output variable over the hazard domain. They can also simply display the probability of arrival of the hazardous phenomenon (e.g. [33, 103, 104]). The second type of map displays the severity of the hazard, in terms of the values of the output variable (i.e. intensity measure), over the hazard domain, for a given threshold of probability of exceedance. This definition applies

to probabilistic hazard analyses. Sometimes, hazard maps can be constructed for eruptive scenarios so the probability of the hazardous event is not considered but the hazard severity expected for such scenario is shown (e.g. [41, 44]). Finally, hazard curves are the synthetic probabilistic expression of probability maps and (probabilistic) hazard maps (e.g. [23, 53, 70, 76]). They are bivariate graphs showing, for a given grid point: on the x-axis, the severity of the hazard, typically in units of the intensity measure (e.g. meters for dense-PDC depth); and, on the y-axis, the exceedance probability for each value of the output variable (see subsection 8.3.1). If a line parallel to the y-axis (and starting from a given value, i.e. threshold, of the output variable) is drawn, its intersection with the hazard curve will indicate a value of exceedance probability corresponding to the threshold. If hazard curves are available at each grid point over the hazard domain, as in the work we present here, then a value of exceedance probability can be extracted for each grid point and a probability map is obtained (see 8.3.3).
On the other hand, if a line parallel to the x-axis (and starting from a given value, i.e. threshold, of exceedance probability) is drawn, its intersection with the hazard curve will indicate a value of the output variable expected to be overcome with probability equal to the threshold. By calculating the value of the output value corresponding to the aforementioned probability threshold at each grid point over the hazard domain, a hazard map can be computed (see 8.3.2).

8.3 Results

We divide the main findings derived from our probabilistic hazard assessment of dense PDCs at Somma-Vesuvius (Italy) into three categories (see section 8.1): (i) hazard curves; (ii) hazard maps; and (iii) probability maps. For each of these categories, we describe the results obtained for two output variables of Titan2D: flow depth and flow speed.

8.3.1 Hazard curves

Hazard curves are the basic hazard product extracted from our probabilistic assessment. Actually, the other hazard products (hazard and probability maps) are built from the information contained in the hazard curves (Figs. 8.4, 8.5).
For each grid point across the hazard domain, we provide a best-estimate (mean)

hazard curve (solid lines in Figures 8.4, 8.5), which is a complete description of the aleatory uncertainty; and alternative hazard curves (e.g. dashed lines in Figures 8.4, 8.5), which give a measure of the dispersion around the best-estimate curve and are a description of epistemic uncertainty (e.g. [53, 70, 76]). In Figures 8.4 and 8.5, we display such hazard curves at three selected locations and for two dense-PDC variables: flow depth and speed, respectively. These locations are: (1) Torre Annunziata (TA), southwards from the central crater; (2) San Sebastiano al Vesuvio (SSaV), westwards from the central crater; and (3) Somma Vesuviana (SoVe), northwards from the central crater.

Maximum flow depth

The values of flow depth recorded around Somma-Vesuvius range from very low values (close to 0 m) up to flow depths greater than 3 m. In particular, the exceedance probability for a flow depth of 3 m is around 4% and 8% at TA and SSaV, according to the mean hazard curve (Fig. 8.4). This probability is very small in the case of SoVe. On the other side of the plots, we observe that the (mean) probability of flow depths close to 0 m to be exceeded ranges from 7% (at SoVe) to 25% (at SSaV), approximately. Taking into account the epistemic uncertainty, the same probabilities range, respectively, from ∼12% and ∼38% (in the 90th-percentile hazard curve) to ∼1% and ∼11% (in the 10th-percentile hazard curve, Fig. 8.4). The general shape of the hazard curves is quite continuous and the strongest changes in the slope of the curves occur over low values of flow depth.

Maximum flow speed

The values of flow speed recorded around Somma-Vesuvius can be greater than 30 m/s. The mean exceedance probabilities of such values of flow speed are below 5% for all the example locations, however (Fig. 8.5). Similarly to what observed in the case of flow depth, the values of flow speed, from highest to lowest, tend to be recorded at SSaV, TA and SoVe, respectively, the latter being located beyond the topographic barrier of Mount Somma. Nonetheless, we notice that the exceedance probabilities of high flow speeds are more similar at SSaV and TA than in the case of high flow depths at these two locations (Figs. 8.4, 8.5). In other words, thick flows are quite more probable to occur at SSaV than at TA but, in terms of flow speed, fast flows are similarly probable to occur at both locations.

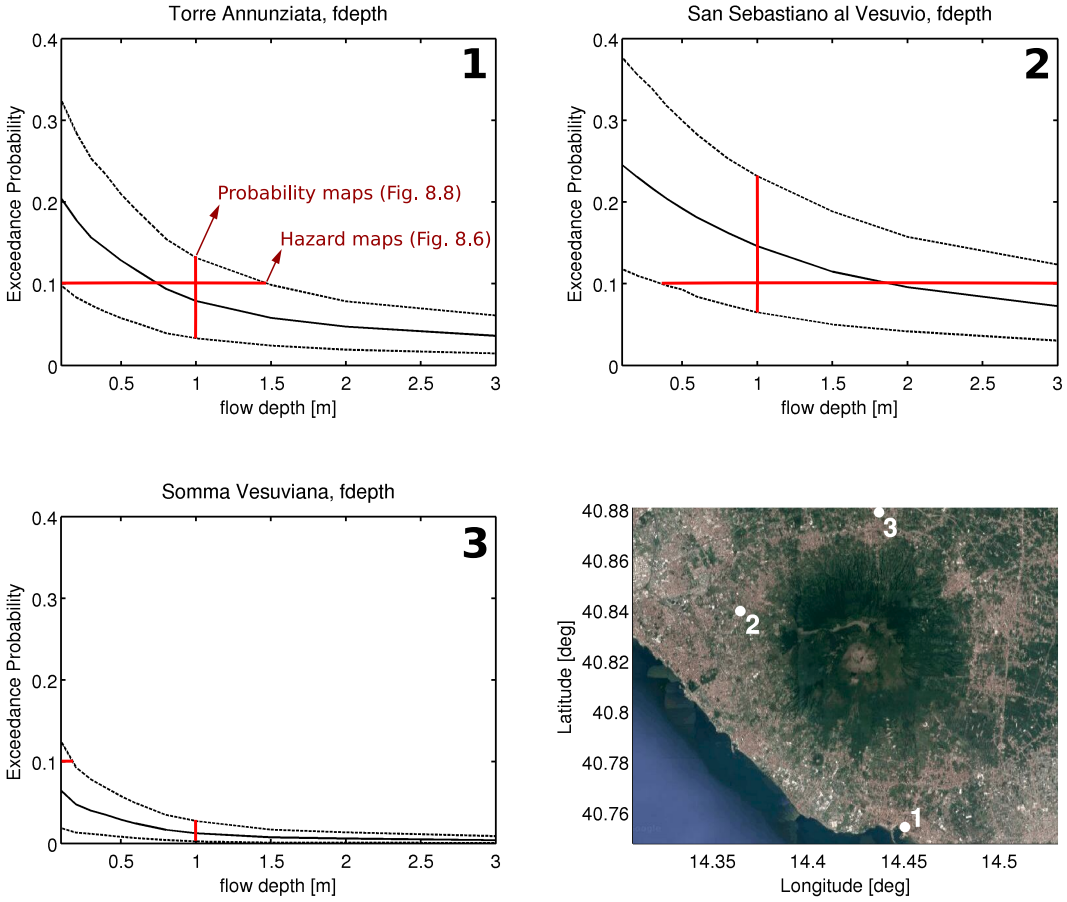

FIGURE 8.4: Examples of hazard curves for the flow depth of dense PDCs at Somma-Vesuvius (SV, Italy), computed from the merging of Titan2D simulations with quantification of uncertainty performed via PCQ and the BET_VH model. The curves display the values of flow depth against the probability that each value of the variable is exceeded, given an eruption from the central crater of Somma-Vesuvius. Solid lines denote the best-estimate (mean) hazard curve while dashed lines indicate the 10th-percentile (lower bound) and 90th-percentile (upper bound) hazard curves. The hazard and probability maps in Figures 8.6 and 8.8, respectively, are obtained by "cutting" (see red lines) the hazard curve of each grid point over the hazard domain. The locations of the hazard curves displayed in this figure (1, 2, 3) are given in the bottom-right inset and are the same as in Figure 9.11 (see Chapter 9). Source: Google, DigitalGlobe, March 1, 2017. From [107].

The exceedance probability for dense PDCs with zero speed is 24%, 26% and 21% at TA, SSaV and SoVe, respectively, according to the mean hazard curve. In the case of the 90th-percentile hazard curve, these probabilities are ∼38%, 40% and 34%, respectively. This implies that, given an eruption of any size happening at the central crater of Somma-Vesuvius, the probabilities of no dense PDCs reaching the example locations are 76%, 74% and 79%, for the mean hazard curve, and 62%, 60% and 66%, for the 90th-percentile hazard curve (Fig. 8.5).
The hazard curves for flow speed generally show the steepest slopes over low values of flow speed while these curves are relatively flat over high values of flow speed, similarly to what related about the flow-depth hazard curves. However, in the (mean) flow-speed hazard curves, there is a break-in-slope at about 5 m/s, 8 m/s and 10 m/s for SoVe, TA and SSaV, respectively. This indicates a moderate-strong decrease in the frequency of arrival of fast dense PDCs with respect to slow dense PDCs at the three example locations (Fig. 8.5).

8.3.2 Hazard maps

Hazard maps are built from the hazard curves at each grid point of the hazard domain. As an illustrative example, we set and show a threshold of exceedance probability along these curves (10% in our case), the values of flow depth or flow speed associated with such threshold can be extracted for each grid point (Figs. 8.4, 8.5). Thus, hazard maps display these values over the hazard domain (Figs. 8.6, 8.7). Given that we quantify aleatory and epistemic uncertainty, there is not only one hazard map available (e.g. mean hazard map) but a set of many hazard maps can be analyzed. In Figures 8.6 and 8.7 we show the mean, 10th-percentile and 90th-percentile hazard maps, plus a zoomed section of the mean hazard map, for the two aforementioned output variables.

Maximum flow depth

In terms of flow depth, the main spatial pattern shows dense PDCs that primarily spread over the southern flank of Somma-Vesuvius and reach their maximum runouts along a SW azimuth from the central crater. Part of this dense-PDC spreading is simulated over seawater, especially in the case of the 90th-percentile hazard map, Fig. 8.6B), and this is a situation that Titan2D does not model [218].

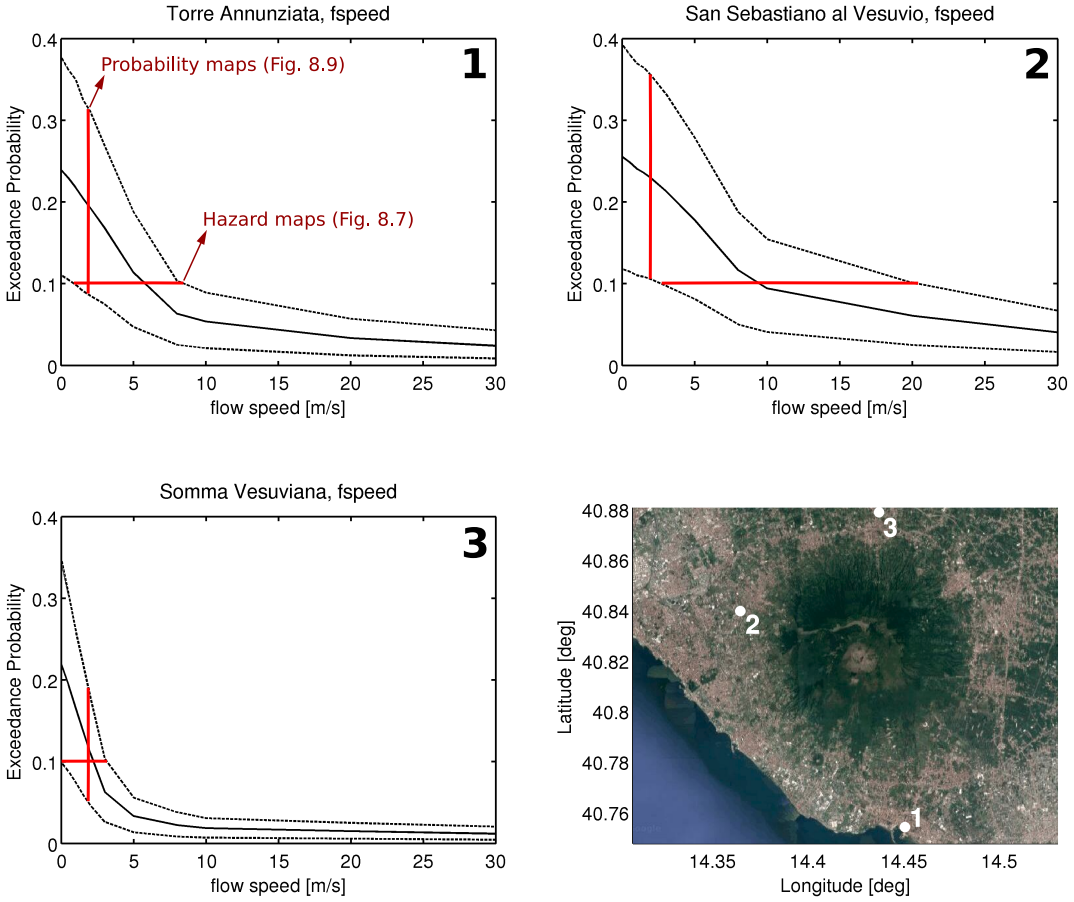

FIGURE 8.5: Examples of hazard curves for the flow speed of dense PDCs at Somma-Vesuvius (SV, Italy), computed from the merging of Titan2D simulations with quantification of uncertainty performed via PCQ and the BET_VH model. The curves display the values of flow speed against the probability that each value of the variable is exceeded, given an eruption from the central crater of Somma-Vesuvius. Solid lines denote the best-estimate (mean) hazard curve while dashed lines indicate the 10th-percentile (lower bound) and 90th-percentile (upper bound) hazard curves. The hazard and probability maps in Figures 8.7 and 8.9, respectively, are obtained by "cutting" (see red lines) the hazard curve of each grid point over the hazard domain. The locations of the hazard curves displayed in this figure (1, 2, 3) are given in the bottom-right inset and are the same as in Figures 8.4 (this chapter) and 9.11 (see Chapter 9). Source: Google, DigitalGlobe, March 1, 2017. From [107].

The lateral extension of dense PDCs towards the south and southeast is also considerable while towards the east and west is more limited (Fig. 8.6). Towards the north, the shortest runouts are recorded and, in the case of the 10th-percentile hazard map (Fig. 8.6A), very few dense PDCs are able to surmount the Mount Somma and propagate further northwards. Note that all the hazard maps in Figure 8.6 refer to an exceedance probability of 10%. If this threshold is set to, say, 60%, the hazard maps will show a much more limited extent. For instance, according to the mean hazard curves (Fig. 8.4), we expect extremely-thin dense PDCs to be overcome in 60% of the eruptions from the central crater at the three example locations. However, we expect dense PDCs with flow depths of ∼1.9, 0.8 and close to zero, to be overcome in 10% of the eruptions from the central crater at SSaV, TA and SoVe, respectively (Fig. 8.4).

In the zoomed section of the mean hazard map, we observe how the occidental sector of Mount Somma seems quite inefficient in blocking dense PDCs with high flow depths, at least for the selected threshold of exceedance probability (10%). The central and oriental sectors of this topographic barrier are more effective in blocking the passage of dense PDCs, although it is also noted that some channels on the north flank of the volcano are able to deliver relatively-thick flows up to the base of the flank, approximately (Fig. 8.6). The lobate morphology of the iso-flow-depth points (see, for instance, the yellow points: flow depth $\sim$ 2 m) stresses the influence of topographic features of several scales (such as small scoria cones, remnants of volcanic-edifice collapses, irregular valleys, etc.) on the dense-PDC propagation simulated by Titan2D.

Maximum flow speed

The hazard maps of flow speed show an approximately rectangular pattern with fast dense-PDCs reaching rather long distances towards the south, with respect to the east and west, and shorter distances towards the north (Fig. 8.7). The latter, however, are comparable to the distances reached by fast dense-PDCs towards the east and west, in particular for the mean and 90th-percentile hazard maps. In the mean hazard map, dense PDCs reaching the sea coast can have flow speeds of 10-20 m/s, for an exceedance probability of 10% (Figs. 8.5, 8.7). Regarding the 10th-percentile hazard map, high flow speeds are restricted to the southern flanks and the area beyond the occidental sector of Mount Somma (Fig. 8.7a). Nonetheless, for all the hazard maps displayed, areas of ∼100 km^2 (or larger)

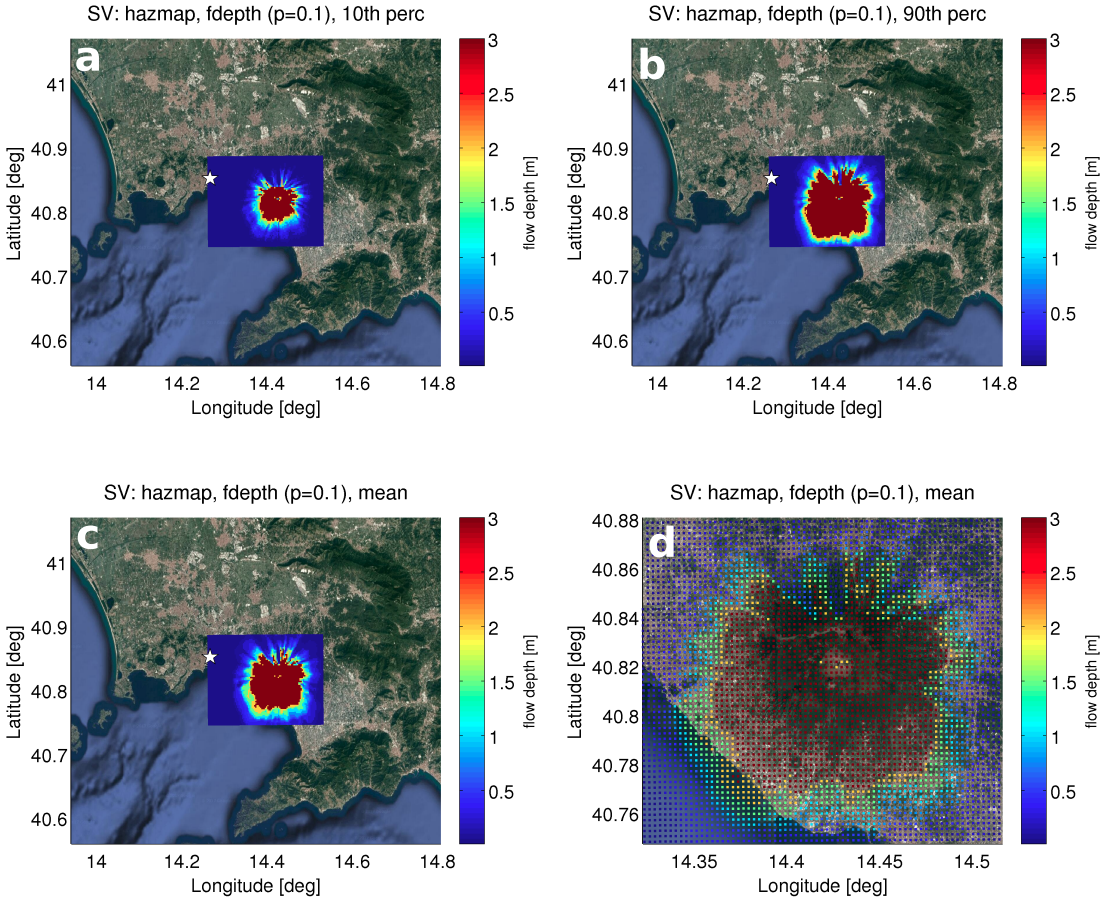

FIGURE 8.6: Hazard maps for dense PDCs, with an exceedance probability of 10%, at Somma-Vesuvius (SV, Italy), computed from the merging of Titan2D simulations with quantification of uncertainty performed via PCQ and the BET_VH model. The maps display the values of flow depth (fdepth, in meters), at each grid point over the hazard domain and given an eruption from the central crater of Somma-Vesuvius, that correspond to the aforementioned threshold of exceedance probability. The white star denotes the downtown of the city of Napoli. Different graphs show the best estimate (mean, inset c -d is a detail of it, centered at the Somma-Vesuvius crater-) for these values of flow depth as well as their dispersion: (a) 10th percentile (perc); and (b) 90th percentile. See text for more details. Source: Google, DigitalGlobe, March 1, 2017. From [107].

around Somma-Vesuvius are covered by flow speed values equal to or greater than 30 m/s.

The homogeneity in the distribution of high flow speeds, even over the northern flank beyond Mount Somma indicates that, notwithstanding this topographic barrier can hinder the occurrence of thick flows over the north flank of the volcano (Fig. 8.6), these dense PDCs can still reach high speeds (Fig. 8.7). In the zoomed section of the mean hazard map, it is seen that only the centermost sector of Mount Somma acts as a really efficient barrier for fast dense PDCs (again, given an exceedance probability of 10%). The lobate morphology of the hazard maps for flow depth is less evident in the case of flow depth. Thus, this variable seems not very sensitive to topographic features of small to medium scale while it is only slightly influenced by large topographic features such as Mount Somma.

8.3.3 Probability maps

Probability maps are built from the hazard curves at each grid point of the hazard domain. As an illustrative example, we set and show a threshold for the output variable of interest along these curves (flow depth = 1 m and flow speed = 2 m/s, in our case), the values of exceedance probability associated with such thresholds can be extracted for each grid point (Figs. 8.4, 8.5). Thus, probability maps display these values over the hazard domain (Figs. 8.8, 8.9). Given that we quantify aleatory and epistemic uncertainty, there is not only one probability map available (e.g. mean probability map) but a set of many probability maps can be analyzed. In Figures 8.8 and 8.9 we show the mean, 10th-percentile and 90th-percentile probability maps, plus a zoomed section of the mean probability map, for the two aforementioned output variables.

Maximum flow depth

The probability maps for the (dense-PDC) flow depth are strongly different depending on the hazard curve they are built from. The 10th-percentile probability map shows that the probabilities of exceeding 1 m of flow depth are well below 50% over the vast majority of the hazard domain (Fig. 8.8a). Only the crater area and the central sector of the calderas' floor (mainly shaped as a result of the Mercato and Pompeii eruption, e.g. [89, 196]) display values of probability around

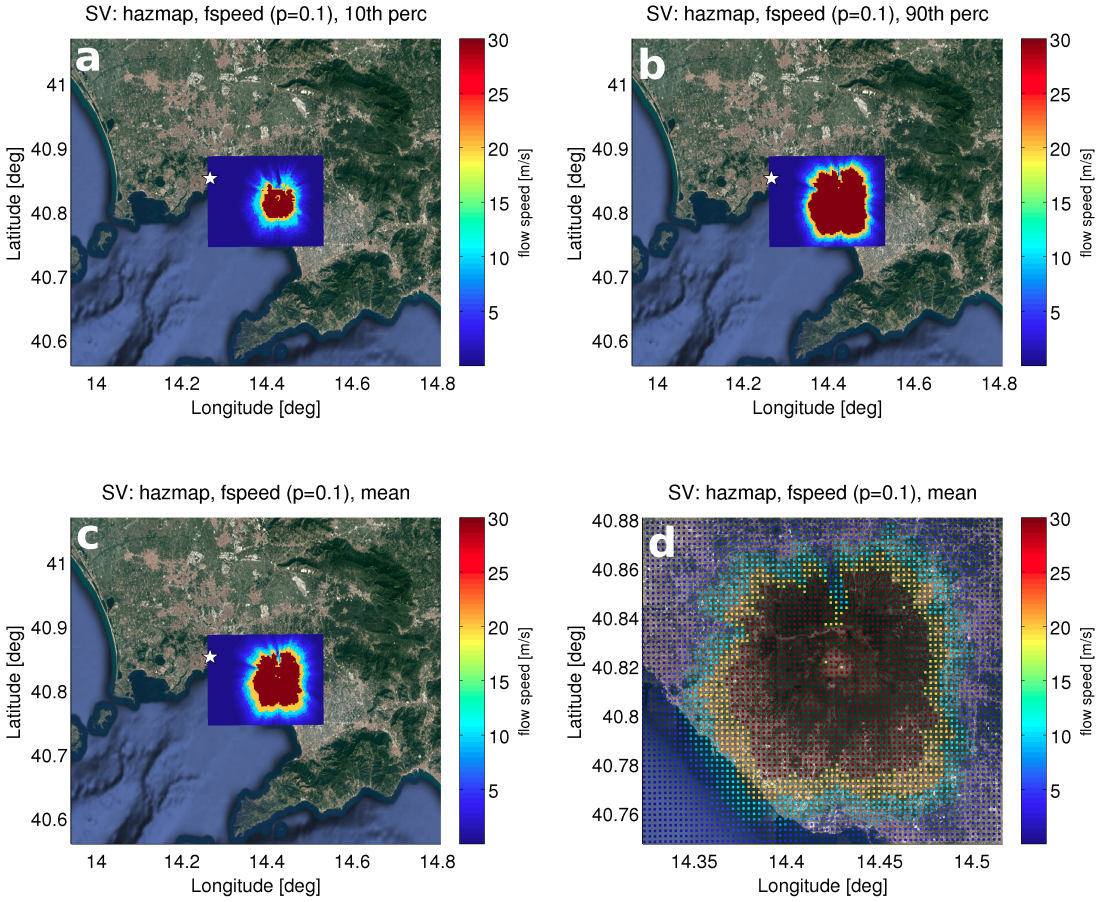

FIGURE 8.7: Hazard maps for dense PDCs, with an exceedance probability of 10%, at Somma-Vesuvius (SV, Italy), computed from the merging of Titan2D simulations with quantification of uncertainty performed via PCQ and the BET_VH model. The maps display the values of flow speed (fspeed, in meters per second), at each grid point over the hazard domain and given an eruption from the central crater of Somma-Vesuvius, that correspond to the aforementioned threshold of exceedance probability. The white star denotes the downtown of the city of Napoli. Different graphs show the best estimate (mean, inset c -d is a detail of it, centered at the Somma-Vesuvius crater-) for these values of flow speed as well as their dispersion: (a) 10th percentile (perc); and (b) 90th percentile. See text for more details. Source: Google, DigitalGlobe, March 1, 2017. From [107].

40-50%. The rest of the volcanic edificed is covered by values of exceedance probability about 20%. In the mean probability map, exceedance probabilities of 40 to 60% are observed over an area that involves the central and, partially, the western sectors of the calderas' floor (the latter sector formed by the Pomici di Base and Avellino eruptions, e.g. [196]). The preferred propagation axis towards the SW and SSE, identified in the hazard maps, is also evidenced by the mean probability map (Fig. 8.8c,d). The effect of Mount Somma in hampering dense-PDC propagation towards the northern sector of the volcano is clear, especially in the mean and 90th-percentile probability maps. Nonetheless, the potentiality of a certain percentage of dense PDCs to overcome Mount Somma and be channelized through some valleys along the north flank is also noticed (Fig. 8.8). On the whole, the colored countours of the probability maps may seem more spiked than those of the hazard maps but the limits of the former (pale blue colors) are rather similar to that of the hazard maps (Figs. 8.6, 8.8).

Maximum flow speed

The probability maps for flow speed are characterized by sharp discontinuities in the exceedance probability between the most proximal sectors (crater area and calderas' floor) and the medial sectors of the volcano (Fig. 8.9). This is consistent with the break-in-slope observed in the hazard curves for flow speed at the three example locations (Fig. 8.5). Dense PDCs with speeds equal to or greater than 2 m/s do not seem to travel further than 8 km, approximately. The highest exceedance probabilities are around 40-60% for the 10th-percentile probability map, 50-70% for the mean probability map, and 70-100% for the 90th-percentile probability map. Outside from the proximal sectors, the exceedance probabilities show small and/or gradual changes for each of the aforementioned maps; respectively: ∼20%, ∼20-30% and ∼40-50% (Fig. 8.9).

The homogeneity in the values of flow speed between the areas beyond Mount Somma and areas over other flanks of the volcano that is noted in the hazard maps of flow speed, can be identified in the probability maps as well. Thus, values of exceedance probability about 35% are present on the eastern and western flanks but also on the northern flank, beyond Mount Somma. Nevertheless, the sharp drop in exceedance probability between points just south of Mount Somma and just beyond the topographic barrier is very significant (Fig. 8.9). It appears that

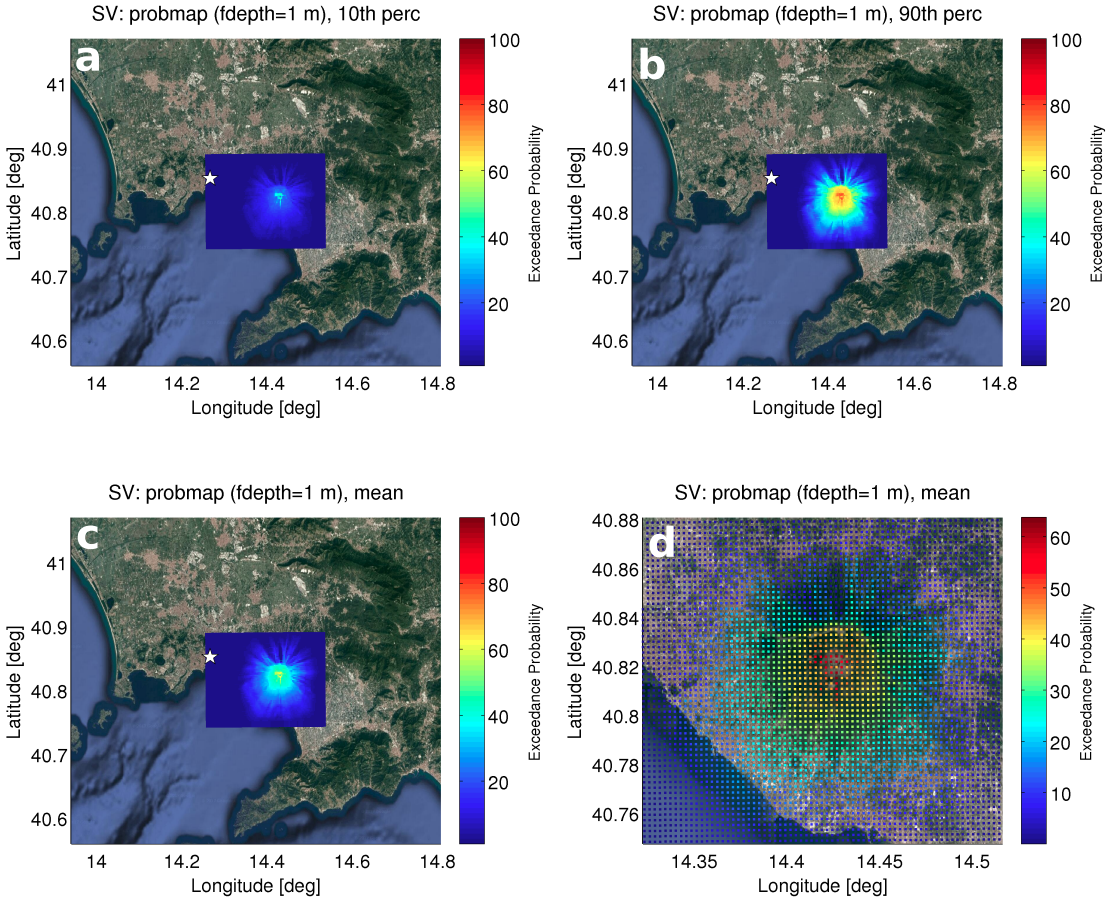

FIGURE 8.8: Probability maps for dense PDCs, with 1 m of flow depth (fdepth), at Somma-Vesuvius (SV, Italy), computed from the merging of Titan2D simulations with quantification of uncertainty performed via PCQ and the BET_VH model. The maps display the exceedance probabilities (in percentage), at each grid point over the hazard domain and given an eruption from the central crater of Somma-Vesuvius, that correspond to the aforementioned threshold of flow depth. The white star denotes the downtown of the city of Napoli. Different graphs show the best estimate (mean, inset c -d is a detail of it, centered at the Somma-Vesuvius crater; note the different colorbar scale-) for these probabilities as well as their dispersion: (a) 10th percentile (perc); and (b) 90th percentile. See text for more details. Source: Google, DigitalGlobe, March 1, 2017. From [107].

this decrease in exceedance probability (for dense PDCs with speed = 2 m/s) is approximately constant (∼30%) for the three maps displayed in Figure 8.9.

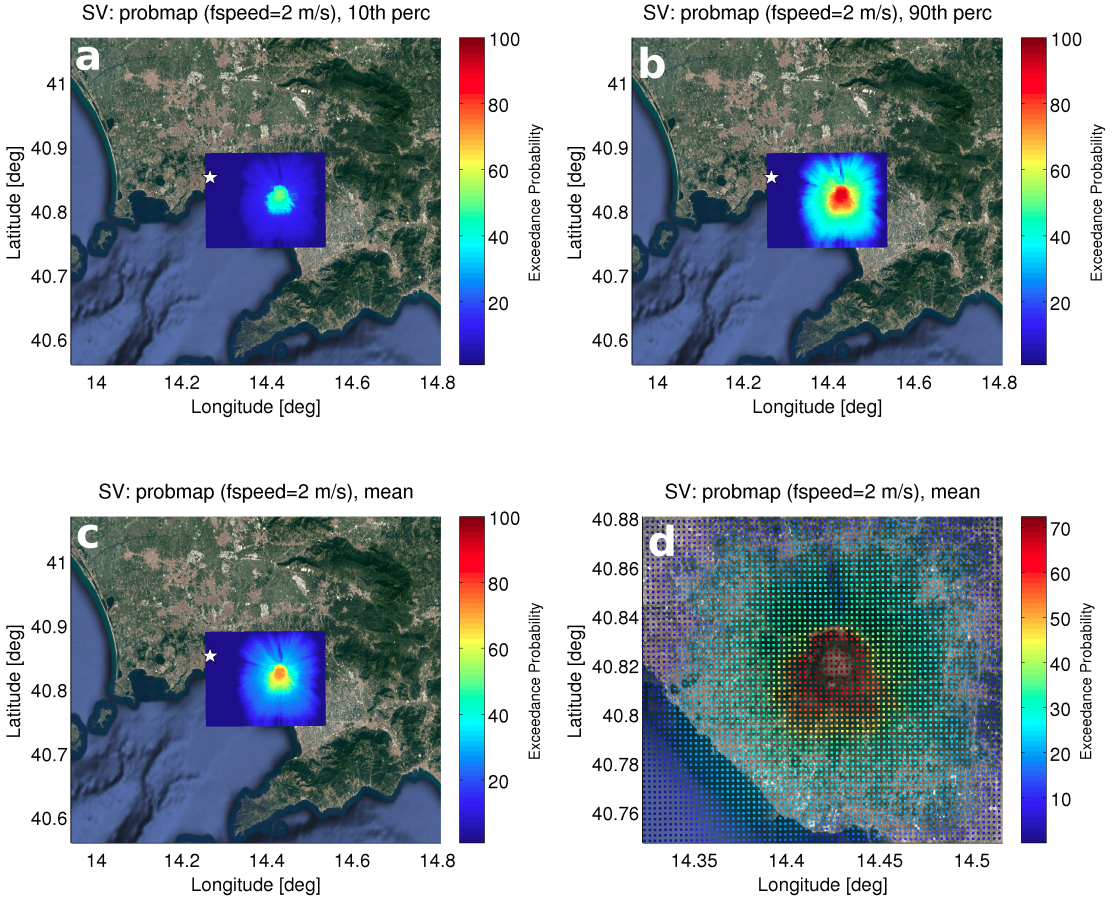

FIGURE 8.9: Probability maps for dense PDCs, with 2 m/s of flow speed (fspeed), at Somma-Vesuvius (SV, Italy), computed from the merging of Titan2D simulations with quantification of uncertainty performed via PCQ and the BET_VH model. The maps display the exceedance probabilities (in percentage), at each grid point over the hazard domain and given an eruption from the central crater of Somma-Vesuvius, that correspond to the aforementioned threshold of flow speed. The white star denotes the downtown of the city of Napoli. Different graphs show the best estimate (mean, inset c -d is a detail of it, centered at the Somma-Vesuvius crater; note the different colorbar scale-) for these probabilities as well as their dispersion: (a) 10th percentile (perc); and (b) 90th percentile. See text for more details. Source: Google, DigitalGlobe, March 1, 2017. From [107].

8.4 Discussion

The three-step procedure presented in this chapter allows us to obtain a comprehensive and homogeneous probabilistic hazard assessment of dense PDCs, formed

by column collapse, at Somma-Vesuvius (Italy). Such a probabilistic assessment is extremely rare in the literature of any type of PDC (e.g. [31, 33, 100, 206]). We consider that the strenghts of our results in comparison to previous works are the following: (1) the aleatory uncertainty is quantified in a robust manner through the PCQ procedure (e.g. [100] ran few Titan2D simulations to properly quantify the aleatory uncertainty); (2) epistemic uncertainty and volcano-specific information are incorporated via the BET_VH model ([31, 33] also quantify the epistemic uncertainty although through different strategies); (3) the whole merging of Titan2D-PCQ-BET_VH allows to compute hazard curves for different dense-PDC variables and diverse thresholds of these variables (e.g. the hazard analysis by [33] can only calculate the probability of PDC arrival while that of [31] focuses on just one threshold of flow depth).

8.4.1 Structural damage expected around Somma-Vesuvius

According to our results, very extensive damage is expected to occur around Somma-Vesuvius when we consider a "standard" threshold of exceedance probability (e.g. 10% for probabilistic seismic hazard assessment [290]). Thus, maximum flow speeds of even 30 m/s may occur over an area of ~ 80 km^2 around the present crater, on average, in 1 out of 10 eruptions (e.g. mean hazard map, Fig. 8.7c,d). If we take the density of these dense PDCs as $\sim 1,250$ kg/km^3 [269], it implies that dynamic pressures greater than 500 kPa could occur associated with that threshold of exceedance probability. These values are two orders of magnitude bigger than most of the thresholds for building collapse defined in vulnerability and risk analyses at Somma-Vesuvius (e.g. [154, 314, 315, 323]).
If a threshold of dense-PDC speed is set at 2 m/s (thus, dynamic pressure is approximately 2.5 kPa), we observe that the mean probability of exceedance related to such dense-PDCs is equal to or greater than 50% only over the calderas' floor, approximately (Fig. 8.9). Nonetheless, exceedance probabilities greater than 20% cover a large area around the volcano. In this case, the threshold of dynamic pressure would correspond to the collapse of only the weakest buildings located in the area around Somma-Vesuvius (e.g. [323]).

Even though our probabilistic hazard analysis might overestimate the mean hazard of dense PDCs (we use whole-eruption PDC volumes, see next subsection 8.4.2), it does not seem in disagreement with the study of [44] which, at Somma-Vesuvius,

has been typically used as the unique hazard reference to estimate building vulnerability and, generally, quantitative volcanic risk from PDCs (e.g. [154, 323, 324]). The hazard analysis of [44] is based upon a few eruptive scenarios for surge-like PDCs. Specifically, the values of dynamic pressure computed by [44], for the most representative scenario (corresponding to our medium-size eruptions), are about 1-70 kPa. The spatial distribution of these values shows a clear discontinuity that delineates the calderas' floor quite precisely (Fig. 13 in [44]).
In our probabilistic hazard analysis, values of dynamic pressure equal to or greater than 2.5 kPa are very likely ($\sim 50\%$[5]) over an area quite similar to the aforementioned.

Two main aspects can be derived from the comparison of our hazard analysis and that of [44]. On the one hand, the PDAC model used by [44] is more suited to simulate the surge-like (dilute) member of PDCs while the Titan2D model is applicable to the other (dense) end-member of PDCs [218]. This has strong implications for the comparison of the two evaluations of dynamic pressure because the mean flow densities of dilute PDCs at Somma-Vesuvius can be two orders of magnitude smaller than mean flow densities of dense PDCs (e.g. [269]). This implies that dilute PDCs must reach flow speeds around 10 times bigger than dense PDCs to cause dynamic pressures that are comparable between them. On the other hand, the spatial distribution of the discontinuity in dynamic-pressure values in [44] could indicate that PDAC simulations respond more faithfully to topography (in this case to the flat surface of the calderas' floor) than the Titan2D model (e.g. Fig. 8.9). The accuracy in describing topography interactions that can be gained through 3D physical models of PDCs is pointed out by the same authors [44]. They show how the effect of Mount Somma in hindering PDC propagation towards the north is well captured with the 3D model (PDAC) but not with a previous 2D version of it [325]. Nevertheless, the use of PDC models with runtimes in the order of days is not compatible with the assessment of probabilistic volcanic hazard for this phenomenon (e.g. [23, 28, 31]).

Our hazard assessment highlights the paramount importance of developing volcanic hazard assessments that address and quantify, at least, the aleatory variability of the hazardous process (e.g. [49, 53, 54]). We contend that scenario-based hazard assessments can be useful to analyze particular hazardous situations: for

[5]Note that, given the coupling of the Titan2D-PCQ assessment with BET_VH, we are also modeling the probability of PDCs occurring, given an eruption of each eruption size. This probability is not 1, especially in the case of small eruptions (see Chapter 7).

instance, whether a sub-Plinian I eruption at Somma-Vesuvius [89] can or cannot generate surge-like PDCs that are able to substantially overcome the topographic barrier of Mount Somma (e.g. [44]). However, structured probabilistic hazard assessments can provide a global view on the aleatory variability (and epistemic uncertainty) that goes beyond the view of single eruptive scenarios (e.g. [49, 70, 326]).

8.4.2 Epistemic uncertainty in modeling dense PDCs via Titan2D

Epistemic uncertainty in volcanic (and natural) hazards can arise from several different sources (e.g. [75]). Each of them needs to be quantified separately in order to understand its specific impact on the simulator outputs (e.g. [327]). In addition, the relevance of a given source of epistemic uncertainty (e.g. input uncertainty, primarily linked to the quality of the DEM used in the simulations) can depend on the volcanic system studied (e.g. [84]) and/or on the values of other model parameters (e.g. [85]). It may also be expected that different PDC models, such as Titan2D and the Energy Cone, do show different sensitivity to the same source of epistemic uncertainty (e.g. input uncertainty). Thus, Titan2D seems much more sensitive to input uncertainty (e.g. [84, 85, 86, 319]) than the Energy Cone model (e.g. [104]), at least in the volcanic systems analyzed.
Therefore, a comprehensive assessment of not only aleatory variability but also different sources of epistemic uncertainty can be very useful to: (1) check which sources of epistemic uncertainty mostly control the output of the PDC model; and (2) prioritize future research in trying to reduce them.

Concerning the Titan2D model, several sources of epistemic uncertainty have been demonstrated to exist (e.g. [318]). Following the classification presented by [104] (adapted from [75], see Chapter 6), we can define:

- **Input uncertainty**: tt was initially explored by [86, 319] and then quantified in a more structured way by [84, 85].
- **Parametric uncertainty**: different PDFs have been explored to model Titan2D parameters such as V_0 and ϕ_{bed}. For V_0, PDFs from Uniform (e.g. [24, 107]) to Pareto distributions (e.g. [23]) have been used. For ϕ_{bed}, [24]

used a Uniform distribution while [31] proposed a PDF that is derived from the PDF selected for V_0. That is, the authors model the theoretical uncertainty (see next item) by defining ϕ_{bed} in terms of V_0 in a way that the higher V_0, the smaller ϕ_{bed} (e.g. [131, 234, 267]). In Figure 8.10, we explore the implications that deriving the PDF for ϕ_{bed} from the PDF V_0 (by using a formula that links the two parameters) may have. We check that the PDF for ϕ_{bed} tends to resemble that of V_0 if the latter is approximately symmetrical around the mean (Fig. 8.10A,D). However, if the PDF for V_0 is strongly asymmetric, then the PDF for ϕ_{bed} is approximately a specular reflection of the former (Fig. 8.10B,C). Other studies have considered other distributions for $\text{atan}(\Delta H/L) \sim \phi_{\text{bed}}$ of dense and dilute PDCs such as the Gaussian PDF (e.g. [103, 136]) or the asymmetric Tukey PDF (e.g. [104]).
Parametric uncertainty in the Titan2D model is also related to the choice of the stopping time for each simulation (e.g. [41, 233]).

- **Theoretical uncertainty**: V_0 and ϕ_{bed} have been modeled as they were correlated (e.g. [31]) or independent (e.g. [24]). We note that theoretical uncertainty not only arises from the type of possible correlation (positive, negative, none; e.g. [104]) but also from the specific form of the correlation function (e.g. [31]).

- **Structural uncertainty**: its quantification can be challenging so only preliminary assessments have been performed so far, by comparing the model predictions with data from past PDC deposits (e.g. [86, 225]).

In this chapter, we do not explicitly model the different sources of epistemic uncertainty, as other recent studies have done (e.g. [31, 84, 85]). However, we do include a measure of epistemic uncertainty through the parameterization of the BET_VH model (see subsection 8.2.4). Given that few studies have quantified epistemic uncertainty in volcanic hazard assessments performed with Titan2D and none of them has provided a ranking or quantitative comparison between the impact of different sources of epistemic uncertainty (e.g. [104]), it is difficult to ensure whether our quantification of epistemic uncertainty does or does not capture the effect of this uncertainty on the Titan2D outputs. Likewise, we cannot assert that the sources of epistemic uncertainty that we try to reduce in our hazard analysis (e.g. input and, partially, parametric uncertainty) are very important, as important as other sources, or relatively unimportant (e.g. [104]).

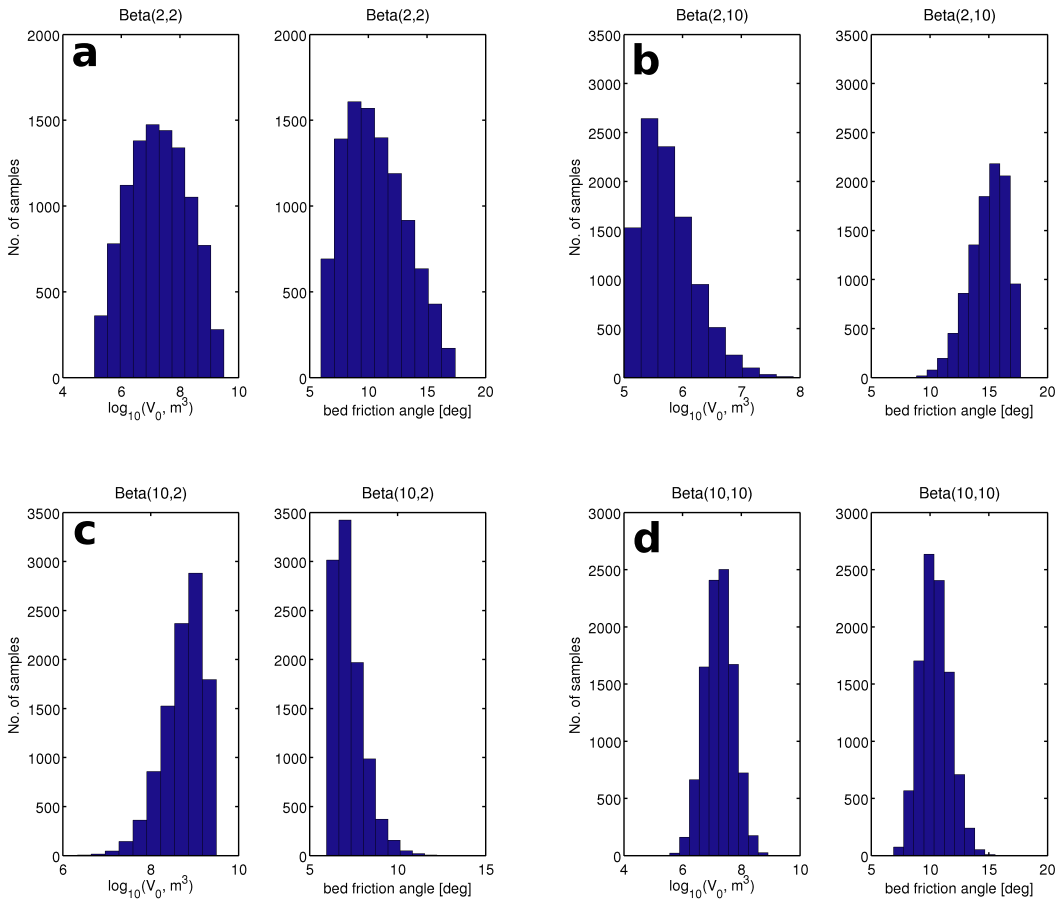

FIGURE 8.10: Examples of the links between the PDFs of V_0 and ϕ_{bed} according to the function presented by [31]: $\phi_{\text{bed}} = \text{atan}(exp(a + b\text{log}V))$. We use $a = 0.1047$ and $b = -0.2490$ (i.e. approximately the median used by [31]), and $log_{10}(V_0, \text{m}^3 \in [5, 9.5]$. Depending on the PDF selected for the V_0 variable, the PDF of ϕ_{bed} is fixed by the relationship between the variables. We randomly sample 10^4 values from different PDFs for V_0 and calculate 10^4 values for ϕ_{bed} by applying the aforementioned formula. (a) Beta distribution with $\alpha = \beta = 2$; (b) Beta distribution with $\alpha = 2$, $\beta = 10$; (c) Beta distribution with $\alpha = 10$, $\beta = 2$; (d) Beta distribution with $\alpha = \beta = 10$. From [107].

In the following, we detail the implications that each source of epistemic uncertainty may have for modeling dense-PDC hazard through Titan2D and how our choices can be relevant for our specific probabilistic hazard assessment of dense pumice flows.

Input uncertainty should not represent an issue for our hazard analysis because: (1) the DEM resolution is high enough (10 m, e.g. [319]); (2) the dense-PDC volumes simulated tend to be large (e.g. [85]); and (3) the study area does not have an extremely rough topographic surface (e.g. [84]).

Concerning parametric uncertainty, we do not explore the influence of using different PDFs for the model parameters: V_0 and ϕ_{bed}. This influence has not been quantified in previous studies so we do not know how much it could affect to the Titan2D outputs. In the case of Energy Cone model, it has been seen that some choices for these PDFs might not result in big changes of the model outputs (e.g. [104]). However, if the PDFs are very different from each other (e.g. Exponential and Uniform PDFs), the impact on the probabilistic hazard assessment can be quite significant (e.g. [105], see Chapter 7). Therefore, more research is needed to properly assess the parametric uncertainty related to the choice of PDFs to model aleatory uncertainty, especially in the case of Titan2D where the specific choice for ϕ_{bed} may modify the model outputs to a great extent (e.g. [27, 222, 225]).
As regards the stopping time of the Titan2D simulations, it is usually overlooked as a source of parametric uncertainty (e.g. [23, 31]). The criterion, presented by [233], to select the stopping time can be very useful to reduce this parametric uncertainty and it has been applied in subsequent works (e.g. [41]). Yet, the results obtained during some calibration tests of Titan2D at Somma-Vesuvius (Fig. 8.3) seem to indicate that there is a strong link between the value of the stopping time, according to [233] criterion, and the value of ϕ_{bed}. In order to reduce this parametric uncertainty, we set up the stopping time of our Titan2D simulations before running them, according to the calculated correlation. Not taking into account this aspect, could result in significant changes in the simulated maximum runouts and areas invaded by dense PDCs. For example, let us assume that we set the stopping time to 200 seconds for all the simulations. Those simulations with low ϕ_{bed} would be stopped about 400 to 550 seconds before the stopping criterion of [233] is met (Fig. 8.3). If we hypothesize that the flow front advances at an average speed of 1 m/s during these 400-550 seconds, the underestimation in the dense-PDC runout could be of 0.4-0.55 km, approximately. In terms of invaded area, the underestimation will depend on the shape and size of the flow-front envelope.

As concerns theoretical uncertainty, we assume that V_0 and ϕ_{bed} are independent, internally to each eruption size analyzed. Previous studies have also assumed this independence between the model parameters (e.g. [24]) and, to our knowledge, there is no probabilistic hazard analysis, performed with Titan2D, that has analyzed eruption sizes separately. Nevertheless, when taking all the eruption sizes as a whole, our simulation setup does approximately follow the inverse correlation between V_0 and ϕ_{bed} that has been recognized at other volcanoes worlwide (Fig. 8.2; [31, 131, 234, 267]). Therefore, we argue that our methodology is not

incompatible with this correlation. Moreover, the selected model parameter space for each eruption size is symmetric with respect to the available data on V_0 and ϕ_{bed} [138] (Fig. 8.2A) so we do not expect our probabilistic hazard assessment to be particularly biased towards overestimating or underestimating the hazard footprints of dense pumice flows, at least in terms of the correlation between these model parameters. We do anticipate, however, that our hazard footprints will be an overestimation because we use total-eruption PDC volumes in our Titan2D runs. Considering whole-eruption PDCs is a common practice in volcanic hazard assessments, especially in the case of pumice flows and pyroclastic surges (e.g. [25, 26, 33, 103, 105, 217, 328]), and it provides an upper-bound, conservative estimate of the PDC hazard.

Finally, the structural uncertainty is tendentially the most difficult source to be quantified (e.g. [75]). Preliminarly, the quantitative comparison of the Titan2D outputs with past PDC deposits may be used as a measure of structural uncertainty (e.g. [75, 104]). Some studies have calculated (maximum) Jaccard coefficients for Titan2D simulations around 0.6-0.7 (e.g. [86, 225]). These values are equal to or smaller than the ones computed by [103] at Somma-Vesuvius and Campi Flegrei (Italy). Assuming, for instance, a dense-PDC area of invasion about 100 km^2, the expected areal misfit [103] would be $\sim 40 - 70$ km^2 while it would rise up to $\sim 80 - 130$ km^2 if the area of invasion is around 200 km^2. Therefore, we presume that structural uncertainty may also represent an important source of epistemic uncertainty in volcanic hazard assessments computed through Titan2D.

8.4.3 Implications for quantitative volcanic multi-hazard assessments

Explosive volcanoes are multi-hazard settings where diverse hazardous processes can occur whether in succession (e.g. lahars triggered by rainfall after a certain volume of pyroclastic material has been deposited around the volcano, e.g. [90]) or in concomitance (e.g. contemporaneous tephra fallout and PDC propagation, e.g. [329]). Current practices in quantitative volcanic hazard analyses are almost exclusively focused on single hazards (e.g. [23, 31, 32, 33, 76, 210]). Some authors have performed volcanic multi-hazard assessments but considering the different hazardous processes independently (e.g. [97, 100]). Very few studies have actually modeled the interaction between hazardous processes (e.g. tephra fallout and

lahars, [101]). Our probabilistic hazard assessment of dense PDCs (and similar ones) could represent an important step towards quantitative multi-hazard assessments in which the volcanic hazard interaction is explicitly accounted for. For instance, the hazard curves of (dense-PDC) flow depth and speed at locations along the coastline southwards and southwestwards of Somma-Vesuvius could be integrated into quantitative hazard analyses of tsunamis triggered by dense PDCs entering the sea (e.g. [330, 331]). Similarly, the probabilistic assessments of flow depth could be extended to calculate dense-PDC volumes over different catchments around the volcano and, therefore, evaluate the volcanic hazard posed, for instance, by rain-triggered lahars (see Chapter 9).

One interesting aspect derived from our hazard analysis is the spatial discontinuity observed between the area where previous volcanic-edifice collapses have occurred (calderas' floor) and the sectors of the volcano located towards the toe of the present edifice. This discontinuity is especially clear in the probability maps of flow speed (Fig. 8.9) and in the selected hazard curves for the same variable (Fig. 8.5), where the discontinuity is seen as a break-in-slope in the exceedance probability. That is, the percentage of dense PDCs that are able to reach the example locations with high speed is scarce and this percentage does not increase much if lower speeds are considered (see right-hand-side part of the hazard curves in Figure 8.5). On the contrary, leftwards of the break-in-slope of the hazard curves, the percentage of dense PDCs able to reach the locations with a given speed (or greater) greatly increases as lower flow speeds are analyzed (Fig. 8.5). In other words, the majority of simulated dense PDCs have difficulties in overcoming the values of flow speed beyond the break-in-slope. Our interpretation is that the relatively-flat area covered by previous volcanic-edifice collapses (e.g. Figure 4 in [26]) produces a deceleration of the dense PDCs over the proximal sectors of the volcano, possibly greater than at other volcanoes where the most proximal sectors may be dominated by steep slopes (e.g. Volcán de Colima, Mexico, [41]). This deceleration should result in an increase of the flow depth over this area. Beyond the calderas' floor, the dense PDCs are expected to regain speed and get thinner because of the steeper slope. Nonetheless, maximum flow speeds may not reach the same values as in proximal sectors, given the momentum already lost during propagation. Regarding the flow depth, we argue that the hazard curves do not show the same break-in-slope as the ones for flow speed because, even though the flow depth decreases as the dense PDCs propagate beyond the calderas' floor, the maximum values can still be high at the discontinuity. Therefore, the percentage

of dense PDCs that are able to overcome each threshold of flow depth over the hazard curve changes in a more gradual way (Figs. 8.4, 8.8).

The implications of the interpreted dense-PDC kinematics highlight how volcanic hazards can arise from complex interactions of different hazardous phenomena (e.g. [92, 166]). We may expect that, if dense PDCs decelerate over the calderas' floor, their associated hazard (in terms of dynamic pressure, for instance) at locations downhill the volcanic edifice will be lower, as the hazard curves demonstrate (Fig. 8.5). However, we may also expect that, as these dense PDCs decelerate, their transport capacity will be reduced (e.g. [35, 148]) and, thus, substantial amounts of pyroclastic material could be deposited over the calderas' floor. This pyroclastic material could subsequently act as the source for rain-triggered lahars that may travel radially, impacting locations that have already been impacted by the passage of dense PDCs (see Chapter 9). The quantification of secondary hazardous processes, such as lahars, is of paramount importance since they can cause long-lasting and more severe damages than primary processes, such as PDCs (e.g. [90, 164]).

8.5 Conclusions

In this chapter, we present a methodology that makes use of one PDC model and two uncertainty quantifications techniques and allows a robust quantification of aleatory and epistemic uncertainty in the volcanic hazard posed by dense pumice flows. The final hazard product is a large set of probablistic hazard curves, one at each grid point over the hazard domain, which represent a full description of uncertainty (e.g. [83]). Such a hazard analysis has been performed for tephra fallout (e.g. [70, 76]) but, to our knowledge, this is the first time that the same is provided for (dense) PDCs. Nevertheless, we contend that other recent strategies to calculate probabilistic volcanic hazard of dense PDCs have the potential to calculate such hazard curves. For instance, statistical emulation implemented on the Titan2D model (e.g. [23, 31, 318]) could provide response surfaces (i.e. functions that estimate the value of flow depth/speed according to the values of one or more model parameters, such as V_0 and ϕ_{bed}) at each grid point over the hazard domain. Moreover, evaluating the emulator to assess all possibles sources of epistemic uncertainty would be feasible in terms of computation time (e.g. [31] quantified theoretical uncertainty at a reduced computational cost).

Other future directions may include the search for a two-layer PDC model that satisfies the following requirements: (1) it can simulate both dense and dilute PDCs (e.g. [133]); (2) it can be run over real terrain (like Titan2D); and (3) it is simple enough to, at least, be run many hundreds of times so a statistical emulator can be built from the outputs of these simulations. Even if a solution to this problem is found in the near future, probabilistic volcanic hazard assessments of PDCs will still have the necessity to incorporate the specific characteristics of the volcanic system under study in terms of probability of eruption, vent-opening probability, etc. This can be accomplished, as it has been done in recent years, through event trees (e.g. [21, 32, 49, 100, 250, 281, 307, 332]), which may also model non-eruption hazardous processes (e.g. [243, 244]), and Bayesian Belief Networks (e.g. [274, 333]).

Finally, the fact that we present a set of hazard curves, that show the hazard description over different thresholds of the hazard variable (dense-PDC flow depth/speed), is of paramount importance. A variety of probability and hazard maps can be easily derived from these hazard curves (Figs. 8.6, 8.7, 8.8, 8.9) but the specific choice of what thresholds in flow speed/depth or exceedance probability, respectively, are representative or informative is a duty that corresponds to decision-making agencies (e.g. [259]). Hazard scientists lack the training and information needed to decide upon those thresholds and, therefore, a separation between scientists and decision makers, in terms of actions, must be clear-cut (e.g. [334]).

Chapter 9

A framework for Probabilistic Volcanic Multi-Hazard Assessment of rain-triggered lahars using Bayesian Belief Networks

Abstract

Secondary water-sediment flows, commonly known as lahars, can pose a higher threat to population and infrastructure than primary volcanic hazardous processes such as tephra fallout and Pyroclastic Density Currents (PDCs). Lahars are dense and highly-viscous flows which may reach high speeds and flow depths causing severe damage by lateral impact and/or burial. Frequently, lahars are triggered by intense or long rainfalls occurring after explosive eruptions at a given volcano. These eruptions provide important amounts of loose pyroclastic material that is consequently remobilized and transported by lahars. The whole process depends on many factors such as: (1) the spatio-temporal rainfall characteristics; (2) the spatial distribution and hydraulic properties of the tephra deposit; (3) the pre- and post-eruption topography. Modeling such a complex system requires the quantification of aleatory variability in the lahar triggering and propagation. In this work, we present a multi-hazard framework to produce probabilistic assessments of lahar hazard. We opt for coupling a simple but flexible probabilistic model (Bayesian Belief Network, BBN) for lahar triggering with a dynamic physical model for lahar

propagation. The BBN model allows to merge varied information about regional rainfall, scientific knowledge about lahar triggering and probabilistic hazard assessments of tephra fallout and dense PDCs, and compute a homogeneous assessment of the probability of lahar volumes. The lahar model serves to propagate the aleatory variability into hazard footprints of lahars. We preliminary apply our multi-hazard procedure to Somma-Vesuvius (Italy) because: (a) the volcano is strongly lahar-prone; (b) there are many possible source areas for lahars; and (c) there is high density of population nearby. Our results indicate that large lahars (initiation volume $\geq 10^5$ m^3) along the volcano flanks are almost 60% probable to occur after large eruptions but less than 40% after medium eruptions. Some lahars over the surrounding topographic reliefs can propagate for 15 km and many lahars are able to produce combined flow depths of 2 m and speeds of 5-10 m/s, even over flat terrain. We argue that probabilistic multi-hazard frameworks like the one presented here can be invaluable for volcanic hazard assessment worldwide.

9.1 Introduction

Very large explosive eruptions can produce volumes of pyroclastic material of up to tens to thousands of cubic kilometres [14]. A substantial proportion of this material is deposited over the areas surrounding the volcano as tephra fallout (e.g. [118, 335]) or transported in Pyroclastic Density Currents, PDCs (e.g. [124]). The deposits from tephra fallout typically affect areas of 10^2 to 10^3 km^2 while PDC deposits usually have areal extents of 10^1 to 10^2 km^2 (e.g. [25]). This input of fresh loose pyroclastic material into the drainage basins around the erupting volcano alters the hydrogeological equilibrium of the basins, leading commonly to the formation of volcanic mudflows or lahars [92] as a response to intense or sustained events of rainfall [163, 169, 336]. The degree to which the drainage basins are disturbed, and their subsequent hydrogeomorphic response, depends on many different factors [92], including total tephra volume deposited, grain size distribution of the deposits, changes in the morphology of the catchments, and the type and extent of vegetation damage/loss. Moreover, the rainfall characteristics associated with the climate of the volcano's region have a profound impact on the frequency and volumes of the generated lahars (e.g. [337]).

The volcanic hazard (and associated risk) due to the occurrence of lahars is very high. In the last four centuries, the number of fatalities caused by lahars is second

only to PDCs when the largest volcanic disasters are removed from the dataset [157]. This confirms the importance of including, in hazard quantifications, the potential interaction of multiple hazards in a multi-risk perspective (e.g. [291, 338, 339]). Similar to other volcanic hazards including tephra fallout and PDCs, the natural variability in the volcanic process and environmental conditions, as well as diverse sources of lack of knowledge, give rise to considerable aleatory and epistemic uncertainties [52, 53, 61], further increased by the evaluation of chains of multiple events. In this context, probabilistic approaches that, at least, address and quantify the aleatory uncertainty linked to the volcanic hazard, tend to be preferred by both scientists and decision-makers (e.g. [53, 54]).

In the case of rain-triggered lahars, the hazardous event can be divided into two major components: (1) a rainfall event with particular characteristics (rainfall spatial distribution, intensity, duration) acts as the trigger for erosive runoff and/or shallow landsliding on the loose tephra deposits and (2) this generates an initial volume of water-sediment mixture that flows down the slope of the volcanic edifice and transforms into a lahar. Frequently, hazard analyses of lahars have focused on one of these two components, either the temporal and/or spatial features of the lahar triggering, or calculating the hazard footprints (i.e. inundated areas) of lahars of specific total volumes. For temporal triggering, rainfall Intensity-Duration (I-D) thresholds have been one of the most utilised methods [163, 164, 180, 340, 341]. Some studies have improved the classical I-D approach (in which just one line marks the occurrence or not of lahars) to produce probabilistic thresholds by performing logistic regressions on the binary dataset, i.e. event/no event, given an I-D combination (e.g. [177]), or through Bayesian data analysis (e.g. [342]). Other studies, have used several diagnostic triggering variables (e.g. antecedent and total rainfall), in addition to I-D, and have explored their potential to compute probabilistic forescasts of lahar occurrence in nearly real time [343]. For spatial triggering, deterministic physical models of slope stability and/or overland erosion have been employed to delimit the areas that can act as sources of water-sediment flows (e.g. [178, 344]). Very few of such studies have considered the spatial availability of tephra before the lahar triggering (e.g. [101]). Some probabilistic assessments of the areal susceptibility of such flows have been implemented by exploring the epistemic uncertainty on soil properties (e.g. [177]) or by coupling the results from deterministic susceptibility models with a probabilistic measure in terms of the recurrence interval for a specific event of triggering rainfall (e.g.

[162]). However, such studies did not merge the lahar triggering with the lahar propagation to compute hazard footprints of lahars.

Diverse approaches have been developed to model lahar hazard footprints, including statistical/empirical models (e.g. *LAHARZ*: [345]) and two-dimensional shallow-layer continuum models formulated using Coulomb-friction (e.g. Titan2D: [218]), whose potential for extension to describe lahar bulking-debulking (i.e. erosion-sedimentation) during transport has been demonstrated [81, 346, 347]. Typically, one crucial input is the lahar volume whether at initiation (if the model incorporates bulking-debulking) or the total lahar volume (if the model does not include this feature). The application of these deterministic models to previous lahar events and specific hazard scenarios has been extensive (e.g. [223, 228, 229, 230]). However, integration of these models into frameworks for probabilistic assessment of lahar hazard is only just beginning. Recent studies have started to explore the coupling of empirical models (*LAHARZ*) with Bayesian statistical descriptions [100]. Moreover, studies like the one presented by [162] could represent a step towards probabilistic hazard assessments of lahars if a physical model is incorporated to such type of analysis. There are some studies which have coupled a physical model for mass-movement susceptibility with simple lahar-propagation models to determine mass-flows hazard (e.g. [101, 348]). Nonetheles, the aleatory variability in the temporal and/or spatial triggering of the hazardous event was not described or quantified. Only very recent research has proposed a methodology to couple the spatial-triggering and the flow propagation in a way that could be extended towards probabilistic hazard assessments [349].

In this chapter, we address some of the aforementioned limitations and present an integrated framework for probabilistic volcanic multi-hazard assessment, with focus on post-eruption rain-triggered lahars (Fig. 9.1). Two are the major goals that we pursue through this integrated approach: (1) create a simple but informative probabilistic model of lahar occurrence and volumes; and (2) couple this probabilistic model with a lahar simulator in order to propagate the uncertainty in lahar triggering towards hazard footprints of lahars. The probabilistic model chosen is a Bayesian Belief Network (BBN, e.g. [247]), a flexible and versatile probabilistic model which allows us to merge information coming from diverse sources (literature data, physical and statistical modeling, probabilistic hazard assessments; see Figure 9.1) and quantify the aleatory uncertainty linked to the lahar triggering. In particular, we propose a generalizable BBN model (*Multihaz*) that quantifies

the aleatory uncertainty in terms of: (i) pyroclastic volume (from tephra fallout and dense PDCs) stored in different catchments around the volcano; (ii) rainfall characteristics over the catchments (specifically the intensity and duration); (iii) response of the catchments to specific conditions of rainfall and pyroclastic volume (in terms of the amount of material that may be remobilized by lahar events); and, finally, (iv) lahar initiation volumes for each of the catchments defined over the hazard domain.

In principle, *Multihaz* can be applied to any volcanic system and coupled with any lahar simulator. In this study, it is coupled with a shallow-water physical model of lahar dynamics [235] which incorporates bulking-debulking and permits, coupled with *Multihaz*, the calculation of probabilistic hazard footprints of lahars. As a study case, we present an inital application of our multi-hazard framework to post-eruption rain-triggered lahars at Somma-Vesuvius (Italy). We select this volcanic system for three reasons: (1) there are data available to quantify the aleatory uncertainty linked to tephra fallout (e.g. [70]) and dense PDCs (e.g. [107], see Chapter 8); (2) the volcano has generated syn-eruptive lahars during/after mid-large explosive eruptions (e.g. [170, 198]) and is prone to form them at many locations around it (e.g. [173, 174]); and (3) the relatively high population density nearby.

In section 9.2, we detail the variables and structure of *Multihaz* as well as a core parameterization that could be applicable to any volcano. In section 9.3, we report the procedure carried out to parameterize *Multihaz* at Somma-Vesuvius. In section 9.5, we show the main results obtained from the probabilistic assessments of *Multihaz* and the hazard footprints computed from some *LaharFlow* simulations. We pay particular attention to three scenarios of lahar generation, selected to emphasize the impact of the eruption size and the efficiency of tephra remobilization on the probabilistic multi-hazard assessment. In section 9.6, our findings are put in the context of previous studies regarding: (i) spatio-temporal triggering of lahars; (ii) lahar hazard assessments worldwide; and (iii) lahar and debris-flow hazard at Somma-Vesuvius. We also propose some future directions in volcanic multi-hazard assessment focused on lahars.

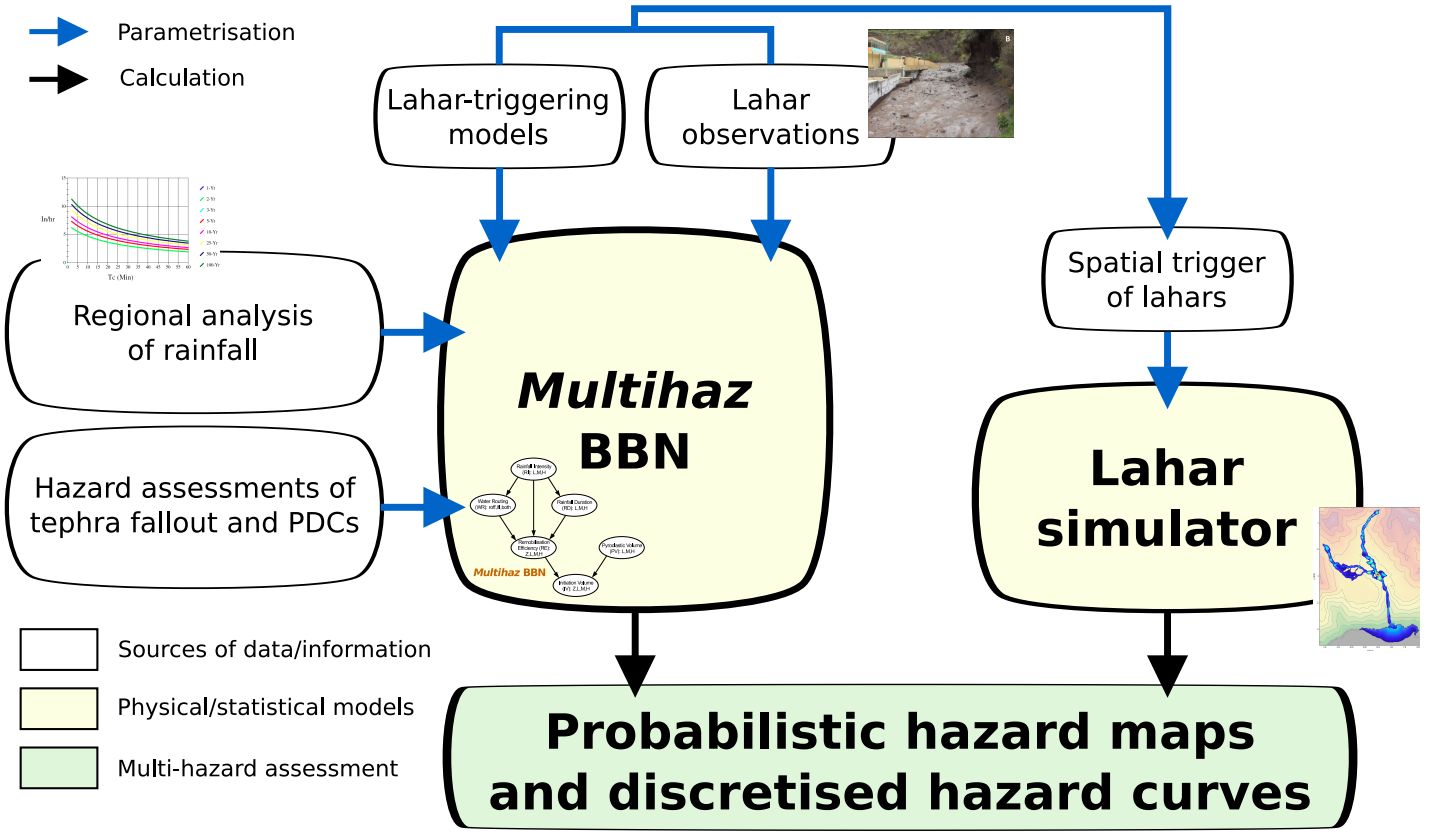

FIGURE 9.1: Scheme of our proposed multi-hazard framework in which varied information or data about rainfall characteristics, lahar-triggering mechanisms and availability of fresh tephra is digested by a BBN structure (*Multihaz*, see Fig. 9.2) and also used to set up the initiation points for the simulations of the dynamic lahar model. The *Multihaz* BBN assessments are then utilised in conjunction with the hazard footprints computed from the lahar simulator to calculate probabilistic hazard maps and discretised hazard curves for rain-triggered lahars (see text for more details). From [109].

9.2 *Multihaz*: a general BBN model for rain-triggered lahars

The volcanological and climatological inputs for a BBN for lahar generation vary significantly from one volcano to another [92, 337, 350]. Our approach here is to create a general-purpose BBN (*Multihaz*; see Figure 9.2 and Table 9.1), with nodes discretised into qualitative states (e.g. low, medium, high), which is applicable to any volcano location. The PTs and CPTs can be parameterized to satisfy the specific characteristics of a given volcano. For instance, the probability of high-intensity rainfalls should be higher at tropical volcanoes (e.g. [163]) than at a temperate-climate volcano (e.g. [351]).

Other CPTs are parameterized to describe the general physical processes for rainfall-triggering of lahars (see Figure 9.3 and Table 9.2) and are thus applicable to different volcanoes. We parameterize these CPTs as follows: (1) we compile information (data and evidential reasoning) from lahar or debris-flows observations and physical or statistical models from the literature (Table 9.2); and (2) we translate this information into quantitative likelihood distributions within the CPTs. In order to reduce the degrees of freedom in our choice of the probabilities inside the CPTs, we adopt a five-fold classification of likelihood following the structure proposed by the Intergovernmental Panel for Climate Change (IPCC) in 2007 (Table 9.3; [352]). We use central measures of each range in probability and, finally, we normalise these values to ensure that the states in the nodes are mutually exclusive and exhaustive.

This BBN parameterization is not unique and epistemic uncertainty, due to incomplete knowledge about the probabilistic triggering of lahars, is present. In this chapter, we focus on quantification of aleatory uncertainty, but note that quantification of epistemic uncertainty could consist of modeling each row of each CPT (e.g. $P(IV|y_i)$, where y_i represents a given combination of remobilisation efficiency and pyroclastic volume) as a Dirichlet multivariate PDF of four variables, that is: $P(IV = zero|y_i)$, $P(IV = low|y_i)$, $P(IV = medium|y_i)$, and $P(IV = high|y_i)$. The mean of each variable could be the best-estimate probability value presented here, while the variance could be modeled as common to all the variables and expressed via the number of equivalent data (Λ, see Chapter 7).

TABLE 9.1: Physical variables included in the BBN model *Multihaz*. All these variables apply to a given area around the volcano, for instance, a hydrological catchment. The qualitative states are meant to be generalizable to any volcano of interest and they can be associated with quantitative thresholds so the probability of each state can vary according to: type of climate, spatial distribution of volcanic products, grain size distribution of these products, etc. PT: Prior Table; CPT: Conditional Probability Table. From [109].

***Multihaz* Variable**	**Abbreviation**	**Definition**	**States**	**PT/CPT**	**# Parameters**
Rainfall Intensity	RI	Maximum rainfall intensity recorded during a given rainfall event.	Low, Medium, High	PT: P(RI)	3
Water-Routing mechanism	WR	Water-routing mechanism that dominates during the rainfall event.	Runoff, Infiltration, Both	CPT: P(WR|RI)	9
Rainfall Duration	RD	Duration of the rainfall event.	Low, Medium, High	CPT: P(RD|RI)	9
Remobilization Efficiency	RE	Remobilization efficiency that a lahar event may have at initiation.	Zero, Low, Medium, High	CPT: P(RE|RI,RD,WR)	81
Pyroclastic Volume	PV	Amount of pyroclastic material accumulated during a recent eruption.	Low, Medium, High	PT: P(PV)	3
Lahar Initiation Volume	IV	Amount of material that a lahar event may incorporate at initiation.	Zero, Low, Medium, High	CPT: P(IV|RE,PV)	27

TABLE 9.2: Summary of all the strands of evidence (first column), and their physical explanation (second column), collected from literature related to rain-triggered of lahars. All this information is used to reason about and set up the parameters of the conditional probability tables of *Multihaz* (third column). All abbreviations for the names of the nodes and the states within the nodes are the same as in Figure 9.3 and Table 9.1. P(·): probability of an event or probability distribution of a variable. From [109].

Evidence	**Physical explanation**	**CPT interpretation**	**Literature examples**
Rainfall intensity and duration tend to be inversely correlated	In a general framework, convective (local) rainfall is characterized by high intensity and short durations while stratiform (regional) rainfall tends to show longer durations and low to moderate intensities. For a given rainstorm event, the duration is linked to the total rainfall volume through the rainfall intensity.	P(RD=H|RI=L) >> P(RD=H|RI=H)	[353, 354, 355]
The predominant water-routing mechanism, in response to a rainfall event, is a function of the rainfall intensity and the hydrological state of the terrain receiving the rainfall	Changes in the infiltration rates caused by explosive eruptions tend to favour runoff and overland flow. Yet, depending on the grain size of the deposit and the rainfall characteristics, partition between runoff and infiltration or only infiltration may dominate.	P(WR=roff|RI) > P(WR=both|RI) > P(WR=ifl|RI)	[92, 162, 170, 356]
The likelihood of lahar occurrence is similar for short-intense and long-weak rainfall events	Lahars may be triggered either by extensive runoff erosion during intense rainfall or by a combination of erosive runoff and shallow landsliding during long-lasting rainfall (i.e. I-D thresholds are representative of rain-triggered lahars).	P(RE≠0|RI=H,RD=L) ~ P(RE≠0|RI=L,RD=H)	[163, 176, 341, 343]
The water-routing main mechanism has an important influence on the lahar occurence, with runoff and slow infiltration being the most-likely triggers of lahars	Tephra deposits can be eroded most efficiently by either erosive runoff and/or shallow landslides (caused by positive pore pressures within the deposit). If (rapid) infiltration dominates, the triggering of lahars becomes less likely.	P(RE≠0|both) > P(RE≠0|roff) > P(RE≠0|ifl)	[92, 162, 356]
Rain duration is the main control on the volume of lahars triggered by shallow landslides	Given that rain intensity is close to the hydraulic conductivity of the deposit, hydraulic diffusivity is the most important parameter controlling the pore-pressure transmission through the deposit and, thus, the potential failure (and volume)	P(RE≠0|RD,both) > P(RE≠0|RI,both)	[162]
Surface runoff can act as triggering for shallow landslides	When rain intensity is much greater than the hydraulic conductivity (thus runoff is promoted), there still can be slope-toe (base) erosion that produces gravitational instability and triggers, in junction with pore-pressure increase, the shallow landslides.	P(RE≠0|RI=H) ~ P(RE≠0|RD=H)	[357]
Rainfall intensity has a weaker impact on the lahar initial volume as compared to rainfall duration	The capability of erosive runoff to incorporate sediment into the lahar may be smaller than the initial volume that can be incorporated via shallow landslides.	P(RE≥M|RD) > P(RE≥M|RI)	[162, 170]
The initiation volume of (medium-large) debris flows triggered by shallow landslides relates to the rainfall intensity (for a fixed duration) by means of a logarithmic function	For a given rainfall duration, there is a limitating rainfall intensity beyond which most of the areas susceptible to fail gravitationally may have done so already. Therefore, increasing the rainfall intensity does not increase the initiation volume significantly.	P(RE≥M|RI=H,both) ~ P(RE≥M|RI=M,both) >> P(RE≥M|RI=L,both)	[177]
Raindrop impact erosion is hindered by water depth	The kinetic energy carried by the raindrops is damped by the thickness of a water flow which can develop through runoff	P(RE≥M|RI=H,roff) ~ P(RE≥M|RI=M,roff)	[358]
When the filling of the deposit with water occurs from the surface of the ground-water table (bottom-up) the failure depth of the shallow landslides may be greater	If the infiltration dominates but the water is not dissipated laterally (e.g. because rainfall duration is high), the rise of the water table can induce positive pore pressures at deep locations within the deposit. Therefore, the potential volume incorporated into a shallow landslide may be greater.	P(RE≥M|RD=H,ifl) > P(RE=L|RD=H,ifl)	[170, 359]
Lahars remove deposits at a rate that depdends in part on the volume of deposited material (i.e. on the eruption size)	The greater the erupted volume deposited, the larger the excess of material that the drainage basin needs to 'convey' before restoring its state of equillibrium.	P(IV|PV=H) > P(IV|PV=L)	[92, 356]

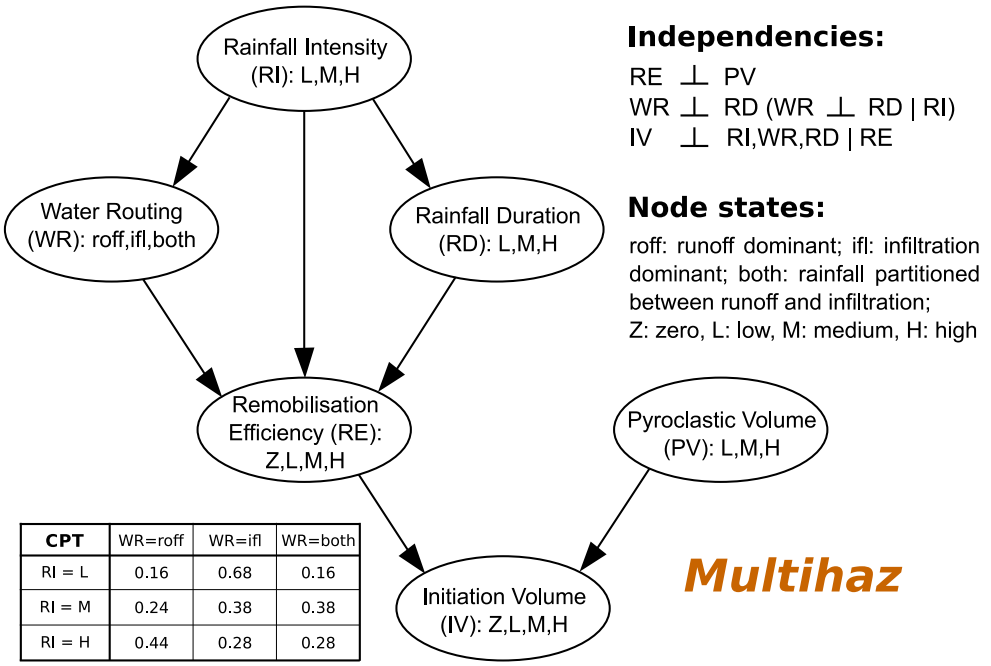

FIGURE 9.2: The generalizable probabilistic model proposed in this study: *Multihaz*. Variables (or nodes) are displayed as ovals while conditional relationships (or arcs) are shown as arrows, with the parents nodes pointing to the children nodes. Abbreviations for the names of the nodes are given in brackets at each node and are used throughout the chapter. The abbreviations for the states of each node as well as the independence relationships between nodes that the *Multihaz* structure implies are reported. On the bottom left, the Conditional Probability Table (CPT) for the WR node is displayed (see text for more details). From [109].

TABLE 9.3: Five-fold classification of likelihood adopted for the parametrisation of *Multihaz* (after [352]). Central values of probability are used for each parameter in the prior tables and conditional probability tables and finally renormalised to ensure the mutually-exclusive-and-exhaustive requirement of BBN models. From [109].

Likelihood terminology	**Range in probability [%]**	**Central Value of probability [%]**
Very Unlikely	0-10	5
Unlikely	10-33	22
About as likely as not	33-66	50
Likely	66-90	78
Very Likely	90-100	95

Our BBN structure does not include antecedent rainfall conditions. This choice is made to keep the parameterization as simple as possible, given that rainfall intensity and duration are typically considered more informative for the likelihood of rain-triggered lahars (e.g. [162, 341, 343]). Moreover, the conditional links between remobilization efficiency and antecedent rainfall are not yet fully understood; antecedent rainfall is commonly considered to increase the likelihood of lahars or debris flows (e.g. [177, 343]), but other physical processes such as "hydro-repellency" have been proposed to decrease the likelihood of lahars when antecedent rainfall is high (e.g. [180]).

9.2.1 Aleatory uncertainty in rainfall intensity and pyroclastic volume

The only two nodes in *Multihaz* that have no parents are RI and PV (Fig. 9.2). Although RI and PV are defined in terms of qualitative states, they can be described in a quantitative way by defining thresholds that characterize their states. These need to be set according to the volcano studied and the potential variability of RI and PV. As mentioned above, the rainfall regime can change significantly depending on regional climate (e.g. [337]). Similarly, the spatial distribution and total amount of pyroclastic material available at the different catchments surrounding the volcano will depend on factors such as: (a) aleatory variability in eruption behaviour: eruption column height, grain size distribution, PDC volume and mobility; (b) aleatory variability in wind-field speed and azimuth at different altitudes; (c) topography of the volcano and surrounding terrain. We quantify all these aspects in our application for Somma-Vesuvius in section 9.3.

9.2.2 Physical insights into lahar triggering and initiation volumes

Lahar initiation is described in *Multihaz* through the parameterization of the CPTs for two nodes: RE and IV. The former has RI, WR and RD as its parent nodes (Fig. 9.2). Both the WR and RD nodes have CPTs derived from their common parent node, RI. The CPT of the IV node is described as a function of the states in its parent nodes: RE and PV.

All these CPTs are parameterized following a general-purpose approach, based on

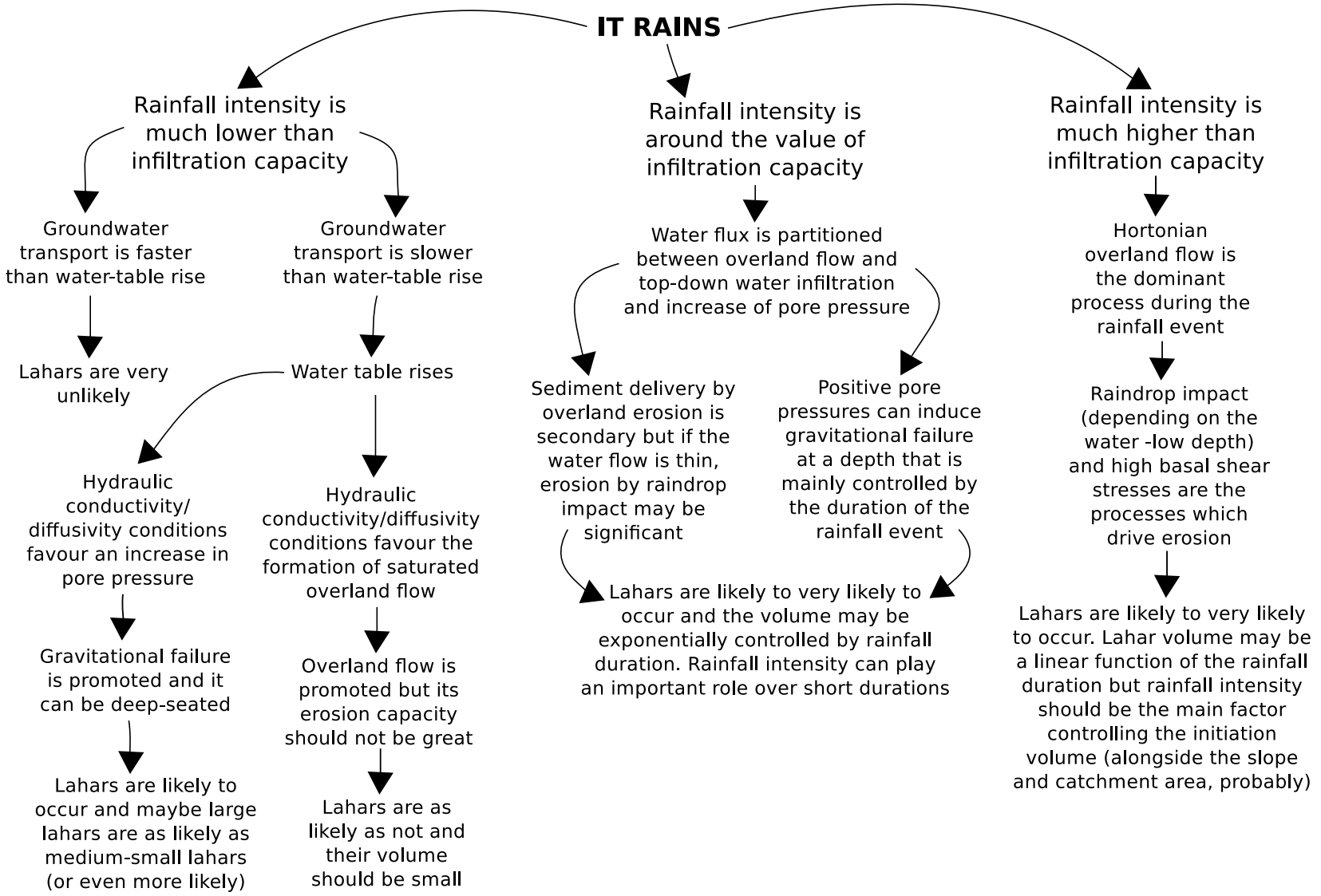

FIGURE 9.3: Scheme of the reasoning about the physical processes associated with the triggering of lahars by means of rainfall utilized to construct our BBN model: *Multihaz* (see Figure 9.2 and Table 9.1). Together with Table 9.2, this reasoning defines the structure and parameterization of *Multihaz* (see text for more details). From [109].

diverse strands of evidence about the physical processes behind the complex interrelationships that exist between the variables modeled by *Multihaz*. This evidence is extracted from the literature and it is summarized in Table 9.2. The majority of data is related to the RE node which has the largest CPT within Multihaz (Table 9.1). In Figure 9.4, we show some probabilistic trends observed within the CPT of the RE node that confirm the evidence listed in Table 9.2 is correctly incorporated into *Multihaz*. For instance, the probability of lahar occurrence (i.e. $P(RE > 0)$) is very similar for long-lasting, low-intensity rainfall events (RI=low, RD=high) and for short-lived but high-intensity rainfall events (RI=high, RD=low), especially when the predominant water-routing mechanism is infiltration (WR=ifl) or a partition between infiltration and runoff (WR=both). When runoff is the dominant water-routing mechanism (WR=roff), the more intense the rainfall, the higher the probability of lahar occurrence (Fig. 9.4d), in particular of medium-large lahars (Fig. 9.4b; e.g. [92, 356]). Additionally, the importance of rainfall duration in controlling lahar occurrence and volume when shallow landsliding is the main triggered mechanism (e.g. [162, 178]) is observed as peaks in probability in all the graphs (especially for medium-large remobilization efficiencies) when WR=both and RD=high.

The probabilistic patterns included in the CPT of the IV node (derived from the information on Table 9.2) show that the probability of having lahars, especially of medium-large sizes, increases more or less linearly with increasing RE and PV. However, we ensure that the probability of any size of lahars increases considerably when the PV available is relatively high (e.g. [356]). Thus, for example, the probability of having medium or large lahars given that PV=high but RE=low is slightly greater than the probability of having such lahars given that PV=low but RE=high. Likewise, the probability of medium-large lahars given that PV=high and RE=medium is higher than the same probability given that PV=medium and RE=high.

9.3 *Multihaz* parameterization at Somma-Vesuvius (Italy)

We parameterize *Multihaz* at Somma-Vesuvius by using the general-purpose CPTs for the WR, RD, RE and IV nodes and setting up volcano-specific prior tables

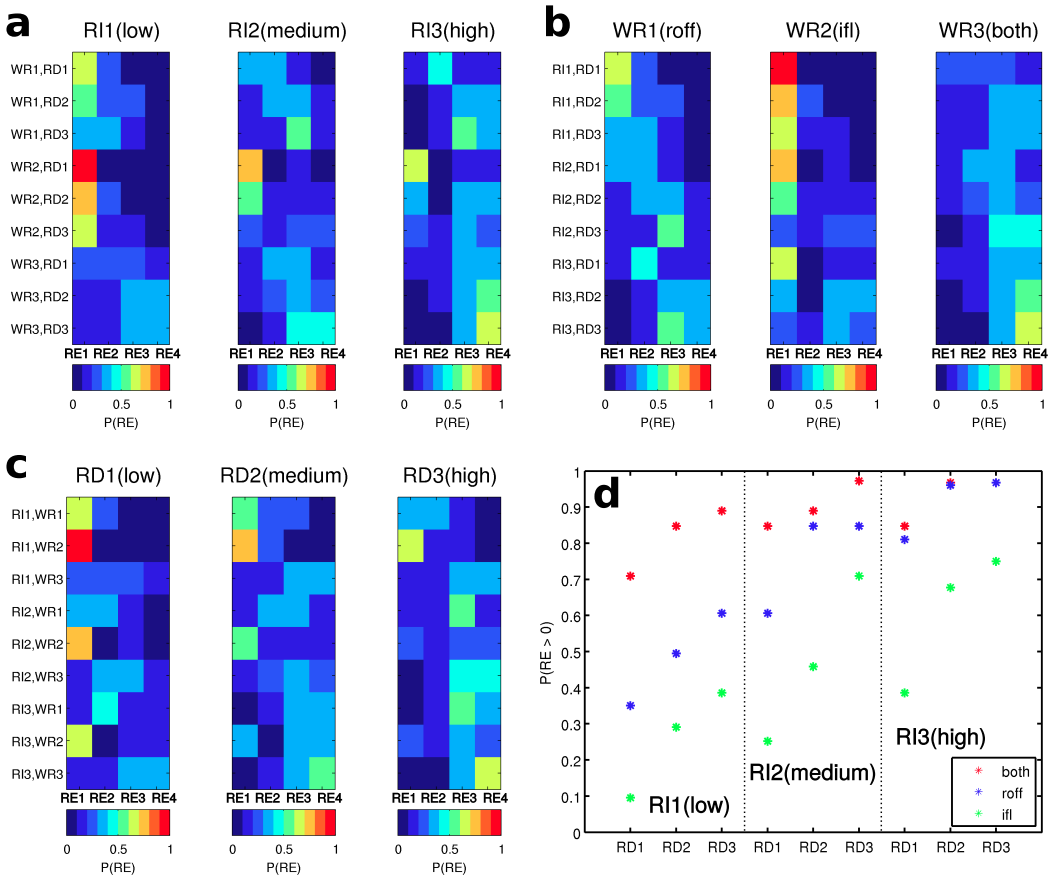

FIGURE 9.4: Probabilistic patterns found within the Conditional Probability Table (CPT) of the Remobilization Efficiency (RE) node, arranged according to its parent nodes: rainfall intensity (RI, a), water-routing mechanism (WR, b) and rainfall duration (RD, c). On graph d: probability of RE > 0 according to the water-routing mechanism and as a function of RI and RD. The patterns displayed are in agreement with the scientific knowledge collected about the physical processes responsible for the rainfall triggering of lahars (see Table 9.2 and text for more details). roff: runoff dominant; ifl: infiltration dominant. RE1, RE2, RE3, RE4 denote the states zero, low, medium and high, respectively. From [109].

(PTs) for the RI and PV nodes. In the first case, we collect information on maximum yearly rainfall intensities at the central Campania region where Somma-Vesuvius is located [360] (see subsection 9.3.2). In the case of the PV node, we take the probabilistic hazard assessments carried out by [70] and [107] (see Chapter 8), for tephra fallout and dense PDCs, respectively, and complete them to finally obtain probabilistic quantifications of the aleatory uncertainty in PV for each of the hydrological catchments selected (see subsection 9.3.1).

Concerning the CPT for the WR node, our parameterization is general-purpose

but it is only valid for the fine-grained deposits which may be found at the uppermost part of the pyroclastic stratigraphic sequences from the Somma-Vesuvius. These sequences, for both tephra-fallout and PDC deposits, are commonly topped by fine-rich pyroclastic layers [144, 170, 196, 232] that have infiltration capacities (∼4-40 mm/h; [170]) within the range of the expected rainfall events at the area [361]. In contrast, the underlying coarse-grained pyroclastic deposits have infiltration capacities ($4 \cdot 10^3$-$4 \cdot 10^5$ mm/h, [170, 362]) that can be orders of magnitude above the maximum rainfall intensities expected in the area (∼ 70 mm/h for a 100yr-event, [361, 363]). Therefore, in order to model lahar triggering on such deposits, the CPT of the WR node would need to have very low values of probability for runoff being true, even in the case of high-intensity rains. We contend that this is not the general case at other volcanoes worldwide, since those located in temperate-climate areas have had recent eruptions with much finer-grained deposits (e.g. [364]), while other volcanoes located in tropical regions can experience typical rainfall intensities in the order of 10^2 mm/h [163, 164]. Still, a more comprehensive hazard analysis of rain-triggered lahars at Somma-Vesuvius could include a spatial model for the grain size distribution across the hazard domain, perhaps as a function of thickness, although this is beyond the objectives of this chapter.

9.3.1 Definition of hydrological catchments

As previously discussed, rain-triggered lahars typically need two principal components to be generated: (1) availability of loose, readily removable pyroclastic material; and (2) a rainfall event that is able to remove a significant amount of this pyroclastic deposit (through erosion or shallow landslides). Additionally, it is thought that steep slopes that favour runoff and/or shallow landslides are a requirement [92, 161, 162, 340]. A value of 30° tends to be considered a threshold for gravitational stability of the deposit [170, 171] and it is this threshold which separates volcaniclastic erosion from deposition at other volcanoes (e.g. [350]).
At Somma-Vesuvius, such steep slopes occur along the volcano edifice and over the topographic reliefs located towards the southeast, east and northeast from the volcano [173, 174]. We deem all the catchments that have a substantial proportion of their upper area covered by slopes greater than 30° as potential sources of rain-triggered lahars (Fig. 9.5). Using a 20m-resolution DEM as the base topography, we develop a procedure to identify and demarcate hydrological catchments that,

in addition, share the following characteristics: (1) their areas are not smaller than about 0.08 km^2 (one third of the spatial resolution used to quantify the aleatory uncertainty in pyroclastic volume; see subsection 9.3.3); (2) they have at least one potential initiation point for lahars located on a slope greater than 5° (so the lahar simulations can have an inertial component at initiation); (3) their outlet points (i.e. the points where all the surficial runoff of the catchment should converge) are located further away than 1.5 km from the sea coast (to give the lahar simulations some distance to propagate through).

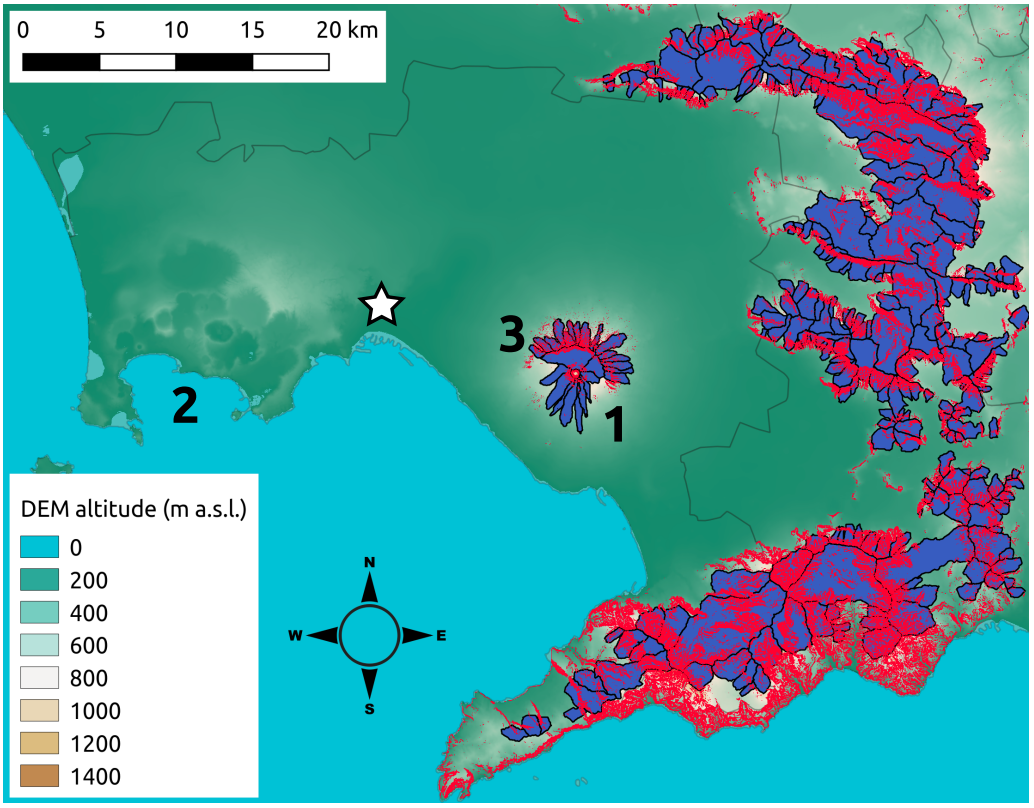

FIGURE 9.5: Digital Elevation Model (DEM) of Somma-Vesuvius (1) and surroundings which include the Campi Flegrei caldera (2) and the city of Napoli (white star). The catchments identified as having potential to generate rain-triggered lahars after explosive eruptions at Somma-Vesuvius are plotted in blue. Red areas indicate the grid points inside the 20m-resolution DEM with slope greater than 30°. The horse-shoe shape of Mount Somma (3) is evidenced by grouping of steep-slope points slightly north of the current crater of Somma-Vesuvius. From [109].

The definition of the hydrological catchments (Fig. 9.5) and the initiation points is done in a semi-aumotatic way by using an application of Quantum Geographical Information System [320]. Specifically, we carry out the following steps (e.g. [365]): (a) we fill the sinks (i.e. local depressions) in the raw DEM to obtain a realistic

flow-direction raster; (b) we derive the flow-accumulation raster and the junctions of the channel network from the filled DEM; and (c) we calculate the watershed basins -or catchments- from the channel network previously derived. Finally, we manually group the catchments and choose the initiation points (from the junctions automatically defined) in order to fulfill the requirements indicated above. We assume that all the catchments delimited will behave in a similar way when they experience a specific rainfall event. This is why we use the general-purpose CPTs of the nodes WR, RD and RE for all the catchments.

9.3.2 Rainfall intensity

The climate of the Campania region can be classified as warm-temperate with dry and warm summers [366]. The area around Somma-Vesuvius receives average monthly precipitations from few tens of mm during summer up to few hundreds of mm during fall (e.g. [199]). In terms of rainfall intensity, average yearly maximum values can be in the order of 10-30 mm/h for rainfall events shorter than 6 hours while these average yearly maxima can be below 5 mm/h for rainfall events equal or longer than 20 hours [360].

Given that we separate rainfall intensity and duration in the structure of *Multihaz*, we build a PDF for RI alone. We separate rainfall intensity and duration because it is easier to obtain a probabilistic quantification of our variable of interest, RI. Nevertheless, we do model the widely-acknowledged inverse relationship between rainfall intensity and duration [353, 355] through the CPT of RD, whose parent node is RI. We use the Two-Component Extreme Value (TCEV) PDF described by [367] and used by [360] to model the (maximum yearly) rainfall intensity at Somma-Vesuvius and surroundings. The cumulative distribution function is written as follows [367]:

$$F_X(X) = exp(-\eta_1 exp(-X/\theta_1) - \eta_2 exp(-X/\theta_2)) \tag{9.1}$$

where X represents the maximum yearly rainfall intensity, η_1, η_2 denote the mean number of independent ordinary and extraordinary events; and θ_1, θ_2 indicate the mean rainfall intensity of the ordinary and extraordinary events. We extract the values of the parameters: η_1, η_2, θ_1, θ_2 for each of the catchments identified in the Somma-Vesuvius area (see subsection 9.3.1) from regional data about the

rainfall regime across the study area [360], including the average altitude of each catchment. Once we build the TCEV distributions for all the catchments, we can define rainfall-intensity thresholds for the study area and, finally, calculate the prior probabilities for each state in the RI node. We choose thresholds at RI ≤ 1 mm/h for RI = low, RI > 10 mm/h for RI = high, and, thus, $1 <$ RI ≤ 10 mm/h for RI = medium. These thresholds are chosen, not only taking into consideration the rainfall phenomenology of the area, but also the values of permeability of the pyroclastic deposits, in order to ensure that our general-purpose CPT table for the WR node is compatible with them. We note that our parameterization of the RI node is likely to be an overestimation of rainfall intensities, since we are using data for yearly maxima of RI. However, the PT of this node could be also filled in by using real-time meteorological data, for instance.

9.3.3 Tephra-fallout and PDC-deposit volumes

Somma-Vesuvius explosive eruptions capable of producing enough pyroclastic material, dispersed along its flanks and medial-distal surrounding areas, to generate considerable lahar activity, range from violent Strombolian up to sub-Plinian and Plinian eruptions [89, 170, 196]. The natural variability of these eruptions, in terms of tephra-fallout dispersal and PDC inundation, is quite large [26, 44, 70, 89, 104, 368]. In this chapter, we quantify this aleatory uncertainty in pyroclastic volume over different catchments around Somma-Vesuvius, conditional to the occurrence of a small, medium, large or any-size eruption, the latter meaning that we weigh each eruption size with their probability of occurrence given that there is an eruption (after [61, 70]). Our procedure is carried out by adapting and extending the methodologies presented by [70] for tephra-fallout dispersal and accumulation, and by [107] for dense PDCs[1] (see Chapter 8).

Aleatory uncertainty in pyroclastic volume, due to tephra fallout, is explored and quantified by running a set of simulations of the HAZMAP model [369] and using its outputs to populate the BET_VH model [49, 242]. The final result are single hazard curves (i.e. only aleatory uncertainty is accounted for), at each selected

[1]Note that our PDC modeling is restricted to dense PDCs. Since dilute PDCs are not simulated, a certain thickness of PDC deposit is expected to be missing from our probabilistic quantification of the PDC volume. Nevertheless, dilute PDCs at Somma-Vesuvius are likely to invade medial and distal sectors from the central crater (e.g. [26]). These areas are predominantly located over the Campanian Plain where conditions that favor lahar generation (e.g. steep slopes) are not likely to occur.

catchment (Fig. 9.5), for the pyroclastic volume due to tephra-fallout accumulation. In the case of dense PDCs, we implement a similar procedure to [107] (see Chapter 8) in which the pyroclastic volume at each selected catchment is calculated through the merging of Titan2D [218] and Polynomial Chaos Quadrature (PCQ, e.g. [24]). In order to convert the maximum flow thickness simulated by Titan2D into expected PDC-deposit thickness, we follow a two step approximation. First, we apply a ratio between Titan2D maximum thickness and PDC-deposit thickness of 0.5, which is approximately the value found by [27, 370]. Secondly, we account for enhanced deposition on low-angle slopes in comparison to high-angle slopes [26, 133] by applying a correction similar to [133]. Instead of setting up a threshold of slope above which there is no PDC deposition, we use the minimum non-zero value of slope over the study area in a way that the final thickness is a fraction of the initial thickness (the greater the slope of a point, the smaller this fraction): $h_f = h_0 \cdot \min(\delta)/\delta_i$, where h_f is the final PDC-deposit thickness estimate, h_0 is the thickness estimate after applying the first correction mentioned above, δ_i is the (non-zero) slope in a given point, and $\min(\delta)$ is the minimum (non-zero) slope in the study area.

Finally, for those catchments on the proximal areas of Somma-Vesuvius in which both tephra-fallout and PDC deposition are expected to occur, we randomly sample the hazard curves of tephra fallout and dense PDCs and sum up the samples to obtain the final quantification of aleatory uncertainty (i.e. single hazard curves) for the variable PV. This step implies that tephra-fallout and dense-PDC propagation are independent. Using these hazard curves of PV, we can parameterize the prior table of the PV node at each selected catchment. We set two thresholds of PV in a way that PV $\leq 10^4 \mathrm{m}^3$ means PV = low; PV $> 10^6 \mathrm{m}^3$ means PV = high; and $10^4 < PV \leq 10^6 \mathrm{m}^3$ means PV = medium.

Figure 9.6 shows some examples of the hazard curves of tephra-fallout and dense-PDC volumes at catchments on the flanks of Somma-Vesuvius. We observe quite different curves depending on: (a) location of the catchment with respect to the central crater and the topographic barrier of Mount Somma; and (b) the size of the eruption considered. Generally, catchments located beyond Mount Somma (Fig. 9.6a, b, c) do not experience significant PDC deposition during small eruptions (i.e. pyroclastic volume is less than 10^2 m^3). On the central and oriental sectors beyond Mount Somma (Fig. 9.6a, b), greater accumulations of pyroclastic material are expected to occur due primarily to tephra fallout rather than PDCs. However, at the westernmost end of Mount Somma (Fig. 9.6c), we see that greater pyroclastic

volumes can result from PDC deposition rather than from tephra fallout. On the southern flank (Fig. 9.6d), small-size PDCs can deposit a substantial amount of pyroclastic volume while medium and large PDCs have the potential to deposit considerably greater amounts of pyroclastic volume in comparison with tephra fallout.

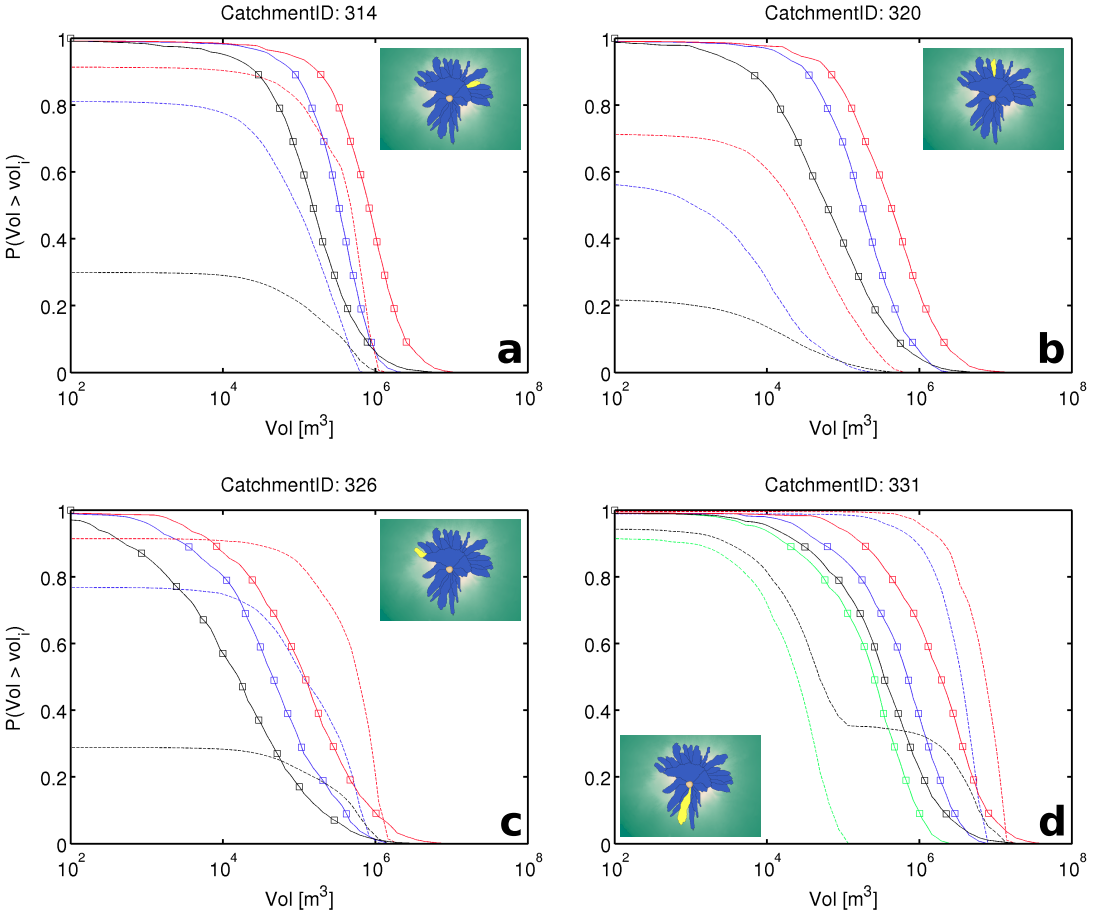

FIGURE 9.6: Hazard curves (or Exceedance Probability curves) for the volume of pyroclastic material (Vol), produced by tephra fallout (solid lines with squares) or PDCs (dashed lines), and available at four selected catchments over the flanks of Somma-Vesuvius (Italy). The colours indicate the eruption size: small (green), medium (blue), large (red) and any size (black, see text for more details). The inset maps show the location of the corresponding catchment (in yellow) and the other catchments on the Somma-Vesuvius flanks (in blue). Napoli downtown is located outside the maps, around 10 km towards the WNW. From [109].

9.4 Boundary conditions of *LaharFlow*

We initiate the model simulations with numerous sources distributed across the study region. At each source, we specify a simple time series to model the release of fluid from the catchment, that acts as source for lahars, with a volume flux $Q_j(t)$ for source j given by:

$$\begin{aligned} Q(t) &= Q_m t/t_0 && \text{for } t < t_0, \\ & Q_m(t_1 - t)/(t_1 - t_0) && \text{for } t_0 < t < t_1, \\ & 0 && \text{for } t > t_1 \end{aligned} \tag{9.2}$$

The total volume released at source j is then $V_j = Q_m t_1/2$ which is specified through *Multihaz*. The specification of flux time series at the sources is preferred over instantaneous releases of a volume as a model of the source, but introduces additional parameters characterizing the release. In our demonstration of the *Multihaz* coupling to the lahar dynamical model we do not explore in detail the sensitivity of the predictions to the parameters in the source model, but take $t_0 =$ 150 s and $t_1 = 300$ s for each source.

The confluence of channels are points of interest in the flow dynamics as the combination of material can lead to overtopping of channels. Thus, the 273 catchments identified from the geospatial analysis of the region (see subsection 9.3.1) are partitioned into 24 groups comprising sources that produce flows that have the potential to interact during their propagation. The flows from multiple sources in each group are simulated together. For simplicity, we model the sources as initiating simultaneously, but note that more sophisticated source initiation models could be adopted.

Our simulations employ the DEM derived from the Shuttle Radar Topographic Mission, at 30 m horizontal resolution, which is interpolated to the resolution of the computational model (here taken to be 10 m). The topography used in the model could in principle be modified to include the topographical changes (in altitude and slope, for instance) induced by an eruption in the volcanic system (e.g. [90, 92, 162]). Furthermore, given that the lahar simulator models the erosion during propagation of the lahar and the alteration of the topography,

the morphological changes predicted by the model could be assessed against field observations following an eruption. The morphodynamic changes are expected to be greater when large volumes of pyroclastic material deposited by PDCs have modified the pre-eruption topography substantially and the post-eruption lahars erode the PDC deposits strongly and rapidly [92].

The parameters in the lahar model are held fixed in this study, as our primary aim is to illustrate the coupling of *Multihaz* to *LaharFlow*. In applications, the parameters should be calibrated to represent the properties of typical flows in the region of interest, through comparison of model predictions with observations. Where observations are imprecise (which is typical, if not ubiquitous) the uncertainty in the calibration should be propagated through the flow model and quantified in the resulting model predictions. In this preliminary demonstration of the modeling, we use model parameters calibrated for lahars at volcanoes other than Somma-Vesuvius, and we do not conduct an uncertainty quantification. Thus, the predictions of the lahar model must be considered as illustrative and highly uncertain. Nevertheless, they provide indications of the possible lahar dynamics and demonstrate the utility of coupling the statistical model of lahar initiation volume to a deterministic flow simulator.

9.5 Probabilistic Volcanic Multi-Hazard Assessment at Somma-Vesuvius

9.5.1 *Multihaz* assessments and behavior

Once *Multihaz* is parameterized, a variety of probabilistic queries can be done on the model. These can be classified into two principal categories: causal (i.e. forecast) and evidential (i.e. inference) queries. In the first case, a given node is instantiated (i.e. one of its states is set to be true) and the probability distributions over the path through its children nodes are examined. In the case of evidential inference, the reasoning is done by analysing the probability distributions of nodes which are ancestors of the instantiated node. That is, the forecast focuses on the outcome while the inference is an investigation about the causes of a specific outcome. Let us consider the largest catchment in our dataset (#14, area $\sim$ 23km^2) after the occurrence of an eruption of any size. The *Multihaz* assessments

for this situation are shown in Figure 9.7. If no node is instantiated (i.e. we do not have any evidence to input into the BBN), we observe that the probability of no lahars occurring, i.e. $P(IV = zero)$, is around 30% while large lahars have a 10% chance to occur (Fig. 9.7a). However, if the RI is instantiated to the state "low" (Fig. 9.7b), we see that the probabilities at the nodes WR, RD, RE and IV are all modified. In particular, the probability of no lahars being triggered becomes 54%, as a result of the increase in probability of WR=ifl (Figs. 9.4d, 9.7b). If the instantiation of *Multihaz* is RD=high, the situation is quite different (Fig. 9.7c): the probability of no lahars is 15%, that of large lahars is similar (14%) and low and medium lahars are the most likely outcomes (32% and 39%, respectively). This responds to the probability distribution at the RE node (Fig. 9.7c) which is mostly influenced by the combination of: (i) RD being high; and (ii) WR=roff and WR=both being relatively likely. Thus, the whole effect is that, for example, the probability of no lahars occurring clearly diminishes (Figs. 9.4, 9.7c).

In addition, we note that the probability distribution at the PV node does not change after the instantiation of the RI and RD nodes (Fig. 9.7b, 9.7c, respectively). This is owing to the fact that, according to the *Multihaz* structure, PV is independent of RE (and hence of its ancestors) unless IV is observed (Fig. 9.2; e.g. [252]). Finally, while instantiating RI to "low" causes a jump in P(RD=high) from 11% (Fig. 9.7a) to 63% (Fig. 9.7b), it is seen that instantiating RD to "high" does not cause such jump in the probability of RI=low (which changes from 0.01% to 0.057%). This is due to the way in which Bayesian updating is performed in BBN models (see Chapter 4). The probability P(RI=low|RD=high) in Figure 9.7c is calculated as follows:

$$P(RI = low|RD = high) = \frac{P(RD = high|RI = low) \cdot P(RI = low)}{P(RD = high)} \tag{9.3}$$

where P(RI=low) and P(RD=high) are the probabilities shown in Figure 9.7a (i.e. 0.01% and 11%, respectively). Therefore, even though P(RD=high|RI=low) is quite big (63%), the very small probability of RI=low, before instantiation, makes RI=low to be very unlikely, notwithstanding that the evidence says that RD=high (Fig. 9.7c).

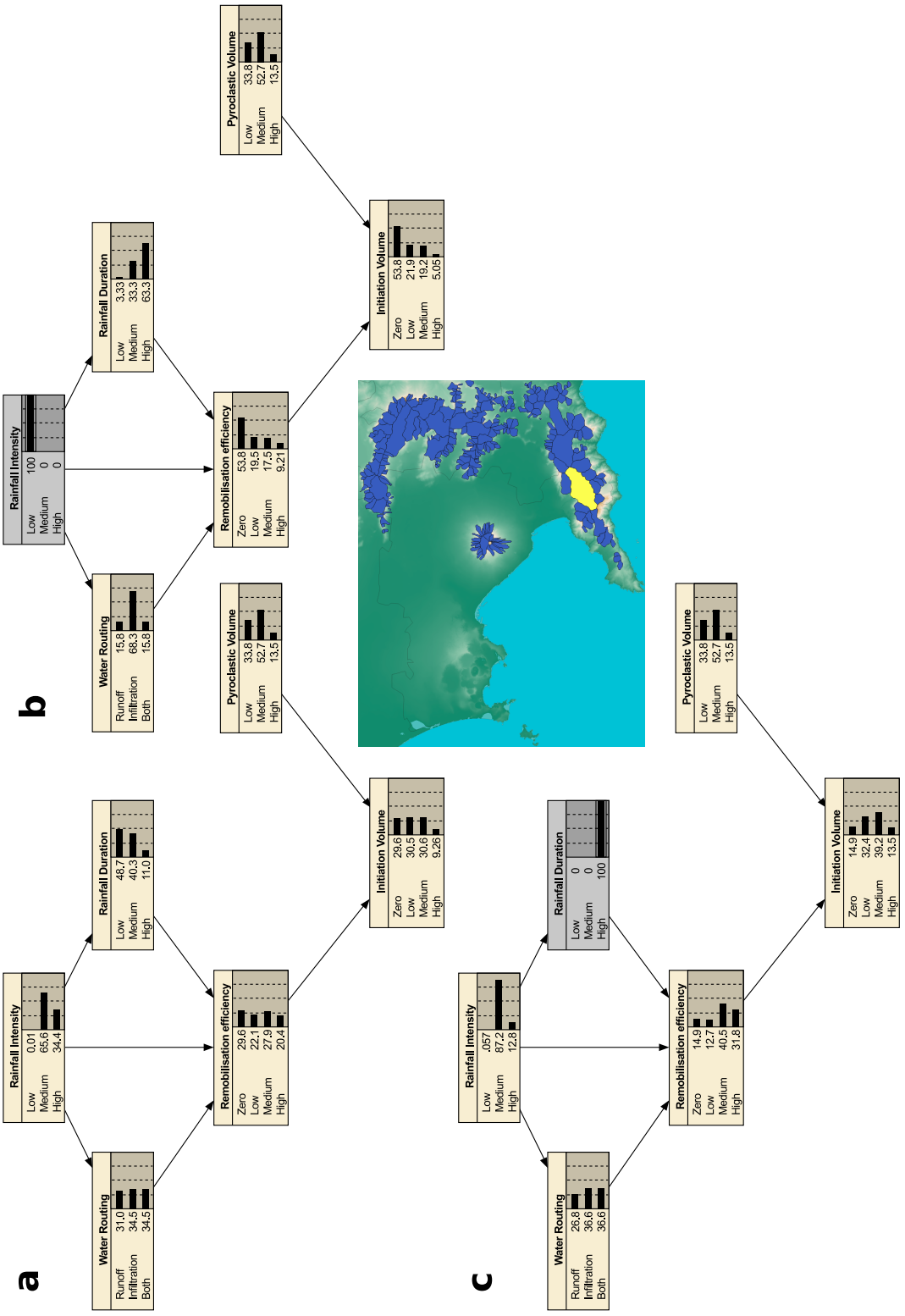

FIGURE 9.7: Example of the probabilistic behaviour of *Multihaz* implemented at Somma-Vesuvius (Italy), taking the catchment #14 (in yellow in the map above) as an example. All the BBNs are linked to the occurrence of an eruption of an unknown (any) size. Causal (forecast) and evidential inferences can be done by instantiating different nodes of the network (highlighted in grey; see text for more details): (a) initial parameterization of the BBN; b, updated probabilities across the BBN after instantiating the RI node to the state "low"; (c) updated probabilities across the BBN after instantiating the RD node to the state "high". From [109].

Similarly to our observations of the pyroclastic volume from tephra fallout and dense PDCs (see subsection 9.3.3), the probability estimates of *Multihaz* parameterized at Somma-Vesuvius depend on the location of the catchment with respect to the expected spatial distribution of the PV variable. For medial-distal catchments located over the Apenninic reliefs, tephra-fallout accumulation is expected to be greater towards the east and southeast of Somma-Vesuvius in comparison to the northeast (Fig. 9.8; [70]). Therefore, the *Multihaz* assessments reflect this spatial distribution on the PV node. In particular, the changes in probability at the IV node are more evident when the RE is likely to be medium or high (Fig. 9.8). This is because the influence of the PV node on the IV node is also related to the probabilistic distribution on the RE node. In other words, even if it is likely to have a large volume of pyroclastic material at one catchment, if this material cannot be mobilised by rainfall by runoff or landsliding (so that RE=low or even RE=zero), the probability of having large lahars will be small. Moreover, the spatial distribution of pyroclastic volumes is not the only factor to be considered in the parameterization of the PV node. It may be possible that a very small catchment, situated on the tephra dispersion axis, is expected to store an amount of pyroclastic material that is equal to or lower than a much larger catchment situated further the dispersion axis but still downwind from the volcanic vent. We test such situations by looking at *Multihaz*, in the eventuality of a large eruption occurring, and for the following catchments (Fig. 9.8): #195 ($\sim$ 2km^2, northeast), #225 ($\sim$ 10km^2, northeast), and #277 ($\sim$ 2km^2, east). If we instantiate the rainfall-intensity node to RI=high and water-routing node to WR=both (that is, rainfall is quite intense but not enough for the water to be routed predominantly by runoff and, thus, there is also infiltration and a consequent rapid increase in the pore-pressure within the deposit) we can find that the probabilities at the RD and RE nodes mimic each other for all three catchments, since they all share the same parameterization of the CPTs for RD and RE (Fig. 9.8). However, in terms of initiation volume, we notice the important differences in probability for small, medium and large lahars, especially if we compare: (1) catchments with similar area but that are located at two different azimuths from the volcano (e.g. catchments #195 and #277, Fig. 9.8a, c); or (2) catchments with similar locations but with greatly differing areas (e.g. catchments #195 and #277, Fig. 9.8a, b). In the case of catchments #225 and #277 (Fig. 9.8b, c), the differences due to catchment size are offset by the location of the catchments relative to the primary dispersion axis. Nevertheless, we find that the probability of having large lahars

is still around 3% greater at the small catchment (#277, Fig. 9.8b, c).

As a further check of our BBN parameterization, if we instantiate the WR node to "infiltration" (that is, even though the rainfall is intense, the deposit is able to route water predominantly through infiltration), the probability of RE=zero raises to 55% for all catchments and the differences in the probability of non-zero IV states between the catchments become smaller. For instance, P(IV=high | RE,PV) become 10% and 11% for catchments #225 and #277, respectively, and P(IV=low | RE,PV) is 22%, 13% and 12% for catchments #195, #225 and #277, respectively. In the situation deployed in Figure 9.8, the latter probabilities are 44%, 28% and 25%, respectively. Note that all the previous reasoning about the *Multihaz* assessments and behaviour is done for specific eruption sizes: any size in Figure 9.7 and large size in Figure 9.8. However, we parameterize *Multihaz* models for each catchment (273) and four different eruption sizes: small, medium, large and any, thus the total number of *Multihaz* models built is 1,092. In the following subsection, we concentrate on some selected scenarios to illustrate the coupling between *Multihaz* and the lahar simulator, *LaharFlow*.

9.5.2 Scenario-based probabilities for initiation volumes

Given the large computational cost that would be required to explore all the possible combinations in terms of: (1) the size of the eruption that preceeds the rainfall-triggering of lahars; and (2) the lahar volumes that could be generated from each of the 273 catchments defined; we focus our preliminary application of the proposed probabilistic multi-hazard framework on three specific scenarios. These scenarios are fixed as a function of: (i) an eruption of a specific size occurring at Somma-Vesuvius; (ii) a specific value of RE triggering the rainfall lahars; and (iii) the maximum value of IV that a specific catchment can produce, given (i) and (ii). The multi-hazard scenarios are:

- Scenario 1: a large eruption occurs at Somma-Vesuvius and lahars are triggered by means of high remobilization efficiencies (i.e. RE=high).
- Scenario 2: a medium eruption occurs at Somma-Vesuvius and lahars are triggering by means of medium remobilization efficiencies (i.e. RE=medium).

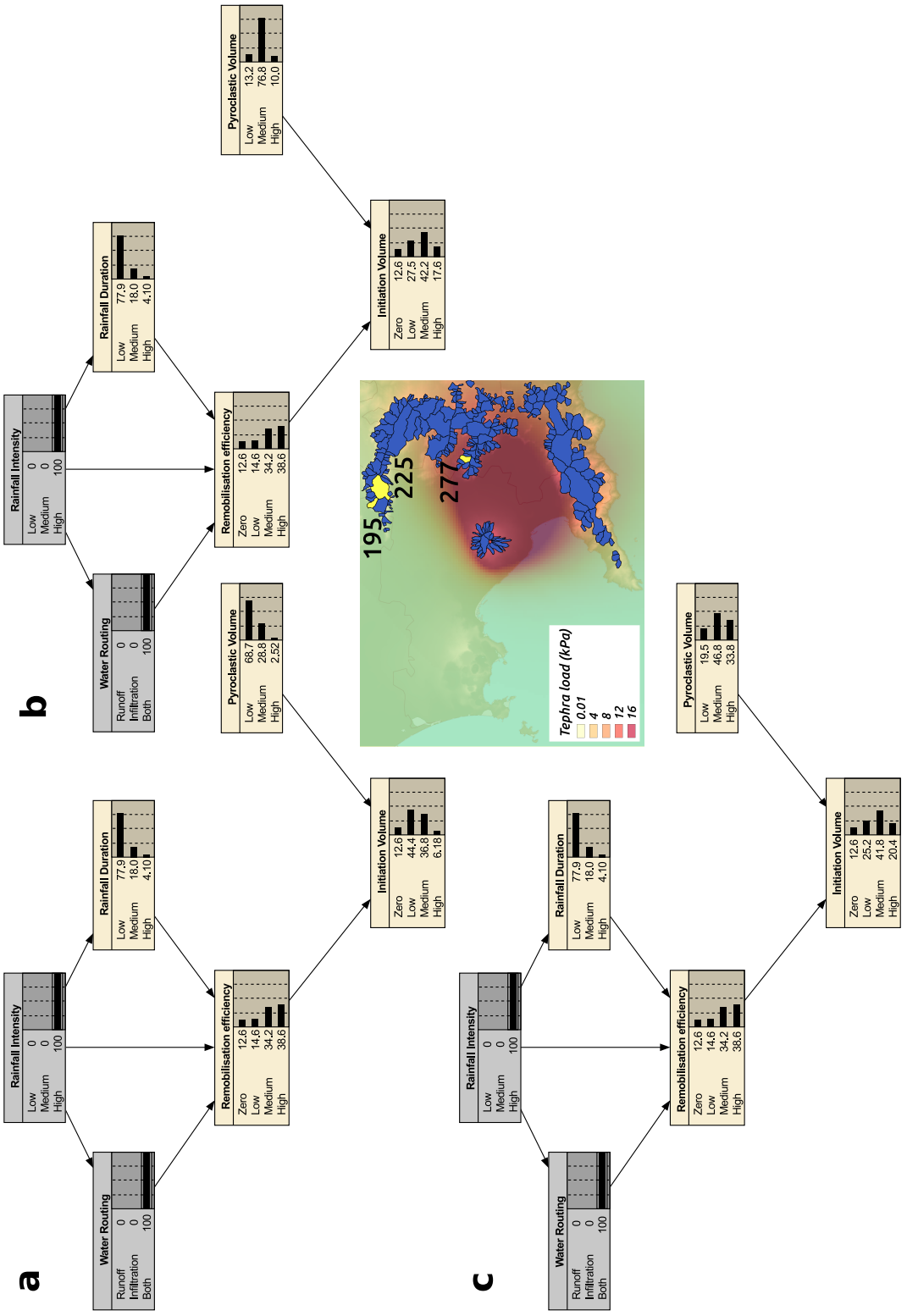

FIGURE 9.8: Example of the probabilistic behavior of *Multihaz* implemented at Somma-Vesuvius (Italy), taking three catchments (#195 -inset a-, #225 -inset b-, and #277 -inset c-) as an example of variability in catchment area and position with respect to the expected maximum accumulation of tephra (see text for more details). All the BBNs are linked to the occurrence of a large eruption and are instantiated on the RI and WR nodes to the states: RI=high and WR=both (infiltration and runoff). In the map above, the aforementioned catchments are highlighted in yellow. In addition, the expected tephra load (median value), given the occurrence of a large eruption, is displayed. From [109].

- Scenario 3: an eruption of an unknown size (i.e. any) occurs at Somma-Vesuvius and lahars are triggered by means of low remobilization efficiencies (i.e. RE=low).

Even though our multi-hazard assessment is scenario-based, our integrated framework gives the possibility to select a variety of scenarios depending on the scope of the hazard analysis. For each selected scenario, the *Multihaz* model can provide the probability of lahars of specific volumes happening (Fig. 9.9). By coupling these probabilistic assessements with the lahar simulator, the aleatory uncertainty modeled by *Multihaz* can be propagated into hazard footprints of lahars (see next subsection 9.5.3; e.g. [31, 83]). In this subsection, we detail the probabilistic assessments provided by *Multihaz* for each catchment and scenario explored.

As related previously, the *Multihaz* model, for each catchment, shares a common parameterization of the WR, RD, RE and IV nodes but it has its own parameterization for the RI and PV nodes (see section 9.3). Figure 9.9 shows the probabilities for the different states of the IV node, for each of the explored scenarios. To aid in visualising the results, we divide the catchments into four big zones: (1) medial-distal catchments (∼20-30 km from the vent) towards the SE and E; (2) medial-distal catchments towards the NE; (3) medial catchments (∼15-20 km from the vent) towards the E; and (4) proximal catchments (within a radius of about 3-4 km from the vent). The first scenario (Fig. 9.9a) is characterized by an almost constant probability for the occurrence of medium lahars while the probabilities for small and large lahars are both smaller than the former and tend to mirror each other[2]. In the catchments of zone 4, the probability of small lahars goes down up to be virtually zero over the catchments located on the south flank of Somma-Vesuvius. In these catchments, IV=high is the most likely state, given scenario 1 (Fig. 9.9a).

The second scenario (Fig. 9.9b) is characterized by small and medium lahars having relatively similar probabilities of occurrence in zones 1 and 3. The probability of large lahars increases slightly over zone 3 and more significantly over zone 4, similarly to what observed in scenario 1 (Fig. 9.9a, b). Nonetheless, large lahars are never the most likely outcome of scenario 2.

The third scenario is strongly dominated by all catchments having IV=low as their

[2]Note that the states of each node are mutually exclusive and exhaustive, so the sum of their probabilities must be 1. Besides, $P(IV = zero|RE \neq zero) = 0$ in our parameterization of *Multihaz*).

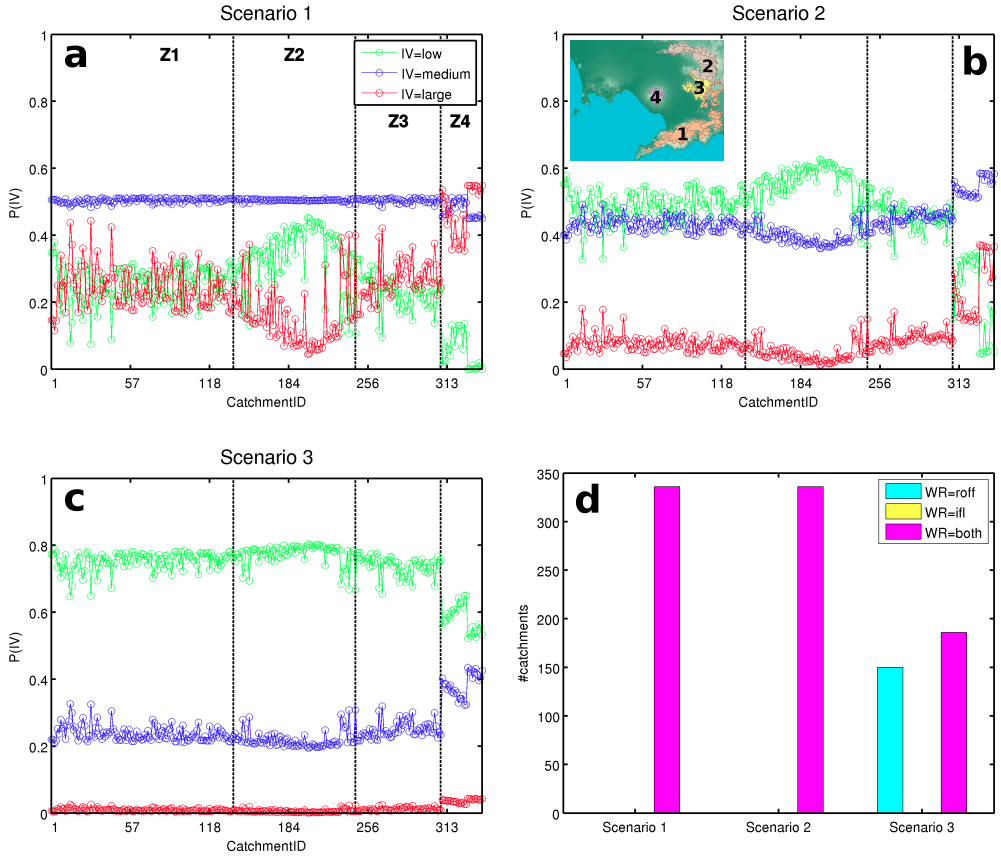

FIGURE 9.9: Probability distributions for the initiation volume (IV) node across all the catchments defined at Somma-Vesuvius (Italy) and surroundings, according to three different scenarios: (a) high remobilization efficiency taking place after a large eruption; (b) medium remobilization efficiency taking place after a medium eruption; and (c) low remobilization efficiency taking place after an eruption of any size. Z1, Z2, Z3 and Z4 are large grouping of catchments (or zones) and their locations are shown in the inset map of graph (b). Graph (d) displays the number of catchments for which the most-likely water-routing mechanism (WR) is runoff (roff), infiltration (ifl) or both, according to the *Multihaz* assessments for each scenario (see text for more details). From [109].

most likely state (Fig. 9.9c). The probability of having medium lahars increases over zone 4 coinciding with a very slight increase in the probability of large lahars, up to 4-5% (Fig. 9.9c). The jump in probability of occurrence for small and medium lahars inside zone 4 marks the separation between the catchments located on the north flank of the volcano, where small lahars are much more likely in scenario 3, and those on the south flank, where small lahars are only slightly more probable than medium lahars (Fig. 9.9c). Finally, we examine which water-routing mechanism is the most likely state for each of the three scenarios explored (Fig. 9.9d). It is clear that the predominant mechanism is the partition between runoff

and infiltration (WR=both) in the cases in which the remobilization efficiency is medium or high (scenarios 1 and 2). When RE=small (scenario 3), approximately half of the catchments still have WR=both as the most-likely state. The remaining half display WR=roff as their most-likely state (Fig. 9.9d).

9.5.3 Probabilistic scenario-based hazard assessment

The results shown in the previous subsection can be merged with lahar simulations to map the possible impact of such lahars in probabilistic terms. For each of the selected scenarios, we run *LaharFlow* simulations at each of the 24 simulation groups aforementioned (see section 9.4). We define our final hazard domain as a grid with 100 m of spatial resolution that, for each simulation group, extends from the source areas of lahars through the areas over which they propagate. In the end, at each grid point of the hazard domain, we are able to compute three values of lahar flow depth and speed and three values of probability associated with such event, according to the *Multihaz* assessments. In reality, we derive these probability values by multiplying the probability of each catchment to generate the volume of lahars simulated with *LaharFlow*, given a specific scenario:

$$p_{ij} = \prod_{k}^{N_j} P_k(IV_{max}|sce_i) \tag{9.4}$$

where p_{ij} is the probability assigned to the hazard footprint computed with *LaharFlow* for the scenario i and the simulation group j; N_j is the number of catchments that form the simulation group j; $P_k(IV_{max}|sce_i)$ is the probability of the catchment k to trigger lahars with the maximum possible volume for the catchment (IV_{max}, the volume simulated with *LaharFlow*), given the scenario i (sce_i). These P_k values come from the *Multihaz* model implemented at each catchment and for an eruption of the size indicated by a specific scenario.

Our way of calculating p_{ij} implies that some assumptions about the probabilistic independence between the P_k values, in a simulation group, are thought to hold: (1) the triggering rainfall is homogeneous over the catchments of the same simulation group; (2) the catchments of the same simulation group are located close enough to each other that changes in available tephra volume (i.e. PV) are only due to the catchment area (and not to the spatial distribution of PV);

and (3) the spatial distribution of the catchment area does not show any clustering pattern, that is: small and large catchments do not tend to cluster together, spatially. We acknowledge that some of these assumptions may not be accurate in some cases: e.g. assumption (2) could be reasonable for tephra fallout but it may be questionable for dense PDCs in the presence of topographic barriers, such as Mount Somma. Relaxing these assumptions would require to develop another probabilistic model to assess the dependencies among the P_k values for each simulation group and this is beyond the scope of this chapter. Here we intend to present an initial application of the proposed probabilistic multi-hazard framework at Somma-Vesuvius and surroundings.

Hazard footprints of lahars

The lahar flows simulated at Somma-Vesuvius and surroundings tend to be channelized following the main (narrow) valleys that descend from their initiation points but there are also cases in which steep short valleys lead to lahars that converge and accumulate a certain amount material over larger flat areas, like in the area near Sarno. We summarize the observed patterns in lahar propagation in Figure 9.10. We select four simulation groups which are characterized by: (a) including catchments with large areas; (b) representing one of the big zones defined in the previous subsection; and (c) having densely-populated areas nearby. Thus, the simulation groups are the following:

- Simulation group 3 (Fig. 9.10a): it is located in the area of Gragnano in zone 1, in particular in medial sectors towards the SE.
- Simulation group 19-20 (Fig. 9.10b): it is located in the area of Avella in zone 2, that is: medial-distal sectors towards the NE.
- Simulation group 24 (Fig. 9.10c): it is located on the flanks of Somma-Vesuvius in zone 4, i.e, the most proximal sector (within 3-4 km from the vent).
- Simulation group 22 (Fig. 9.10d): it is located in the area of Sarno in zone 3, i.e. medial sectors towards the E.

In Figure 9.10, we show the hazard footprints of the flow-depth of lahars computed for scenario 1, the one which produces the most voluminous lahars. In simulation

group 3, the flows propagate following the principal valleys of the catchments from SE to NE, primarily, and they spread out after reaching the flat area where Castellammare di Sabbia is located. The longest runout of lahars in the simulation group is about 7-8 km (Fig. 9.10a). The maximum values of flow depth tend to be around 10 m while the maximum values of speed are greater than 25 m/s, close to the initiation of some lahars, but they are around 5-10 m/s over the flat lowlands.

In simulation group 19-20, the flows propagate following the principal valleys in some cases, especially on the eastern and southeastern sectors of the hazard domain (Fig. 9.10b). The largest flow, formed over the southeastern sector, can develop cross-section widths of few hundreds of metres while keeping flow depths not far away from 10 m (Fig. 9.10b). The flow crosses the area where Mugnano di Cardinale, Avella and other municipalities are located and stops after approximately 15 km of propagation. The maximum speeds recorded in the simulation can be 30 m/s at the initiation areas but they descend up to about 5 m/s over the flat areas.

In simulation group 24, the flows trigger from the upper part of the Somma-Vesuvius edifice, including the north flank beyond Mt Somma, and propagate radially developing braided patters as the topography is less confining than in the previous two simulation groups (Fig. 9.10c). The majority of the lahars simulated on the south flank reach the sea after having traveled for approximately 5-6 km. The lahars on the other flanks of the volcano have similar maximum runouts (Fig. 9.10c). The maximum flow depths are around 10 m in some proximal sectors where flows might get channelized. Maximum flow speeds can reach 25 m/s and be maintained around 10-12 m/s over proximal-medial sectors (up to ∼4 km). On distal sectors (∼4-6 km), the lahars slow down to speeds of 5 m/s or lower (Figs. 9.10c, 9.1a).

Finally, in simulation group 22, the flows propagate short distances along quite straight valleys before reaching the flat area on the Campanian Plain where Episcopio and Sarno are located. The lahars on the oriental part of the hazard domain converge over the Campanian Plain to produce an extended inundated area, dominated by flow depths equal to or greater than 10 m (Fig. 9.10d). The maximum runouts of the whole simulation group are not greater than 3 km. In terms of lahar speed, maximum values can be above 30 m/s nearby the initiation and be sustained around 10-15 m/s over the initial part (∼1 km) of the Campanian Plain.

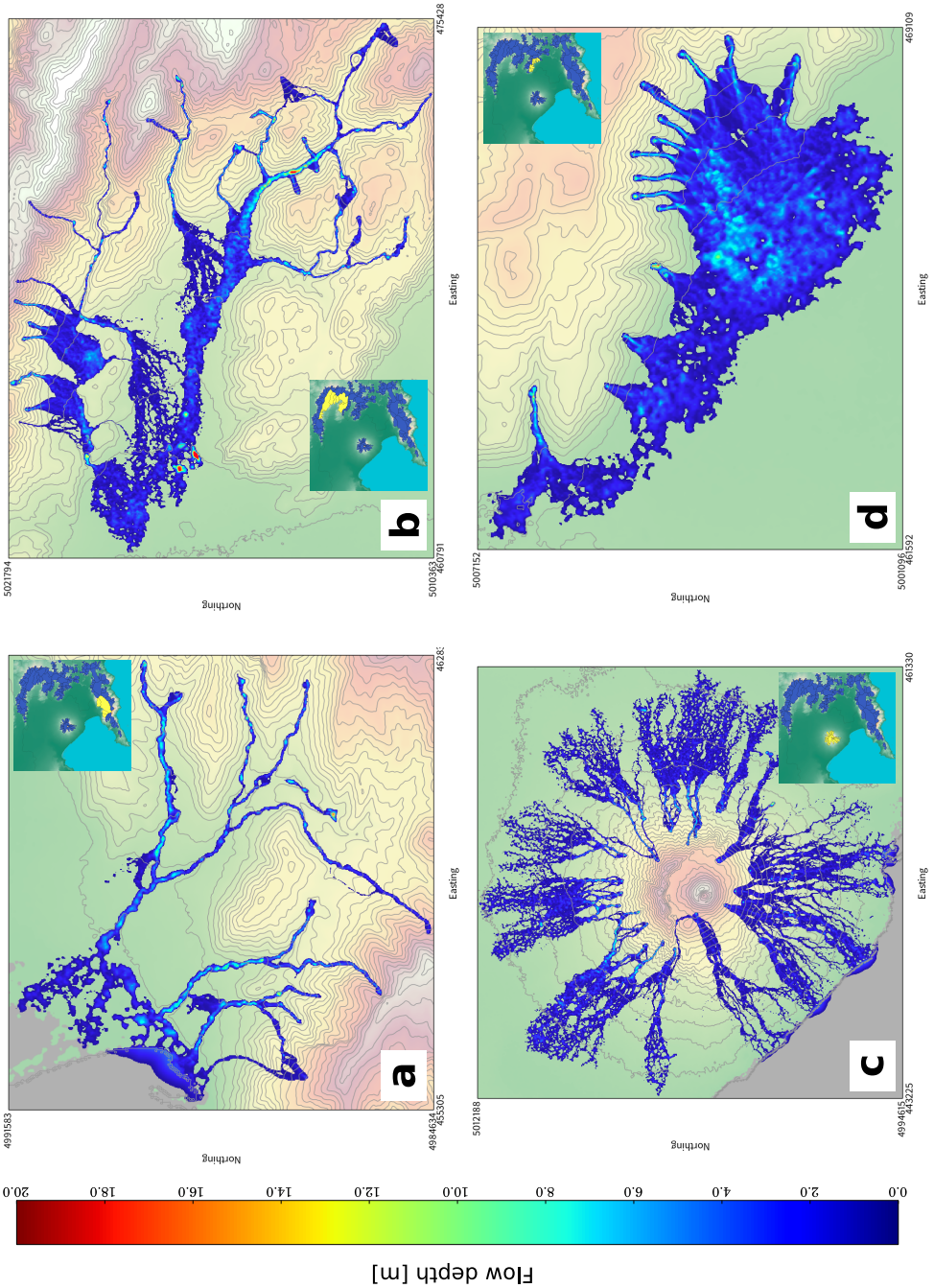

FIGURE 9.10: Hazard footprints of flow depth for rain-triggered lahars at four selected locations (simulation groups) on Somma-Vesuvius and surroundings (Italy) computed with the *LaharFlow* physical model. The locations of the catchments belonging to each simulation group are given in yellow within the inset of each plot: (a) simulation group 03, (b) simulation group 19-20, (c) simulation group 24, (d) simulation group 22. From [109].

Probabilistic output distributions

Combining the probabilistic assessments performed by *Multihaz* with the hazard footprints of lahars computed with *LaharFlow*, we are able to extract discrete probabilistic output distributions for the hazard variables: lahar flow-depth and lahar speed. In Figure 9.11, we show such probabilistic quantification of the lahar hazard for the flow speed and considering the simulation group 24 (Somma-Vesuvius flanks). As previously reported, having three different scenarios permits us to compute three values of the hazard variable (e.g. lahar speed) and having a quantitative description of the likelihood of each initial volume of lahars, plus some assumptions about probabilistic independence between them, allow us to compute the probability value to attach to each lahar speed. The final result, discrete probabilistic distributions of lahar speed, is shown in Figure 9.11c, for the same three example points (red filled circles) used in Chapter 8 (see Figs. 8.4, 8.5). Nevertheless, our hazard analysis permits the evaluation of any desired point along the hazard domain.

We see that the fastest lahars are expected to occur during scenario 1, with the maximum speed recorded at Somma Vesuviana (~ 7 m/s). Scenario 3 is associated with lahars of maximum speeds between 0 and 2 m/s while, during scenario 2, lahars can reach maximum speeds around 2 m/s at Torre Annunziata and Somma Vesuviana and about 0.2 m/s at San Sebastiano al Vesuvio. The probabilities attached to scenarios 1 and 3 are much lower than those assigned to scenario 2 (Fig. 9.11d). The range of lahar speed at San Sebastiano al Vesuvio is narrower than the speed ranges at the other two locations. Thus, the maximum lahar speed at Torre Annunziata during scenario 1 is three times the maximum lahar speed at San Sebastiano al Vesuvio but, during scenario 3, the former is 0 m/s while the latter is around 0.2 m/s. This implies that relatively slow lahars are expected to impact San Sebastiano al Vesuvio, more or less independently of the magnitude of the event, while lahars may reach Torre Annunziata only during large events but these lahars could have much higher speeds than those impacting areas closer to the Somma-Vesuvius central crater (Fig. 9.11).

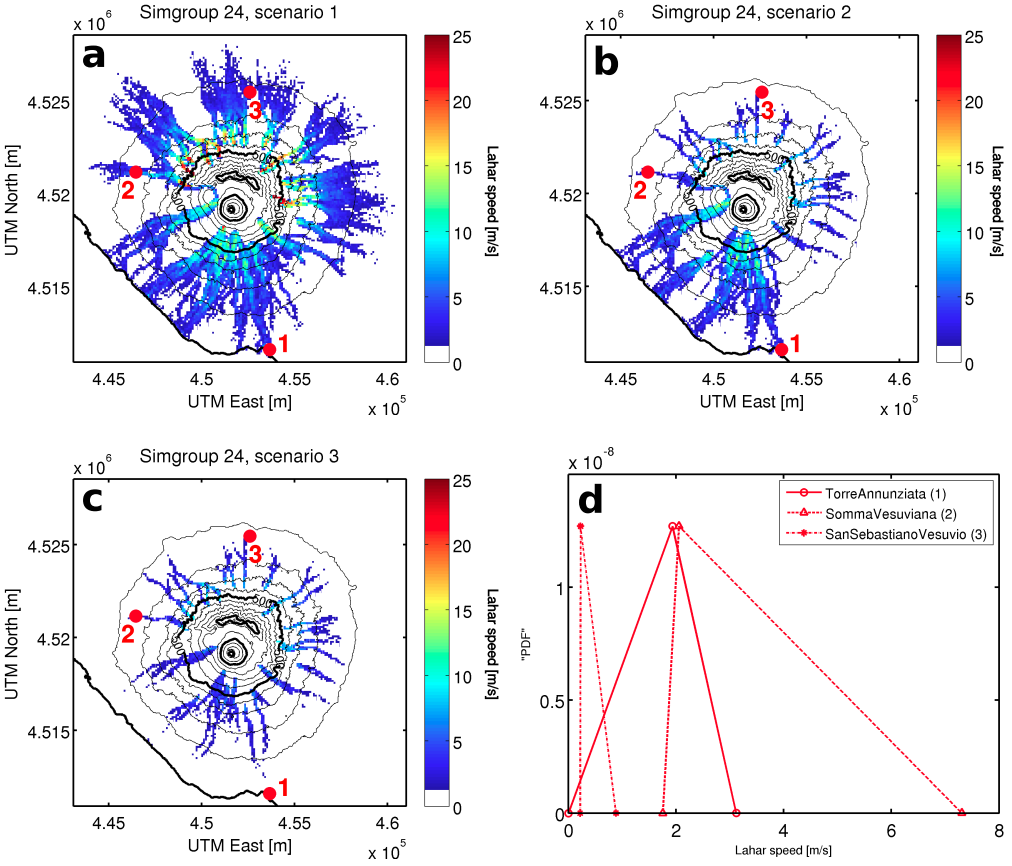

FIGURE 9.11: Probabilistic multi-hazard assessment of rain-triggered lahars at Somma-Vesuvius (Italy). On graphs a, b and c: hazard footprints of lahar speed at simulation group (simgroup) 24 according to the three selected scenarios: scenario 1 (a), scenario 2 (b) and scenario 3 (c). On graph d, probabilistic output distributions for the hazard variable of interest: lahar speed. Note that these distributions are discrete: lines connecting the different points are used to aid visualisation but the actual density of probability between the points is not known (that is why we use "PDF" to refer to the Probability Density Function of the output hazard variable (see text for more details). From [109].

9.6 Discussion and future directions

9.6.1 Use of BBNs in the context of rain-triggering of lahars

The complexity in the spatial and temporal triggering of lahars makes them quite difficult to forecast accurately. In terms of spatial triggering, deterministic physical models of erosive runoff (e.g. [371, 372]) and/or shallow-landsliding (e.g. [162, 178, 373]) are one of the most common strategies to forecast lahar initiation. These approaches are able to describe the main physical processes which are thought to cause the initiation of the hazardous event but, sometimes, their

application is restricted to a small set of values of the model parameters because exploring the aleatory uncertainty (e.g. rainfall intensity and duration) and/or the epistemic uncertainty (e.g. tephra-deposit properties such as infiltration capacity or hydraulic conductivity) may become very challenging computationally. A second main strategy is that of computing probabilities for the lahar/debris-flow/landslide initiation. Some studies use simple physical models in conjunction with PDFs to model the epistemic uncertainty in soil properties (e.g. [177]) while others treat the initiation thresholds (e.g. I-D) as random variables instead of fixed values (e.g. [177, 342]). Our BBN approach follows this second main strategy to deal with the spatial triggering of lahars. We target a simple model that can be easily adapted to many volcanoes, provided that there is a probabilistic description available in terms of: (1) rainfall intensity at the volcano's region; (2) spatial distribution of tephra deposits around the volcano. It is also likely that the specific parameterization of the CPT for the WR node needs to be adapted to each specific volcano, depending on the characteristic median grain size of the volcanic products (e.g. Figure 4 in [92]).

We argue that the point (2) above is one of the major strengths of our multi-hazard framework. The coupling between the areas which are expected to be affected by tephra deposition, given an eruption, and the areas which may act as lahar sources subsequently is rare in the literature (e.g. [101]). However, the links between the spatial distribution of tephra accumulation (as well as the type of tephra deposit) and the magnitude and frequency of triggered lahars have been evidenced at several volcanoes after recent eruptions (e.g. [90, 92, 94, 169]). Morever, the importance of quantifying the aleatory uncertainty in tephra accumulation is highlighted by the presented results. For instance, let us assume that we do not describe this aleatory uncertainty in PV. We can instantiate the PV node to its most-likely state to model this. We take as an example the *Multihaz* model in Figure 9.8a (catchment #195, large-size eruption): PV=low is the most-likely state but PV=medium and PV=high are still possible (Fig. 9.8a). If we set PV=low, we observe that the probability of a large lahar decreases from 6% to 0%. That is, the model is informing that large lahars are impossible (they were unlikely but possible before instantiating the node, when the aleatory uncertainty in PV was considered, Fig. 9.8a). Such low-probability high-consequence situations are very relevant not only in volcanic hazards but in any kind of natural hazard (e.g. [53, 259, 338, 374]). Therefore, recent probabilistic hazard assessments of tephra fallout (e.g. [71, 72, 375]) and/or PDC thickness (e.g. [23, 31]) could be used to

quantify the aleatory uncertainty in pyroclastic volumes expected in catchments of other volcanoes worldwide.

Regarding the probabilistic quantification of rainfall intensity, Intensity-Duration-Frequency (IDF) curves (e.g. [376]) can be available at many volcanic regions around the world (e.g. [162]). From them, a PDF to model the rainfall intensity at the region of interest may be derived, as illustrated in this chapter. The link between rainfall intensity and duration is here assumed to be inverse, that is: the higher the intensity, the shorter the duration. Nonetheless, a model like *Multihaz* can be easily adapted to situations in which these two variables (RI, RD) are thought to be independent [377] or even positively-correlated (e.g. [378]).
We also note that, in some volcanoes, the separation between lahar and no-lahar events, in terms of I-D thresholds, for instance, may not be very clear (e.g. [180]). On the one hand, it is possible that strong mismatches occur between the rainfall measured at the available raingauges and the actual rainfall happening at the lahar-initiation areas (e.g. [176, 379]). This could be corrected either semi-quantitatively (e.g. [380]) or by using the raingauge data in combination with high-resolution meteorological models (e.g. [381, 382]). On the other hand, it seems that multi-parametric analysis (e.g. [343]) and/or physical models for lahar triggering (e.g. [162]) could provide more informative forecasts of lahar activity than simplified I-D thresholds. The approach presented here is an intermediate solution since it uses few variables but can incorporate physical information into the lahar triggering and it describes the natural variability in pyroclastic budgets around the volcano, as detailed previously.

In terms of the triggering mechanism for lahar initiation, *Multihaz* is an attempt to merge two "schools of thought": one that considers erosive runoff as the principal initiation mechanism (e.g. [92, 164, 165, 343, 383]) and the other that deem shallow-landsling as the primary generation mechanism for lahars (e.g. [101, 162, 178]). Discrepancies in interpretation of volcanological phenomena can lead to contrasting model assessments (e.g. [274]) and it is important that the selected model is able to incorporate this information. In *Multihaz*, the key relationships among variables such as RI and RD and the lahar-triggering mechanism are stored in the marginal distributions of the RE node (Fig. 9.4). *Multihaz* could be simply adapted to model only erosive runoff or shallow-landsliding by permanently instantiating WR to "runoff" or "both", respectively (even though WR=ifl also implies the possibility of landslides triggering lahars, Figs. 9.2, 9.3). Deeper

changes in *Multihaz* could be done on the structure, by removing the WR node and adding variables (nodes) which were thought to cause an important effect on the triggering in case of each mechanism, e.g. hydraulic diffusivity (e.g. [162]).

Nevertheless, there are some drawbacks in *Multihaz* and our integrated multi-hazard framework. Regarding the lahar triggering, the most crucial deficiency of our model is that it does not describe the timing of the lahar initiation, only whether a given rainfall event may lead to the formation of lahars of a certain volume or not. The fact of modeling the possible volume at initiation is a step forward compared to other studies in which the outputs are binary: event or no event (e.g. [163, 342, 343]). Still, *Multihaz* is unable to give a detailed temporal analysis of the triggering (e.g. [162, 178]) or even of the spatial changes in lahar susceptibility with time (e.g. [349]).

9.6.2 A probabilistic multi-hazard assessment of lahars

Secondary hazardous volcanic processes, such as lahars, represent a further challenge for hazard assessments in comparison with primary processes such as tephra fallout and PDCs. This is largely due to the fact that the aleatory (and epistemic) uncertainty in the primary processes conditions the spatial and temporal variability in the secondary process (e.g. [92]). Moreover, lahar models can range from semi-empirical approaches (e.g. *LAHARZ*, [345]) to depth-averaged simulators with different degrees of complexity (e.g. [81, 218, 235, 346]). They are readily applicable to scenario-based hazard assessments of lahars (e.g. [230, 365, 384]) but in probabilistic assessments, where uncertainty must be quantified, there is the necessity of finding a balance between how sophisticated the lahar simulator is (i.e. how long their runs take) and how efficient the uncertainty-quantification technique is (i.e. how many runs are needed to quantify uncertainty, e.g. [82]). In this case, it arises a dichotomy among simple and complex physical models, which is common not only to other volcanic hazardous processes (e.g. [28, 70, 103, 115]) but also to other disciplines (e.g. [289]). On the one hand, simple models are computationally fast but their predictions need to be tested against observations (e.g. [103]). On the other hand, complex models are believed to give accurate predictions but their long runtimes tend to be an issue in terms of quantifying uncertainty (e.g. [82, 385]).

Our proposed multi-hazard framework fundamentally relies on the strategy of separating the calculation of the probability of a specific event and the hazard footprint that ensues from this event [23, 31]. This is a great advantage because it implies that changes in the probability distributions of *Multihaz*, for instance due to a modification in the prior table of RI, do not inevitably result in more *LaharFlow* simulations needed to be run. The final probabilistic products that we obtain (discrete output distributions for the lahar speed, Fig. 9.11; or flow depth) are an important output because, similarly to hazard curves, they link the hazard intensity and its probability of occurrence at a given point of the hazard domain. However, our probabilistic output distributions are too discrete (they are based on 3 values only) and we decide not to compute hazard curves from them, since we actually have little information about the exceedance probabilities of extreme values, either small or, more importantly, large extreme values (e.g. [83]). This limitation could be overcome by building a BBN model that used continuous PDFs at each of its nodes (e.g. [386]). Moreover, we find that modeling the dependencies between the probability of lahar occurrence (and volumes) at the different catchments around the volcano can be one crucial aspect to pursue during future research. We observe that, while marginal probabilities at each catchment may be reasonable (Fig. 9.9), the computed joint probabilities, when assuming independence between the probability of lahars at each catchment, may be too low (Fig. 9.11).

We present a parameterization of *Multihaz* that is based upon scientific knowledge about rainfall-triggering of lahars compiled from the literature but BBN models can be parameterized in a more robust manner by expert elicitation procedures (e.g. [274, 294]) or when a substantial amount of data is available so the BBN parameters can be learned directly from these data (e.g. [252, 253]). At volcanic systems where lahars are relatively frequent (e.g. Merapi volcano, Indonesia), large datasets of lahar observations (e.g. [164, 181, 387]) can be available to set up the *Multihaz* parameters. Likewise, lahar observations at any volcano can be used to test the *Multihaz* assessments (Fig. 9.12) for any of its nodes or for groups of nodes (e.g. [253]). The observations that might be collected with this purpose of testing the BBN behaviour can range from: (1) direct observations of the water-routing mechanism, given rainfall intensity, through slope plots (e.g. [350, 364, 388, 389]); (2) discrimination between event/no event, given rainfall intensity and duration, through acoustic flow monitoring (e.g. [181, 343, 390]); (3) estimation of averages or single-event initiation volumes through image and field

analyses (e.g. [169, 391, 392, 393, 394]). The compilation of some of these lahar observations might be boosted by exploiting new technologies such as unmanned aerial vehicles (e.g. [395]).

9.6.3 Lahar hazard at Somma-Vesuvius

As far as we are concerned, the presented results represent the first time in which the following aspects have been developed in a hazard assessment of lahars at Somma-Vesuvius: (1) an explicit and quantitative coupling between the lahar triggering and propagation; and (2) a probabilistic assessment of the lahar initiation volumes. Previous studies have mostly dealt with the analysis of the stratigraphical sequences and historical data of syn-eruptive and post-eruptive lahars (e.g. [170, 172, 198, 200, 396]). These studies indicate that lahar hazard at Somma-Vesuvius can be a persistent and relatively-frequent phenomenon even many years after significant explosive eruptions (e.g. [171, 175, 200]). Nevertheless, we conjecture that persistent lahar activity at Somma-Vesuvius (exclusively linked to new tephra deposits) may be much shorter than in other volcanic systems due to the non-confining topography that dominates the proximal-medial areas around the Somma-Vesuvius' cone. This clearly contrasts with the situation at volcanoes such as Mt Saint Helens, USA [94] or Mt Pinatubo, Philippines [90]. For instance, after the 1991 eruption at Mt Pinatubo, approximately 1 km^3 of PDC deposits was stored by the Marella-Santo Tomas watershed (area $\sim$71 km^2, [179, 337]). In contrast, a similar volume of PDC deposits from the Avellino eruption at Somma-Vesuvius spread over an area of nearly 700 km^2 [26, 232], which, besides, is characterized by predominantly low-angle slopes.

Other hazard studies of water-sediment flows at Somma-Vesuvius have focused on the detailed description of the susceptibility of different catchments (both around the volcano and in very distal sectors) to act as sources for these volcaniclastic flows according to: (a) the spatial distribution of past pyroclastic deposits; and (b) the hydrogeomorphological characteristics of these catchments (e.g. [173, 174]). Very few studies have analysed the propagation of lahars at Somma-Vesuvius (e.g. [362]). In their study, [362] focused on the maximum expected eruptive event at the volcano which, according to the emergency plan implemented by the Italian civil protection, is a sub-Plinian I eruption similar to the 1631 AD eruption (e.g. [89,

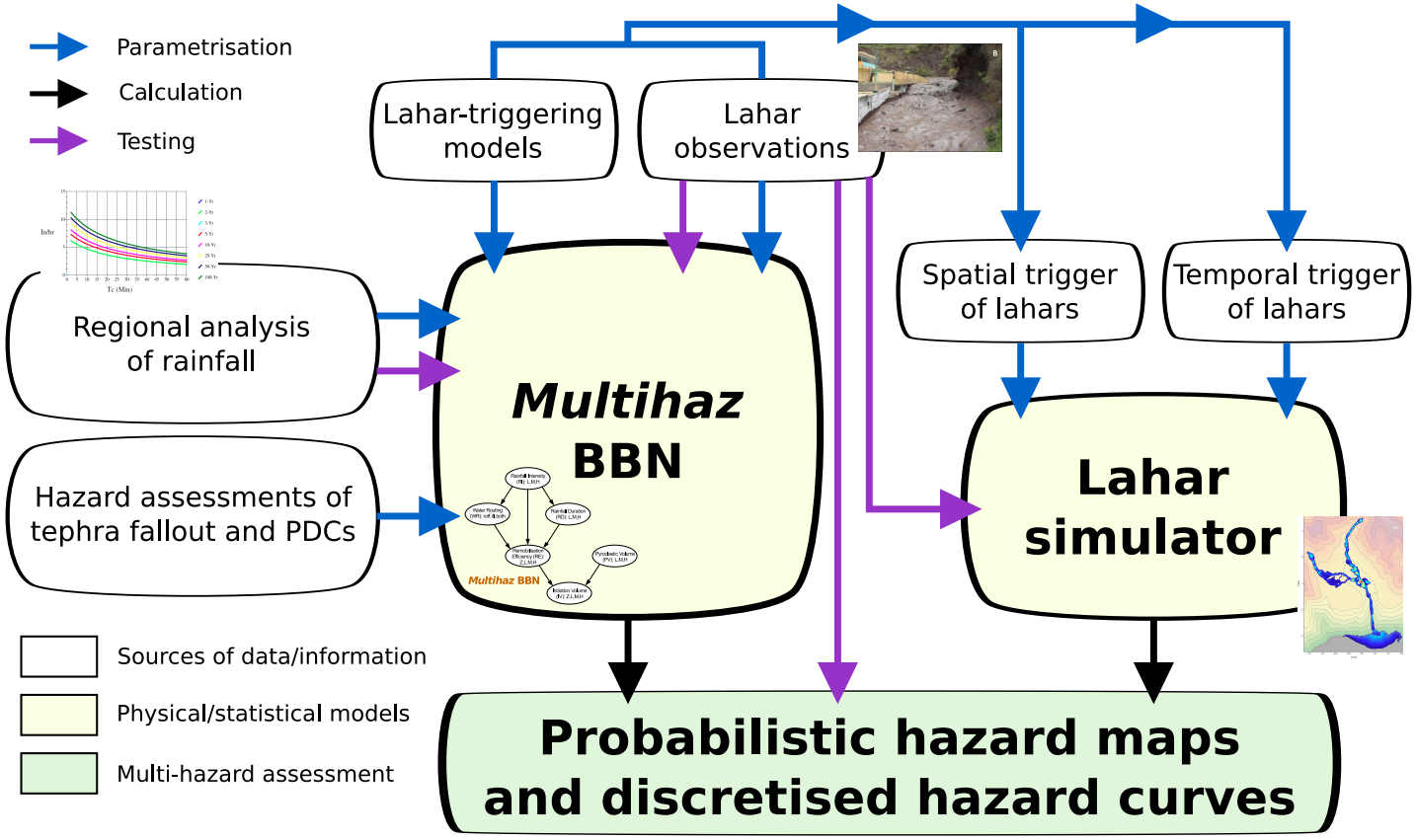

FIGURE 9.12: Summarizing scheme of the presented framework for probabilistic volcanic multi-hazard assessment with focus on rain-triggered lahars (see Figure 9.1), including some possible future research directions to improve such multi-hazard assessment (or similar ones). Observations coming from the regional rainfall phenomenology and the lahar events at the volcano of interest can be used to test the assessments made by the *Multihaz* BBN (purple arrows). Moreover, the lahar observations can serve to test the performance of the lahar simulator and, if there is a certain amount of data, the probabilistic multi-hazard assessment. Likewise, different sources of information (white boxes) may be utilised to refine the *Multihaz* and the lahar-model parametrisations, including the temporal trigger of lahars (which is not treated in our study). See text for more details. From [109].

198]). We overcome this limitation by modeling the aleatory uncertainty in tephra-fallout dispersion and dense-PDC deposition, as previously discussed. However, our modeling of tephra dispersal does not explicitly consider the occurrence of long-lasting violent Strombolian/ash-emission eruptions [89] which might produce a long-term tephra availability for lahars over the proximal sectors of the volcano (e.g. [343]).

Contrarily to what stated by [362], our results do not identify the Acerra-Nola plain as, possibly, the most-hazardous area in term of rain-triggered lahars. The closest catchments to the central part of the plain (approximately catchments #200-225, Figs. 9.8, 9.9, zone 3) show the lowest probability of producing large lahars of all our selected catchments (Fig. 9.9). Additionally, the *LaharFlow* runs for the simulation group 19-20 do inundate the eastern part of the Acerrra-Nola plain but do not have maximum runouts as long as the flows simulated by [362]. We argue that the value of rainfall intensity used by the authors (peak intensity at 108 mm/h during 0.5 h of rainfall) might be too elevated, taking into account the results presented in the recent hydrological report for the central Campania region [360], where the maximum rainfall intensity, for an infinitesimal short rainfall (i.e. duration approaches 0), is estimated to be just above 85 mm/h for the area where the Acerra-Nola plain is located.

Finally, we compare our hazard footprints computed for the simulation group 22 (Sarno-Episcopio area) with the tragical event of the 5 May 1998 (e.g. [171, 172, 397]). Leaving aside the potential differences in the triggering mechanism of lahars or debris flows among syn-eruptive flows on fresh pyroclastic material and inter-eruptive flows on pyroclastic soils (e.g. [170, 398]), we concentrate our attention in the hazard footprints, including the specific values computed for the flow depth and speed. In terms of spatial extent of the flows, we find the scenario 3 to be, qualitatively, the one that resembles the actual flows the most. Scenario 2 and, particularly, scenario 1, have larger areal extents. Moreover, the hazard footprint for scenario 1 (Fig. 9.10c) displays high values of lahar flow depth (around 10 m) over a considerable flat area over Episcopio. Similar high values may have occurred on sectors close to the initiation (e.g. [399]) but not after the main break in slope. Likewise, the maximum speeds for the lahars simulated in scenario 1 (up to 25-30 m/s) confirm that this scenario could be potentially more dangerous than the event in 5 May 1998, where flows reached maximum speeds around 14-20 m/s (e.g. [172]).

Chapter 10

Summary and general conclusions

This PhD was conceived with the major goal of developing structured, robust and transparent procedures to compute probabilistic hazard of PDCs and multiple volcanic hazardous processes, specifically in a target region that is crucial for Italian volcanic risk: the Campania region. The starting point were simple physical models of PDCs which could be run a great many times thus easing the quantification of the large uncertainties linked to the volcanic hazard assessment.

One first step was to check the suitability of the Energy Cone model [132] to calculate probabilistic hazard assessments of PDCs. The findings derived from a robust statistical testing of Monte Carlo outputs of the Energy Cone model against data from past PDC deposits at Somma-Vesuvius and Campi Flegrei, in Italy (see Chapter 3), indicated that the Energy Cone performs quite well, provided that the volcanic system of interest is not characterized by PDCs that are predominantly channelized, even through small topographical features (see Chapter 5 and [103]).

The search for improving the quantification of epistemic uncertainty in probabilistic volcanic hazard assessment led to the implementation of a Monte Carlo procedure to explore and quantify different sources of epistemic uncertainty in modeling of PDCs through the Energy Cone (see Chapter 6). The computed ranking of uncertainties permitted the identification of theoretical uncertainty (related to possible the relationship between collapse height and effective friction coefficient) as the largest source of epistemic uncertainty. Other sources have a smaller impact on the model outputs. Particularly, input uncertainty (linked to the DEM resolution) is almost negligible, which is in clear contrast to what has

been seen in other more complex PDC models, like Titan2D (see Chapters 6, 8 and [104]).

Having checked positively the suitability of the Energy Cone for probabilistic volcanic hazard assessment and having obtained an objective quantification of epistemic uncertainty, the logical successive step was to utilize this PDC model to populate the final nodes of the BET_VH model [49, 242]. Moreover, the BET_VH provided the opportunity for homogeneizing the hazard assessments coming from the two volcanoes (Somma-Vesuvius and Campi Flegrei). Thus, a first-ever probabilistic volcanic hazard assessment of PDCs from multiple volcanoes, a single target area (the city of Napoli and surroundings) and quantification of both aleatory and epistemic uncertainty was computed. The results point out that the downtown of Napoli has a ∼2% probability of being invaded by PDCs, from at least one of the two volcanoes, in the next 50 years. This same probability is about 5% over the western part of the city and it is around 8-10% along the whole southern flank of Somma-Vesuvius (see Chapter 7 and [105]).

In order to extend the previous PDC hazard analyses to probabilistic assessments that could be informative for the quantification of volcanic risk, the Titan2D model [218] was selected to simulate dense pumice flows at Somma-Vesuvius (PDCs at Campi Flegrei are predominantly dilute, see Chapter 3). The long runtimes of the model forced us to use Polynomial Chaos Quadrature (PCQ), instead of Monte Carlo sampling, to quantify aleatory uncertainty. The initial Titan2D-PCQ analysis was then combined with the BET_VH model to assess epistemic uncertainty and probabilistic hazard curves (e.g. [76, 83]), for flow depth and speed, were computed at each grid point over the hazard domain around Somma-Vesuvius. Dense PDCs with depths equal to or greater than 1 m and speeds equal to or greater than 2 m/s are 40-70% probable to cover proximal areas (2-3 km) and 10-30% probable to cover medial areas (5-6 km) around the current central crater, in the event of an eruption from this position. Dynamic pressures of few hundreds of kPa (which would likely produce extensive devastation on the buildings around Somma-Vesuvius) could occur, on average, one every ten eruptions of the volcano (see Chapter 8 and [107]).

The final step was to perform a probabilistic volcanic multi-hazard assessment through the development of a framework that combines probabilistic hazard analyses of tephra fallout and dense PDCs via Bayesian Belief Networks (BBNs, e.g.

[253]) with a physical model for lahar propagation (*LaharFlow*, [235]). The flexibility and high modularity of BBNs permits modeling of (aleatory) uncertainty more explicitly and at a level of refinement that the BET_VH does not include. Thus, our BBN model (*Multihaz*), implemented at Somma-Vesuvius, can estimate the spatial probability of occurrence (and volumes) of rain-triggered lahars by considering in detail: (1) physical mechanisms of lahar triggering; (2) probabilistic analyses of regional rainfall; and (3) probabilistic hazard assessments of tephra fallout [70] and dense PDCs (adapted from Chapter 8, [107]). The *LaharFlow* model served to propagate aleatory uncertainty in lahar triggering towards hazard footprints of these volcaniclastic flows. The probabilistic multi-hazard assessment was found very dependent on the eruption size considered and the location of the hydrological catchments. Catchments towards the ENE (main tephra-fallout dispersion axis) and, especially, those located over the volcano flanks (dense-PDC sedimentation) have the greatest potential for triggering medium and large lahars. However, we find that probabilities of exceeding different thresholds of lahar speed at points around Somma-Vesuvius may be too small due to oversimplifications in the process of combining the probabilities calculated by *Multihaz* at each catchment. Robust spatial analyses that allow to correlate the availability of tephra at different catchments could solve this issue in future research. Additionally, the use of BBNs as sub-models to parameterize the BET_VH model in a more robust way could bring substantial improvements to probabilistic volcanic multi-hazard analyses.

Four main general conclusions can be extracted from this PhD. Firstly, probabilistic volcanic hazard assessments need to stem from multi-disciplinary collaboration (e.g. [31, 33, 103, 107, 318]). Improving the knowledge on how volcanic systems work or how a particular volcanic system works; developing adequate and effective numerical models of the physical and chemical processes occurring at volcanoes; applying efficient uncertainty quantification techniques depending on the specific hazard problem: all them are required to better our volcanic hazard assessments. Reaching these objectives will demand growing and sharing expertise in geology, physics, chemistry, mathematics, through multi-disciplinary research.

Secondly, the refinement of probabilistic volcanic hazard assessments will likely derive from developing future research with a hazard-oriented view. That is, future efforts can be directed towards critical aspects of volcanic hazard. For instance,

given the crucial importance of the relationship between the effective friction coefficient and whether PDC volume or collapse height (e.g. [31, 104]), future efforts, in volcanic hazard assessment of PDCs, may be directed towards understanding this relationship further (e.g. [234]). Likewise, given the current absence of a sophisticated PDC model that can simulate both dense and dilute PDCs at a reduced computational cost, future research directions could pursue the construction of such a model, under a hazard perspective: for instance, focusing on the interaction between PDCs and topography (e.g. [28, 80, 152, 400]).

Thirdly, after a bit more than a decade from the first attempts to assess volcanic hazard in probabilistic terms (e.g. [21]), it is now clearer than ever that there is still a long way to go. In particular, as this PhD study has tried to examine in depth, the paramount role of the epistemic uncertainty associated with probabilistic hazard assessement is far to be fully quantified, and it will be a key issue in the forthcoming years (e.g. [53, 54]).

Last, but not least, this PhD thesis highlights how the results from different probabilistic volcanic hazard assessments, if homogeneously computed (at common grids, time windows and hazard metrics, which are probabilistic hazard curves in this PhD), can be quantitatively combined to produce a second-order volcanic hazard assessment, in which cascade effects (such as secondary lahars in this PhD) are accounted for.

Appendix A

Definition of the Energy Cone parameter space (Chapter 5)

The parameter space for the Energy Cone (EC) model in Chapter 5 is defined to capture, in probabilistic terms, the expected broad variety of PDCs that might be generated, during an eruption of a given size, at a volcanic system similar to Somma-Vesuvius or Campi Flegrei. In other words, the selected EC parameter space is not intended to reproduce the available past events but it is designed to capture any plausible event, given an eruption of a specific size.
In order to explore the possible outcomes that may unfold during an eruption of a given size, Probability Density Functions (PDFs) for the model parameters (H_0, ϕ) must be defined. The use of PDFs has the purpose of reproducing as best as possible the randomness in PDC formation (aleatory uncertainty estimation). Therefore, we need to identify suitable PDFs for H_0 and ϕ, and assign sound and coherent values to their parameters (note that the "proper" PDFs and their parameterization are themselves not known. This gives rise to epistemic uncertainty in the form of parametric uncertainty: [75, 104], see Chapter 6).

A.1 PDF for H_0

Pyroclastic Density Currents (PDCs) can be generated during explosive eruptions in different ways, which span from gravitational instability (i.e. dome collapses) to fountaining processes (pyroclastic fountain collapse and partial column collapses,

e.g. [124], see Chapter 2). Being PDCs at both Somma-Vesuvius and Campi Flegrei not related to dome collapses, we consider in the following only the generation of PDCs from column or fountain collapses.

The maximum possible source height of PDCs in these cases is the end of the lower basal gas-thrust or jet region, dominated by inertial forces caused by magma acceleration and fragmentation in the uppermost part of the volcanic conduit (e.g. [114]). This region is characterized by an abrupt decrease of the mixture velocity due to loss of momentum and extends up to a small fraction of the total column height (H_T). For a sustained column, the height of the gas-thrust zone (H_{g-t}) can be roughly estimated as 10% of H_T [110].

For the PDF of H_0, we assume an Exponential PDF, characterized by only one shape parameter (λ), and in which the most likely values are by far the small ones:

$$f(X) = \lambda \cdot e^{-\lambda X} \tag{A.1}$$

or, expressed in the form of the Cumulative Distribution Function (CDF):

$$F(X) = P(X \leq x) = 1 - e^{-\lambda X} \tag{A.2}$$

As in [104] (see Chapter 6), in order to obtain plausible λ ranges, we consider values of H_T picked up from thousands of potential eruption column heights for the three different eruption sizes considered at Somma-Vesuvius and Campi Flegrei [70]. The calculation of λ is consequently performed by sampling H_T from the above-mentioned simulations and, for each H_T realization, assuming that the 95th percentile of the Exponential PDF is equal to H_{g-t}, the gas-thrust height, for that specific H_T value. That is:

$$F(H_{g-t}) = 1 - e^{-(\lambda \cdot 0.1 H_T)} = 0.95 \tag{A.3}$$

Since it can be argued that column collapses forming at heights $H_0 = 0$ m or $H_0 = +\infty$ m are not physically consistent, the Exponential PDFs are truncated at $H_0 = 20$ m (lower bound) and $H_0 = 0.1 H_T$ m (upper bound) and normalized accordingly to build the final Truncated Exponential PDFs [104]. The lower limit at 20 m is set as an arbitrary minimum collapse height. Nevertheless, it has been

checked that limits at $H_0 = 5$ m and $H_0 = 50$ m do not have a large effect on the results.

A.2 PDF for ϕ

PDCs generated from column or fountain collapses can show quite different values of mobility depending on: total mass that participates in the collapse, average density of the pyroclasts forming the PDC, volume partition between gas and pyroclasts, fluidization processes (e.g. [124]). The degree of knowledge about how these processes control the value of ϕ is limited. [136] fit Gaussian PDFs to values of ϕ measured on PDCs at Volcán de Colima, Mexico. [104] used Truncated Gaussian PDFs and Asymmetric Tukey Window PDFs (a variant of a Uniform PDF with cosine-shaped tails) at Somma-Vesuvius and found the impact of this choice on the EC outputs to be small. Here, we use a different type of PDF depending on the volcanic system of interest. This is motivated by the difference in the amount of ϕ data available for Somma-Vesuvius and Campi Flegrei. In particular, as we base the PDF shape and parameters on data coming from analog volcanoes, there are many more data for volcanic systems which are analog to Somma-Vesuvius than to Campi Flegrei. For Somma-Vesuvius, a worldwide database of ϕ values is available [138]. We add to the database four extra values of ϕ from PDCs simulated via EC. These values come from Guagua Pichincha, Ecuador [279]; La Soufrière, Guadeloupe [216] and Somma-Vesuvius [137]. We use the dataset to: (a) check which PDF choice seems most appropriate, given the data; and (b) set the PDF parameters for each eruption size. In the case of Campi Flegrei, we lack such a database and, therefore, we select a very non-informative distribution: the Uniform PDF.

A.2.1 PDF for ϕ at Somma-Vesuvius

At Somma-Vesuvius, reported PDCs range from column collapse-generated PDCs with variable volumes (VEI4, VEI$\geq$5) to small PDCs and hot avalanches during VEI$\sim$3 eruptions, e.g. 1944 eruption [193] (see Chapter 3). As introduced before, we assume that the world database [138] covers the ϕ values which can describe this typology of PDCs as far as the volcanic systems in the database are similar to Somma-Vesuvius.

We perform a series of non-parametric hypothesis tests (one-sample Kolmogorov-Smirnov, K-S) in conjunction with information criteria (corrected Akaike Information Criterion, AICc, [401]) to shed some light on which choice seems more appropriate and reasonable. For this purpose, we divide the data of [138] into different categories (Table A.1). Among them, PDCm3, PDC4 and PDCM5 represent all the ϕ values of Pumice Flows (PFs) related to VEI$\leq$3, VEI4, and VEIgeq5 eruptions (Table A.1). The null hypothesis we want to test through K-S is that the ϕ values in [138] may have been sampled from a given type of theoretical PDF. In particular, we test four different types of PDFs (Table A.1): Uniform, Asymmetric Tukey Window, Beta and Truncated Gaussian (NB. truncation of the Gaussian PDFs is needed since values of ϕ cannot be either negative or greater than 90 degrees). For the Uniform PDFs, maximum and minimum values in the database are used as the limits of the distributions. PDFs parameters for Tukey and Truncated Gaussian PDFs are set as in [104] (see Chapter 6). For the Beta PDFs, Maximum-Likelihood Estimation (MLE) of the PDF parameters is performed, considering the available ϕ data per each group. Note that for (truncated) Gaussian PDFs, the MLE parameters (given the ϕ data in [138]) are the same as if the mean and standard deviation were calculated from the data. Out of the 32 K-S tests we carry out, only four of them lead to rejection (at the 1% significance level) of the null hypothesis (marked in red in Table A.1): PFs do not seem compatible with sampling from the Uniform PDF while BAFs only seem compatible with sampling from the Truncated Gaussian PDF (i.e. the other three PDFs are rejected, at the 1% significance level and in light of the BAF data; Table A.1).

AICc represents an enhancement of the Akaike Information Criterion (AIC) particularly useful when the sample size is small or the number of parameters in the model is not considerably smaller than that sample size (e.g. [402]). Small values of AICc correspond to "better" models compared to high values. The index rewards both goodness-of-fit (by means of the log-likelihood) and model simplicity, expressed as the number of parameters in the model, with a correction for small sample sizes. The calculated AICc indexes for PDCm3 and PDCM5 are similar as concerns Uniform and Truncated Gaussian PDFs but are higher for Tukey and Beta PDFs (Table A.1). In the case of PDC4, Beta and Truncated Gaussian PDFs have the lowest AICc values. Nonetheless, this case is not very representative as the number of data available equals the number of parameters of some of the explored PDFs. By and large, Tukey and Beta PDFs are affected by very low log-likelihood values on the boundaries of the PDF as well as their complexity. On

TABLE A.1: Hypothesis testing (Kolmogorov-Smirnov test, K-S) and information criteria (corrected Akaike Information Criterion, AICc) for different types of Probability Density Functions (PDFs) checked against data of PDC mobility in [138], arranged in different PDC groups (in brackets the sample size of each group). Bold underlined text indicates sample sizes which are small enough that may hinder the null hypothesis rejection, i.e. K-S critical values are inversely related to the degrees of freedom: the smaller the sample, the larger the critical value. Testing decision is displayed as 1 (reject null hypothesis) or 0 (do not reject null hypothesis), at 1% of significance level. The p-value indicates the probability of observing a test statistic which is equal or more extreme than the calculated statistic. Note that when p-value < 0.01 the null hypothesis is rejected (bold red text). Trunc. Gauss: Truncated Gaussian; BAFs: Block-and-Ash Flows; Ign: Ignimbrites; PFs: Pumice Flows; HAv: Hot Avalanches; pfha: PFs + HAv; PDCm3: PFs for which VEI$\leq$3; PDC4: PFs for which VEI4; PDCM5: PFs for which VEI$\geq$5; MLE: Maximum-Likelihood Estimation; NP: Not Performed. From [103].

PDF $\rightarrow$	**Uniform**			**Tukey**			**MLE Beta**			**MLE Trunc. Gaussian**		
Parameters $\rightarrow$	k = 2 (A, B)			k = 4 (A, a, b, B)			k = 4 (α, β, A, B)			k = 4 (μ, σ, A, B)		
	K-S	p-value	AICc	K-S	p-value	AICc	K-S	p-value	AICc	K-S	p-value	AICc
BAFs (141)	**1**	**$< 10^{-5}$**	NP	**1**	**$< 10^{-5}$**	NP	**1**	**0.008**	NP	0	0.1	NP
Ign (**12**)	0	0.645	NP	0	0.508	NP	0	0.614	NP	0	0.668	NP
PFs (42)	**1**	**0.004**	NP	0	0.033	NP	0	0.899	NP	0	0.63	NP
HAv (**6**)	0	0.84	NP	0	0.559	NP	0	0.733	NP	0	0.861	NP
pfha (48)	0	0.09	NP	0	0.108	NP	0	0.625	NP	0	0.636	NP
PDCm3 (17)	0	0.065	109	0	0.089	131	0	0.496	122	0	0.162	115
PDC4 (**4**)	0	0.832	40	0	0.859	7	0	0.643	-5	0	0.847	-7
PDCM5 (21)	0	0.1	125	0	0.711	138	0	0.605	137	0	0.574	128

the other hand, the Uniform statistical model benefits from its simplicity and a constant log-likelihood value along its domain ($\mathcal{L}(\text{Uniform}) = f(X|\theta) = \text{constant}$; where $\mathcal{L}$ denotes the log-likelihood and θ the PDF parameters).

On the whole, taking into account both criteria (hypothesis testing and information index) and insights from the literature (e.g. [136]), we decide that Truncated Gaussian PDF is an appropriate and defensible choice for the PDF of ϕ at Somma-Vesuvius [104]. Thus, we use the mean (μ), standard deviation (σ), minimum and maximum ϕ values of PDCm3, PDC4 and PDCM5 to set the equivalent PDF parameters for the small, medium and large eruption sizes at Somma-Vesuvius (Table 5.1).

A.2.2 PDF for ϕ at Campi Flegrei

At Campi Flegrei, PDC generation is strongly affected by the existence of well-established aquifers along a mature hydrothermal system (e.g. [188, 209]), which has led to the generation of moderately to highly mobile pyroclastic surges, e.g. [25] (see Chapter 3). The present study takes only into account the epoch III of volcanic activity at Campi Flegrei (after [195]), meaning that the formation of very large ignimbrites (i.e. the Campanian Ignimbrite and Neapolitan Yellow Tuff) is not considered.

For each eruption size, the Uniform PDF parameters (i.e. minimum and maximum limits) are based upon independent information regarding realistic values of PDC mobility at Campi Flegrei. We first search in the collapse caldera worldwide database [403] calderas with similar: (1) spatial-temporal pattern of post-caldera vent-opening; (2) local tectonic faulting; and (3) geochemistry of the magmas involved. Out of 14 volcanic systems which share more than one feature, no specific constraints on ϕ values can be extracted. Therefore, we try to gather some independent information from: (a) published works about possible ϕ values for surges [137]; (b) published works about ϕ values and PDC mobility, in general [138, 404]; and (c) published works in which a relation between PDC total volume and ϕ values is given [131].
Minimum limits of the Uniform PDFs are set at 4° for small and medium sizes and 3° for large size. The first corresponds to the minimum ϕ value reported by [137] for surges at Vulcano and Lipari (Italy). The large-size limit is just a conservative choice as far as only one large-size eruption has been recorded during the III Epoch

of Campi Flegrei (e.g. [195]): the Agnano-Monte Spina eruption. Concerning the maximum limits of the Uniform PDFs, we take into consideration the fact that (very) low-mobility PDCs are not expected to form at Campi Flegrei. [404] links low-mobility BAFs to ϕ values around 18-21°. In the PFs data from [138], a clear gap between a group of PDCs with $10° \leq \phi \leq 20°$ (intermediate mobility) and another group with $\phi \geq 24°$ (low to very-low mobility) is clearly observed (Fig. A.1B). Hence, we identify a delimiter for low-mobility PDCs (which we do not expect to form at Campi Flegrei) around $\phi = 20°$. Given that PDC mobility is thought to be related to PDC volume and, hence, eruption size (Fig. A.1A); we choose the maximum ϕ limits to be slightly shifted between sizes, that is: 22°, 20°, 18° for small, medium and large eruption sizes, respectively.

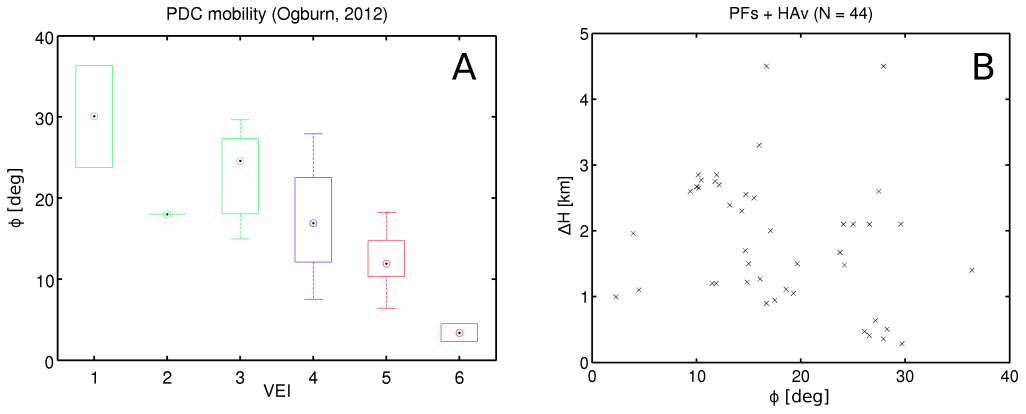

FIGURE A.1: Data collected from the PDC mobility database [138]. A: values of ϕ arranged by VEI size (only Pumice Flows, PFs; and Hot Avalanches, HAv). Target symbols denote the 50th percentile of the ϕ Empirical Cumulative Distribution Functions (ECDFs). Box edges indicate the 25th and 75th percentiles while whiskers mark the 5th and 95th percentiles of these ECDFs (note that for VEI1 and VEI6 the sample size is 2 -no whiskers-; while for VEI2, the sample size is 1 -no box, no whiskers-). B: values of ϕ against ΔH (PFs and HAv). From [103].

Finally, we check out that the values of ϕ derived from the empirical formula published by [131], which relates PDC total volume and H/L (hence ϕ), are in agreement with our Uniform PDF parameters. Values of ϕ estimated in this way are about 7.5-9.5° for small size, around 7° for medium size and 5.5° for large size; hence, they are coherent with our PDF parametrization (Table 5.1).

Appendix B

Modeling procedure (Chapter 7)

B.1 Definition of the two end-member probability distributions for H_0

B.1.1 Truncated Exponential distribution

In this case, we adopt the same paradygm as in [103, 104]. For each eruption size class, we first account for the total column heights derived from eruption column simulations at Somma-Vesuvius and Campi Flegrei in [70]. In that work, total column height (H_T) values were calculated through the fourth power relationship presented by [265], using Mass Eruption Rates computed by randomly sampling values of total erupted mass and eruption duration from adequate PDFs built for our two target volcanoes. Secondly, we assume that the top of the gas-thrust region top is roughly estimated as 10% of the total height of the eruption column [110]. In this way, the parameter λ defining the truncated Exponential PDF for H_0 is inferred by assuming that the top of the gas-thrust region marks the 95th percentile of the corresponding non-truncated exponential PDF [103]. The obtained Exponential PDFs are then truncated and renormalized between $H_{0_{min}}$ =20 m and $H_{0_{max}} = 0.1H_T$ m.

In our simulation scheme, for each volcano and eruptive size class, we sample 1,000 H_T values from [70]. For each of these, we retrieve a λ value and so a truncated Exponential distribution, from which we sample 10 values of H_0. Thus, we end up with 10,000 H_0 values for each volcano and eruptive size class. Correspondingly,

we sample 10,000 ϕ values given the volcano and eruptive size class. Finally, we run EC model 10,000 times (one for each pair (H_0, ϕ)) for every volcano studied (2), possible vent position (441 and 460 for Vesuvius and Campi Flegrei, respectively) and size class (3 for each volcano), totalling: $10^4 * 441 * 3$ and $10^4 * 460 * 3$ simulations for Somma-Vesuvius and Campi Flegrei, respectively. Such a large number of simulations is necessary to sample correctly the tail of the exponential PDF adopted. In order to lower the computational time, in the case of the 392 lateral vents at Somma-Vesuvius (which have very low probability of opening), we only run 1,000 simulations. Thus, in the end we run the EC model $10^4 * 49 * 3 + 10^3 * 392 * 3 \sim 2.5M$ times at this volcano. At Campi Flegrei, we run 10,000 simulations for all vents so the final number of EC runs is about 14 M.

Uniform distribution

In this case, we again account for the total column heights derived from eruption column simulations at Somma-Vesuvius and Campi Flegrei [70], and assume that the top of the gas-thrust region top is roughly estimated as 10% of the total height of the eruption column [110]. In this way,the uniform distribution is set between $H_{0_{min}}$=20 m and $H_{0_{max}} = 0.1H_T$.

In our simulation scheme, for each volcano and eruptive size class, we again sample 1,000 H_T values from [70] and define 1,000 Uniform distributions. From each one of these, we sample one value of H_0. Thus, we end up with 1,000 H_0 values for each volcano and eruptive size class. Correspondingly, we sample 1,000 ϕ values given the volcano and eruptive size class. Finally, we run EC model 1,000 times (one for each pair (H_0, ϕ)) for every volcano studied, possible vent position and size class. In the case of uniform distributions the number of samples can be lower as it is not too difficult to effectively sample the whole range of possible values of H_0 (the uniform distribution has no real "tail").

EC simulations

The EC model is implemented in MATLAB [405] and the simulations are run, using a 40m DEM, at the Center for Computational Research (CCR) of the University at Buffalo (USA). For Somma-Vesuvius, [104] demonstrated that the use of a 40m DEM, instead of a finer-resolution DEM (e.g. 10 m), does not alter the

output of the EC simulations considerably. Other sources of epistemic uncertainty, such as theoretical uncertainty (linked to the relationship between H_0 and ϕ, see Chapter 6), can be one to two order of magnitues larger than epistemic uncertainty linked to the DEM horizontal resolution [104]. For Campi Flegrei, such a systematic quantification of different sources of epistemic uncertainty is not available. We are aware that, in the case of calderas, the absence of a predominant topographical structure could give a more relevant role to DEM resolution, compared to other sources of uncertainty. However, given the overwhelming difference in the importance of theoretical uncertainty with respect to input uncertainty (i.e., DEM resolution) in the case of Somma-Vesuvius, we assume that for Campi Flegrei the usage of a 40m DEM does not affect the results too much.

The output of the simulations are then interpolated on a 100m grid for the PVHA. This reduction is necessary to keep the computational time of BET_VH model acceptable. The final domain of PVHA is thus on a 100m grid with lower left and upper right corners respectively at [402575,4486891] and [483375,4546091] in meters (UTM, zone 33).

Bibliography

[1] Davidson, J., Morgan, D., Charlier, B., Harlou, R., and Hora, J. Microsampling and isotopic analysis of igneous rocks: implications for the study of magmatic systems. *Annual Review of Earth and Planetary Sciences*, 35: 273–311, 2007.

[2] Cashman, K. V. and Sparks, R. S. J. How volcanoes work: A 25 year perspective. *Geological Society of America Bulletin*, 125(5-6):664–690, 2013.

[3] Sigurdsson, H., Houghton, B. F., McNutt, S. R., Rymer, H., and Stix, J. *Encyclopedia of Volcanoes*. Academic Press, San Diego, 2000.

[4] Parfitt, L. and Wilson, L. *Fundamentals of physical volcanology*. John Wiley & Sons, 2009.

[5] Dingwell, D. B. Volcanic dilemma: flow or blow? *Science*, 273(5278):1054, 1996.

[6] Cas, R. A. and Wright, J. V. *Volcanic successions, modern and ancient: a geological approach to processes, products, and successions*. Allen & Unwin, 1987.

[7] Walker, G. P., Self, S., and Wilson, L. Tarawera 1886, New Zealand—a basaltic plinian fissure eruption. *Journal of Volcanology and Geothermal Research*, 21(1-2):61–78, 1984.

[8] Coltelli, M., Del Carlo, P., and Vezzoli, L. Discovery of a Plinian basaltic eruption of Roman age at Etna volcano, Italy. *Geology*, 26(12):1095–1098, 1998.

[9] Druitt, T. Pyroclastic density currents. *Geological Society, London, Special Publications*, 145(1):145–182, 1998.

[10] White, J. D. L. and Ross, P. S. Maar-diatreme volcanoes: A review. *Journal of Volcanology and Geothermal Research*, 201(1-4):1–29, 2011.

[11] Gudmundsson, M. T., Thordarson, T., Höskuldsson, Á., Larsen, G., Björnsson, H., Prata, F. J., Oddsson, B., Magnússon, E., Högnadóttir, T., Petersen, G. N., et al. Ash generation and distribution from the April-May 2010 eruption of Eyjafjallajökull, Iceland. *Scientific reports*, 2:572, 2012.

[12] Tatsumi, Y. and Eggins, S. *Subduction zone magmatism*, volume 1. Wiley, 1995.

[13] Perfit, M. R. and Davidson, J. Plate tectonics and volcanism. *Encyclopedia of volcanoes, edited by: Sigurdsson, H., Houghton, B. F., McNutt, S. R., Rymer, H., and Stix, J.*, pages 89–113, 2000.

[14] Newhall, C. G. and Self, S. The volcanic explosivity index (VEI) an estimate of explosive magnitude for historical volcanism. *Journal of Geophysical Research: Oceans (1978–2012)*, 87(C2):1231–1238, 1982.

[15] Crosweller, H. S., Arora, B., Brown, S. K., Cottrell, E., Deligne, N. I., Guerrero, N. O., Hobbs, L., Kiyosugi, K., Loughlin, S. C., Lowndes, J., et al. Global database on large magnitude explosive volcanic eruptions (LaMEVE). *Journal of Applied Volcanology*, 1(1):4, 2012.

[16] Blong, R. *Volcanic hazards. A sourcebook on the effects of eruptions*. Academic Press, Inc., Orlando, FL, 1984.

[17] Loughlin, S. C., Sparks, S., Brown, S. K., Vye-Brown, C., and Jenkins, S. F. *Global volcanic hazards and risk*. Cambridge University Press, 2015.

[18] Calder, E., Wagner, K., and Ogburn, S. Volcanic hazard maps. *Global Volcanic Hazards and Risk. Cambridge University Press, Cambridge*, pages 335–342, 2015.

[19] Selva, J., Costa, A., Marzocchi, W., and Sandri, L. BET_VH: exploring the influence of natural uncertainties on long-term hazard from tephra fallout at Campi Flegrei (Italy). *Bulletin of Volcanology*, 72(6):717–733, 2010.

[20] Hall, M. L., Robin, C., Beate, B., Mothes, P., and Monzier, M. Tungurahua Volcano, Ecuador: structure, eruptive history and hazards. *Journal of Volcanology and Geothermal Research*, 91(1):1–21, 1999.

[21] Newhall, C. and Hoblitt, R. Constructing event trees for volcanic crises. *Bulletin of Volcanology*, 64(1):3–20, 2002.

[22] Simpson, J. and Weiner, E. *Oxford English Dictionary*. Oxford University Press, 1989. URL https://en.oxforddictionaries.com/.

[23] Bayarri, M., Berger, J. O., Calder, E. S., Dalbey, K., Lunagomez, S., Patra, A. K., Pitman, E. B., Spiller, E. T., and Wolpert, R. L. Using statistical and computer models to quantify volcanic hazards. *Technometrics*, 51(4), 2009.

[24] Dalbey, K., Patra, A., Pitman, E., Bursik, M., and Sheridan, M. Input uncertainty propagation methods and hazard mapping of geophysical mass flows. *Journal of Geophysical Research: Solid Earth (1978–2012)*, 113(B5), 2008.

[25] Orsi, G., Di Vito, M. A., and Isaia, R. Volcanic hazard assessment at the restless Campi Flegrei caldera. *Bulletin of Volcanology*, 66(6):514–530, 2004.

[26] Gurioli, L., Sulpizio, R., Cioni, R., Sbrana, A., Santacroce, R., Luperini, W., and Andronico, D. Pyroclastic flow hazard assessment at Somma–Vesuvius based on the geological record. *Bulletin of Volcanology*, 72(9):1021–1038, 2010.

[27] Charbonnier, S. J. and Gertisser, R. Evaluation of geophysical mass flow models using the 2006 block-and-ash flows of Merapi Volcano, Java, Indonesia: Towards a short-term hazard assessment tool. *Journal of Volcanology and Geothermal Research*, 231:87–108, 2012.

[28] Ongaro, T. E., Orsucci, S., and Cornolti, F. A fast, calibrated model for pyroclastic density currents kinematics and hazard. *Journal of Volcanology and Geothermal Research*, 327:257–272, 2016.

[29] Saucedo, R., Macías, J. L., Sheridan, M. F., Bursik, M. I., and Komorowski, J. C. Modeling of pyroclastic flows of Colima Volcano, Mexico: Implications for hazard assessment. *Journal of Volcanology and Geothermal Research*, 139(1-2):103–115, 2005.

[30] Widiwijayanti, C., Voight, B., Hidayat, D., and Schilling, S. Objective rapid delineation of areas at risk from block-and-ash pyroclastic flows and surges. *Bulletin of Volcanology*, 71(6):687–703, 2009.

[31] Spiller, E. T., Bayarri, M., Berger, J. O., Calder, E. S., Patra, A. K., Pitman, E. B., and Wolpert, R. L. Automating emulator construction for geophysical hazard maps. *SIAM/ASA Journal on Uncertainty Quantification*, 2(1):126–152, 2014.

[32] Sandri, L., Jolly, G., Lindsay, J., Howe, T., and Marzocchi, W. Combining long-and short-term probabilistic volcanic hazard assessment with cost-benefit analysis to support decision making in a volcanic crisis from the Auckland Volcanic Field, New Zealand. *Bulletin of Volcanology*, 74(3):705–723, 2012.

[33] Neri, A., Bevilacqua, A., Esposti Ongaro, T., Isaia, R., Aspinall, W. P., Bisson, M., Flandoli, F., Baxter, P. J., Bertagnini, A., Iannuzzi, E., et al. Quantifying volcanic hazard at Campi Flegrei caldera (Italy) with uncertainty assessment: 2. Pyroclastic density current invasion maps. *Journal of Geophysical Research: Solid Earth*, 120(4):2330–2349, 2015.

[34] Lavigne, F., Morin, J., and Surono, D. *The atlas of Merapi volcano*. Laboratoire de Géographie Physique, Meudon, 2015.

[35] Branney, M. J. and Kokelaar, B. P. *Pyroclastic density currents and the sedimentation of ignimbrites*. Geological Society of London, 2002.

[36] Allen, S. R., Bryner, V. F., Smith, I. E., and Ballance, P. F. Facies analysis of pyroclastic deposits within basaltic tuff-rings of the Auckland volcanic field, New Zealand. *New Zealand Journal of Geology and Geophysics*, 39(2): 309–327, 1996.

[37] Di Vito, M., Isaia, R., Orsi, G., Southon, J., De Vita, S., d'Antonio, M., Pappalardo, L., and Piochi, M. Volcanism and deformation since 12,000 years at the Campi Flegrei caldera (Italy). *Journal of Volcanology and Geothermal Research*, 91(2):221–246, 1999.

[38] Legros, F. Tephra stratigraphy of Misti volcano, Peru. *Journal of South American Earth Sciences*, 14(1):15–29, 2001.

[39] Aramaki, S. Formation of the Aira caldera, southern Kyushu, ∼22,000 years ago. *Journal of Geophysical Research: Solid Earth (1978–2012)*, 89(B10): 8485–8501, 1984.

[40] Wilson, C. J. The 26.5 ka Oruanui eruption, New Zealand: an introduction and overview. *Journal of Volcanology and Geothermal Research*, 112(1): 133–174, 2001.

[41] Sulpizio, R., Capra, L., Sarocchi, D., Saucedo, R., Gavilanes-Ruiz, J., and Varley, N. Predicting the block-and-ash flow inundation areas at Volcán de Colima (Colima, Mexico) based on the present day (February 2010) status. *Journal of Volcanology and Geothermal Research*, 193(1):49–66, 2010.

[42] Siebert, L., Simkin, T., and Kimberly, P. *Volcanoes of the World*. Univ of California Press, 2010.

[43] Rougier, J., Sparks, S. R., and Cashman, K. V. Global recording rates for large eruptions. *Journal of Applied Volcanology*, 5(1):11, 2016.

[44] Esposti Ongaro, T., Neri, A., Menconi, G., De'Michieli Vitturi, M., Marianelli, P., Cavazzoni, C., Erbacci, G., and Baxter, P. Transient 3D numerical simulations of column collapse and pyroclastic density current scenarios at Vesuvius. *Journal of Volcanology and Geothermal Research*, 178(3):378–396, 2008.

[45] Oramas-Dorta, D., Cole, P. D., Wadge, G., Alvarado, G. E., and Soto, G. J. Pyroclastic flow hazard at Arenal volcano, Costa Rica: Scenarios and assessment. *Journal of Volcanology and Geothermal Research*, 247:74–92, 2012.

[46] Mastrolorenzo, G., Petrone, P., Pappalardo, L., and Sheridan, M. F. The Avellino 3780-yr-BP catastrophe as a worst-case scenario for a future eruption at Vesuvius. *Proceedings of the National Academy of Sciences of the United States of America*, 103(12):4366–4370, 2006.

[47] Dufek, J. and Bergantz, G. W. Dynamics and deposits generated by the Kos Plateau Tuff eruption: Controls of basal particle loss on pyroclastic flow transport. *Geochemistry, Geophysics, Geosystems*, 8(12), 2007.

[48] Ongaro, T. E., Widiwijayanti, C., Clarke, A., Voight, B., and Neri, A. Multiphase-flow numerical modeling of the 18 May 1980 lateral blast at Mount St. Helens, USA. *Geology*, 39(6):535–538, 2011.

[49] Marzocchi, W., Sandri, L., and Selva, J. BET_VH: a probabilistic tool for long-term volcanic hazard assessment. *Bulletin of Volcanology*, 72(6): 705–716, 2010.

[50] Sobradelo, R., Bartolini, S., and Martí, J. HASSET: a probability event tree tool to evaluate future volcanic scenarios using Bayesian inference. *Bulletin of Volcanology*, 76(1):770, 2014.

[51] Marzocchi, W., Taroni, M., and Selva, J. Accounting for epistemic uncertainty in PSHA: logic tree and ensemble modeling. *Bulletin of the Seismological Society of America*, 105(4):2151–2159, 2015.

[52] Woo, G. *The mathematics of natural catastrophes*. London: Imperial College Press, 1999.

[53] Rougier, J., Sparks, S. R., and Hill, L. J. *Risk and uncertainty assessment for natural hazards*. Cambridge University Press, 2013.

[54] Riley, K., Webley, P., and Thompson, M. *Natural Hazard Uncertainty Assessment: Modeling and Decision Support*, volume AGU Geophysical Monograph Series 223. John Wiley & Sons, Inc., 2016.

[55] Woods, A. The fluid dynamics and thermodynamics of eruption columns. *Bulletin of Volcanology*, 50(3):169–193, 1988.

[56] Sparks, R. Forecasting volcanic eruptions. *Earth and Planetary Science Letters*, 210(1):1–15, 2003.

[57] Lipman, P. W. and Mullineaux, D. R. *The 1980 eruptions of Mount St. Helens, Washington*. US Dept. of the Interior, US Geological Survey, 1981.

[58] López, C., Blanco, M., Abella, R., Brenes, B., Cabrera Rodríguez, V., Casas, B., Domínguez Cerdeña, I., Felpeto, A., Villalta, M. F., Fresno, C., et al. Monitoring the volcanic unrest of El Hierro (Canary Islands) before the onset of the 2011–2012 submarine eruption. *Geophysical Research Letters*, 39(13), 2012.

[59] Wadge, G., Voight, B., Sparks, R., Cole, P., Loughlin, S., and Robertson, R. An overview of the eruption of Soufriere Hills Volcano, Montserrat from 2000 to 2010. *Geological Society, London, Memoirs*, 39(1):1–40, 2014.

[60] Voight, B., Constantine, E., Siswowidjoyo, S., and Torley, R. Historical eruptions of Merapi Volcano, Central Java, Indonesia, 1768–1998. *Journal of Volcanology and Geothermal Research*, 100:69–138, 2000.

[61] Marzocchi, W., Sandri, L., Gasparini, P., Newhall, C., and Boschi, E. Quantifying probabilities of volcanic events: the example of volcanic hazard at Mount Vesuvius. *Journal of Geophysical Research: Solid Earth (1978–2012)*, 109(B11), 2004.

[62] Marzocchi, W. and Jordan, T. H. Testing for ontological errors in probabilistic forecasting models of natural systems. *Proceedings of the National Academy of Sciences*, 111(33):11973–11978, 2014.

[63] Sigurdsson, H. Mount Vesuvius before the Disaster. *The Natural History of Pompeii*, pages 29–36, 2002.

[64] Kolmogorov, A. N. *Foundations of the Theory of Probability.* Chelsea Publishing Co., 1950.

[65] Gelman, A., Carlin, J. B., Stern, H. S., and Rubin, D. B. *Bayesian data analysis.* Chapman & Hall/CRC, 1995.

[66] Grimmett, G. and Stirzaker, D. *Probability and random processes.* Oxford university press, 2001.

[67] Aspinall, W., Woo, G., Voight, B., and Baxter, P. Evidence-based volcanology: application to eruption crises. *Journal of Volcanology and Geothermal Research*, 128(1):273–285, 2003.

[68] Marzocchi, W., Sandri, L., and Selva, J. BET_EF: a probabilistic tool for long-and short-term eruption forecasting. *Bulletin of Volcanology*, 70(5): 623–632, 2008.

[69] Kalbfleisch, J. G. *Probability and statistical inference*, volume 2. Springer-Verlag, New York, 1979.

[70] Sandri, L., Costa, A., Selva, J., Tonini, R., Macedonio, G., Folch, A., and Sulpizio, R. Beyond eruptive scenarios: assessing tephra fallout hazard from Neapolitan volcanoes. *Scientific reports*, 6, 2016.

[71] Bonadonna, C., Connor, C. B., Houghton, B., Connor, L., Byrne, M., Laing, A., and Hincks, T. Probabilistic modeling of tephra dispersal: Hazard assessment of a multiphase rhyolitic eruption at Tarawera, New Zealand. *Journal of Geophysical Research: Solid Earth (1978–2012)*, 110(B3), 2005.

[72] Costa, A., Dell'Erba, F., Di Vito, M., Isaia, R., Macedonio, G., Orsi, G., and Pfeiffer, T. Tephra fallout hazard assessment at the Campi Flegrei caldera (Italy). *Bulletin of Volcanology*, 71(3):259, 2009.

[73] Vitturi, M. d., Engwell, S., Neri, A., and Barsotti, S. Uncertainty quantification and sensitivity analysis of volcanic columns models: Results from the integral model PLUME-MoM. *Journal of Volcanology and Geothermal Research*, 326:77–91, 2016.

[74] Spiegelhalter, D. J. and Riesch, H. Don't know, can't know: embracing deeper uncertainties when analysing risks. *Philosophical Transactions of the Royal Society A: Mathematical, Physical and Engineering Sciences*, 369 (1956):4730–4750, 2011.

[75] Rougier, J. and Beven, K. Model limitations: the sources and implications of epistemic uncertainty. *Risk and uncertainty assessment for natural hazards, edited by: Rougier, J. C., Sparks, R. S. J., and Hill, L. J.*, pages 40–63, 2013.

[76] Selva, J., Costa, A., Sandri, L., Macedonio, G., and Marzocchi, W. Probabilistic short-term volcanic hazard in phases of unrest: A case study for tephra fallout. *Journal of Geophysical Research: Solid Earth*, 119(12):8805–8826, 2014.

[77] Jenkins, S., Magill, C., McAneney, J., and Blong, R. Regional ash fall hazard I: a probabilistic assessment methodology. *Bulletin of Volcanology*, 74(7):1699–1712, 2012.

[78] Madankan, R., Pouget, S., Singla, P., Bursik, M., Dehn, J., Jones, M., Patra, A., Pavolonis, M., Pitman, E. B., Singh, T., et al. Computation of probabilistic hazard maps and source parameter estimation for volcanic ash transport and dispersion. *Journal of Computational Physics*, 271:39–59, 2014.

[79] Iverson, R. M. The physics of debris flows. *Reviews of Geophysics*, 35(3): 245–296, 1997.

[80] Dufek, J. The fluid mechanics of pyroclastic density currents. *Annual Review of Fluid Mechanics*, 48:459–485, 2016.

[81] Fagents, S. A. and Baloga, S. M. Toward a model for the bulking and debulking of lahars. *Journal of Geophysical Research: Solid Earth (1978–2012)*, 111(B10), 2006.

[82] Dalbey, K. R. *Predictive simulation and model based hazard maps of geophysical mass flows.* State University of New York at Buffalo, 2009.

[83] Rougier, J. Quantifying hazard losses. *Risk and uncertainty assessment for natural hazards, edited by: Rougier, J. C., Sparks, R. S. J., and Hill, L. J.*, pages 19–39, 2013.

[84] Stefanescu, E., Bursik, M., Cordoba, G., Dalbey, K., Jones, M., Patra, A., Pieri, D., Pitman, E., and Sheridan, M. Digital elevation model uncertainty and hazard analysis using a geophysical flow model. *Proceedings of the Royal Society A: Mathematical, Physical and Engineering Science*, 468(2142):1543–1563, 2012.

[85] Stefanescu, E., Bursik, M., and Patra, A. Effect of digital elevation model on Mohr-Coulomb geophysical flow model output. *Natural Hazards*, 62(2): 635–656, 2012.

[86] Charbonnier, S. J., Connor, C., Connor, L., Dixon, T. H., and Gertisser, R. Application of Field Observationsand Remote Sensing to Numerical Modeling and Hazard Assessment of Volcanic Flows: An Example from Merapi Volcano, Indonesia. In *Conference Proceedings - Remote Sensing, Natural Hazards and Environmental Change*, volume 3, pages 35–38, 2011.

[87] Doyle, E. E., McClure, J., Johnston, D. M., and Paton, D. Communicating likelihoods and probabilities in forecasts of volcanic eruptions. *Journal of Volcanology and Geothermal Research*, 272:1–15, 2014.

[88] Thompson, M. A., Lindsay, J. M., and Gaillard, J.-C. The influence of probabilistic volcanic hazard map properties on hazard communication. *Journal of Applied Volcanology*, 4(1):6, 2015.

[89] Cioni, R., Bertagnini, A., Santacroce, R., and Andronico, D. Explosive activity and eruption scenarios at Somma-Vesuvius (Italy): towards a new

classification scheme. *Journal of Volcanology and Geothermal Research*, 178 (3):331–346, 2008.

[90] Newhall, C. G. and Punongbayan, R. S. *Fire and mud: eruptions and lahars of Mount Pinatubo, Philippines*. PHIVOLCS (Quezon City) and University of Washington Press (Seattle), 1996.

[91] Komorowski, J.-C., Jenkins, S., Baxter, P. J., Picquout, A., Lavigne, F., Charbonnier, S., Gertisser, R., Preece, K., Cholik, N., Budi-Santoso, A., and Surono. Paroxysmal dome explosion during the Merapi 2010 eruption: Processes and facies relationships of associated high-energy pyroclastic density currents. *Journal of Volcanology and Geothermal Research*, 261:260–294, 2013.

[92] Pierson, T. C. and Major, J. J. Hydrogeomorphic Effects of Explosive Volcanic Eruptions on Drainage Basins. *Annual Review of Earth and Planetary Sciences*, 42(1):469–507, 2014.

[93] Manville, V., Németh, K., and Kano, K. Source to sink: a review of three decades of progress in the understanding of volcaniclastic processes, deposits, and hazards. *Sedimentary Geology*, 220(3):136–161, 2009.

[94] Major, J. J., Pierson, T. C., Dinehart, R. L., and Costa, J. E. Sediment yield following severe volcanic disturbance - A two-decade perspective from Mount St. Helens. *Geology*, 28(9):819–822, 2000.

[95] Gran, K. B., Montgomery, D. R., and Halbur, J. C. Long-term elevated post-eruption sedimentation at Mount Pinatubo, Philippines. *Geology*, 39 (4):367–370, 2011.

[96] Navarro, C., Cortés, A., and Téllez, A. Mapa de peligros del Volcán de Fuego de Colima. *Universidad de Colima, Observatorio Vulcanológico. Gobierno del Estado de Colima, Mexico*, 2003.

[97] Magill, C. and Blong, R. Volcanic risk ranking for Auckland, New Zealand. I: Methodology and hazard investigation. *Bulletin of Volcanology*, 67(4): 331–339, 2005.

[98] Magill, C. and Blong, R. Volcanic risk ranking for Auckland, New Zealand. II: Hazard consequences and risk calculation. *Bulletin of Volcanology*, 67(4): 340–349, 2005.

[99] Thierry, P., Stieltjes, L., Kouokam, E., Nguéya, P., and Salley, P. M. Multi-hazard risk mapping and assessment on an active volcano: the GRINP project at Mount Cameroon. *Natural Hazards*, 45(3):429–456, 2008.

[100] Sandri, L., Thouret, J.-C., Constantinescu, R., Biass, S., and Tonini, R. Long-term multi-hazard assessment for El Misti volcano (Peru). *Bulletin of Volcanology*, 76(2):1–26, 2014.

[101] Volentik, A., Connor, C. B., Connor, L., and Bonadonna, C. Aspects of volcanic hazard assessment for the bataan nuclear power plant, luzon peninsula, philippines. *Volcanic and Tectonic Hazard Assessment for Nuclear Facilities*, pages 229–256, 2009.

[102] Garcia-Aristizabal, A., Di Ruocco, A., Marzocchi, W., Fleming, K., Tyagunov, S., Vorogushyn, S., Parolai, S., and Desramaut, N. Identifying and structuring scenarios of cascade events in the MATRIX project. *New Multi-Hazard and Multi-Risk Assessment Methods for Europe*, 2013.

[103] Tierz, P., Sandri, L., Costa, A., Zaccarelli, L., Di Vito, M. A., Sulpizio, R., and Marzocchi, W. Suitability of energy cone for probabilistic volcanic hazard assessment: validation tests at Somma-Vesuvius and Campi Flegrei (Italy). *Bulletin of Volcanology*, 78(11):79, 2016.

[104] Tierz, P., Sandri, L., Costa, A., Sulpizio, R., Zaccarelli, L., Di Vito, M. A., and Marzocchi, W. Uncertainty Assessment of Pyroclastic Density Currents at Mount Vesuvius (Italy) Simulated Through the Energy Cone Model. *Natural Hazard Uncertainty Assessment: Modeling and Decision Support, edited by: Riley, K., Webley, P., and Thompson, M.*, AGU Geophysical Monograph Series 223:125–145, 2016.

[105] Sandri, L., Tierz, P., Costa, A., and Marzocchi, W. Probabilistic hazard from Pyroclastic Density Currents in the Neapolitan area (Southern Italy). *TBD*, in prep.

[106] Tierz, P., Ramona Stefanescu, E., Sandri, L., Patra, A., Marzocchi, W., and Sulpizio, R. Probabilistic hazard analysis of dense Pyroclastic Density Currents at Vesuvius (Italy) via parametric uncertainty characterization of TITAN2D numerical simulator. In *EGU General Assembly Conference Abstracts*, volume 16, page 12229, 2014.

[107] Tierz, P., Stefanescu, R. E., Sandri, L., Sulpizio, R., Marzocchi, W., and Patra, A. K. Hazard curves of dense pumice flows around Somma-Vesuvius (Italy): aleatory and epistemic uncertainty quantification. *TBD*, in prep.

[108] Tierz, P., Charbonnier, S., Sandri, L., Ogburn, S., Capra, L., Sulpizio, R., Marzocchi, W., and Patra, A. On the use of Titan2D for probabilistic hazard assessment of Pyroclastic Density Currents: a statistical model for the stopping time. *TBD*, in prep.

[109] Tierz, P., Woodhouse, M., Phillips, J., Sandri, L., Selva, J., Marzocchi, W., and Odbert, H. A framework for probabilistic multi-hazard assessment of rain-triggered lahars using Bayesian Belief Networks. *Volcanic hazard assessment: rising to the challenges of data and model integration*, in prep.

[110] Wilson, L., Sparks, R., Huang, T., and Watkins, N. The control of volcanic column heights by eruption energetics and dynamics. *Journal of Geophysical Research: Solid Earth (1978–2012)*, 83(B4):1829–1836, 1978.

[111] Papale, P. Strain-induced magma fragmentation in explosive eruptions. *Nature*, 397(6718):425–428, 1999.

[112] Alidibirov, M. and Dingwell, D. B. Magma fragmentation by rapid decompression. *Nature*, 380(6570):146, 1996.

[113] Mastin, L. G. Insights into volcanic conduit flow from an open-source numerical model. *Geochemistry, Geophysics, Geosystems*, 3(7):1–18, 2002.

[114] Sparks, R. The dimensions and dynamics of volcanic eruption columns. *Bulletin of Volcanology*, 48(1):3–15, 1986.

[115] Costa, A., Suzuki, Y. J., Cerminara, M., Devenish, B. J., Ongaro, T. E., Herzog, M., Van Eaton, A. R., Denby, L., Bursik, M., Vitturi, M. d., et al. Results of the eruptive column model inter-comparison study. *Journal of Volcanology and Geothermal Research*, 326:2–25, 2016.

[116] Woods, A. W. The dynamics of explosive volcanic eruptions. *Reviews of geophysics*, 33(4):495–530, 1995.

[117] Pfeiffer, T., Costa, A., and Macedonio, G. A model for the numerical simulation of tephra fall deposits. *Journal of Volcanology and Geothermal Research*, 140(4):273–294, 2005.

[118] Bonadonna, C. and Costa, A. Modeling of tephra sedimentation from volcanic plumes. *Modeling volcanic processes: the physics and mathematics of volcanism. Cambridge University Press, Cambridge*, pages 173–202, 2013.

[119] Carey, S. and Sparks, R. Quantitative models of the fallout and dispersal of tephra from volcanic eruption columns. *Bulletin of Volcanology*, 48(2): 109–125, 1986.

[120] Webley, P. and Mastin, L. Improved prediction and tracking of volcanic ash clouds. *Journal of Volcanology and Geothermal Research*, 186(1):1–9, 2009.

[121] Spence, R., Kelman, I., Baxter, P., Zuccaro, G., and Petrazzuoli, S. Residential building and occupant vulnerability to tephra fall. *Natural Hazards and Earth System Sciences*, 5(4):477–494, 2005.

[122] Ayris, P. M. and Delmelle, P. The immediate environmental effects of tephra emission. *Bulletin of Volcanology*, 74(9):1905–1936, 2012.

[123] Bundschuh, J., Farias, B., Martin, R., Storniolo, A., Bhattacharya, P., Cortes, J., Bonorino, G., and Albouy, R. Groundwater arsenic in the chaco-pampean plain, argentina: case study from robles county, santiago del estero province. *Applied Geochemistry*, 19(2):231–243, 2004.

[124] Sulpizio, R., Dellino, P., Doronzo, D., and Sarocchi, D. Pyroclastic density currents: state of the art and perspectives. *Journal of Volcanology and Geothermal Research*, 283:36–65, 2014.

[125] Fisher, R. V. Decoupling of pyroclastic currents: hazards assessments. *Journal of Volcanology and Geothermal Research*, 66(1):257–263, 1995.

[126] Sulpizio, R. and Dellino, P. Sedimentology, depositional mechanisms and pulsating behaviour of pyroclastic density currents. *Developments in Volcanology*, 10:57–96, 2008.

[127] Valentine, G. A. and Wohletz, K. H. Numerical models of Plinian eruption columns and pyroclastic flows. *Journal of Geophysical Research: Solid Earth (1978–2012)*, 94(B2):1867–1887, 1989.

[128] Dellino, P., Dioguardi, F., Zimanowski, B., Büttner, R., Mele, D., La Volpe, L., Sulpizio, R., Doronzo, D. M., Sonder, I., Bonasia, R., Calvari, S., and

Marotta, E. Conduit flow experiments help constraining the regime of explosive eruptions. *Journal of Geophysical Research: Solid Earth (1978–2012)*, 115(4):1–17, 2010.

[129] Sheridan, M. F. Emplacement of pyroclastic flows: a review. *Geological Society of America Special Papers*, 180:125–136, 1979.

[130] Belousov, A., Voight, B., and Belousova, M. Directed blasts and blast-generated pyroclastic density currents: A comparison of the Bezymianny 1956, Mount St Helens 1980, and Soufrière Hills, Montserrat 1997 eruptions and deposits. *Bulletin of Volcanology*, 69(7):701–740, 2007.

[131] Hayashi, J. and Self, S. A comparison of pyroclastic flow and debris avalanche mobility. *Journal of Geophysical Research: Solid Earth (1978–2012)*, 97(B6): 9063–9071, 1992.

[132] Malin, M. C. and Sheridan, M. F. Computer-assisted mapping of pyroclastic surges. *Science*, 217(4560):637–640, 1982.

[133] Doyle, E., Hogg, A., Mader, H., and Sparks, R. A two-layer model for the evolution and propagation of dense and dilute regions of pyroclastic currents. *Journal of Volcanology and Geothermal Research*, 190(3):365–378, 2010.

[134] Córdoba, G. *Dilute particle-laden currents: dynamics and deposit patterns*. PhD thesis, University of Bristol, 2007.

[135] Sparks, R. S. J. Grain size variations in ignimbrites and implications for the transport of pyroclastic flows. *Sedimentology*, 23(2):147–188, 1976.

[136] Sheridan, M. F. and Macías, J. Estimation of risk probability for gravity-driven pyroclastic flows at Volcán Colima, Mexico. *Journal of Volcanology and Geothermal Research*, 66(1):251–256, 1995.

[137] Sheridan, M. F. and Malin, M. C. Application of computer-assisted mapping to volcanic hazard evaluation of surge eruptions: Vulcano, lipari, and vesuvius. *Journal of Volcanology and Geothermal Research*, 17(1):187–202, 1983.

[138] Ogburn, S. E. FlowDat: Mass Flow Database, Nov 2012. URL https://vhub.org/groups/massflowdatabase.

[139] Dellino, P. and La Volpe, L. Structures and grain size distribution in surge deposits as a tool for modelling the dynamics of dilute pyroclastic density currents at La Fossa di Vulcano (Aeolian Islands, Italy). *Journal of Volcanology and Geothermal Research*, 96(1):57–78, 2000.

[140] Woods, A. W. and Kienle, J. The dynamics and thermodynamics of volcanic clouds: theory and observations from the April 15 and April 21, 1990 eruptions of Redoubt Volcano, Alaska. *Journal of Volcanology and Geothermal Research*, 62(1-4):273–299, 1994.

[141] Valentine, G. A. Stratified flow in pyroclastic surges. *Bulletin of Volcanology*, 49(4):616–630, 1987.

[142] Woods, A. W. and Wohletz, K. Dimensions and dynamics of co-ignimbrite eruption columns. *Nature*, 350(6315):225, 1991.

[143] Engwell, S., de'Michieli Vitturi, M., Esposti Ongaro, T., and Neri, A. Insights into the formation and dynamics of coignimbrite plumes from one-dimensional models. *Journal of Geophysical Research: Solid Earth*, 121(6): 4211–4231, 2016.

[144] Sulpizio, R., Mele, D., Dellino, P., and La Volpe, L. A complex, Subplinian-type eruption from low-viscosity, phonolitic to tephri-phonolitic magma: the AD 472 (Pollena) eruption of Somma-Vesuvius, Italy. *Bulletin of Volcanology*, 67(8):743–767, 2005.

[145] Ogburn, S. E., Calder, E. S., Cole, P. D., and Stinton, A. J. The effect of topography on ash-cloud surge generation and propagation. *Geological Society, London, Memoirs*, 39(1):179–194, 2014.

[146] Aguirre-Díaz, G. J., Labarthe-Hernández, G., Tristán-González, M., Nieto-Obregón, J., and Gutiérrez-Palomares, I. The ignimbrite flare-up and graben calderas of the Sierra Madre Occidental, México. *Developments in Volcanology*, 10:143–180, 2008.

[147] Cas, R. A., Wright, H. M., Folkes, C. B., Lesti, C., Porreca, M., Giordano, G., and Viramonte, J. G. The flow dynamics of an extremely large volume pyroclastic flow, the 2.08-Ma Cerro Galán Ignimbrite, NW Argentina, and comparison with other flow types. *Bulletin of Volcanology*, 73(10):1583–1609, 2011.

[148] Doronzo, D. M. Two new end members of pyroclastic density currents: forced convection-dominated and inertia-dominated. *Journal of Volcanology and Geothermal Research*, 219:87–91, 2012.

[149] Doronzo, D. M., de Tullio, M. D., Pascazio, G., Dellino, P., and Liu, G. On the interaction between shear dusty currents and buildings in vertical collapse: theoretical aspects, experimental observations, and 3d numerical simulation. *Journal of Volcanology and Geothermal Research*, 302:190–198, 2015.

[150] Wright, J. V., Smith, A. L., Roobol, M. J., Mattioli, G. S., and Fryxell, J. E. Distal ash hurricane (pyroclastic density current) deposits from a ca. 2000 yr bp plinian-style eruption of mount pelée, martinique: Distribution, grain-size characteristics, and implications for future hazard. *Geological Society of America Bulletin*, 128(5-6):777–791, 2016.

[151] Doronzo, D. M., Valentine, G. A., Dellino, P., and de Tullio, M. D. Numerical analysis of the effect of topography on deposition from dilute pyroclastic density currents. *Earth and Planetary Science Letters*, 300(1):164–173, 2010.

[152] Andrews, B. J. and Manga, M. Effects of topography on pyroclastic density current runout and formation of coignimbrites. *Geology*, 39(12):1099–1102, 2011.

[153] Valentine, G. A. Damage to structures by pyroclastic flows and surges, inferred from nuclear weapons effects. *Journal of Volcanology and Geothermal Research*, 87(1):117–140, 1998.

[154] Zuccaro, G., Cacace, F., Spence, R., and Baxter, P. Impact of explosive eruption scenarios at Vesuvius. *Journal of Volcanology and Geothermal Research*, 178(3):416–453, 2008.

[155] Baxter, P., Neri, A., and Todesco, M. Physical Modelling and Human Survival in Pyroclastic Flows. *Natural Hazards*, 17(2):163–176, 1998.

[156] Cioni, R., Gurioli, L., Lanza, R., and Zanella, E. Temperatures of the AD 79 pyroclastic density current deposits (Vesuvius, Italy). *Journal of Geophysical Research: Solid Earth (1978–2012)*, 109(B2), 2004.

[157] Auker, M., Sparks, R., Siebert, L., Crosweller, H., and Ewert, J. A statistical analysis of the global historical volcanic fatalities record. *Journal of Applied Volcanology*, 2(1):2, 2013.

[158] Fisher, R. V., Smith, A. L., and Roobol, M. J. Destruction of St. Pierre, Martinique, by ash-cloud surges, May 8 and 20, 1902. *Geology*, 8(10):472–476, 1980.

[159] Taylor, G. A. The 1951 eruption of Mount Lamington, Papua. *Australian Bureau of Mineral Resources, Geology and Geophysics Bulletin*, 38:1–117, 1958.

[160] Sigurdsson, H., Carey, S., and Espindola, J. The 1982 eruptions of El Chichón volcano, Mexico: stratigraphy of pyroclastic deposits. *Journal of Volcanology and Geothermal Research*, 23(1):11–37, 1984.

[161] Vallance, J. W. Lahars. *Encyclopedia of volcanoes, edited by: Sigurdsson, H., Houghton, B. F., McNutt, S. R., Rymer, H., and Stix, J.*, 2000.

[162] Mead, S., Magill, C., and Hilton, J. Rain-triggered lahar susceptibility using a shallow landslide and surface erosion model. *Geomorphology*, 273:168–177, 2016.

[163] van Westen, C. J. and Daag, A. S. Analysing the relation between rainfall characteristics and lahar activity at Mount Pinatubo, Philippines. *Earth Surface Processes and Landforms*, 30(13):1663–1674, 2005.

[164] Lavigne, F., Thouret, J., Voight, B., Suwa, H., and Sumaryono, A. Lahars at Merapi volcano, Central Java: an overview. *Journal of Volcanology and Geothermal Research*, 100(1-4):423–456, 2000.

[165] Arguden, A. T. and Rodolfo, K. S. Sedimentologic and dynamic differences between hot and cold laharic debris flows of Mayon Volcano, Philippines. *Bulletin of the Geological Society of America*, 102(7):865–876, 1990.

[166] Pierson, T. C., Janda, R. J., Thouret, J.-C., and Borrero, C. A. Perturbation and melting of snow and ice by the 13 november 1985 eruption of nevado del ruiz, colombia, and consequent mobilization, flow and deposition of lahars. *Journal of Volcanology and Geothermal Research*, 41(1-4):17–66, 1990.

[167] Pistolesi, M., Cioni, R., Rosi, M., Cashman, K. V., Rossotti, A., and Aguilera, E. Evidence for lahar-triggering mechanisms in complex stratigraphic sequences: The post-twelfth century eruptive activity of Cotopaxi Volcano, Ecuador. *Bulletin of Volcanology*, 75(3):1–18, 2013.

[168] Manville, V. and Cronin, S. J. Breakout lahar from New Zealand's crater lake. *Eos, Transactions American Geophysical Union*, 88(43):441–442, 2007.

[169] Pierson, T. C., Major, J. J., Amigo, Á., and Moreno, H. Acute sedimentation response to rainfall following the explosive phase of the 2008-2009 eruption of Chaitén volcano, Chile. *Bulletin of Volcanology*, 75(5):1–17, 2013.

[170] Sulpizio, R., Zanchetta, G., Demi, F., Di Vito, M. A., Pareschi, M. T., and Santacroce, R. The Holocene syneruptive volcaniclastic debris flows in the Vesuvian area: Geological data as a guide for hazard assessment. *Geological Society of America Special Papers*, 402:217–235, 2006.

[171] Pareschi, M. T., Favalli, M., Giannini, F., Sulpizio, R., Zanchetta, G., and Santacroce, R. May 5, 1998, debris flows in circum-Vesuvian areas (Southern Italy): Insights for hazard assessment. *Geology*, 28(7):639–642, 2000.

[172] Zanchetta, G., Sulpizio, R., Pareschi, M. T., Leoni, F. M., and Santacroce, R. Characteristics of May 5-6, 1998 volcaniclastic debris flows in the Sarno area (Campania, southern Italy): Relationships to structural damage and hazard zonation. *Journal of Volcanology and Geothermal Research*, 133(1-4):377–393, 2004.

[173] Bisson, M., Sulpizio, R., Zanchetta, G., Demi, F., and Santacroce, R. Rapid terrain-based mapping of some volcaniclastic flow hazard using Gis-based automated methods: A case study from southern Campania, Italy. *Natural Hazards*, 55(2):371–387, 2010.

[174] Bisson, M., Spinetti, C., and Sulpizio, R. Volcaniclastic flow hazard zonation in the Sub-apennine vesuvian area using gis and remote sensing. *Geosphere*, 10(6):1419–1431, 2014.

[175] Bisson, M., Pareschi, M. T., Zanchetta, G., Sulpizio, R., and Santacroce, R. Volcaniclastic debris-flow occurrences in the Campania region (Southern Italy) and their relation to Holocene - Late Pleistocene pyroclastic fall deposits: Implications for large-scale hazard mapping. *Bulletin of Volcanology*, 70(2):157–167, 2007.

[176] Barclay, J., Alexander, J., and Sušnik, J. Rainfall-induced lahars in the Belham Valley , Montserrat , West Indies. *Journal of the Geological Society*, 164:815–827, 2007.

[177] Frattini, P., Crosta, G., and Sosio, R. Approaches for defining thresholds and return periods for rainfall-triggered shallow landslides. *Hydrological Processes*, 23(10):1444–1460, 2009.

[178] Iverson, R. M. Landslide triggering by rain infiltration. *Water Resources Research*, 36(7):1897, 2000.

[179] Rodolfo, K. S., Umbal, J. V., Alonso, R. A., Remotigue, C. T., Paladio-Melosantos, M. L., Salvador, J. H., Evangelista, D., and Miller, Y. Two years of lahars on the western flank of Mount Pinatubo: Initiation, flow processes, deposits, and attendant geomorphic and hydraulic changes. *Fire and mud, eruptions and lahars of Mt Pinatubo, Philippines, edited by: Newhall, C. G., and Punongbayan, R. S.*, pages 989–1013, 1996.

[180] Capra, L., Borselli, L., Varley, N., Gavilanes-Ruiz, J. C., Norini, G., Sarocchi, D., Caballero, L., and Cortes, A. Rainfall-triggered lahars at Volcán de Colima, Mexico: Surface hydro-repellency as initiation process. *Journal of Volcanology and Geothermal Research*, 189(1-2):105–117, 2010.

[181] Lavigne, F., Thouret, J.-C., Voight, B., Young, K., LaHusen, R., Marso, J., Suwa, H., Sumaryono, a., Sayudi, D. S., and Dejean, M. Instrumental lahar monitoring at Merapi Volcano, Central Java, Indonesia. *Journal of Volcanology and Geothermal Research*, 100(1-4):457–478, 2000.

[182] Martinez, M. M. L., Arboleda, R. A., Delos Reyes, P., Gabinete, E., and Dolan, M. T. Observations of 1992 lahars along the Sacobia-Bamban River system. *Fire and mud, eruptions and lahars of Mt Pinatubo, Philippines, edited by: Newhall, C. G., and Punongbayan, R. S.*, pages 1033–1045, 1996.

[183] Neall, V. E. Lahars as major geological hazards. *Bulletin of the International Association of Engineering Geology*, 13(1):233–240, 1976.

[184] Scott, K. M., Janda, R. J., De La Cruz, E., Gabinete, E., Eto, I., Isada, M., Sexon, M., and Hadley, K. C. Channel and sedimentation responses to large volumes of 1991 volcanic deposits on the east flank of Mount Pinatubo. *Fire and mud, eruptions and lahars of Mt Pinatubo, Philippines, edited by: Newhall, C. G., and Punongbayan, R. S.*, pages 971–988, 1996.

[185] Iverson, R. M. Debris flows: behaviour and hazard assessment. *Geology today*, 30(1):15–20, 2014.

[186] Orsi, G., Gallo, G., and Zanchi, A. Simple-shearing block resurgence in caldera depressions. A model from Pantelleria and Ischia. *Journal of Volcanology and Geothermal Research*, 47(1-2):1–11, 1991.

[187] Orsi, G., Piochi, M., Campajola, L., D'Onofrio, A., Gialanella, L., and Terrasi, F. 14 C geochronological constraints for the volcanic history of the Island of Ischia (Italy) over the last 5000 years. *Journal of Volcanology and Geothermal Research*, 71(2):249–257, 1996.

[188] Chiodini, G., Paonita, A., Aiuppa, A., Costa, A., Caliro, S., De Martino, P., Acocella, V., and Vandemeulebrouck, J. Magmas near the critical degassing pressure drive volcanic unrest towards a critical state. *Nature communications*, 7, 2016.

[189] Brancaccio, L., Cinque, A., Romano, P., Rosskopf, C., Russo, F., Santangelo, N., and Santo, A. Geomorphology and neotectonic evolution of a sector of the Tyrrhenian flank of the Southern Apennines (Region of Naples, Italy). *Zeitschrift für Geomorphologie*, 82:47–58, 1991.

[190] Santacroce, R., Cioni, R., Marianelli, P., Sbrana, A., Sulpizio, R., Zanchetta, G., Donahue, D. J., and Joron, J. L. Age and whole rock-glass compositions of proximal pyroclastics from the major explosive eruptions of Somma-Vesuvius: A review as a tool for distal tephrostratigraphy. *Journal of Volcanology and Geothermal Research*, 177(1):1–18, 2008.

[191] Smith, V., Isaia, R., and Pearce, N. Tephrostratigraphy and glass compositions of post-15 kyr campi flegrei eruptions: implications for eruption history and chronostratigraphic markers. *Quaternary Science Reviews*, 30 (25):3638–3660, 2011.

[192] Santacroce, R. and Sbrana, A. Geological map of Vesuvius. *SELCA Firenze*, 2003.

[193] Hazlett, R. W., Buesch, D., Anderson, J. L., Elan, R., and Scandone, R. Geology, failure conditions, and implications of seismogenic avalanches of the 1944 eruption at Vesuvius, Italy. *Journal of Volcanology and Geothermal Research*, 47(3):249–264, 1991.

[194] Sevink, J., van Bergen, M. J., van der Plicht, J., Feiken, H., Anastasia, C., and Huizinga, A. Robust date for the Bronze Age Avellino eruption (Somma-Vesuvius): 3945±10 calBP (1995±10 calBC). *Quaternary Science Reviews*, 30(9):1035–1046, 2011.

[195] Orsi, G., Di Vito, M. A., Selva, J., and Marzocchi, W. Long-term forecast of eruption style and size at Campi Flegrei caldera (Italy). *Earth and Planetary Science Letters*, 287(1):265–276, 2009.

[196] Cioni, R., Santacroce, R., and Sbrana, A. Pyroclastic deposits as a guide for reconstructing the multi-stage evolution of the Somma-Vesuvius Caldera. *Bulletin of Volcanology*, 61(4):207–222, 1999.

[197] Bertagnini, A., Landi, P., Rosi, M., and Vigliargio, A. The pomici di base plinian eruption of somma-vesuvius. *Journal of Volcanology and Geothermal Research*, 83(3):219–239, 1998.

[198] Rosi, M., Principe, C., and Vecci, R. The 1631 vesuvius eruption. a reconstruction based on historical and stratigraphical data. *Journal of Volcanology and Geothermal Research*, 58(1-4):151–182, 1993.

[199] Fiorillo, F. and Wilson, R. C. Rainfall induced debris flows in pyroclastic deposits, Campania (southern Italy). *Engineering Geology*, 75(3-4):263–289, 2004.

[200] Lirer, L., Vinci, A., Alberico, I., Gifuni, T., Bellucci, F., Petrosino, P., and Tinterri, R. Occurrence of inter-eruption debris flow and hyperconcentrated flood-flow deposits on Vesuvio volcano, Italy. *Sedimentary Geology*, 139(2): 151–167, 2001.

[201] Pareschi, M. T., Santacroce, R., Sulpizio, R., and Zanchetta, G. Volcaniclastic debris flows in the Clanio Valley (Campania, Italy): Insights for the assessment of hazard potential. *Geomorphology*, 43(3-4):219–231, 2002.

[202] Zanchetta, G., Sulpizio, R., and Di Vito, M. A. The role of volcanic activity and climate in alluvial fan growth at volcanic areas: An example from southern Campania (Italy). *Sedimentary Geology*, 168(3-4):249–280, 2004.

[203] Fedele, F. G., Giaccio, B., Isaia, R., and Orsi, G. The Campanian Ignimbrite Eruption, Heinrich Event 4, and Palaeolithic Change in Europe: A High-Resolution Investigation. *Volcanism and the Earth's Atmosphere, edited by:*

Robock, A., and Oppenheimer, C., AGU Geophysical Monograph Series 139: 301–325, 2003.

[204] Deino, A. L., Orsi, G., de Vita, S., and Piochi, M. The age of the Neapolitan Yellow Tuff caldera-forming eruption (Campi Flegrei caldera–Italy) assessed by 40 Ar/39 Ar dating method. *Journal of Volcanology and Geothermal Research*, 133(1):157–170, 2004.

[205] Selva, J., Orsi, G., Di Vito, M. A., Marzocchi, W., and Sandri, L. Probability hazard map for future vent opening at the Campi Flegrei caldera, Italy. *Bulletin of Volcanology*, 74(2):497–510, 2012.

[206] Bevilacqua, A., Isaia, R., Neri, A., Vitale, S., Aspinall, W. P., Bisson, M., Flandoli, F., Baxter, P. J., Bertagnini, A., Esposti Ongaro, T., et al. Quantifying volcanic hazard at Campi Flegrei caldera (Italy) with uncertainty assessment: 1. Vent opening maps. *Journal of Geophysical Research: Solid Earth*, 120(4):2309–2329, 2015.

[207] Dvorak, J. J. and Berrino, G. Recent ground movement and seismic activity in Campi Flegrei, southern Italy: Episodic growth of a resurgent dome. *Journal of Geophysical Research: Solid Earth (1978–2012)*, 96(B2):2309–2323, 1991.

[208] D'Auria, L., Pepe, S., Castaldo, R., Giudicepietro, F., Macedonio, G., Ricciolino, P., Tizzani, P., Casu, F., Lanari, R., Manzo, M., et al. Magma injection beneath the urban area of Naples: a new mechanism for the 2012–2013 volcanic unrest at Campi Flegrei caldera. *Scientific reports*, 5, 2015.

[209] De Siena, L., Del Pezzo, E., and Bianco, F. Seismic attenuation imaging of Campi Flegrei: Evidence of gas reservoirs, hydrothermal basins, and feeding systems. *Journal of Geophysical Research: Solid Earth (1978–2012)*, 115(9): 1–18, 2010.

[210] Del Negro, C., Cappello, A., Neri, M., Bilotta, G., Hérault, A., and Ganci, G. Lava flow hazards at Mount Etna: constraints imposed by eruptive history and numerical simulations. *Scientific reports*, 3, 2013.

[211] Strehlow, K., Sandri, L., Gottsmann, J. H., Kilgour, G., Rust, A. C., and Tonini, R. Phreatic eruptions at crater lakes: occurrence statistics and probabilistic hazard forecast. *Journal of Applied Volcanology*, 6(1):4, 2017.

[212] Heim, A. *Bergsturz und menschenleben*, volume 30. Fretz & Wasmuth, 1932.

[213] Beget, J. E. and Limke, A. J. Two-dimensional kinematic and rheological modeling of the 1912 pyroclastic flow, Katmai, Alaska. *Bulletin of Volcanology*, 50(3):148–160, 1988.

[214] Calder, E., Cole, P., Dade, W., Druitt, T., Hoblitt, R., Huppert, H., Ritchie, L., Sparks, R., and Young, S. Mobility of pyroclastic flows and surges at the Soufriere Hills volcano, Montserrat. *Geophysical Research Letters*, 26(5): 537–540, 1999.

[215] Wohletz, K. and Heiken, G. *Volcanology and geothermal energy*. University of California Press Berkeley, 1992.

[216] Sheridan, M. Pyroclastic block flow from the September, 1976, eruption of La Soufrière volcano, Guadeloupe. *Bulletin of Volcanology*, 43(2):397–402, 1980.

[217] Alberico, I., Lirer, L., Petrosino, P., and Scandone, R. A methodology for the evaluation of long-term volcanic risk from pyroclastic flows in Campi Flegrei (Italy). *Journal of Volcanology and Geothermal Research*, 116(1): 63–78, 2002.

[218] Patra, A. K., Bauer, A. C., Nichita, C. C., Pitman, E. B., Sheridan, M. F., Bursik, M., Rupp, B., Webber, A., Stinton, A. J., Namikawa, L. M., and Renschler, C. S. Parallel adaptive numerical simulation of dry avalanches over natural terrain. *Journal of Volcanology and Geothermal Research*, 139 (1-2):1–21, 2005.

[219] Iverson, R. M. and Denlinger, R. P. Flow of variably fluidized granular masses across three-dimensional terrain: 1. Coulomb mixture theory. *Journal of Geophysical Research: Solid Earth (1978–2012)*, 106(B1):537–552, 2001.

[220] *TITAN2D User Guide*. Geophysical Mass Flow Group, (GMFG), University at Buffalo, NY, USA, 2007.

[221] Mehta, A. and Barker, G. The dynamics of sand. *Reports on Progress in Physics*, 57(4):383, 1994.

[222] Sheridan, M., Stinton, A., Patra, A., Pitman, E., Bauer, A., and Nichita, C. Evaluating Titan2D mass-flow model using the 1963 Little Tahoma Peak avalanches, Mount Rainier, Washington. *Journal of Volcanology and Geothermal Research*, 139(1):89–102, 2005.

[223] Macías, J. L., Capra, L., Arce, J. L., Espíndola, J. M., García-Palomo, A., and Sheridan, M. F. Hazard map of El Chichón volcano, Chiapas, México: Constraints posed by eruptive history and computer simulations. *Journal of Volcanology and Geothermal Research*, 175(4):444–458, 2008.

[224] Charbonnier, S. J. and Gertisser, R. Numerical simulations of block-and-ash flows using the Titan2D flow model: examples from the 2006 eruption of Merapi Volcano, Java, Indonesia. *Bulletin of Volcanology*, 71(8):953–959, 2009.

[225] Procter, J. N., Cronin, S. J., Platz, T., Patra, A., Dalbey, K., Sheridan, M., and Neall, V. Mapping block-and-ash flow hazards based on Titan 2D simulations: a case study from Mt. Taranaki, NZ. *Natural Hazards*, 53(3): 483–501, 2010.

[226] Hendrickson, B. and Devine, K. Dynamic load balancing in computational mechanics. *Computer methods in applied mechanics and engineering*, 184 (2):485–500, 2000.

[227] Constantinescu, R., Thouret, J.-C., and Irimus, I. Computer modeling as tool for volcanic hazards assessment: An example of pyroclastic flow modeling at El Misti volcano, southern Peru. *Geographia Technica*, 2:1–14, 2011.

[228] Hubbard, B. E., Sheridan, M. F., Carrasco-Núñez, G., Díaz-Castellón, R., and Rodríguez, S. R. Comparative lahar hazard mapping at Volcan Citlaltépetl, Mexico using SRTM, ASTER and DTED-1 digital topographic data. *Journal of Volcanology and Geothermal Research*, 160(1-2):99–124, 2007.

[229] Williams, R., Stinton, A. J., and Sheridan, M. F. Evaluation of the Titan2D two-phase flow model using an actual event: Case study of the 2005 Vazcún Valley Lahar. *Journal of Volcanology and Geothermal Research*, 177(4):760–766, 2008.

[230] Procter, J., Cronin, S., Fuller, I., Sheridan, M., Neall, V., and Keys, H. Lahar hazard assessment using Titan2D for an alluvial fan with rapidly changing

geomorphology: Whangaehu River, Mt. Ruapehu. *Geomorphology*, 116(1): 162–174, 2010.

[231] Sheridan, M. F., Patra, A. K., Dalbey, K., and Hubbard, B. Probabilistic digital hazard maps for avalanches and massive pyroclastic flows using TITAN2D. *Geological Society of America Special Papers*, 464:281–291, 2010.

[232] Sulpizio, R., Bonasia, R., Dellino, P., Mele, D., Di Vito, M., and La Volpe, L. The Pomici di Avellino eruption of Somma–Vesuvius (3.9 ka BP). part II: sedimentology and physical volcanology of pyroclastic density current deposits. *Bulletin of Volcanology*, 72(5):559–577, 2010.

[233] Yu, B., Dalbey, K., Webb, A., Bursik, M., Patra, A., Pitman, E. B., and Nichita, C. Numerical issues in computing inundation areas over natural terrains using Savage-Hutter theory. *Natural Hazards*, 50(2):249–267, 2009.

[234] Ogburn, S. E., Berger, J., Calder, E. S., Lopes, D., Patra, A., Pitman, E. B., Rutarindwa, R., Spiller, E., and Wolpert, R. L. Pooling strength amongst limited datasets using hierarchical bayesian analysis, with application to pyroclastic density current mobility metrics. *Statistics in Volcanology*, 2(1): 1, 2016.

[235] Woodhouse, M. J., Hogg, A. J., and Phillips, J. C. A dynamic model of lahars for hazard assessments. *TBD*, in prep.

[236] Raudkivi, A. *Loose boundary hydraulics*. Oxford: Pergamon Press, 1976.

[237] Pouliquen, O. Scaling laws in granular flows down rough inclined planes. *Physics of fluids*, 11(3):542–548, 1999.

[238] Robert, C. P. *Monte carlo methods*. Wiley Online Library, 2004.

[239] Tarantola, A. *Inverse problem theory and methods for model parameter estimation*. SIAM, 2005.

[240] Madankan, R., Singla, P., Patra, A., Bursik, M., Dehn, J., Jones, M., Pavolonis, M., Pitman, B., Singh, T., and Webley, P. Polynomial chaos quadrature-based minimum variance approach for source parameters estimation. *Procedia Computer Science*, 9:1129–1138, 2012.

[241] Bellman, R. Dynamic programming and Lagrange multipliers. *Proceedings of the National Academy of Sciences*, 42(10):767–769, 1956.

[242] Tonini, R., Sandri, L., and Thompson, M. A. PyBetVH: a Python tool for probabilistic volcanic hazard assessment and for generation of Bayesian hazard curves and maps. *Computers & Geosciences*, 79:38–46, 2015.

[243] Rouwet, D., Sandri, L., Marzocchi, W., Gottsmann, J., Selva, J., Tonini, R., and Papale, P. Recognizing and tracking volcanic hazards related to non-magmatic unrest: a review. *Journal of Applied Volcanology*, 3(1):17, 2014.

[244] Tonini, R., Sandri, L., Rouwet, D., Caudron, C., and Marzocchi, W. A new Bayesian Event Tree tool to track and quantify volcanic unrest and its application to Kawah Ijen volcano. *Geochemistry, Geophysics, Geosystems*, 17(7):2539–2555, 2016.

[245] Constantinescu, R., Robertson, R., Lindsay, J. M., Tonini, R., Sandri, L., Rouwet, D., Smith, P., and Stewart, R. Application of the probabilistic model BET_UNREST during a volcanic unrest simulation exercise in Dominica, Lesser Antilles. *Geochemistry, Geophysics, Geosystems*, 2016.

[246] Neyman, J. Outline of a theory of statistical estimation based on the classical theory of probability. *Philosophical Transactions of the Royal Society of London. Series A, Mathematical and Physical Sciences*, 236(767):333–380, 1937.

[247] Jensen, F. V. *An introduction to Bayesian networks*, volume 210. UCL press London, 1996.

[248] Aspinall, W. Structured elicitation of expert judgment for probabilistic hazard and risk assessment in volcanic eruptions. *Statistics in Volcanology, edited by: Mader, H. M., Coles, S. G., Connor, C. B., and Connor, L. J.*, pages 15–30, 2006.

[249] Marzocchi, W. and Bebbington, M. S. Probabilistic eruption forecasting at short and long time scales. *Bulletin of Volcanology*, 74(8):1777–1805, 2012.

[250] Newhall, C. G. and Pallister, J. S. Using multiple data sets to populate probabilistic volcanic event trees. *Volcanic Hazards, Risks, and Disasters, edited by: Papale, P., Eichelberger, J.C., Nakada, S., Loughlin, S., and Yepes, H.*, 203, 2014.

[251] Charniak, E. Bayesian networks without tears. *AI magazine*, 12(4):50, 1991.

[252] Murphy, K. P. The Bayes Net Toolbox for Matlab. *Computing Science and Statistics*, 33(2):1024–1034, 2001.

[253] Koller, D. and Friedman, N. *Probabilistic graphical models: principles and techniques*. MIT press, 2009.

[254] Favalli, M., Chirico, G. D., Papale, P., Pareschi, M. T., and Boschi, E. Lava flow hazard at Nyiragongo volcano, DRC. *Bulletin of Volcanology*, 71(4): 363–374, 2009.

[255] Salt, J. The seven habits of highly defective simulation projects. *Journal of Simulation*, 2(3):155–161, 2008.

[256] Jaccard, P. *Le coefficient generique et le coefficient de communaute dans la flore marocaine*. Impr. Commerciale, 1926.

[257] Tarquini, S. and Favalli, M. Mapping and DOWNFLOW simulation of recent lava flow fields at Mount Etna. *Journal of Volcanology and Geothermal Research*, 204(1):27–39, 2011.

[258] De Vita, S., Orsi, G., Civetta, L., Carandente, A., D'Antonio, M., Deino, A., Di Cesare, T., Di Vito, M., Fisher, R., Isaia, R., et al. The Agnano–Monte Spina eruption (4100 years BP) in the restless Campi Flegrei caldera (Italy). *Journal of Volcanology and Geothermal Research*, 91(2):269–301, 1999.

[259] Marzocchi, W., Newhall, C., and Woo, G. The scientific management of volcanic crises. *Journal of Volcanology and Geothermal Research*, 247:181–189, 2012.

[260] Wadge, G., Jackson, P., Bower, S., Woods, A., and Calder, E. Computer simulations of pyroclastic flows from dome collapse. *Geophysical Research Letters*, 25(19):3677–3680, 1998.

[261] Calder, E., Pitman, B., Wolpert, R., Bayarri, S., Spiller, E., and Berger, J. Towards a new approach for generating probabilistic hazard maps for pyroclastic flows during lava dome eruptions. In *AGU Spring Meeting Abstracts*, volume 1, page 07, 2009.

[262] Tarquini, S., Isola, I., Favalli, M., Mazzarini, F., Bisson, M., Pareschi, M. T., and Boschi, E. Tinitaly/01: a new triangular irregular network of Italy. *Annals of Geophysics*, 2007.

[263] Massey, F. J. The Kolmogorov-Smirnov test for goodness of fit. *Journal of the American statistical Association*, 46(253):68–78, 1951.

[264] Selva, J., Sandri, L., Costa, A., Tonini, R., Folch, A., and Macedonio, G. Exploring the full natural variability of eruption sizes within probabilistic hazard assessment of tephra dispersal. In *EGU General Assembly Conference Abstracts*, volume 16, page 7612, 2014.

[265] Mastin, L., Guffanti, M., Servranckx, R., Webley, P., Barsotti, S., Dean, K., Durant, A., Ewert, J., Neri, A., Rose, W., et al. A multidisciplinary effort to assign realistic source parameters to models of volcanic ash-cloud transport and dispersion during eruptions. *Journal of Volcanology and Geothermal Research*, 186(1):10–21, 2009.

[266] Siebert, L. Large volcanic debris avalanches: characteristics of source areas, deposits, and associated eruptions. *Journal of Volcanology and Geothermal Research*, 22(3):163–197, 1984.

[267] Toyos, G., Cole, P., Felpeto, A., and Marti, J. A GIS-based methodology for hazard mapping of small volume pyroclastic density currents. *Natural Hazards*, 41(1):99–112, 2007.

[268] Cole, P. D. and Scarpati, C. The 1944 eruption of Vesuvius, Italy: combining contemporary accounts and field studies for a new volcanological reconstruction. *Geological Magazine*, 147(03):391–415, 2010.

[269] Sulpizio, R., Mele, D., Dellino, P., and La Volpe, L. Deposits and physical properties of pyroclastic density currents during complex Subplinian eruptions: the AD 472 (Pollena) eruption of Somma-Vesuvius, Italy. *Sedimentology*, 54(3):607, 2007.

[270] Rolandi, G., Barrella, A., and Borrelli, A. The 1631 eruption of Vesuvius. *Journal of Volcanology and Geothermal Research*, 58(1):183–201, 1993.

[271] Mele, D., Sulpizio, R., Dellino, P., and La Volpe, L. Stratigraphy and eruptive dynamics of a pulsating Plinian eruption of Somma-Vesuvius: the Pomici di Mercato (8900 years BP). *Bulletin of Volcanology*, 73(3):257–278, 2011.

[272] Carey, S. and Sigurdsson, H. Temporal variations in column height and magma discharge rate during the 79 AD eruption of Vesuvius. *Geological Society of America Bulletin*, 99(2):303–314, 1987.

[273] Davis, J. C. *Statistics and data analysis in geology*. John Wiley & Sons, New York, 3rd edition, 2002.

[274] Hincks, T. K., Komorowski, J.-C., Sparks, S. R., and Aspinall, W. P. Retrospective analysis of uncertain eruption precursors at La Soufrière volcano, Guadeloupe, 1975–77: volcanic hazard assessment using a Bayesian Belief Network approach. *Journal of Applied Volcanology*, 3(1):1–26, 2014.

[275] Doyle, E. E., McClure, J., Paton, D., and Johnston, D. M. Uncertainty and decision making: Volcanic crisis scenarios. *International Journal of Disaster Risk Reduction*, 10:75–101, 2014.

[276] Abrahamson, N. A. and Bommer, J. J. Probability and uncertainty in seismic hazard analysis. *Earthquake Spectra*, 21(2):603–607, 2005.

[277] Stucchi, M., Meletti, C., Montaldo, V., Crowley, H., Calvi, G. M., and Boschi, E. Seismic Hazard Assessment (2003–2009) for the Italian Building Code. *Bulletin of the Seismological Society of America*, 101(4):1885–1911, 2011.

[278] Wadge, G. and Isaacs, M. Mapping the volcanic hazards from Soufriere Hills Volcano, Montserrat, West Indies using an image processor. *Journal of the Geological Society*, 145(4):541–551, 1988.

[279] Barberi, F., Ghigliotti, M., Macedonio, G., Orellana, H., Pareschi, M., and Rosi, M. Volcanic hazard assessment of Guagua Pichincha (Ecuador) based on past behaviour and numerical models. *Journal of Volcanology and Geothermal Research*, 49(1):53–68, 1992.

[280] Crandell, D. R. and Mullineaux, D. R. Potential hazards from future eruptions of Mount St. Helens volcano, Washington. *Geological Survey Bulletin*, 1383, 1978.

[281] Martí, J., Aspinall, W., Sobradelo, R., Felpeto, A., Geyer, A., Ortiz, R., Baxter, P., Cole, P., Pacheco, J., Blanco, M., et al. A long-term volcanic hazard event tree for Teide-Pico Viejo stratovolcanoes (Tenerife, Canary

Islands). *Journal of Volcanology and Geothermal Research*, 178(3):543–552, 2008.

[282] Marzocchi, W. and Woo, G. Principles of volcanic risk metrics: Theory and the case study of Mount Vesuvius and Campi Flegrei, Italy. *Journal of Geophysical Research: Solid Earth (1978–2012)*, 114:B03213, 2009.

[283] Kelfoun, K. and Druitt, T. Numerical modelling of the emplacement of the 7500 BP Socompa rock avalanche, Chile. *Journal of Geophysical Research: Solid Earth (1978–2012)*, 110:B12202, 2005.

[284] Clarke, A., Voight, B., Neri, A., and Macedonio, G. Transient dynamics of vulcanian explosions and column collapse. *Nature*, 415(6874):897–901, 2002.

[285] Dellino, P., Mele, D., Sulpizio, R., La Volpe, L., and Braia, G. A method for the calculation of the impact parameters of dilute pyroclastic density currents based on deposit particle characteristics. *Journal of Geophysical Research: Solid Earth (1978–2012)*, 113:B07206, 2008.

[286] Sheridan, M. F., Hubbard, B., Carrasco-Nunez, G., and Siebe, C. Pyroclastic flow hazard at Volcán Citlaltépetl. *Natural Hazards*, 33(2):209–221, 2004.

[287] Huppert, H. E. and Simpson, J. E. The slumping of gravity currents. *Journal of Fluid Mechanics*, 99(04):785, 1980.

[288] Hsu, K. Catastrophic debris streams (sturzstroms) generated by rockfalls. *Geological Society of America Bulletin*, 86:129–140, 1975.

[289] Best, M. J., Abramowitz, G., Johnson, H., Pitman, A., Balsamo, G., Boone, A., Cuntz, M., Decharme, B., Dirmeyer, P., Dong, J., et al. The plumbing of land surface models: benchmarking model performance. *Journal of Hydrometeorology*, 16(3):1425–1442, 2015.

[290] Senior Seismic Hazard Analysis Committee (SSHAC). *Recommendations for probabilistic seismic hazard analysis-guidance on uncertainty and use of experts*. U.S. Nuclear Regulatory Commission, NUREG/CR- 6372., 1997.

[291] Selva, J. Long-term multi-risk assessment: statistical treatment of interaction among risks. *Natural Hazards*, 67:701–722, 2013.

[292] Lirer, L., Petrosino, P., and Alberico, I. Hazard and risk assessment in a complex multi-source volcanic area: the example of the Campania Region, Italy. *Bulletin of Volcanology*, 2010.

[293] Alberico, I., Petrosino, P., and Lirer, L. Volcanic hazard and risk assessment in a multi-source volcanic area: the example of Napoli city (Southern Italy). *Natural Hazards and Earth System Sciences*, 11:1057–1070, 2011.

[294] Selva, J., Marzocchi, W., Papale, P., and Sandri, L. Operational eruption forecasting at high-risk volcanoes: the case of Campi Flegrei, Naples. *Journal of Applied Volcanology*, 1:5, 2012.

[295] Bevilacqua, A., Flandoli, F., Neri, A., Isaia, R., and Vitale, S. Temporal models for the episodic volcanism of Campi Flegrei caldera (Italy) with uncertainty quantification. *Journal of Geophysical Research: Solid Earth*, 121: 7821–7845, 2016.

[296] Marzocchi, W., Sandri, L., and Selva, J. Probability estimation at the nodes: general aspects. *Bulletin of Volcanology - Electronic Supplementary Material*, pages 1–20, 2008.

[297] Cioni, R., Sulpizio, R., and Garruccio, N. Variability of the eruption dynamics during a subplinian event: the Greenish Pumice eruption of Somma–Vesuvius (Italy). *Journal of Volcanology and Geothermal Research*, 124(1): 89–114, 2003.

[298] Cioni, R., Levi, S., and Sulpizio, R. Apulian Bronze Age pottery as a long-distance indicator of the Avellino Pumice eruption (Vesuvius, Italy). *Geological Society, London, Special Publications*, 171(1):159–177, 2000.

[299] Andronico, D. and Cioni, R. Contrasting styles of Mount Visuvius activity in the period between the Avellino and Pompeii Plinian eruptions, and some implications for assessment of future hazards. *Bulletin of Volcanology*, 64 (6):372–391, 2002. ISSN 02588900. doi: 10.1007/s00445-002-0215-4.

[300] Johnston-Lavis, H. J. The Geology of Monte Somma and Vesuvius, being a study in Vulcanology. *Quarterly Journal of the Geological Society*, 40(1-4): 35–119, 1884.

[301] Andronico, D., Calderoni, G., Cioni, R., Sbrana, A., Sulpizio, R., and Santacroce, R. Geological map of Somma-Vesuvius volcano. *Periodico di Mineralogia*, 64(1-2):77–78, 1995.

[302] Cioni, R., Bertagnini, A., Andronico, D., Cole, P., and Mundula, F. The 512 AD eruption of Vesuvius: complex dynamics of a small scale subplinian event. *Bulletin of Volcanology*, 73(7):789–810, 2011.

[303] Arrighi, S., Principe, C., and Rosi, M. Violent strombolian and subplinian eruptions at Vesuvius during post-1631 activity. *Bulletin of Volcanology*, 63 (2-3):126–150, 2001.

[304] Pesce, A. and Rolandi, G. *Vesuvio 1944. L'ultima eruzione.* S. Sebastiano al Vesuvio, 1994.

[305] Lindsay, J., Marzocchi, W., Jolly, G., Constantinescu, R., Selva, J., and Sandri, L. Towards real-time eruption forecasting in the Auckland Volcanic Field: application of BET_EF during the New Zealand National Disaster Exercise "Ruaumoko". *Bulletin of Volcanology*, 72:185–204, 2010.

[306] Tonini, R., Sandri, L., Costa, A., and Selva, J. Brief Communication: The effect of submerged vents on probabilistic hazard assessment for tephra fallout. *Natural Hazards and Earth System Sciences*, 15:409–415, 2015.

[307] Neri, A., Aspinall, W. P., Cioni, R., Bertagnini, A., Baxter, P. J., Zuccaro, G., Andronico, D., Barsotti, S., Cole, P. D., Esposti Ongaro, T., Hincks, T. K., Macedonio, G., Papale, P., Rosi, M., Santacroce, R., and Woo, G. Developing an Event Tree for probabilistic hazard and risk assessment at Vesuvius. *Journal of Volcanology and Geothermal Research*, 178(3):397–415, 2008.

[308] Todesco, M., Neri, A., Ongaro, T. E., Papale, P., Macedonio, G., Santacroce, R., and Longo, A. Pyroclastic flow hazard assessment at Vesuvius (Italy) by using numerical modeling. I. Large-scale dynamics. *Bulletin of Volcanology*, 64(3-4):155–177, 2002.

[309] Marzocchi, W. and Woo, G. Probabilistic eruption forecasting and the call for an evacuation. *Geophysical Research Letters*, 34(22), 2007.

[310] Jordan, T., Marzocchi, W., Michael, A., and Gerstenberger, M. Operational earthquake forecasting can enhance earthquake preparedness, 2014.

[311] Baxter, P. J., Boyle, R., Cole, P., Neri, A., Spence, R., and Zuccaro, G. The impacts of pyroclastic surges on buildings at the eruption of the Soufrière Hills volcano, Montserrat. *Bulletin of Volcanology*, 67(4):292–313, 2005.

[312] Simkin, T., Siebert, L., and Blong, R. Volcano fatalities–lessons from the historical record. *Science*, 291(5502):255–255, 2001.

[313] Spence, R., Kelman, I., Brown, A., Toyos, G., Purser, D., and Baxter, P. Residential building and occupant vulnerability to pyroclastic density currents in explosive eruptions. *Natural Hazards and Earth System Sciences*, 7 (2):219–230, 2007.

[314] Spence, R. J., Baxter, P. J., and Zuccaro, G. Building vulnerability and human casualty estimation for a pyroclastic flow: a model and its application to Vesuvius. *Journal of Volcanology and Geothermal Research*, 133(1):321–343, 2004.

[315] Spence, R. J., Zuccaro, G., Petrazzuoli, S., and Baxter, P. J. Resistance of buildings to pyroclastic flows: analytical and experimental studies and their application to Vesuvius. *Natural Hazards Review*, 5(1):48–59, 2004.

[316] Esposti Ongaro, T., Neri, A., Todesco, M., and Macedonio, G. Pyroclastic flow hazard assessment at Vesuvius (Italy) by using numerical modeling. II. Analysis of flow variables. *Bulletin of Volcanology*, 64(3):178–191, 2002.

[317] Murcia, H., Sheridan, M., Macías, J., and Cortés, G. TITAN2D simulations of pyroclastic flows at Cerro Machín Volcano, Colombia: Hazard implications. *Journal of South American Earth Sciences*, 29(2):161–170, 2010.

[318] Bayarri, M., Berger, J., Calder, E., Patra, A. K., Pitman, E. B., Spiller, E. T., and Wolpert, R. L. Probabilistic quantification of hazards: A methodology using small ensembles of physics-based simulations and statistical surrogates. *International Journal for Uncertainty Quantification*, 5(4), 2015.

[319] Capra, L., Manea, V., Manea, M., and Norini, G. The importance of digital elevation model resolution on granular flow simulations: a test case for Colima volcano using TITAN2D computational routine. *Natural Hazards*, 59(2):665–680, 2011.

[320] QGIS Development Team. *QGIS Geographic Information System*. Open Source Geospatial Foundation, 2016. URL http://qgis.osgeo.org.

[321] Sandri, L., Guidoboni, E., Marzocchi, W., and Selva, J. Bayesian event tree for eruption forecasting (BET_EF) at Vesuvius, Italy: a retrospective forward application to the 1631 eruption. *Bulletin of Volcanology*, 71(7): 729–745, 2009.

[322] Rolandi, G., Mastrolorenzo, G., Barrella, A., and Borrelli, A. The Avellino plinian eruption of Somma-Vesuvius (3760 yBP): the progressive evolution from magmatic to hydromagmatic style. *Journal of Volcanology and Geothermal Research*, 58(1-4):67–88, 1993.

[323] Zuccaro, G. and De Gregorio, D. Time and space dependency in impact damage evaluation of a sub-Plinian eruption at Mount Vesuvius. *Natural Hazards*, 68(3):1399–1423, 2013.

[324] Baxter, P. J., Aspinall, W. P., Neri, A., Zuccaro, G., Spence, R. J. S., Cioni, R., and Woo, G. Emergency planning and mitigation at Vesuvius: A new evidence-based approach. *Journal of Volcanology and Geothermal Research*, 178(3):454–473, 2008.

[325] Neri, A., Esposti Ongaro, T., Macedonio, G., and Gidaspow, D. Multiparticle simulation of collapsing volcanic columns and pyroclastic flow. *Journal of Geophysical Research: Solid Earth (1978–2012)*, 108(B4), 2003.

[326] Bonadonna, C. Probabilistic modelling of tephra dispersion. *Statistics in Volcanology, edited by: Mader, H. M., Coles, S. G., Connor, C. B., and Connor, L. J.*, pages 243–259, 2006.

[327] Saltelli, A., Tarantola, S., Campolongo, F., and Ratto, M. *Sensitivity analysis in practice: a guide to assessing scientific models*. John Wiley & Sons, 2004.

[328] Alberico, I., Lirer, L., Petrosino, P., and Scandone, R. Volcanic hazard and risk assessment from pyroclastic flows at Ischia island (southern Italy). *Journal of Volcanology and Geothermal Research*, 171(1):118–136, 2008.

[329] Valentine, G. A. and Giannetti, B. Single pyroclastic beds deposited by simultaneous fallout and surge processes: Roccamonfina volcano, Italy. *Journal of Volcanology and Geothermal Research*, 64(1-2):129–137, 1995.

[330] Watts, P. and Waythomas, C. Theoretical analysis of tsunami generation by pyroclastic flows. *Journal of Geophysical Research: Solid Earth (1978–2012)*, 108(B12), 2003.

[331] Paris, R. Source mechanisms of volcanic tsunamis. *Philosophical Transactions of the Royal Society of London. Series A, Mathematical and Physical Sciences*, 373(2053):20140380, 2015.

[332] Bartolini, S., Geyer, A., Martí, J., Pedrazzi, D., and Aguirre-Díaz, G. Volcanic hazard on Deception Island (South Shetland Islands, Antarctica). *Journal of Volcanology and Geothermal Research*, 285:150–168, 2014.

[333] Aspinall, W. P. and Woo, G. Santorini unrest 2011–2012: an immediate Bayesian belief network analysis of eruption scenario probabilities for urgent decision support under uncertainty. *Journal of Applied Volcanology*, 3(1): 12, 2014.

[334] Simoncini, M. When Science Meets Responsibility: The Major Risks Commission and the L'Aquila Earthquake. *The European Journal of Risk Regulation*, page 146, 2014.

[335] Bursik, M. Tephra dispersal. *Geological Society, London, Special Publications*, 145(1):115–144, 1998.

[336] Paguican, E. M. R., Lagmay, A. M. F., Rodolfo, K. S., Rodolfo, R. S., Tengonciang, A. M. P., Lapus, M. R., Baliatan, E. G., and Obille, E. C. Extreme rainfall-induced lahars and dike breaching, 30 November 2006, Mayon Volcano, Philippines. *Bulletin of Volcanology*, 71(8):845–857, 2009.

[337] Pierson, T. C., Janda, R. J., Umbal, J. V., and Daag, A. S. Immediate and long-term hazards from lahars and excess sedimentation in rivers draining Mt. Pinatubo, Philippines. *US Geological Survey Water-Resources Investigations Report*, 92:4039, 1992.

[338] Mignan, A., Wiemer, S., and Giardini, D. The quantification of low-probability–high-consequences events: part I. A generic multi-risk approach. *Natural Hazards*, 73(3):1999–2022, 2014.

[339] Liu, Z., Nadim, F., Garcia-Aristizabal, A., Mignan, A., Fleming, K., and Luna, B. Q. A three-level framework for multi-risk assessment. *Georisk:*

Assessment and Management of Risk for Engineered Systems and Geohazards, 9(2):59–74, 2015.

[340] Rodolfo, K. S. and Arguden, A. T. Rain-lahar generation and sediment delivery systems at Mayon Volcano, Philippines. *Special Publications of SEPM*, 1991.

[341] Tuñgol, N. M. and Regalado, M. T. M. Rainfall, acoustic flow monitor records, and observed lahars of the Sacobia River in 1992. *Fire and mud, eruptions and lahars of Mt Pinatubo, Philippines, edited by: Newhall, C. G., and Punongbayan, R. S.*, 1996.

[342] Berti, M., Martina, M., Franceschini, S., Pignone, S., Simoni, A., and Pizziolo, M. Probabilistic rainfall thresholds for landslide occurrence using a Bayesian approach. *Journal of Geophysical Research: Earth Surface (2003–2012)*, 117(F4), 2012.

[343] Jones, R., Manville, V., and Andrade, D. Probabilistic analysis of rain-triggered lahar initiation at Tungurahua volcano. *Bulletin of Volcanology*, 77(8), 2015.

[344] Frattini, P., Crosta, G. B., Fusi, N., and Dal Negro, P. Shallow landslides in pyroclastic soils: A distributed modelling approach for hazard assessment. *Engineering Geology*, 73(3-4):277–295, 2004.

[345] Iverson, R. M., Schilling, S. P., and Vallance, J. W. Objective delineation of lahar-inundation hazard zones. *Bulletin of the Geological Society of America*, 110(8):972–984, 1998.

[346] Iverson, R. M. and George, D. L. A depth-averaged debris-flow model that includes the effects of evolving dilatancy. I. Physical basis. *Proceedings of the Royal Society of London A: Mathematical, Physical and Engineering Sciences*, 470(2170), 2014.

[347] Iverson, R. M., George, D. L., Allstadt, K., Reid, M. E., Collins, B. D., Vallance, J. W., Schilling, S. P., Godt, J. W., Cannon, C., Magirl, C. S., et al. Landslide mobility and hazards: implications of the 2014 Oso disaster. *Earth and Planetary Science Letters*, 412:197–208, 2015.

[348] Gomes, R. A. T., Guimarães, R. F., Carvalho, O. A., Fernandes, N. F., Vargas, E. A., and Martins, É. S. Identification of the affected areas by mass

movement through a physically based model of landslide hazard combined with an empirical model of debris flow. *Natural Hazards*, 45(2):197–209, 2008.

[349] Fan, L., Lehmann, P., McArdell, B., and Or, D. Linking rainfall-induced landslides with debris flows runout patterns towards catchment scale hazard assessment. *Geomorphology*, 280:1–15, 2017.

[350] Chinen, T. Surface erosion associated with tephra deposition on Mt. Usu and other volcanoes. *Environmental science, Hokkaido: journal of the Graduate School of Environmental Science, Hokkaido University, Sapporo*, 9(1):137–149, 1986.

[351] Crosta, G. B. and Dal Negro, P. Observations and modelling of soil slip-debris flow initiation processes in pyroclastic deposits: the Sarno 1998 event. *Natural Hazards and Earth System Sciences*, 3(1/2):53–69, 2003.

[352] Le Treut, H., Somerville, R., Cubasch, U., Ding, Y., Mauritzen, C., Mokssit, A., Peterson, T., and Prather, M. Historical overview of climate change. *Climate change 2007: The physical science basis*, 2007.

[353] Houze, R. A. *Cloud dynamics*. Academic Press, 1993.

[354] Bernard, M. M. Formulas for rainfall intensities of long duration. *Transactions of the American Society of Civil Engineers*, 96(1):592–606, 1932.

[355] Chow, V. T., Maidment, D. R., and Mays, L. W. *Applied hydrology*. McGraw-Hill: New York, 1988.

[356] Thouret, J.-C. and Lavigne, F. Lahars: occurrence, deposits and behaviour of volcano-hydrologic flows. *Volcaniclastic Rocks, from Magmas to Sediments, edited by: Leyrit, H., and Montenat, C.*, pages 151–174, 2000.

[357] Yang, H., Wang, F., Vilímek, V., Araiba, K., and Asano, S. Investigation of rainfall-induced shallow landslides on the northeastern rim of Aso caldera, Japan, in July 2012. *Geoenvironmental Disasters*, 2(1):20, 2015.

[358] Gabet, E. J. and Dunne, T. Sediment detachment by rain power. *Water Resources Research*, 39(1), 2003.

[359] Reid, M. E. and Iverson, R. M. Gravity-driven groundwater flow and slope failure potential: 2. Effects of slope morphology, material properties, and hydraulic heterogeneity. *Water Resources Research*, 28(3):939–950, 1992.

[360] Tolentino, P. et al. Piano Stralcio per l'Assetto Idrogeologico: Relazione Idrologica (in Italian). Technical report, Autorità di Bacino Regionale della Campania Centrale, 2015. URL http://www.adbcampaniacentrale2.it/documenti/psai/relazioni/RelazioneIdrologica.pdf.

[361] Rossi, F. and Villani, P. Regional flood estimation methods. *Coping with floods, edited by: Rossi, G., Harmancioğlu, N., and Yevjevich, V.*, pages 135–169, 1994.

[362] Favalli, M., Pareschi, M., and Zanchetta, G. Simulation of syn-eruptive floods in the circumvesuvian plain (southern Italy). *Bulletin of Volcanology*, 68(4):349–362, 2006.

[363] De Vita, P., Agrello, D., and Ambrosino, F. Landslide susceptibility assessment in ash-fall pyroclastic deposits surrounding Mount Somma-Vesuvius: Application of geophysical surveys for soil thickness mapping. *Journal of Applied Geophysics*, 59(2):126–139, 2006.

[364] Leavesley, G., Lusby, G., and Lichty, R. Infiltration and erosion characteristics of selected tephra deposits from the 1980 eruption of Mount St. Helens, Washington, USA. *Hydrological Sciences Journal*, 34(3):339–353, 1989.

[365] Pistolesi, M., Cioni, R., Rosi, M., and Aguilera, E. Lahar hazard assessment in the southern drainage system of Cotopaxi volcano, Ecuador: Results from multiscale lahar simulations. *Geomorphology*, 207:51–63, 2014.

[366] Kottek, M., Grieser, J., Beck, C., Rudolf, B., and Rubel, F. World map of the Köppen-Geiger climate classification updated. *Meteorologische Zeitschrift*, 15(3):259–263, 2006.

[367] Rossi, F., Fiorentino, M., and Versace, P. Two-component extreme value distribution for flood frequency analysis. *Water Resources Research*, 20(7): 847–856, 1984.

[368] Macedonio, G., Costa, A., and Folch, A. Ash fallout scenarios at Vesuvius: numerical simulations and implications for hazard assessment. *Journal of Volcanology and Geothermal Research*, 178(3):366–377, 2008.

[369] Macedonio, G., Costa, A., and Longo, A. A computer model for volcanic ash fallout and assessment of subsequent hazard. *Computers & Geosciences*, 31(7):837–845, 2005.

[370] Ogburn, S. E. *Reconciling field observations of pyroclastic density currents with conceptual and computational analogs using a GIS and a newly developed global database*. PhD thesis, State University of New York at Buffalo, 2015.

[371] Díaz, M. C., Fernández-Nieto, E. D., and Ferreiro, A. Sediment transport models in shallow water equations and numerical approach by high order finite volume methods. *Computers & Fluids*, 37(3):299–316, 2008.

[372] Kean, J. W., McCoy, S. W., Tucker, G. E., Staley, D. M., and Coe, J. A. Runoff-generated debris flows: Observations and modeling of surge initiation, magnitude, and frequency. *Journal of Geophysical Research: Earth Surface*, 118(4):2190–2207, 2013.

[373] Reid, M. E. A pore-pressure diffusion model for estimating landslide-inducing rainfall. *The Journal of Geology*, 102(6):709–717, 1994.

[374] Bretton, R. J., Gottsmann, J., Aspinall, W. P., and Christie, R. Implications of legal scrutiny processes (including the L'Aquila trial and other recent court cases) for future volcanic risk governance. *Journal of Applied Volcanology*, 4(1):18, 2015.

[375] Thompson, M. A., Lindsay, J. M., Sandri, L., Biass, S., Bonadonna, C., Jolly, G., and Marzocchi, W. Exploring the influence of vent location and eruption style on tephra fall hazard from the Okataina Volcanic Centre, New Zealand. *Bulletin of Volcanology*, 77(5):38, 2015.

[376] Koutsoyiannis, D., Kozonis, D., and Manetas, A. A mathematical framework for studying rainfall intensity-duration-frequency relationships. *Journal of Hydrology*, 206(1-2):118–135, 1998.

[377] Valdes, J. B., Rodriguez-Iturbe, I., and Gupta, V. K. Approximations of temporal rainfall from a multidimensional model. *Water Resources Research*, 21(8):1259–1270, 1985.

[378] Goel, N., Kurothe, R., Mathur, B., and Vogel, R. A derived flood frequency distribution for correlated rainfall intensity and duration. *Journal of Hydrology*, 228(1):56–67, 2000.

[379] Suwa, H. and Sumaryono, A. Sediment discharge by storm runoff from a creek on Merapi volcano. *Journal of the Japan Society of Erosion Control Engineering*, 48(Special):117–128, 1996.

[380] Thouret, J.-C., Oehler, J.-F., Gupta, A., Solikhin, A., and Procter, J. N. Erosion and aggradation on persistently active volcanoes—a case study from Semeru Volcano, Indonesia. *Bulletin of Volcanology*, 76(10):857, 2014.

[381] Huffman, G. J., Adler, R. F., Arkin, P., Chang, A., Ferraro, R., Gruber, A., Janowiak, J., McNab, A., Rudolf, B., and Schneider, U. The global precipitation climatology project (GPCP) combined precipitation dataset. *Bulletin of the American Meteorological Society*, 78(1):5–20, 1997.

[382] Sinclair, S. and Pegram, G. Combining radar and rain gauge rainfall estimates using conditional merging. *Atmospheric Science Letters*, 6(1):19–22, 2005.

[383] Collins, B. D. and Dunne, T. Erosion of tephra from the 1980 eruption of mount st. helens. *Geological Society of America Bulletin*, 97(7):896–905, 1986.

[384] Huggel, C., Schneider, D., Miranda, P. J., Delgado Granados, H., and Kääb, A. Evaluation of ASTER and SRTM DEM data for lahar modeling: A case study on lahars from Popocatépetl Volcano, Mexico. *Journal of Volcanology and Geothermal Research*, 170(1-2):99–110, 2008.

[385] Gu, M., Berger, J. O., et al. Parallel partial Gaussian process emulation for computer models with massive output. *The Annals of Applied Statistics*, 10 (3):1317–1347, 2016.

[386] Hanea, A. M., Kurowicka, D., and Cooke, R. M. Hybrid method for quantifying and analyzing Bayesian belief nets. *Quality and Reliability Engineering International*, 22(6):709–729, 2006.

[387] De Bélizal, E., Lavigne, F., Hadmoko, D. S., Degeai, J. P., Dipayana, G. A., Mutaqin, B. W., Marfai, M. A., Coquet, M., Mauff, B. L., Robin, A. K., Vidal, C., Cholik, N., and Aisyah, N. Rain-triggered lahars following the 2010

eruption of Merapi volcano, Indonesia: A major risk. *Journal of Volcanology and Geothermal Research*, 261:330–347, 2013.

[388] Major, J. J. and Yamakoshi, T. Decadal-scale change of infiltration characteristics of a tephra-mantled hillslope at Mount St Helens, Washington. *Hydrological Processes*, 19(18):3621–3630, 2005.

[389] Ogawa, Y., Daimaru, H., and Shimizu, A. Experimental study of post-eruption overland flow and sediment load from slopes overlain by pyroclastic-flow deposits, Unzen volcano, Japan. *Géomorphologie: relief, processus, environnement*, 13(3):237–246, 2007.

[390] Marcial, S., Melosantos, A. A., Hadley, K. C., LaHusen, R. G., and Marso, J. N. Instrumental lahar monitoring at Mount Pinatubo. *Fire and mud: eruptions and lahars of Mount Pinatubo, Philippines, edited by: Newhall, C. G., and Punongbayan, R. S.*, pages 1015–1022, 1996.

[391] Ferrucci, M., Pertusati, S., Sulpizio, R., Zanchetta, G., Pareschi, M. T., and Santacroce, R. Volcaniclastic debris flows at La Fossa Volcano (Vulcano Island, southern Italy): Insights for erosion behaviour of loose pyroclastic material on steep slopes. *Journal of Volcanology and Geothermal Research*, 145(3-4):173–191, 2005.

[392] Hodgson, K. A. and Manville, V. R. Sedimentology and flow behavior of a rain-triggered lahar, Mangatoetoenui Stream, Ruapehu volcano, New Zealand. *Bulletin of the Geological Society of America*, 111(5):743–754, 1999.

[393] Waythomas, C. F., Scott, W. E., and Nye, C. J. The Geomorphology of an Aleutian Volcano following a Major Eruption: the 7–8 August 2008 Eruption of Kasatochi Volcano, Alaska, and Its Aftermath. *Arctic, Antarctic, and Alpine Research*, 42:260–275, 2010.

[394] Bremer, M. and Sass, O. Combining airborne and terrestrial laser scanning for quantifying erosion and deposition by a debris flow event. *Geomorphology*, 138(1):49–60, 2012.

[395] Amici, S., Turci, M., Giammanco, S., Spampinato, L., and Giulietti, F. UAV thermal infrared remote sensing of an Italian mud volcano. *Advances in Remote Sensing*, 2013, 2013.

[396] Calcaterra, D., Parise, M., and Palma, B. Combining historical and geological data for the assessment of the landslide hazard: a case study from Campania, Italy. *Natural Hazards and Earth System Sciences*, 3(1/2):3–16, 2003.

[397] Del Prete, M., Guadagno, F., and Hawkins, A. Preliminary report on the landslides of 5 May 1998, Campania, southern Italy. *Bulletin of Engineering Geology and the Environment*, 57(2):113–129, 1998.

[398] de Vita, P., Napolitano, E., Godt, J. W., and Baum, R. L. Deterministic estimation of hydrological thresholds for shallow landslide initiation and slope stability models: Case study from the Somma-Vesuvius area of southern Italy. *Landslides*, 10(6):713–728, 2013.

[399] D'Ambrosio, D., Di Gregorio, S., Iovine, G., Lupiano, V., Rongo, R., and Spataro, W. First simulations of the Sarno debris flows through cellular automata modelling. *Geomorphology*, 54(1):91–117, 2003.

[400] Doronzo, D. M. and Dellino, P. Pyroclastic density currents and local topography as seen with the conveyer model. *Journal of Volcanology and Geothermal Research*, 278:25–39, 2014.

[401] Hurvich, C. M. and Tsai, C.-L. Regression and time series model selection in small samples. *Biometrika*, pages 297–307, 1989.

[402] Cavanaugh, J. E. Unifying the derivations for the Akaike and corrected Akaike information criteria. *Statistics & Probability Letters*, 33(2):201–208, 1997.

[403] Geyer, A. and Marti, J. The new worldwide collapse caldera database (CCDB): A tool for studying and understanding caldera processes. *Journal of Volcanology and Geothermal Research*, 175(3):334–354, 2008.

[404] Nakada, S. Hazards from pyroclastic flows and surges. *Encyclopedia of volcanoes, edited by: Sigurdsson, H., Houghton, B. F., McNutt, S. R., Rymer, H., and Stix, J.*, pages 945–956, 2000.

[405] *MATLAB Release 2012b*. The MathWorks, Inc., Natick, Massachusetts, United States, 2012.